

**OXYGEN AND SULFUR FUGACITIES OF GRANITOIDS:
IMPLICATIONS FOR ORE-FORMING PROCESSES**

by

Daniel P. Core

A dissertation submitted in partial fulfillment
of the requirements for the degree of
Doctor of Philosophy
(Geology)
in The University of Michigan
2004

Doctoral Committee:

Professor Eric J. Essene, Co-Chair
Professor Stephen E. Kesler, Co-Chair
Professor Roy Clarke
Research Scientist Jeffrey C. Alt

© Daniel P. Core 2004
All Rights Reserved

To Sarah

Acknowledgments

I would like to start by thanking my my father, Douglas Core. He took me out in the field with him starting when I was about 10 years old and gave me a great foundation for my education as a geologist. I would also like to thank Lori Bettison-Varga of the College of Wooster for getting me started in geological research.

This dissertation would not be possible without academic support from many people. First of all I would like to thank my advisors, Eric Essene and Steve Kesler, who expended considerable effort and funds in helping me complete this dissertation. Without such deep involvement from both of them this project would have been much less interesting and fruitful..

Many other faculty and staff at Michigan contributed to the work in this thesis and other research I completed in the process. Carl Henderson provided valuable guidance in doing SEM and EMPA work. Jeff Alt helped improve my understanding of sulfur geochemistry. Bjorn Klaue helped to develop a new sulfur extraction technique for sulfur isotope analysis.. Roy Clarke and Eric Dufresne of the Physics Department provided guidance in doing synchrotron XRF analyses. Jim Hinchcliff made in excess of 1000 polished thin sections for this work and was very accommodating for special requests and rush jobs. Lora Wingate and Ted Moore assisted by providing equipment and reagents for sulfur extractions. Dale Austin drafted several maps including those shown in *Chapter V*.

Several people outside of the department also provided academic support. I would like to start off with a special thank you to Ian Campbell and Charlotte Allen of Australian National University for giving me the opportunity to travel to Australia to learn LA-ICPMS dataing and geochemical analysis. This study would have been incomplete without Tom Vogel of Michigan State University, who provided numerous samples from the intrusive and volcanic rocks of the Wasatch Range. I also had many discussions with Tom that improved my understanding of the petrology of the Wasatch Range. Lina Patino of Michigan State University made LA-ICPMS measurements of Batu Hijau zircons for *Chapter III*. John Dilles of Oregon State University provided samples from the Yerington district and helped me understand the importance of apatite during the crystallization of granitoids. Steve Garwin of GeoInformex provided samples from Batu Hijau and greatly assisted in my understanding of the geology of that district. Paula Cornejo and Steve Matthews of Sernageomin guided field work in Chile and provided me with a good background on the geology of central Chile. Enrique Tidy of Codelco arranged for me to receive about 225 samples from Codelco studies of El Teniente and Rio Blanco-Los Bronces. Bob North, Dave Princehouse, Paul Novotny, Jeff Gerwe, and Will Wilkinson of PhelpsDodge guided much of my field work in New Mexico and Arizona. Mark Rivers of the University of Chicago provided necessary equipment and software and a great deal of advice on synchrotron XRF measurements. Dohn Arms and Don Walko of Argonne National Labs assisted with synchrotron XRF measurements. Ezra Inan and Patrick Redmond of Stanford University guided my sampling of the Last Chance stock at the Bingham Mine in Utah and provided samples of the porphyritic intrusions at Bingham. Ed Harrison of Kennecott Utah Copper graciously provided access to drill core and outcrops at the Bingham Mine for

sampling. Cam Allen, Fernando Teliz, Alberto Toledo, and Diego Fernandez of Cominco arranged for my access to mine properties in Mexico. Rafael Paz of Cominco was my field assistant in Mexico and was essential to my completion of that field work. Panteleon Trejo of Penoles provided unlimited access to any of Penoles's Pb-Zn CRD deposits. Jim Lange of Lange Geosciences provided 50 thin sections from Copper Mountain and Afton in British Columbia. Fred Graybeal of Asarco arranged for access to the Ray Mine and David Borrok assisted with sampling at the Ray Mine.

In addition to all the academic support, I would like to thank my friends at Michigan that were there to have discussions both academic and not. I particularly want to thank Chris Palenik, Holli Frey, Kate Kenedi, Bret Peppard, Chris Smith, and Martin Reich. I would also like to thank all my friends outside of the U of M. Especially Joe Dzuban who was my field assistant during my fieldwork in the western US.

I want to thank my family for their support and being there when I needed to complain. Hopefully they can finally stop making fun of me for being an eternal student. I would never have been able to get where I am without the love and support of my Mom and Dad. I would also like to thank my brother Doug for being my field assistant in British Columbia and for helping me write computer programs for data reduction. My brother Eric helped me get through the writing process. Finally, I would like to thank Sarah Belfield, my wife; though not around for much of this journey she gave me the incentive I needed to finish.

This work was funded under NSF grant EAR 0230098 to Eric Essene and an industry grant from BHPBilliton to Steve Kesler. Additional funding was provided by PhelpsDodge, Asarco, and Cominco. Student grants were obtained from the Geological Society of America

and Society of Economic Geologists. Two Turner Grants were awarded to support this work. The microprobes used in this work were purchased by University and NSF funds with grants EAR 82-12764 and EAR 99-11352 to EJE.

Table of Contents

Dedication	ii
Acknowledgments	iii
List of Figures	x
List of Tables	xii
List of Appendices	xiv
Chapter I: Introduction	1
References	4
Chapter II: Evaluation of Oxygen Fugacity in Intermediate Igneous Rocks	6
Abstract	6
Introduction	6
Experimental Technique	8
Analytical Methods	10
Description of Charges and Mineral Compositions	10
<i>Clinopyroxene</i>	<i>12</i>
<i>Plagioclase</i>	<i>12</i>
<i>Magnetite</i>	<i>17</i>
<i>Hematite</i>	<i>17</i>
Indications of Equilibrium	17
<i>Textural Observations</i>	<i>17</i>
<i>Chemical Constraints</i>	<i>23</i>
Calculations of fO_2	23
<i>Methods</i>	<i>23</i>
<i>Results</i>	<i>25</i>
Discussion	30
<i>Two-oxide thermometry</i>	<i>30</i>
<i>Two-oxide fO_2 calculations</i>	<i>33</i>
<i>Clinopyroxene-oxide equilibria</i>	<i>35</i>
<i>Pyroxene-plagioclase-oxide equilibria</i>	<i>36</i>
Conclusions	37
References	38
Chapter III: Oxygen Fugacity of Granitoids: Implications for Magma Source Regions and Genesis of Sulfur-Rich Magmas	40
Abstract	40
Introduction	41
fO_2 of Calc-Alkaline Magmas	42
Geologic Settings	43

<i>Bingham-Park City belt, Utah</i>	43
<i>Batu Hijau, Indonesia</i>	44
<i>El Teniente-Andina belt, Chile</i>	44
<i>Copper Mountain, British Columbia</i>	45
<i>Providencia-Concepcion del Oro district, Zacatecas, Mexico</i>	45
Analytical Methods	46
<i>Electron Microprobe</i>	46
<i>SEM-EDS Analyses</i>	46
<i>Laser ablation ICP-MS</i>	47
Mineral Compositions	48
<i>Clinopyroxene</i>	50
<i>Orthopyroxene</i>	50
<i>Magnetite</i>	56
<i>Ilmenite</i>	56
<i>Sphene</i>	65
fO₂ Calculations	65
<i>Reactions for fO₂ Calculations</i>	65
<i>Estimating aSiO₂</i>	66
<i>Results</i>	66
Zircon Analyses	67
Discussion	67
<i>Recording of fO₂</i>	67
<i>Magmatic source regions of granitoids</i>	76
<i>Behavior of sulfur in granitoids</i>	77
<i>Evaluation of zircon oxybarometer</i>	80
<i>Implications for formation of magmatic-hydrothermal ore deposits</i>	81
References	84
Chapter IV: Thermodynamic Properties of Sulfatite Apatite: Constraints on the Behavior of Sulfur in Calc-Alkaline Systems	91
Abstract	91
Introduction	91
Experimental Technique	92
Occurrence of Apatite in Experimental Charges	93
Free Energy Calculations	95
Independent Estimation of Entropy	97
Discussion	100
<i>Controls on sulfur content of apatite</i>	100
<i>Implications for sulfur zoning in apatite</i>	103
Conclusions	106
References	108
Chapter V: Cu-rich Source Region for Giant Porphyry Copper Deposits:	111
Last Chance Stock, Bingham, Utah	111
Abstract	111
Introduction	111
Geologic Setting of the Sulfide-rich Enclaves	112

Discussion	116
<i>Source of enclaves</i>	<i>116</i>
<i>Cu-rich source region for Bingham magmas</i>	<i>119</i>
<i>Genesis of Cu-rich source regions</i>	<i>120</i>
References	122
Chapter VI: Conclusions	124
Introduction	124
Role of sulfides in magmatic processes	124
Biotite as a sulfur barometer	126
References	128

List of Figures

Figure 2.1. BSE images of charges.	11
Figure 2.2. Ternary diagram showing the major M1 cations in the experimental clinopyroxene.	16
Figure 2.3. Ternary diagram showing the composition of experimental plagioclase.	16
Figure 2.4. Ternary diagram showing composition of experimental oxides.	22
Figure 2.5. Oxide compositions plotted on log Mg/Mn (ilmenite) vs log Mg/Mn (magnetite) plot as suggested by Bacon and Hirschmann (1988) as a test for equilibrium.	22
Figure 2.6. Temperature difference between calculated values and experiments for the charges using reaction 1 (Fe-Ti exchange).	27
Figure 2.7. Difference between calculated fO_2 and experimental fO_2 vs T using reaction 2 (magnetite-hematite).	28
Figure 2.8. A. Difference between calculated and experimental fO_2 for Reactions 3 (ferrosilite- magnetite-quartz) and 4 (ferrosilite-hematite-quartz) using QUILF activity models.	29
Figure 2.9. Difference between calculated and experimental fO_2 for Reactions 7 (hedenbergite- anorthite-magnetite-esseneite-quartz) and 8 (hedenbergite-anorthite-hematite-esseneite- quartz) using MELTS mixing models.	31
Figure 3.1. BSE images showing occurrence of silicate and oxide minerals.	49
Figure 3.3. Ternary plot showing oxide compositions with the regions of interest blown up. ...	63
Figure 3.4. Mg/Mn plot of oxide composition.	64
Figure 3.5. Histograms showing the distribution of calculated fO_2	70
Figure 3.6. Plot showing calculated Ce^{4+}/Ce^{3+} of zircon vs. sample fO_2	72
Figure 3.7. Plot showing calculated Ce^{4+}/Ce^{3+} in zircon vs. whole rock wt% SiO_2	72
Figure 3.8. Calculated Ce^{4+}/Ce^{3+} for zircon vs. U-Pb zircon ages for samples from Batu Hijau, Indonesia.	73
Figure 3.9. Valence of sulfur calculated using the equation of Wallace and Carmichael (1994) plotted against fO_2	79
Figure 3.10. fO_2 vs. U-Pb zircon age for samples from Batu Hijau, Indonesia.	83
Figure 3.11. fO_2 vs. U-Pb zircon age for samples from Bingham-Park City belt in Utah.	83
Figure 4.1. A. BSE image showing euhedral grains in a glassy matrix. The vapor bubbles	

demonstrate that the charge was vapor-saturated. The image also shows the occurrence of apatite in the vapor bubbles. B. BSE image showing euhedral oxides and plagioclase in glassy matrix. Apatite occurs as a euhedral grain with plagioclase.	94
Figure 4.2 ΔG vs T diagram for $\text{Ca}_{10}(\text{SiO}_4)_3(\text{SO}_4)_3(\text{OH})_2$ using Reactions 1-3.	98
Figure 4.3. $f\text{O}_2$ - $f\text{S}_2$ diagram showing the locus of Reactions 1-3.	102
Figure 4.4. A. Cathodoluminescence image of apatite from the Ruby Star granodiorite, Arizona. B. Element map of sulfur K α peak made using an electron microprobe. The core is enriched in sulfur, followed by an intermediate zone, and a depleted rim. C. Element map of the Ce L α peak showing that the distribution of REE is identical to the cathodoluminescence.	105
Figure 4.5. Core to rim traverse of grain shown above showing variations in sulfur content. .	105
Figure 5.1. Geological map of the Bingham Park City Belt showing location of major intrusions.	113
Figure 5.2. Geological map of the Bingham district showing major intrusions and dikes.	113
Figure 5.3. View of the largest enclave showing abundant oxide and sulfide grains.	114
Figure 5.4. BSE images showing textures in the enclaves from the Last Chance stock.	115
Figure A1.1. User interface for zircon data reduction showing the program options.	132
Figure A1.2. Screen shot of analysis start and end selection.	134
Figure A1.3. Screen shot of user interface for drift correction.	136
Figure A3.1. Flow chart showing the steps of the sulfur extraction procedure.	207
Figure A3.2. Geologic map of the Hanover-Fierro and Santa Rita districts showing intrusions and locations of deposits.	210
Figure A3.3. Textural relationships of anhydrite and pyrite in the Hanover-Fierro stock.	211
Figure A3.4. Geologic map of the Bingham-Park City belt showing location of intrusive rocks and ore bodies	213
Figure A3.5. Fraction of sulfide sulfur plotted against the $\delta^{34}\text{S}$ of the sulfide sulfur.	221

List of Tables

Table 2.1. Experimental conditions of charges from Luhr (1990).	9
Table 2.2. Clinopyroxene compositions from the experimental charges.	13
Table 2.3. Plagioclase compositions with activities calculated using the MELTS activity models. 15	
Table 2.4. Spinel compositions for the charges including activities calculated using both MELTS and QUILF activity models.	18
Table 2.5. Hematite compositions for the charges with activities calculated using the QUILF and MELTS activity models.	20
Table 2.6A. fO_2 and T calculated using the QUILF activity models	26
Table 2.6B. fO_2 and T calculated using the MELTS activity models	26
Table 3.1. Clinopyroxene compositions determined by EMPA.	51
Table 3.2. Orthopyroxene compositions determined by EMPA.	54
Table 3.3. Magnetite compositions determined by EDS and EMPA.	57
Table 3.4. Ilmenite compositions determined by EDS.	61
Table 3.5. fO_2 calculated for all samples using MELTS activity models relative to NNO.	68
Table 3.5 (cont'd). fO_2 calculated for all samples using MELTS activity models relative to NNO.	69
Table 3.6. Age and Ce^{4+}/Ce^{3+} for zircons determined by LA-ICPMS.	71
Table 5.1. Mineral compositions of mafic silicates in the enclaves and adjacent Last Chance stock showing that the compositions are similar.	117
Table 5.2. Analyses of sulfides from enclaves in the Last Chance stock.	118
Table A1.1. File format for input into zircon data reduction.	131
Table A1.2. Format for comma delimited standard composition file 610.comp.	134
Table A2.1. Format of Excel file for submitting data to MELTS website for feldspars.	187
Table A2.2. Blank form for submitting data to MELTS website for plagioclase compositions. 188	
Table A2.3. Format for input reactions.	194.
Table A3.1. Results of standard extractions.	215
Table A3.2A. Sulfur content of granitoid sample in ppm for various forms of sulfur.	216

Table A3.2B. Sulfur isotopic composition of granitoid samples in per mil relative to Canyon Diablo Troilite for various forms of sulfur.	217
Table A4.1. SXRF analyses of unaltered biotite.	230
Table A4.2. SXRF analyses of high-Cu biotite.	231
Table A4.3. SXRF analyses of chlorite.	232
Table A4.4. SXRF analyses unaltered clinopyroxene.	232
Table A4.5. SXRF analyses of high-Cu clinopyroxene.	232
Table A4.6. SXRF analyses of unaltered hornblende.	233
Table A4.7. SXRF analyses of high-Cu hornblende.	233
Table A4.8. SXRF analyses of unaltered magnetite.	234
Table A4.9. SXRF analyses of high-Cu magnetite.	234
Table A4.10. SXRF analyses of unaltered ilmenite.	235
Table A4.11. SXRF analyses of unaltered feldspars.	235
Table A4.12. SXRF analyses of unaltered feldspars.	236
Table A5.1. Additional field areas not included in <i>Chapter III</i>	245

List of Appendices

Appendix I: Source Code for Zircon U-Pb Age Dating and REE Chemistry	130
Appendix II: Source Code for MELTS fO_2 Calculations	186
Appendix III: Sulfur Isotopic Composition of Sulfide and Sulfate in Granitoids	203
Appendix IV: Copper and Zinc Content of Magmatic Silicate and Oxide Minerals	226
Appendix V: Additional Field Locations	244

Chapter I

Introduction

Intermediate magmas are important for their potential in forming ore deposits and impacting the environment with their eruptions. They represent the largest volume of magma that reaches the upper crust and surface in subduction zones. Therefore, the genesis and crystallization of intermediate magmas is crucial to our understanding of subduction zone magmatism. The variables oxygen fugacity (fO_2) and sulfur fugacity (fS_2) are important in determining the conditions during formation and crystallization of calc-alkaline magmas.

This work was undertaken in order to systematically evaluate the oxidation and sulfidation history of granitoids and their implications for the formation and crystallization of granitoid magmas. It has long been recognized that granitoids crystallize under variable fO_2 conditions (Haggerty, 1976). The classification of magnetite and ilmenite series granitoids was related to variations in oxidation (Ishihara, 1981). Although useful in distinguishing granitic rocks of different source regions, this classification is an oversimplification because in each of these groups there is a large variation in fO_2 , and at high fO_2 magmas will saturate with respect to hematite-rich ilmenite in addition to magnetite. Detailed studies of the fO_2 of intrusive rocks are necessary to understand the processes occurring during crystallization.

Previous attempts to quantify fO_2 in granitoids using the two-oxide method of Buddington and Lindsley (1964) failed to produce meaningful results (Dilles, 1987; Cornejo and Mahood, 1997). These results may have been due to resetting or lack of calibration of the activity models for magnetite and ilmenite. In *Chapter II*, the two oxide

method is applied to experimental charges from Luhr (1990) in order to evaluate the latest calibration of the MELTS (Ghiorso and Sack, 1995) and QUILF (Andersen et al., 1993) mixing models. Equilibria between clinopyroxene and oxides are also evaluated. The mixing models are compared to determine the cause of discrepancies between them and expected errors are evaluated for MELTS and QUILF calculations. Problems with previous calculations on intrusive rocks are discussed and a method is described for calculating fO_2 of oxidized samples.

In *Chapter III* the equilibria discussed in *Chapter II* are applied to granitoids from the western United States, British Columbia, Chile, Mexico, and Batu Hijau. Estimated fO_2 is compared to literature data on fO_2 of andesites to evaluate the source regions of granitoids (Carmichael and Ghiorso, 1990; Lange and Carmichael, 1996). Zircons were analyzed by LA-ICPMS for U-Pb geochronology and trace element composition. A potential oxybarometer using zircon geochemistry is evaluated by comparing Ce^{4+}/Ce^{3+} in zircon to calculated fO_2 for a range of samples (Ballard et al., 2002). Variation of Ce^{4+}/Ce^{3+} and fO_2 with time provides information on the evolution of arcs. The valence of sulfur in the magma is determined using the method of Wallace and Carmichael (1994) and the effect of fO_2 on the compositions of magmatic vapor phases is evaluated (Giggenbach, 1987).

The stability of sulfur-bearing phases and the solubility of sulfur during crystallization of granitoids are dependent on the magmatic fO_2 - fS_2 conditions. Most granitoids lack significant levels of magmatic sulfide or anhydrite, making it difficult to determine magmatic fS_2 . In most oxidized intrusions the primary host of sulfur is apatite. In *Chapter IV* the thermodynamic properties of sulfatian apatite (Rouse and Dunn, 1982) are estimated using equilibria between apatite, silicates, oxides and melt in the experimental charges of Luhr (1990). Magmatic fS_2 is estimated for several intrusions in the western United States, Chile, and Mexico using equilibria involving apatite. Sulfur zoning of apatite has been reported in granitoid intrusions (Streck and Dilles, 1998).

Similar zoning is described from intrusions in the western United States and the controls on such zoning are evaluated.

Granitoid magmas can be associated with ore deposit formation and sulfur-rich volcanic eruptions. Average granitoid stocks carry enough metals and sulfur to form small porphyry copper deposits (Cline and Bodnar, 1991). However, magmas associated with giant ore deposits that contain more than an order of magnitude more copper and sulfur must be enriched with respect to these elements. In *Chapter V* sulfide-rich mafic enclaves from the Last Chance stock are described. Implications for the source regions of copper- and sulfur-rich magmas are discussed with emphasis on the distribution of copper and sulfur in the lower crust.

References

- Andersen, D. J., Lindsley, D. H., and Davidson, P. M., 1993, QUILF: a Pascal program to assess equilibria among Fe-Mg-Mn-Ti oxides, pyroxenes, olivine, and quartz: Computers & Geosciences, v. 19, p. 1333-1350.
- Ballard, J. R., Palin, J. M., and Campbell, I. H., 2002, Relative oxidation states of magmas inferred from Ce(IV)/Ce(III) in zircon: application to porphyry copper deposits of northern Chile: Contributions to Mineralogy and Petrology, v. 144, p. 347-364.
- Carmichael, I. S. E., and Ghiorso, M. S., 1990, The effect of oxygen fugacity on the redox state of natural liquids and their crystallizing phases: Reviews in Mineralogy, v. 24, p. 191-212.
- Cline, J. S., and Bodnar, R. J., 1991, Can economic porphyry copper mineralization be generated by a typical calc-alkaline melt?: Journal of Geophysical Research, B, Solid Earth and Planets, v. 96, p. 8113-8126.
- Cornejo, P. C., and Mahood, G. A., 1997, Seeing past the effects of re-equilibration to reconstruct magmatic gradients in plutons; La Gloria Pluton, central Chilean Andes: Contributions to Mineralogy and Petrology, v. 127, p. 159-175.
- Dilles, J. H., 1987, Petrology of the Yerington Batholith, Nevada; evidence for evolution of porphyry copper ore fluids: Economic Geology, v. 82, p. 1750-1789.
- Ghiorso, M. S., and Sack, R. O., 1995, Chemical mass transfer in magmatic processes. IV. A revised and internally consistent thermodynamic model for the interpolation and extrapolation of liquid-solid equilibria in magmatic systems at elevated temperatures and pressures: Contributions to Mineralogy and Petrology, v. 119, p. 197-212.
- Giggenbach, W. F., 1987, Redox processes governing the chemistry of fumarolic gas discharges from White Island, New Zealand: Applied Geochemistry, v. 2, p. 143-161.
- Haggerty, S. E., 1976, Opaque mineral oxides in terrestrial igneous rocks, *in* Douglas

- Rumble, I., ed., Oxide Minerals: Reviews in Mineralogy, p. 1-177.
- Ishihara, S., 1981, The granitoid series and mineralization, *in* Skinner, B., ed., Economic Geology 75th Anniversary Volume: Economic Geology Publishing Company, Lancaster, PA, p. 458-484.
- Lange, R. A., and Carmichael, I. S. E., 1996, The Aurora volcanic field, California-Nevada; oxygen fugacity constraints on the development of andesitic magma: Contributions to Mineralogy and Petrology, v. 125, p. 167-185.
- Luhr, J. F., 1990, Experimental phase relations of water- and sulfur-saturated arc magmas and the 1982 eruptions of El Chichon Volcano: Journal of Petrology, v. 31, p. 1071-1114.
- Rouse, R. C., and Dunn, P. J., 1982, A contribution to the crystal chemistry of ellestadite and the silicate sulfate apatites: American Mineralogist, v. 67, p. 90-96.
- Streck, M. J., and Dilles, J. H., 1998, Sulfur evolution of oxidized arc magmas as recorded in apatite from a porphyry copper batholith: Geology, v. 26, p. 523-526.
- Wallace, P. J., and Carmichael, I. S. E., 1994, S speciation in submarine basaltic glasses as determined by measurements of S K- α X-ray wavelength shifts: American Mineralogist, v. 79, p. 161-167.

Chapter II

Evaluation of Oxygen Fugacity in Intermediate Igneous Rocks

Abstract

Mineral equilibria were applied to experimental charges from Luhr (1990) to evaluate the use of mineral equilibria to determine fO_2 of oxidized intermediate igneous rocks. Two-oxide and pyroxene-oxide equilibria were applied using both the MELTS (Ghiorso and Sack, 1995) and QUILF (Andersen et al., 1993). Two-oxide thermometry fails in all cases with MELTS overestimating and QUILF underestimating temperature. Using the experimental temperature calculated fO_2 was within 0.4 log units using both methods for charges equilibrated at the manganosite-hausmanite (MnH) oxygen buffer using the two-oxide method. These errors increase to 0.7 log units for charges equilibrated at magnetite-hematite (MH). Evaluation of the mixing models shows that most of the differences in the calculations involve the treatment of the rhombohedral oxide. Pyroxene-oxide equilibria produced similar results with fO_2 estimates approximately 0.5 log units too low at MnH and 1 log unit too low at MH. The MELTS models produced more consistent results than the QUILF models and produced more accurate results at high temperature. Calculations using the esseneite component of clinopyroxene with the MELTS mixing models produce estimates of fO_2 more than 2 log units above the experimental value at 800°C but is accurate at 950°C. This is most likely due to ordering of Al and Fe^{3+} at low temperature, changing the a-X relations in the clinopyroxene.

Introduction

Oxygen fugacity plays an important role in the stability of iron- and sulfur-bearing minerals during crystallization of intermediate magmas. Estimates of fO_2 in volcanic rocks

are commonly based on their bulk $\text{Fe}^{3+}/\text{Fe}^{2+}$ ratio (Kress and Carmichael, 1991). This technique only works when applied to rocks that correspond in composition to the parent magma. Intermediate intrusive rocks (i.e. granitoids) probably do not have the same composition as the magma that formed them. The evolving magmas generally exsolve hydrothermal fluids and often undergo subsolidus alteration and reequilibration. Mafic intrusive rocks form cumulates and undergo fractionation, such that no single rock composition ever corresponds to the parent liquid.

Estimation of $f\text{O}_2$ in plutonic rocks is based on mineral equilibria involving O_2 and knowledge of temperature. The most commonly used method, known as the “two-oxide method”, is based on reactions between magnetite-ulvöspinel and hematite-ilmenite solid solutions (Buddington and Lindsley, 1964). It uses the reaction:



to determine temperature and the reaction:



for calculation of $f\text{O}_2$. This method is currently only applicable to samples that equilibrated at $f\text{O}_2$ less than one log unit above the nickel-nickel oxide oxygen buffer (NNO+1) because experiments at higher $f\text{O}_2$ have not been incorporated into the mixing models. Application of this method to felsic intrusive rocks that crystallized at $f\text{O}_2$ above NNO+1 typically produces temperatures well below possible magmatic conditions and yields unreasonably high $f\text{O}_2$ (Dilles, 1987; Cornejo and Mahood, 1997). This method often overestimates both temperature and $f\text{O}_2$ when applied to oxidized, felsic volcanic rocks that formed at $f\text{O}_2$ above NNO+1 (Scaillet and Evans, 1999).

Experimental data at high $f\text{O}_2$ are required to improve the mixing models for magnetite and hematite for application of the two oxide method to more oxidized conditions. The available experimental data on natural compositions at high $f\text{O}_2$ are on dacite and rhyolite bulk compositions (Scaillet and Evans, 1999) or on the pure Fe-Ti-O system (Lattard et al., 2003). Scaillet and Evans (1999) found that the model of Ghiorso

and Sack (1991) overestimates both T and fO_2 under oxidized conditions. They determined that the Pinatubo dacite most likely crystallized at 1.7 log units above NNO instead of 2.5-3 log units above NNO determined by previous studies (Hattori, 1993; Imai et al., 1993; Hattori, 1996). Lattard et al. (2003) showed that ilmenite compositions do not change significantly with T at high fO_2 where $X_{ilm} < 0.64$. This is consistent with the newly revised version of the Ghiorso and Sack (1991) mixing model by Ghiorso et al. (2003) but does not fit the QUILF mixing model. This study was undertaken in order to evaluate the application of mineral equilibria in Table 1 to oxidized igneous rocks of intermediate composition. The composition of oxides and silicates were analyzed in the experimental run products of Luhr (1990) on a trachyandesite that was equilibrated at high fO_2 . Variations of the mineral compositions in this study provide a new set of data for use in improving activity models for oxides and silicates. They also offer a means of estimating the expected errors for fO_2 calculations in andesites and granitoids.

Experimental Technique

Luhr (1990) presented details of the experimental technique. The starting material for all experiments in his study was an El Chichon trachyandesite doped with anhydrite. The experiments were run at temperatures of 800, 850, 900, or 950°C and pressures of 2, 2.5, or 4 kbar in an internally heated pressure vessel (Table 2.1). All experiments were run under volatile saturated conditions as evidenced by the presence of voids in the glass (Fig. 2.1). Oxygen fugacity of the charges was buffered using manganosite-hausmanite (MnH) or magnetite-hematite (MH) in double gold capsules. The experiments were not reversed, so mineralogical and chemical evidence must be used to test whether equilibrium was approached. Luhr (1990) demonstrated systematic changes in mineralogy and glass compositions of the charges with changing fO_2 , T, and P. Housh and Luhr (1991) showed systematic compositional changes in plagioclase, with Ca increasing with T, and Na decreasing with T. Equilibrium was evaluated further in this study using mineral compositions.

Table 2.1. Experimental conditions of charges from Luhr (1990). H_2O was calculated as the difference between the microprobe total for the glass and 100. Also shown are the $a(SiO_2)$ relative to both silica glass and quartz.

Samples	104	105	114	119	139	149	165	169
fO_2 buffer	MnH	MH	MH	MH	MH	MnH	MnH	MnH
Absolute fO_2	-7.30	-9.46	-7.35	-6.42	-8.35	-9.98	-9.00	-8.12
fO_2 rel MH	-0.88	0.00	0.00	0.00	0.00	-0.52	-0.65	-0.77
$T(^{\circ}C)$	950	800	900	950	850	800	850	900
P(bars)	2000	2000	2000	2000	2000	2000	2000	2000
H_2O (wt. %)	7.98	8.7	8.25	6.97	8.48	8.89	10.1	8.31
$a(SiO_2)$ (rel. silica glass)	0.374	0.456	0.404	0.379	0.433	0.452	0.418	0.399
$a(SiO_2)$ (rel. quartz)	0.504	0.691	0.565	0.512	0.629	0.684	0.606	0.558
Samples	181	189	193	195	203	263	268	
fO_2 buffer	MH	MnH	MH	MH	MnH	MnH	MH	
Absolute fO_2	-7.31	-7.99	-9.42	-9.42	-9.83	-9.94	-9.45	
fO_2 rel MH	0.00	-0.67	0.00	0.00	-0.41	-0.49	0.00	
$T(^{\circ}C)$	900	900	800	800	800	800	800	
P(bars)	4000	4000	4000	4000	4000	2500	2500	
H_2O (wt. %)	12.51	11.23	10.56	12.21	10.8	9.87	10.25	
$a(SiO_2)$ (rel. silica glass)	0.371	0.362	0.421	0.479	0.423	0.444	0.446	
$a(SiO_2)$ (rel. quartz)	0.570	0.556	0.706	0.804	0.711	0.689	0.694	

MH = Magnetite-hematite. MnH = Manganosite-hausmanite

Analytical Methods

The necessary phases in each charge were analyzed using the Cameca SX-100 electron microprobe at the University of Michigan. Plagioclase, pyroxene, magnetite, and ilmenite were analyzed with a 15 kV accelerating potential and beam currents of 10, 15, 20, and 20 nA, respectively. A focused beam was used to analyze all minerals except plagioclase, which was analyzed with a 5 μm rastered beam in order to minimize beam damage. All analyses were corrected using the Cameca PAP program. The following standards were used for pyroxenes: Na and Fe on acmite (ACM), Ca, Si, and Mg on diopside (PX69), Al on jadeite (JADE), Ti on synthetic geikielite (GEIK), and Mn on rhodonite (BHRH). The following standards were used for magnetite and ilmenite: Fe on Elba hematite (HEMA), Ti on natural ilmenite (ILM), Al and Si on Ingamells almandine (IALM), Mg on synthetic geikielite (GEIK), Mn on synthetic MnFe_2O_4 (JACB) or Broken Hill rhodonite (BHRH), V on synthetic V_2O_5 (V2O5), Ca on Irving diopside (PX69), and Cr on synthetic Cr_2O_3 (CROX), or synthetic uvarovite (UVAR). The following standards were used for plagioclase: Na on Tiburon albite (TAB), Ca and Al on natural tanzanite (TANZ), K and Si on natural microcline (GKFS), Fe on Ingamells almandine (IALM), Mg on synthetic geikielite (GEIK), and Ba on synthetic Ba-chlorapatite (BACL). Pyroxene and oxide analyses were evaluated for $\text{Fe}^{3+}/\text{Fe}^{2+}$ using the method of Droop (1987). Measurements of glass composition were obtained with 12 kV accelerating potential and 1-2 nA sample current and confirmed the accuracy of the results obtained by Luhr (1990).

Description of Charges and Mineral Compositions

The charges consist of coarse, euhedral crystals of clinopyroxene, plagioclase, apatite, magnetite \pm hematite \pm hornblende \pm biotite \pm K-feldspar in a groundmass of glass (Figure 2.1). Compositions were determined for magnetite, hematite, clinopyroxene, and plagioclase for mineral equilibrium calculations. Glass analyses from Luhr (1990) were used for the glass chemistry.

Several grains of each mineral were analyzed and average compositions were

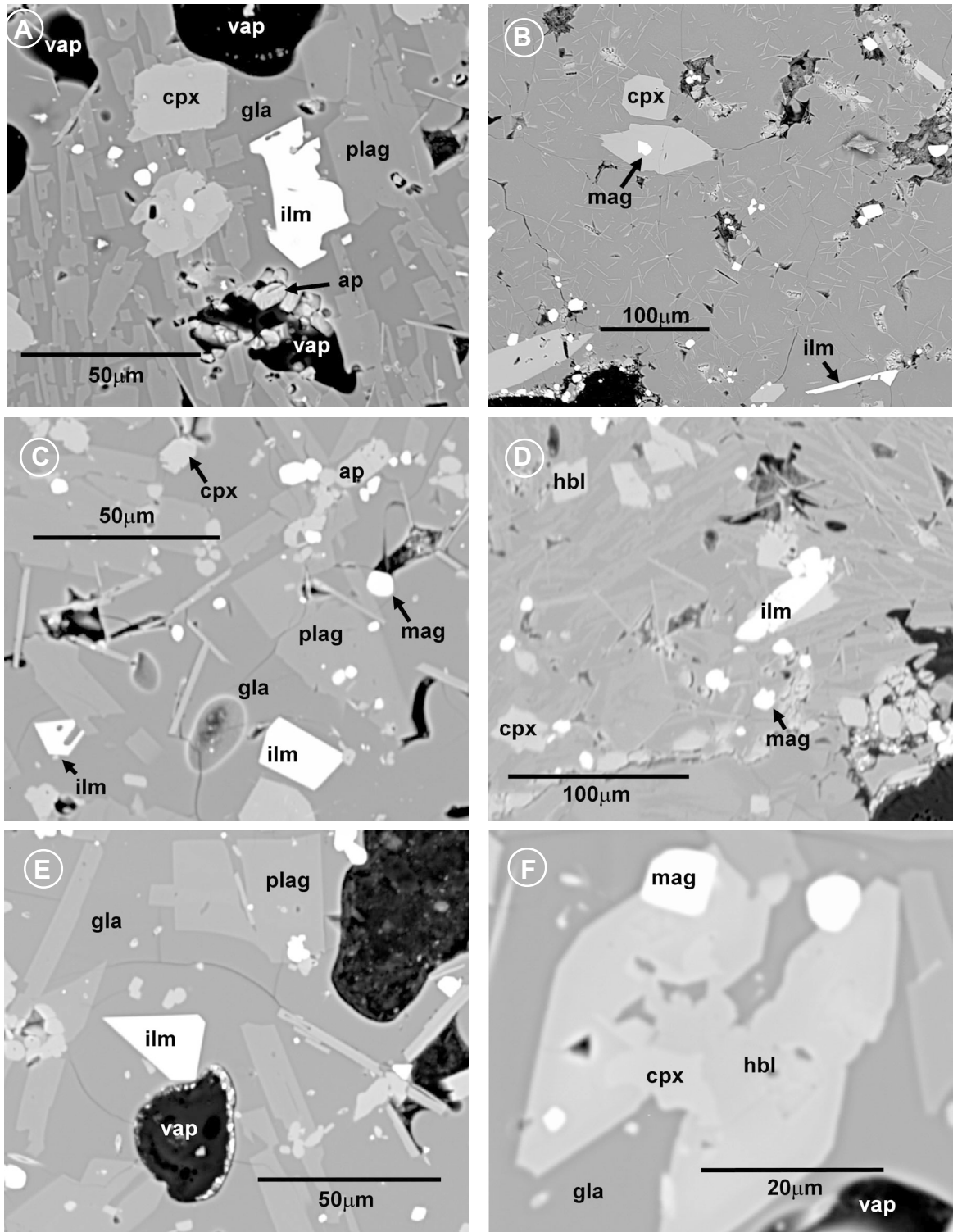


Figure 2.1. BSE images of charges. A. Charge 105 - skeletal ilmenite with clinopyroxene and vapor bubble. B. Charge 189 - magnetite inclusion in cpx and elongate ilmenite. C. Charge 139 - euhedral ilmenite, magnetite, clinopyroxene, and plagioclase. D. Charge 149 - euhedral ilmenite with clinopyroxene and hornblende. E. Charge 165 - euhedral ilmenite with plagioclase and vapor bubble. F. Charge 165 - euhedral hornblende and magnetite with residual clinopyroxene. cpx = clinopyroxene, hbl = hornblende, ilm = ilmenite, mag = magnetite, plag = plagioclase, gla = glass, vap = vapor, ap = apatite

calculated (Tables 2.2-2.5). Grains were excluded from the average if the analytical total was less than 98.5 or greater than 101.5 oxide wt.% for all minerals except magnetite. The small size of the magnetite grains made it difficult to obtain acceptable totals, so a cutoff of 98 wt.% was used for all samples except 263 and 268, where a cutoff of 97.5 wt.% had to be used since no totals reached 98 wt.% after estimation of Fe^{3+} . Cores and rims of larger grains were analyzed and no consistent variation was observed. In general there was less than 5% compositional variation between grains in each charge. The only exception to this was the magnetite in samples 105 and 203, which had large variations in Cr content between grains making it difficult to get an accurate average composition. This uncertainty did not significantly affect the activity calculations for ulvöspinel or magnetite.

Clinopyroxene

Clinopyroxene occurs as euhedral grains that often have an elongate habit and optically appear to be hornblende (Fig. 2.1). The pyroxene has an average formula $(\text{Na}_{0.04}\text{Ca}_{0.95})(\text{Mg}_{0.59}\text{Fe}^{2+}_{0.05}\text{Fe}^{3+}_{0.25}\text{Al}_{0.06}\text{Ti}_{0.05})(\text{Si}_{1.62}\text{Al}_{0.38})\text{O}_6$. It is dominantly a diopside-esseneite solid solution with minor Ca-Tschermaks (CaTs) and hedenbergite (Fig. 2.2). The Ca and Na typically sum to less than one, indicating that the clinopyroxene is sub-calcic with minor ferrosilite and enstatite solid solution. The Fe^{3+} substitutes as esseneite ($\text{CaFe}^{3+}\text{AlSiO}_6$) rather than acmite ($\text{NaFe}^{3+}\text{Si}_2\text{O}_6$). The composition of pyroxene varies little with changes in temperature and pressure of the experiments. Titanium and tetrahedral Al increase somewhat with increasing P and decrease with increasing T. Magnesium increases with increasing T whereas Fe^{2+} decreases with T. There is no correlation between $f\text{O}_2$ and either the calculated Fe^{3+} or Fe^{2+} .

Plagioclase

Plagioclase forms euhedral laths ranging in width from 20-200 μm that increase in Na and K content and decrease in Ca with decreasing temperature (Fig. 2.3), as observed by Housh & Luhr (1991). Lower temperature experiments have compositions of about $\text{An}_{42-45}\text{Ab}_{50-55}\text{Or}_{3-5}$, compared to about $\text{An}_{70}\text{Ab}_{29}\text{Or}_{<1}$ in higher temperature runs.

Table 2.2. Clinopyroxene compositions from the experimental charges. Formula units are calculated on the basis of 6 oxygens. Activities calculated using both the QUILF and MELTS models.

N	15	15	15	13	16	18	17
Samples	104	105	114	119	139	149	165
fO ₂ buffer	MnH	MH	MH	MH	MH	MnH	MnH
SiO ₂	43.55	43.08	43.18	43.57	42.65	41.60	42.74
TiO ₂	1.50	1.86	1.78	1.61	1.70	1.70	1.75
Al ₂ O ₃	8.74	9.76	9.29	8.70	10.07	10.90	10.15
Fe ₂ O ₃	9.54	8.62	8.88	9.47	8.85	9.94	8.60
FeO	1.19	1.75	1.63	1.36	1.41	1.30	1.52
MgO	11.11	10.64	10.79	11.05	10.48	9.67	10.42
MnO	0.28	0.31	0.29	0.30	0.31	0.32	0.30
CaO	23.43	23.39	23.32	23.45	23.41	23.55	23.35
Na ₂ O	0.46	0.47	0.48	0.46	0.46	0.48	0.51
Totals	99.80	99.88	99.64	99.97	99.34	99.47	99.34
Si	1.644	1.625	1.633	1.643	1.617	1.582	1.620
Al(IV)	0.356	0.375	0.367	0.357	0.383	0.418	0.380
Ti	0.043	0.053	0.051	0.046	0.048	0.049	0.050
Al(VI)	0.033	0.059	0.047	0.030	0.067	0.071	0.073
Fe ³⁺	0.271	0.245	0.253	0.269	0.253	0.285	0.245
Fe ²⁺	0.037	0.055	0.051	0.043	0.045	0.042	0.048
Mg	0.625	0.598	0.608	0.621	0.592	0.548	0.589
Mn	0.009	0.010	0.009	0.010	0.010	0.010	0.010
Ca	0.948	0.945	0.945	0.948	0.951	0.960	0.948
Na	0.034	0.035	0.035	0.034	0.034	0.035	0.037
<u>MELTS Activities</u>							
CaMgSi ₂ O ₆	0.68	0.68	0.67	0.68	0.67	0.67	0.67
Mg ₂ Si ₂ O ₆	0.16	0.21	0.18	0.15	0.15	0.03	0.14
CaFeSi ₂ O ₆	0.05	0.07	0.06	0.05	0.06	0.06	0.06
CaFeAlSiO ₆	0.46	0.49	0.45	0.45	0.49	0.55	0.48
NaAlSi ₂ O ₆	0.01	0.01	0.01	0.01	0.01	0.01	0.01
Fe ₂ Si ₂ O ₆	0.00	0.01	0.01	0.00	0.01	0.00	0.01
<u>QUILF Activities</u>							
Mg ₂ Si ₂ O ₆	1.05	1.12	1.03	1.02	1.12	1.18	1.10
Fe ₂ Si ₂ O ₆	0.0043	0.0090	0.0082	0.0056	0.0061	0.0054	0.0073
CaMgSi ₂ O ₆	0.83	0.85	0.83	0.83	0.85	0.87	0.84
CaFeSi ₂ O ₆	0.030	0.035	0.039	0.035	0.031	0.027	0.034

Table 2.2 (cont'd)

N	16	16	16	2	5	14	14
Samples	169	181	189	193	203	263	268
fO ₂ buffer	MnH	MH	MnH	MH	MnH	MnH	MH
SiO ₂	43.66	42.20	43.32	41.98	42.16	42.85	43.15
TiO ₂	1.59	1.89	1.81	2.11	1.77	1.91	1.73
Al ₂ O ₃	9.62	10.10	9.54	10.69	10.68	9.24	9.64
Fe ₂ O ₃	8.04	9.88	8.28	8.79	8.80	8.42	8.11
FeO	2.04	0.81	1.84	1.96	2.21	1.75	2.39
MgO	10.71	10.37	10.65	9.69	9.50	10.67	10.41
MnO	0.32	0.25	0.27	0.29	0.27	0.25	0.28
CaO	23.39	23.39	23.38	23.53	23.39	23.19	23.28
Na ₂ O	0.48	0.57	0.51	0.52	0.57	0.48	0.45
Totals	99.86	99.45	99.60	99.56	99.34	98.77	99.44
Si	1.645	1.600	1.637	1.594	1.605	1.634	1.636
Al(IV)	0.355	0.400	0.363	0.406	0.395	0.366	0.364
Ti	0.045	0.054	0.051	0.060	0.051	0.055	0.049
Al(VI)	0.072	0.052	0.062	0.073	0.084	0.050	0.067
Fe ³⁺	0.228	0.282	0.235	0.251	0.252	0.242	0.232
Fe ²⁺	0.064	0.026	0.058	0.062	0.070	0.056	0.076
Mg	0.601	0.586	0.600	0.548	0.539	0.607	0.588
Mn	0.010	0.008	0.009	0.009	0.009	0.008	0.009
Ca	0.944	0.950	0.947	0.957	0.954	0.948	0.946
Na	0.035	0.042	0.038	0.038	0.042	0.035	0.033
<u>MELTS Activities</u>							
CaMgSi ₂ O ₆	0.66	0.68	0.67	0.67	0.66	0.69	0.67
Mg ₂ Si ₂ O ₆	0.16	0.07	0.13	0.02	0.03	0.19	0.19
CaFeSi ₂ O ₆	0.08	0.04	0.07	0.08	0.09	0.07	0.09
CaFeAlSiO ₆	0.43	0.49	0.43	0.49	0.49	0.48	0.47
NaAlSi ₂ O ₆	0.01	0.01	0.01	0.01	0.01	0.01	0.01
Fe ₂ Si ₂ O ₆	0.01	0.00	0.01	0.00	0.00	0.01	0.02
<u>QUILF Activities</u>							
Mg ₂ Si ₂ O ₆	0.96	1.16	0.98	1.04	0.98	1.12	0.99
Fe ₂ Si ₂ O ₆	0.0126	0.0022	0.0106	0.0133	0.0170	0.0094	0.0174
CaMgSi ₂ O ₆	0.82	0.85	0.82	0.84	0.83	0.85	0.83
CaFeSi ₂ O ₆	0.050	0.019	0.045	0.043	0.050	0.036	0.051

Table 2.3. Plagioclase compositions with activities calculated using the MELTS activity models.

N	15	9	8	14	11	9	11	12	11	2	12
Samples	104	105	114	119	139	165	169	193	203	263	268
fO ₂ buffer	MnH	MH	MH	MH	MH	MnH	MnH	MH	MnH	MnH	MH
SiO ₂	49.06	56.41	51.84	49.15	54.90	54.65	52.17	55.29	54.67	56.69	56.48
Al ₂ O ₃	31.06	26.58	29.30	30.89	27.47	27.78	29.37	27.60	27.86	26.63	26.75
FeO	1.16	0.57	0.90	1.28	0.68	0.66	0.81	0.50	0.44	0.52	0.57
MgO	0.081	0.035	0.070	0.084	0.046	0.056	0.065	0.029	0.024	0.032	0.079
BaO	0.034	0.087	0.042	0.024	0.095	0.046	0.026	0.030	0.019	0.121	0.061
CaO	14.56	8.83	12.20	14.51	9.89	10.09	12.01	9.74	10.20	8.54	8.89
Na ₂ O	2.97	5.95	4.25	3.02	5.53	5.34	4.34	5.62	5.43	5.93	5.94
K ₂ O	0.16	0.79	0.27	0.17	0.49	0.47	0.28	0.44	0.25	0.76	0.68
Totals	99.08	99.25	98.88	99.13	99.11	99.08	99.07	99.25	98.89	99.22	99.45
Si	2.268	2.560	2.384	2.272	2.502	2.491	2.391	2.511	2.492	2.569	2.556
Al	1.692	1.422	1.588	1.683	1.476	1.492	1.587	1.477	1.497	1.423	1.427
Fe	0.040	0.019	0.031	0.044	0.023	0.022	0.028	0.017	0.015	0.018	0.019
Mg	0.006	0.002	0.005	0.006	0.003	0.004	0.004	0.002	0.002	0.002	0.005
Ba	0.001	0.002	0.001	0.001	0.002	0.001	0.001	0.001	0.000	0.002	0.001
Ca	0.721	0.429	0.601	0.719	0.483	0.493	0.590	0.474	0.498	0.415	0.431
Na	0.266	0.524	0.379	0.271	0.488	0.472	0.385	0.495	0.480	0.521	0.521
K	0.009	0.046	0.016	0.010	0.029	0.027	0.016	0.025	0.015	0.044	0.039
NaAlSi ₃ O ₈	0.319	0.496	0.400	0.321	0.474	0.465	0.405	0.484	0.478	0.503	0.500
CaAl ₂ Si ₂ O ₈	0.791	0.584	0.710	0.788	0.619	0.631	0.704	0.616	0.634	0.576	0.584
KAlSi ₃ O ₈	0.226	0.751	0.337	0.243	0.501	0.501	0.340	0.518	0.341	0.727	0.681

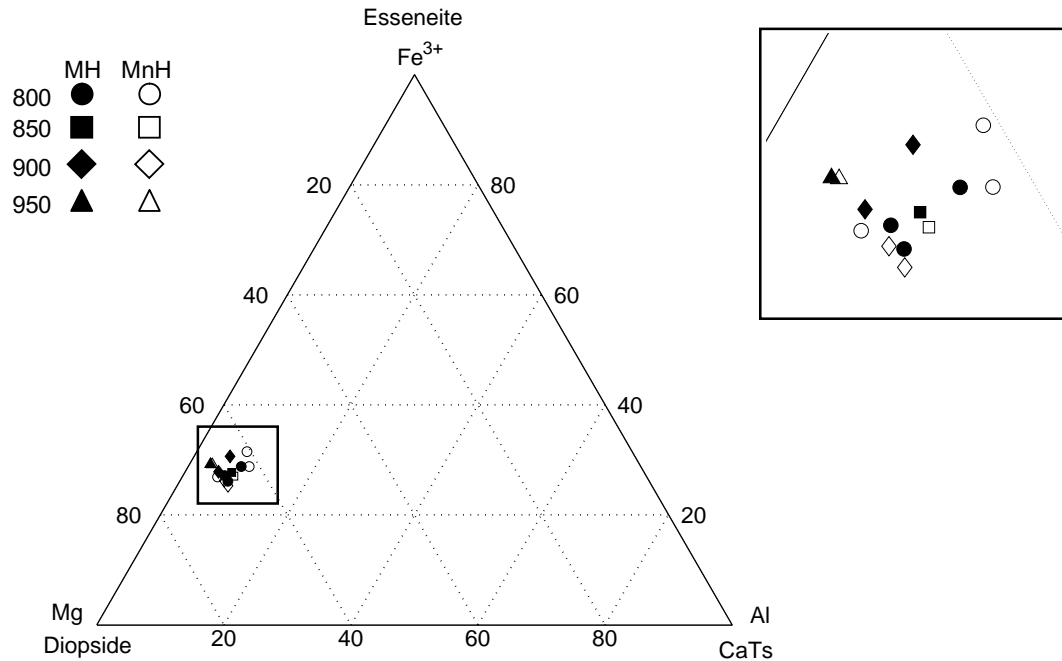


Figure 2.2. Ternary diagram showing the major M1 cations in the experimental clinopyroxene. The clinopyroxenes in this study are mainly diopside-esseneite solid solutions. Clinopyroxene composition does not correlate with T or $f\text{O}_2$. Although Fe^{3+} content of the MH equilibrated grains appears to be higher in the inset, most analyses are in indistinguishable because of uncertainties in Fe^{3+} calculations from microprobe analyses.

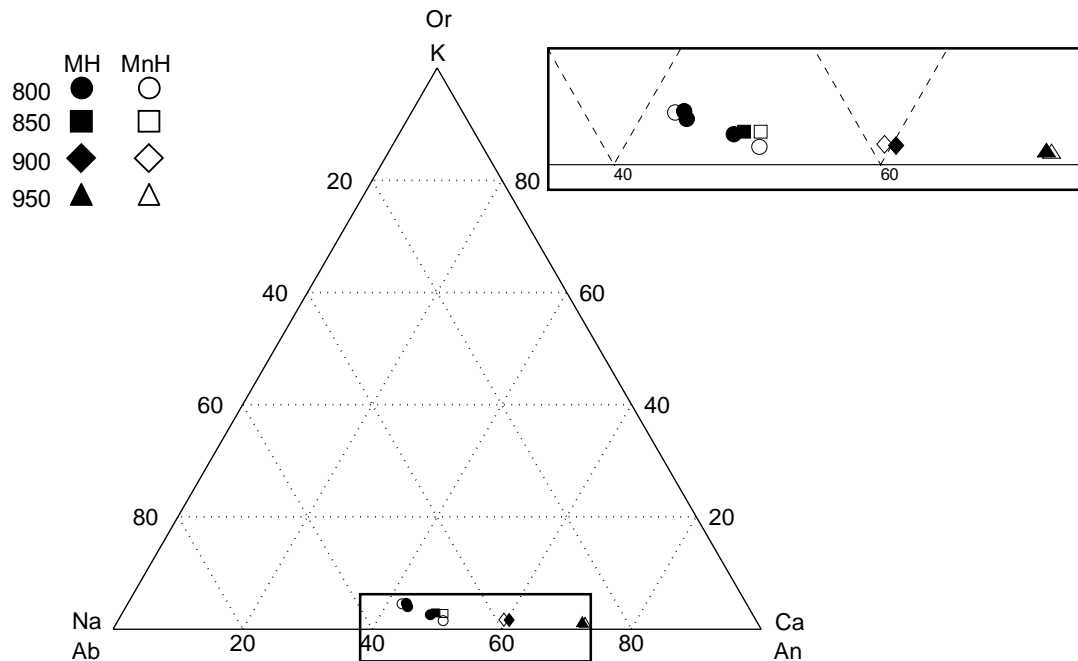


Figure 2.3. Ternary diagram showing the composition of experimental plagioclase. Na and K contents increase and Ca contents decrease with decreasing T as indicated by the symbols.

Magnetite

Magnetite grains are typically very small (5-10 μm diameter) and rounded, occurring most frequently in the groundmass and also as inclusions in plagioclase or clinopyroxene phenocrysts. The magnetite has an average formula $\text{Mg}_{0.23}\text{Mn}_{0.05}\text{Fe}^{2+}_{0.76}\text{Al}_{0.12}\text{Ti}_{0.04}\text{Cr}_{0.01}\text{Fe}^{3+}_{1.77}\text{O}_4$, or about 72% magnetite, 12% spinel, 11% magnesioferrite, 5% jacobsite and 3-6% ulvöspinel (Figure 2.4). Magnetite composition varies with experimental $f\text{O}_2$ and T. It shows a slight decrease in Fe^{2+} and Ti with increasing $f\text{O}_2$, an increase in Al and Mg with T and a decrease in Fe^{2+} decreases with T. There is no significant compositional correlation with the P of the experiments.

Hematite

Hematite grains are large (50-100 μm platelets), subhedral to euhedral and locally skeletal (Fig. 2.1). The hematite grains have average composition $\text{Mg}_{0.05}\text{Mn}_{0.01}\text{Fe}^{2+}_{0.20}\text{Fe}^{3+}_{1.44}\text{Al}_{0.03}\text{Ti}_{0.26}\text{O}_3$ with 69-80% hematite, 17-25% ilmenite, 5% geikielite, 2% corundum and 1% pyrophanite (Figure 2.4). The Fe^{3+} and Cr contents of the hematite increase with increasing experimental $f\text{O}_2$ while the Ti and Fe^{2+} contents decrease with $f\text{O}_2$. None of the other elements correlate with $f\text{O}_2$. The composition of hematite also changes with T. Manganese, Ti, and Fe^{2+} decrease with T while Al and Mg increase with T. There is no significant correlation between hematite composition and P.

Indications of Equilibrium

Textural Observations

A necessary condition for application of reactions for phase equilibria is that the phases reached equilibrium. This can be assessed, in part, by observation of textures (Figure 2.1). Most of the grains that crystallized in the charges are euhedral and are relatively large and unzoned, suggesting that they were stable as they grew. The skeletal crystals of hematite do not appear to have reacted with the surrounding glass or minerals indicating that the skeletal nature of the crystals is most likely due to rapid crystal growth. Less than 5% of pyroxenes have rims consisting of amphibole, which could indicate an

Table 2.4. Spinel compositions for the charges including activities calculated using both MELTS and QUILF activity models.

N	4	14	7	4	6	4
Sample	104	105	114	139	149	169
fO ₂ buffer	MnH	MH	MH	MH	MnH	MnH
SiO ₂	0.13	0.34	0.11	0.19	0.12	0.28
TiO ₂	1.10	1.71	1.47	0.97	1.84	2.68
Al ₂ O ₃	3.82	3.09	3.16	2.20	1.57	2.82
V ₂ O ₃	0.00	0.10	0.01	0.00	0.00	0.10
Cr ₂ O ₃	0.27	0.62	0.11	0.13	0.14	0.00
Fe ₂ O ₃	64.49	62.23	64.56	65.04	63.59	61.47
FeO	20.34	24.45	21.98	23.08	26.86	25.65
MgO	7.01	4.38	5.85	4.19	2.38	4.11
MnO	1.29	1.79	1.72	2.47	2.25	1.96
CaO	0.00	0.26	0.07	0.00	0.00	0.19
Totals	98.45	98.96	99.04	98.25	98.75	99.24
Si	0.005	0.012	0.004	0.007	0.004	0.010
Ti	0.030	0.047	0.040	0.027	0.052	0.074
Al	0.163	0.134	0.136	0.097	0.070	0.122
V	0.000	0.003	0.000	0.000	0.000	0.003
Cr	0.008	0.018	0.003	0.004	0.004	0.000
Fe ³⁺	1.759	1.726	1.772	1.831	1.812	1.705
Fe ²⁺	0.617	0.753	0.670	0.722	0.851	0.791
Mg	0.379	0.240	0.318	0.234	0.134	0.226
Mn	0.040	0.056	0.053	0.078	0.072	0.061
Ca	0.000	0.010	0.003	0.000	0.000	0.007
<u>MELTS Activities</u>						
FeCr ₂ O ₄	0.000	0.000	0.000	0.000	0.000	0.000
FeAl ₂ O ₄	0.052	0.083	0.051	0.039	0.035	0.058
Fe ₃ O ₄	0.593	0.676	0.639	0.719	0.777	0.664
MgAl ₂ O ₄	0.204	0.272	0.183	0.116	0.069	0.152
Fe ₂ TiO ₄	0.013	0.016	0.012	0.008	0.019	0.043
<u>QUILF Activities</u>						
MgFe ₂ O ₄	0.319	0.196	0.264	0.212	0.112	0.168
MnFe ₂ O ₄	0.045	0.052	0.054	0.081	0.058	0.048
Mg ₂ TiO ₄	0.001	0.003	0.002	0.001	0.002	0.003
Fe ₃ O ₄	0.590	0.675	0.618	0.670	0.743	0.660
Fe ₂ TiO ₄	0.001	0.006	0.002	0.001	0.009	0.010
X _{mag}	0.587	0.706	0.630	0.695	0.798	0.716
X _{us}	0.030	0.047	0.040	0.027	0.052	0.074
<u>MELTS γ</u>						
γ_{mag}	1.010	0.957	1.014	1.034	0.974	0.927
γ_{us}	0.421	0.338	0.285	0.307	0.353	0.576
<u>QUILF γ</u>						
γ_{mag} QUILF	1.005	0.956	0.982	0.965	0.931	0.921
γ_{us} QUILF	0.034	0.121	0.059	0.055	0.173	0.134

na = not analyzed

Table 2.4. (cont'd)

N	6	9	5	5	9
Sample	181	189	203	263	268
fO ₂ buffer	MH	MnH	MnH	MnH	MH
SiO ₂	0.08	0.13	0.10	0.16	0.15
TiO ₂	0.57	1.54	1.24	1.33	1.04
Al ₂ O ₃	4.12	3.91	3.22	1.51	1.60
V ₂ O ₃	0.00	0.07	0.04	0.00	0.04
Cr ₂ O ₃	0.42	0.15	2.78	0.08	0.26
Fe ₂ O ₃	64.43	62.97	60.19	63.60	64.43
FeO	22.20	25.24	26.54	26.60	25.29
MgO	5.58	4.35	2.96	2.10	2.69
MnO	1.16	0.91	1.21	2.10	2.26
CaO	0.00	0.29	0.07	0.00	0.08
Totals	98.56	99.57	98.34	97.48	97.83
Si	0.003	0.005	0.004	0.006	0.006
Ti	0.016	0.042	0.035	0.038	0.030
Al	0.178	0.169	0.141	0.068	0.072
V	0.000	0.002	0.001	0.000	0.001
Cr	0.012	0.004	0.081	0.002	0.008
Fe ³⁺	1.773	1.731	1.700	1.841	1.848
Fe ²⁺	0.679	0.771	0.833	0.856	0.806
Mg	0.304	0.237	0.165	0.120	0.153
Mn	0.036	0.028	0.039	0.069	0.073
Ca	0.000	0.012	0.003	0.000	0.003
<u>MELTS Activities</u>					
FeCr ₂ O ₄	0.000	0.000	0.000	0.000	0.000
FeAl ₂ O ₄	0.075	0.086	0.105	0.032	0.032
Fe ₃ O ₄	0.645	0.662	0.721	0.784	0.784
MgAl ₂ O ₄	0.255	0.230	0.250	0.074	0.074
Fe ₂ TiO ₄	0.005	0.014	0.013	0.010	0.010
<u>QUILF Activities</u>					
MgFe ₂ O ₄	0.267	0.188	0.140	0.105	0.139
MnFe ₂ O ₄	0.042	0.027	0.036	0.059	0.069
Mg ₂ TiO ₄	0.000	0.001	0.001	0.001	0.001
Fe ₃ O ₄	0.669	0.710	0.761	0.770	0.744
Fe ₂ TiO ₄	0.000	0.004	0.005	0.006	0.003
X _{mag}	0.663	0.729	0.797	0.817	0.777
X _{us}	0.016	0.042	0.035	0.038	0.030
<u>MELTS γ</u>					
γ_{mag}	0.973	0.909	0.903	0.960	1.010
γ_{us}	0.297	0.340	0.375	0.261	0.337
<u>QUILF γ</u>					
γ_{mag}	1.009	0.975	0.955	0.943	0.959
γ_{us}	0.029	0.098	0.142	0.146	0.101

na = not analyzed

Table 2.5. Hematite compositions for the charges with activities calculated using the QUILF and MELTS activity models.

N	10	6	16	10	11	4
Sample	105	114	139	149	181	189
fO ₂ buffer	MH	MH	MH	MnH	MH	MnH
SiO ₂	0.36	0.03	0.21	0.03	0.05	0.06
TiO ₂	12.95	13.37	11.96	15.34	9.54	14.27
Al ₂ O ₃	0.58	1.02	0.77	0.51	1.43	1.26
V ₂ O ₃	0.26	0.08	0.00	0.00	0.00	0.10
Cr ₂ O ₃	0.06	0.04	0.02	0.00	0.04	0.02
Fe ₂ O ₃	74.06	73.31	76.01	70.35	80.73	71.42
FeO	9.37	7.78	7.98	11.38	6.10	9.64
MgO	1.06	2.12	1.42	1.05	1.32	1.60
MnO	0.64	0.35	0.49	0.57	0.17	0.20
CaO	0.12	0.11	0.00	0.00	0.00	0.17
Totals	99.45	98.21	98.87	99.24	99.38	98.74
Si	0.009	0.001	0.005	0.001	0.001	0.002
Ti	0.253	0.262	0.235	0.301	0.186	0.279
Al	0.018	0.031	0.024	0.016	0.044	0.039
V	0.005	0.002	0.000	0.000	0.000	0.002
Cr	0.001	0.001	0.001	0.000	0.001	0.001
Fe ³⁺	1.450	1.440	1.495	1.381	1.580	1.397
Fe ²⁺	0.204	0.170	0.174	0.248	0.133	0.210
Mg	0.041	0.082	0.055	0.041	0.051	0.062
Mn	0.014	0.008	0.011	0.013	0.004	0.004
Ca	0.003	0.003	0.000	0.000	0.000	0.005
<u>MELTS Activities</u>						
MgTiO ₃	0.028	0.045	0.031	0.033	0.019	0.036
Fe ₂ O ₃	0.562	0.545	0.587	0.501	0.652	0.522
FeTiO ₃	0.118	0.087	0.085	0.169	0.046	0.110
MnTiO ₃	0.009	0.004	0.006	0.010	0.001	0.002
<u>QUILF Activities</u>						
FeTiO ₃	0.239	0.127	0.149	0.306	0.084	0.177
MgTiO ₃	0.072	0.135	0.094	0.070	0.082	0.106
Fe ₂ O ₃	0.608	0.553	0.606	0.563	0.638	0.517
MnTiO ₃	0.029	0.015	0.021	0.025	0.007	0.009
X _{ilm}	0.204	0.170	0.174	0.248	0.133	0.210
X _{hem}	0.725	0.720	0.747	0.690	0.790	0.699
X _{geik}	0.041	0.082	0.055	0.041	0.051	0.062
<u>MELTS γ</u>						
γ_{ilm}	0.581	0.513	0.486	0.680	0.349	0.525
γ_{hem}	0.774	0.757	0.785	0.726	0.826	0.747
<u>QUILF γ</u>						
γ_{ilm}	1.171	0.751	0.858	1.235	0.632	0.847
γ_{hem}	0.838	0.768	0.811	0.816	0.808	0.739

na = not analyzed

Table 2.5 (cont'd).

N	17	11	21
Sample	203	263	268
fO ₂ buffer	MnH	MnH	MH
SiO ₂	0.01	0.05	0.04
TiO ₂	14.38	15.00	12.77
Al ₂ O ₃	0.70	0.50	0.56
V ₂ O ₃	0.08	0.00	0.06
Cr ₂ O ₃	0.02	0.01	0.03
Fe ₂ O ₃	71.85	70.37	74.63
FeO	10.94	11.38	9.37
MgO	0.90	0.93	0.95
MnO	0.39	0.51	0.45
CaO	0.02	0.00	0.02
Totals	99.29	98.75	98.87
Si	0.000	0.001	0.001
Ti	0.282	0.296	0.252
Al	0.021	0.015	0.017
V	0.002	0.000	0.001
Cr	0.001	0.000	0.001
Fe ³⁺	1.411	1.390	1.475
Fe ²⁺	0.239	0.250	0.206
Mg	0.035	0.036	0.037
Mn	0.009	0.011	0.010
Ca	0.000	0.000	0.001
<u>MELTS Activities</u>			
MgTiO ₃	0.026	0.025	0.025
Fe ₂ O ₃	0.525	0.567	0.567
FeTiO ₃	0.151	0.120	0.120
MnTiO ₃	0.006	0.006	0.006
<u>QUILF Activities</u>			
FeTiO ₃	0.299	0.308	0.245
MgTiO ₃	0.061	0.062	0.065
Fe ₂ O ₃	0.576	0.566	0.610
MnTiO ₃	0.017	0.023	0.020
X _{ilm}	0.239	0.250	0.206
X _{hem}	0.706	0.695	0.737
X _{geik}	0.035	0.036	0.037
<u>MELTS γ</u>			
γ_{ilm}	0.635	0.481	0.584
γ_{hem}	0.745	0.816	0.769
<u>QUILF γ</u>			
γ_{ilm}	1.251	1.234	1.194
γ_{hem}	0.816	0.815	0.828

na = not analyzed

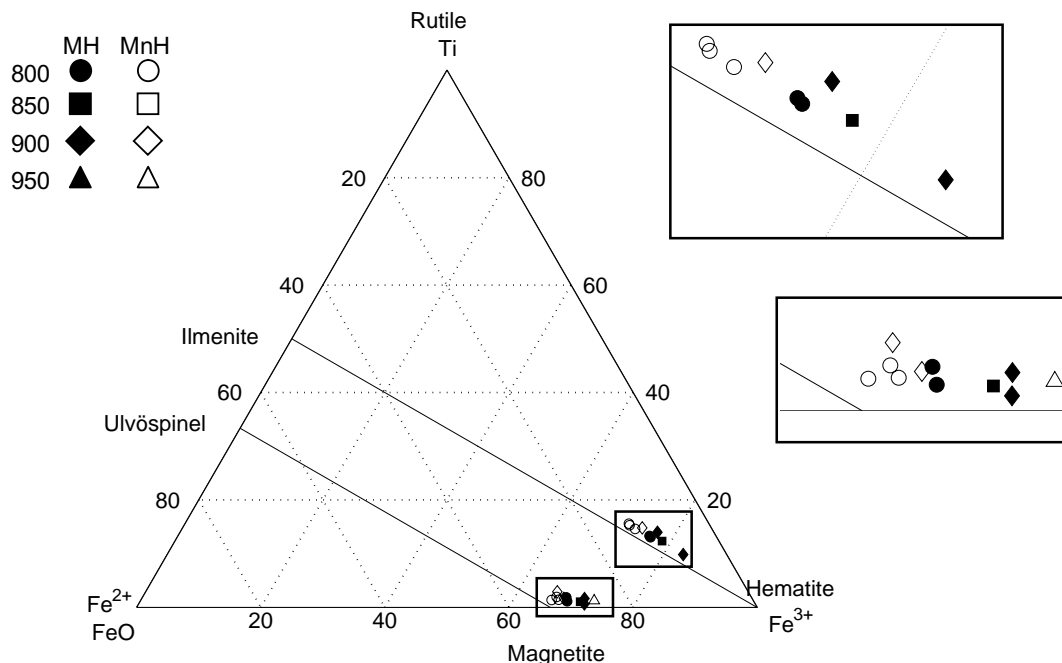


Figure 2.4. Ternary diagram showing composition of experimental oxides. Insets show the compositions of hematite and magnetite. The lines show the positions of hematite-ilmenite and magnetite-ulvöspinel solid solutions. The compositions vary with $f\text{O}_2$ with the MH charges having higher contents of the Fe^{3+} end-member.

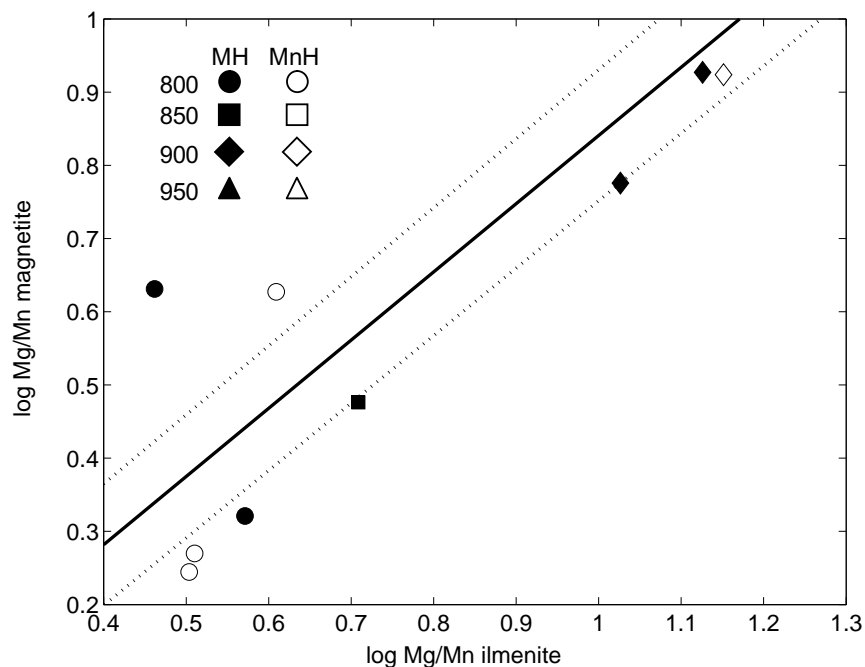


Figure 2.5. Oxide compositions plotted on $\log \text{Mg/Mn}$ (ilmenite) vs $\log \text{Mg/Mn}$ (magnetite) plot as suggested by Bacon and Hirschmann (1988) as a test for equilibrium. The solid line is the average for equilibrium compositions and the two dotted lines are the 2σ error envelope.

increase in water activity during crystallization of anhydrous phases. Only a few grains were observed that appeared to show clinopyroxene reacting to form hornblende. In most cases the clinopyroxene appeared to act as a nucleation site for the hornblende in equilibrium with stable clinopyroxene. Additional textural evidence for equilibrium is provided by sharp grain boundaries, which indicate that minerals did not react to form other minerals. It is inferred that most minerals were stable at the time they crystallized.

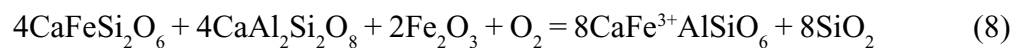
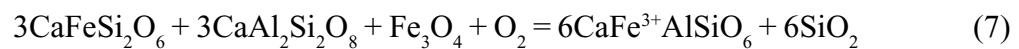
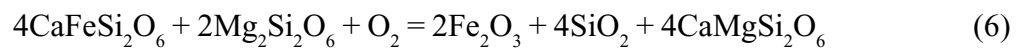
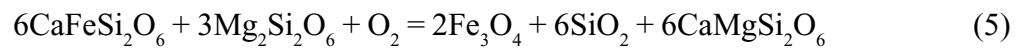
Chemical Constraints

Additional evidence for equilibrium can be seen in the composition of minerals in the run products. The silicate and oxide grains are usually homogeneous and show only minor variations in composition across large grains. An indication that the oxides equilibrated with one another is provided by elemental partitioning. For instance, Mg/Mn ratios for magnetite and hematite are very close to the equilibrium range determined by Bacon & Hirschmann (1988) (Figure 2.6). The slight departure of the samples from the equilibrium line may be due to the presence of Mn^{3+} .

Calculations of fO_2

Methods

Oxygen fugacity and T were calculated from Reactions 1 and 2 using thermodynamic databases and mixing models from both MELTS (Ghiorso and Sack, 1995) and QUILF (Andersen et al., 1993). Silicate-oxide-melt equilibria were also evaluated using the following reactions:

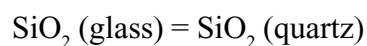


Reactions 3 and 4 were calculated using only the QUILF mixing models because they

involve the ferrosilite component of clinopyroxene, which is not explicitly included in the MELTS thermodynamic database. Reactions 5 and 6 were evaluated using MELTS in lieu of reactions 3 and 4. Reactions 7 and 8 were calculated using only the MELTS mixing model because they involve the esseneite component of clinopyroxene, which is not included in the QUILF data set.

For the calculations using MELTS, activities and free energies were calculated for clinopyroxene and plagioclase using the internet-based MELTS supplemental calculator (Ghiorso and Sack, 1995) and for magnetite and hematite using a spreadsheet obtained from Mark Ghiorso (pers. comm., 2004) that contains a more up-to-date mixing model for rhombohedral oxides. A MatLab program was written to automate the submission of composition data and retrieval of activity and free energy data from the MELTS supplemental calculator website. MatLab was also used for calculating oxygen fugacity using the MELTS thermodynamic data (*Appendix II*). The fO_2 and T were directly calculated by entering compositions for clinopyroxene, magnetite and hematite into the QUILF computer program.

Reactions 3-6 require knowledge of the $aSiO_2$ because the experiments are undersaturated with respect to quartz. The activity of SiO_2 relative to a silica glass standard state was determined by entering the glass compositions into the MELTS supplemental calculator. This standard state is appropriate for calculations using the MELTS mixing models, but QUILF requires that $aSiO_2$ be relative to a quartz standard state. Conversion from one standard state to another was undertaken using the reaction:



and thus

$$aSiO_2 \text{ (quartz)} = e^{\frac{-\Delta G_R}{RT}} aSiO_2 \text{ (glass)}$$

where ΔG_R is the ΔG of the reaction. The $aSiO_2$ is affected by the water content of the glass, so two different estimates were made to evaluate the importance of the estimate. One estimate was made assuming that the glass was water saturated using the model of

Moore et al. (1998) and a second assuming that water content is the difference between the total on the microprobe analyses of the glass and 100. These estimates produce aSiO₂ estimates that are less than 5% different leading to negligible differences in fO₂ calculations. For all calculations the second estimate was used.

Results

Temperatures calculated from analyses on the experimental products are shown in Table 2.6. Calculations of two-oxide thermometry using reaction 1 produced consistently low temperatures using the QUILF data and consistently high temperatures using the MELTS data (Fig. 2.6). The MELTS temperatures average 290°C higher than the experimental temperature with only one data point within 50°C. The QUILF temperatures average 490°C lower than the experimental temperature with no points within 50°C of experimental temperatures. For both sets of data the calculated temperatures are more accurate for MnH buffered experiments than for the MH experiments.

The fO₂ calculations using Reaction 2 with QUILF data average 0.3±0.5 log units below the experimental value. Most of calculated fO₂ values are less than the experimental values with two points above the expected value. The calculations for charges at MnH are more accurate than those at MH. The fO₂ calculations using Reaction 2 with MELTS data are more consistent than the QUILF data with an average of 0.4±0.2 log units below the experimental value. All of the calculated values are lower than the experimental fO₂ and all the calculations for charges at MnH are more accurate than those at MH (Fig. 2.7).

The fO₂ calculations using reactions 3 and 4 were only made using QUILF data because they require the activity of ferrosilite in clinopyroxene (Fig. 2.8A). These data show more scatter than the two-oxide data with calculated fO₂ ranging from -1.6 to +2.2 log units different than the experimental value. The calculations are an average of 0.55 log units below the experimental value with a one-sigma standard deviation of 0.62 log units. Reactions 5 and 6 are the combination of reactions 3 and 4 and the following exchange reaction:

Table 2.6A. fO_2 and T calculated using the QUILF activity models

Sample	104	105	114	139	149	169	181	189	203	263	268
fO_2 buffer	MnH	MH	MH	MH	MnH	MnH	MH	MnH	MnH	MnH	MH
fO_2 exp. (rel. MH)	-0.9	0.00	0.00	0.00	-0.5	-0.8	0.00	-0.7	-0.4	-0.5	0.00
T(°C exp.)	950	800	900	850	800	900	900	900	800	800	800
T(°C calc.)	na	410	290	160	560	na	na	480	470	490	340
Reaction 2 (rel. MH)	na	-0.6	-0.7	-0.6	-0.1	na	0.5	-1.1	-1.0	-1.0	-0.8
Reaction 3 (rel. MH)	-0.90	-1.1	-1.4	-0.7	-0.2	-1.9	0.6	-1.5	-1.4	-0.8	-1.6
Reaction 4 (rel. MH)	na	-0.9	-1.2	-0.6	-0.4	na	0.2	-1.4	-1.2	-0.9	-1.3

na = not applicable. Necessary phase missing.

Table 2.6B. fO_2 and T calculated using the MELTS activity models

Samples	104	105	114	139	149	169	181	189	203	263	268
fO_2 buffer	MnH	MH	MH	MH	MnH	MnH	MH	MnH	MnH	MnH	MH
fO_2 exp. (rel. MH)	-0.9	0.0	0.0	0.0	-0.5	-0.8	0.0	-0.7	-0.4	-0.5	0.0
T(°C)	950	800	900	850	800	900	900	900	800	800	800
Reaction 2 (rel. MH)	na	-0.5	-0.6	-0.5	-1.0	na	-0.1	-0.7	-0.8	-0.7	-0.7
Reaction 5 (rel. MH)	-0.0	-0.5	-0.5	0.3	2.6	-1.0	2.2	-0.4	1.8	-0.1	-0.9
Reaction 6 (rel. MH)	na	-0.5	-0.5	-0.0	1.4	na	1.5	-0.5	0.9	-0.3	-0.8
Reaction 7 (rel. MH)	-0.6	1.1	-0.3	0.7	na	-0.8	na	na	0.4	0.9	0.5
Reaction 8 (rel. MH)	na	1.6	-0.2	1.1	na	na	na	na	0.9	1.5	1.0

na = not applicable. Necessary phase missing.

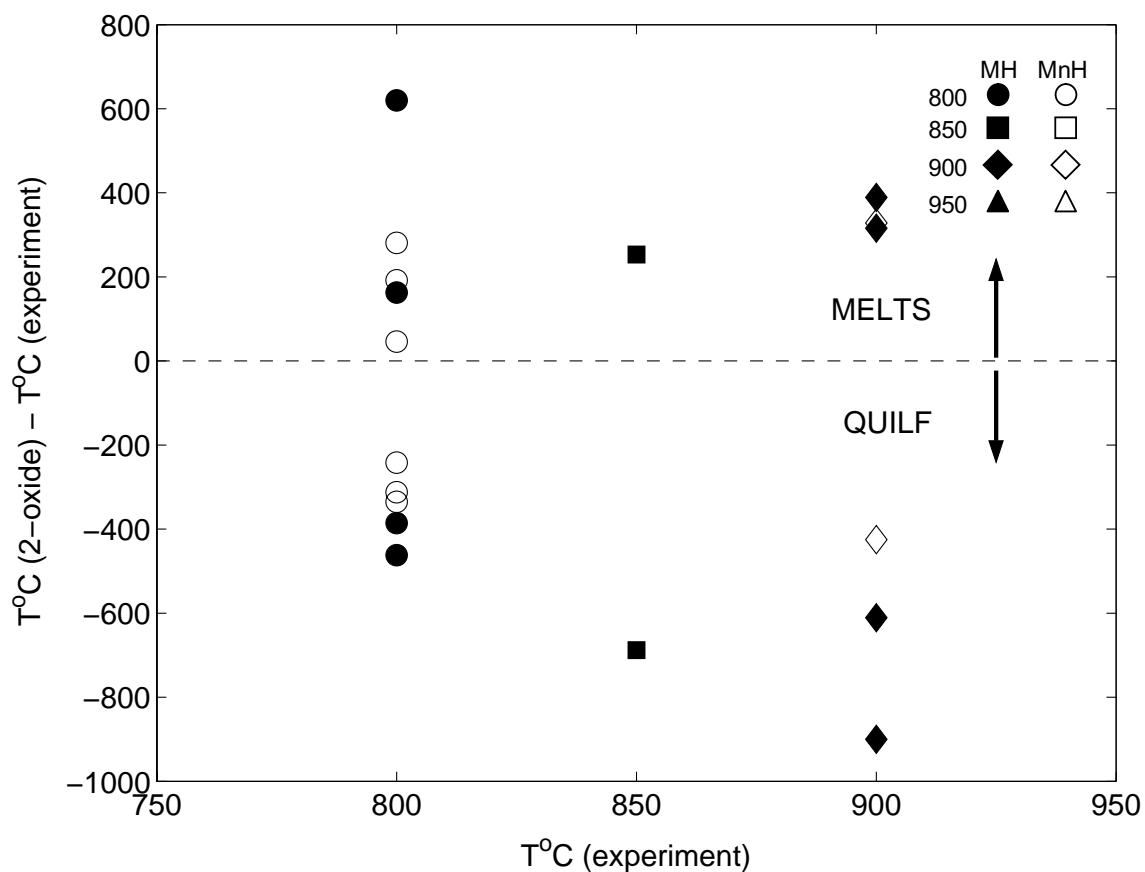


Figure 2.6. Temperature difference between calculated values and experiments for the charges using reaction 1 (Fe-Ti exchange). All of the MELTS calculations produce high temperatures while the QUILF calculations produce low temperatures. The QUILF calculations produce systematically lower T with higher fO_2 while the MELTS calculations do not.

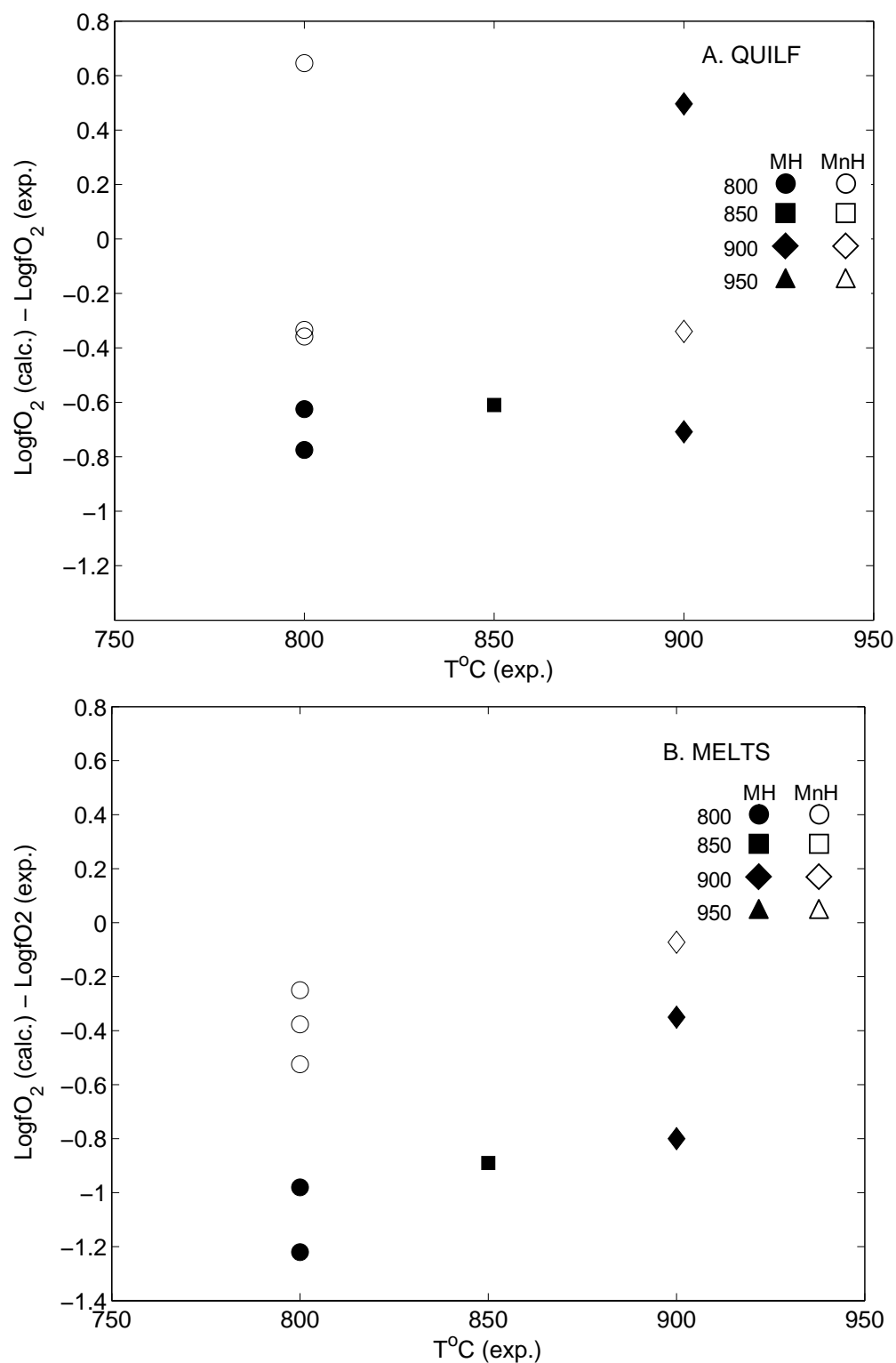


Figure 2.7. Difference between calculated fO_2 and experimental fO_2 vs T using reaction 2 (magnetite-hematite). A. QUILF activity models. Charges equilibrated at MnH produce more consistent and accurate results than those at MH. B. MELTS activity models. Results show a wide range of fO_2 for both sets of charges.

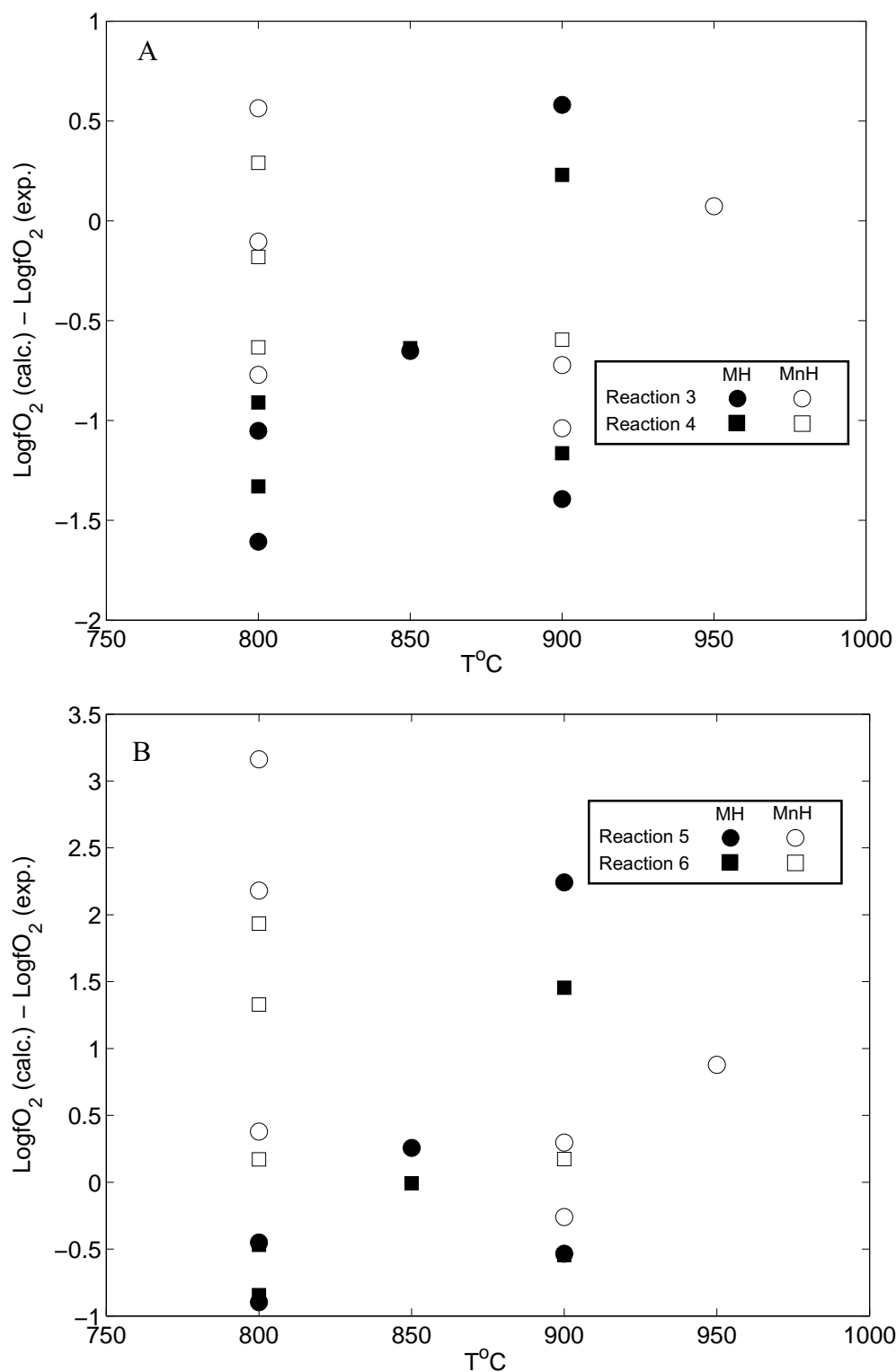
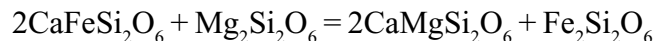


Figure 2.8. A. Difference between calculated and experimental $f\text{O}_2$ for Reactions 3 (ferrosilite-magnetite-quartz) and 4 (ferrosilite-hematite-quartz) using QUILF activity models. The MnH charges produced more consistent values. Four of six charges are within 0.5 log units of the charges. B. Difference between calculated and experimental $f\text{O}_2$ for Reactions 5 (ferrosilite-enstatite-magnetite-diopside-quartz) and 6 (ferrosilite-enstatite-hematite-diopside-quartz) using MELTS activity models.



Calculations using these reactions were made using MELTS data only because they are essentially the same as Reactions 3 and 4 (Fig. 2.8B). Most of the samples plot within 0.5 log units of the expected value with three samples plotting very high. Samples 149, 181, and 203 have clinopyroxene with higher Ca and Na contents than pyroxenes in other samples. The M2 site is nearly filled in these clinopyroxenes leading to very low mole fractions of clinoenstatite. Since clinoenstatite is on the same side of the reaction as oxygen the $f\text{O}_2$ is overestimated. Excluding these three samples, calculations are an average of 0.13 log units below the experimental value with a one-sigma standard deviation of 0.52 log units.

The $f\text{O}_2$ calculations using reactions 7 and 8 involve the esseneite component of clinopyroxene and thus were only calculated for the MELTS activity model (Fig. 2.9). The difference between calculated and experimental $f\text{O}_2$ increases with decreasing temperature. For all but one calculated $f\text{O}_2$ the values were higher than the experimental value. The results with reaction 7 involving magnetite are more accurate than those with reaction 8 involving hematite.

Discussion

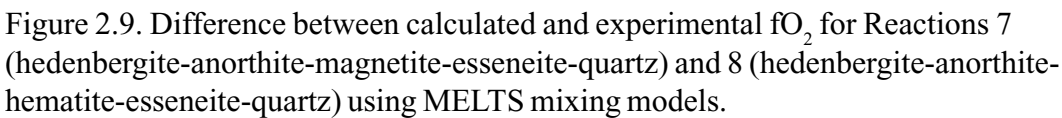
Two-oxide thermometry

For the experimental charges in this study both QUILF and MELTS fail to reproduce experimental temperatures using Reaction 1 (two-oxide reaction). The errors in the two activity models are not consistent, with QUILF calculations producing low T and MELTS calculations producing high T. In order to examine the differences between the mixing models it is useful to look at the γ values where

$$\gamma_i = \frac{a_i}{X_i}$$

for component i.

The major difference in the MELTS vs. QUILF models is the activity of the FeTiO_3 component of the hematite and the Fe_2TiO_4 component of the magnetite. At 800°C the



average $\gamma(\text{FeTiO}_3)$ using MELTS is 0.59 while the value for QUILF is 1.21 and this difference is smaller at higher T. At 900°C the average $\gamma(\text{FeTiO}_3)$ using MELTS is 0.46 while the value for QUILF is 0.74. The large differences in $\gamma(\text{FeTiO}_3)$ in hematite might be related to the structural and magnetic change in hematite at high T. Most of the compositions used to calibrate the activity models are ilmenite-rich and have the $R\bar{3}$ structure whereas the compositions in this study are hematite-rich and would have $R\bar{3}c$ structure (Ghiorso and Sack, 1991). This changes the ordering in the structure of hematite leading to differences in the mixing model, a change that is modeled explicitly in the most recent calibration of MELTS (Ghiorso et al., 2003).

The other major factor that influences thermodynamic calculations with the oxides is the Fe_2TiO_4 activity in magnetite. At 800°C the average $\gamma(\text{Fe}_2\text{TiO}_4)$ using MELTS is 0.33 while the value for QUILF is 0.13. At 900°C the average $\gamma(\text{Fe}_2\text{TiO}_4)$ using MELTS is 0.37 while the value for QUILF is 0.08. For both models the data at 900°C and 800°C are within one standard deviation of each other. Both of these factors lead to QUILF producing lower temperatures than MELTS. The $\gamma(\text{Fe}_3\text{O}_4)$ and $\gamma(\text{Fe}_2\text{O}_3)$ for the two models are very similar and do not affect the thermometry calculations significantly.

Several previous studies have applied two-oxide thermometry to oxidized volcanic and intrusive rocks (Dilles, 1987; Imai et al., 1993; Cornejo and Mahood, 1997). In the volcanic rocks, the MELTS model overestimated the temperature by 50-100°C and overestimated the $f\text{O}_2$ by 1-1.5 log units. In the intrusive rocks QUILF and MELTS models produced temperatures more than 200°C below expected magmatic conditions. The erroneous results could be caused either by resetting of the oxide compositions or errors in the mixing models at high $f\text{O}_2$. Experimental results presented in this study showed that QUILF mixing models should produce low temperature estimates and MELTS mixing models produce high temperature estimates for oxides equilibrated at high $f\text{O}_2$. If the problems with calculations on granitoids were due to lack of calibration of the mixing

models then QUILF should produce low temperatures and MELTS high temperatures. Resetting is therefore the likely cause of the low temperatures obtained for granitoids.

Two-oxide thermometry calculations are strongly dependent on the ulvöspinel component of magnetite, which is very low in magnetite from most granitoids. In rare cases magnetite in granitoids preserves oxy-exsolution lamellae of ilmenite, which could be reintegrated to obtain the magmatic composition of the grains. In these cases temperatures closer to those expected for the mixing models should be obtained.

Two-oxide fO_2 calculations

The fO_2 calculations using reaction 2 were lower than the experimental value for both QUILF and MELTS with only two exceptions. This is inconsistent with published observations from volcanic rocks using either QUILF or MELTS. In volcanic samples the calculated fO_2 is typically high by up to 1 log unit. Experiments also yielded higher calculated fO_2 than experimental fO_2 using the MELTS and QUILF mixing models (Scailliet and Evans, 1999).

The low fO_2 observed in this study must be due to either underestimation of the $a(Fe_2O_3)$ or overestimation of the $a(Fe_3O_4)$. One possible reason for underestimation of $a(Fe_2O_3)$ in hematite might be caused by the structural and magnetic change that occurs in hemo-ilmenite at high T. The $a(Fe_3O_4)$ could be overestimated due to the unusual composition of magnetite in this study. There is very little Fe_2TiO_4 diluting the magnetite component but 13-37% $MgAl_2O_4$ and $MgFe_2O_4$ are present. The studies on which the mixing models are based contain less Mg and Al than the compositions in this study and Mg substitutes as $MgAl_2O_4$ (Ghiorso and Sack, 1991). Dilution by these components is probably not modeled correctly, leading to a systematically shifted value for $\gamma(Fe_3O_4)$.

The expected error for two-oxide fO_2 calculations in intermediate igneous rocks can be estimated using data presented above. The MELTS model for samples equilibrated near MnH should produce results that are approximately 0.3 log units below the experimental fO_2 . Samples equilibrated near MH should have larger errors of about 0.8 log

units below the experimental fO_2 . The errors improve at high temperature due to improved calibration of the mixing models. The QUILF fO_2 calculations are more scattered making it more difficult to evaluate errors in the calculations. Most of the calculations at MnH are within 0.5 log units of the experimental fO_2 while the calculations at MH are within 0.8 log units.

The two-oxide method can be applied reliably up to intermediate igneous rocks with fO_2 levels near MnH. If this method is applied to volcanic rocks the errors should be similar to those estimated above, whereas errors will be larger for intrusive intermediate rocks. Resetting of compositions during cooling will lead to small changes in a_{hm} and a_{mt} . However, resetting mostly affects minor components such as Mn, Mg, and Ti in magnetite and Mn and Mg in ilmenite, and leaves the activity of major components largely unchanged. For example, if 1-2% ulvöspinel is removed from a grain that is 90% magnetite, the $a_{Fe_3O_4}$ will remain nearly unchanged, even if all the ulvöspinel is removed. Previous fO_2 estimates of intrusive rocks produced values above the magnetite-hematite buffer even though the magnetite is almost pure and the hematite is significantly diluted by ilmenite. This results from the use of QUILF and two-oxide thermometry to calculate the temperature, which is then used to calculate fO_2 . If the calculated temperature is low, it leads to overestimation of $a_{Fe_2O_3}$ and thus an overestimate of the fO_2 . If both fO_2 and T are calculated using QUILF for the oxides in this study, the fO_2 estimate is on average over 2 log units too high. If a reasonable magmatic temperature of 750-800°C is assumed, the errors drop to less than 0.5 log units. Above 650°C the estimated temperature does not significantly affect the fO_2 calculation as long as fO_2 is calculated relative to a buffer rather than an absolute value. For the experiments in this study calculations made with temperature estimates of 900°C and 700°C differ by an average of 0.15 log units. Estimation of fO_2 of granitoids therefore should be calculated assuming a reasonable magmatic temperature and reported relative to a standard buffer.

Clinopyroxene-oxide equilibria

The calculation of $f\text{O}_2$ from clinopyroxene-oxide equilibria using reactions 3 and 4 is most strongly affected by the activity of the ferrosilite component of the clinopyroxene. This results from the high degree of dilution of the ferrosilite component of the pyroxene by diopside, esseneite, hedenbergite, and enstatite relative to the dilution of magnetite or hematite by the minor oxide components. The shift of the calculated $f\text{O}_2$ due to dilution of the oxides is about 0.2-0.3 log units while the dilution of the ferrosilite component can lead to shifts of 2 log units or more. The same is true for the dilution of the clinoenstatite component of clinopyroxene in reactions 5 and 6. Therefore, these oxybarometers are almost completely dependent on the clinopyroxene composition. This makes the use of clinopyroxene as an oxybarometer in granitoids appealing because clinopyroxene is more likely to retain its magmatic composition than are oxides. Clinopyroxene-oxide equilibria may reflect magmatic $f\text{O}_2$ even when the oxides have reset to lower temperature. However, the use of such equilibria has not been systematically studied.

The $f\text{O}_2$ calculated using reactions 3 and 4 with QUILF mixing models have large errors, of about 1 log unit. This error should improve significantly in samples with lower $f\text{O}_2$ because the Fe^{2+} content of the pyroxene should increase, leading to an increase in the $a\text{Fe}_2\text{Si}_2\text{O}_6$. Estimates of $a\text{Fe}_2\text{Si}_2\text{O}_6$ for the experimental charges in this study should have large errors because of the relatively low Fe content of the clinopyroxene and because only 15% of the Fe in the clinopyroxene is Fe^{2+} . This results in large errors in the $\text{Fe}^{3+}/\text{Fe}^{2+}$ estimations from microprobe data, which may amplify the error in $f\text{O}_2$. This oxybarometer should be evaluated by experiments at lower $f\text{O}_2$ to determine if it can be applied effectively to intermediate igneous rocks.

Estimates of $f\text{O}_2$ using reactions 5 and 6 with MELTS mixing models were significantly better, with errors of about 0.5 log units and an average that is 0.1 log units below the expected value. These estimates rely most heavily on the $a(\text{Mg}_2\text{Si}_2\text{O}_6)$ in the clinopyroxene. Since the clinopyroxenes have high Mg contents, determination of

$a(\text{Mg}_2\text{Si}_2\text{O}_6)$ is likely to be more accurate than $a(\text{Fe}_2\text{Si}_2\text{O}_6)$. The $a(\text{Mg}_2\text{Si}_2\text{O}_6)$ will be less affected by the $\text{Fe}^{3+}/\text{Fe}^{2+}$ calculations, leading to more accurate estimates of $f\text{O}_2$ with these reactions.

Pyroxene-plagioclase-oxide equilibria

The calculation of $f\text{O}_2$ from clinopyroxene-plagioclase-oxide equilibria using reactions 7 and 8 is dependent on the activity of the esseneite (CaFeAlSiO_6) component of the clinopyroxene and the anorthite content of plagioclase. As with the clinopyroxene-oxide equilibria, these reactions hold promise for determining $f\text{O}_2$ in rocks where oxides have reset. In these reactions esseneite is on the more highly oxidized side indicating that activity of esseneite [$a(\text{CaFeAlSiO}_6)$] will increase with increasing $f\text{O}_2$. This is evidenced by the high $a(\text{CaFeAlSiO}_6)$ in clinopyroxenes from the experimental charges in this study.

The $f\text{O}_2$ calculated using reactions 5 and 6 suggest that MELTS may have systematic errors in $a(\text{CaFeAlSiO}_6)$ that are reduced with increasing temperature. The expected error for these calculations is ca. 1 log unit compared to the experimentally controlled $f\text{O}_2$ at 900°C, but it increases to as much as 2.5 log units at 800°C. The result suggests that MELTS has a systematic error in the mixing model for the esseneite component. The activity of esseneite appears to be overestimated in the current clinopyroxene model leading to high estimates of $f\text{O}_2$.

The calculated $\gamma(\text{CaFeAlSiO}_6)$ from MELTS for the experimental clinopyroxene increases from 1.7 at 900°C to 1.8 at 800°C. It is possible to calculate the $\gamma(\text{CaFeAlSiO}_6)$ needed to produce the correct results using the experimental value of $f\text{O}_2$. The $\gamma(\text{CaFeAlSiO}_6)$ calculated using this method is 1.8 at 900°C and 1.2 at 800°C. The temperature dependence of $\gamma(\text{CaFeAlSiO}_6)$ is much stronger in these calculations and decreases with T instead of increasing with T as in MELTS.

The apparent increase in nonideality of the esseneite component with T is unexpected but may relate to increasing disorder of Al vs. Fe^{3+} in VI and IV sites. High temperature structure refinements of several clinopyroxenes along the diopside-esseneite

join would be necessary to evaluate this effect. The calculations also show that the activity is closer to ideal at lower temperature. There is not a significant difference between the γ_{ess} calculated using reactions 5 or 6. If problems with the activity model can be addressed, these reactions should provide a method for calculating $f\text{O}_2$ of highly oxidized igneous rocks containing the assemblage clinopyroxene-oxide-plagioclase-melt-quartz.

Conclusions

The charges in this study crystallized oxides and silicates in equilibrium allowing application of mineral equilibria for T- $f\text{O}_2$ estimates. The temperatures produced by two-oxide thermometry are inaccurate, mostly due to problems with the determination of the activity of the Fe_2TiO_4 component of the magnetite and the FeTiO_3 component of hematite. Both two-oxide and clinopyroxene-oxide equilibria can be used to determine $f\text{O}_2$ of intermediate magmas if temperature can be estimated independently. The MELTS models produce better results using the two-oxide method for high $f\text{O}_2$ samples with an expected error on $f\text{O}_2$ estimates 0.3 log units for samples equilibrated at or below MnH.

Clinopyroxene-oxide equilibria using QUILF models have an error on $f\text{O}_2$ estimates of about 1 log unit. This method probably cannot be improved unless more detailed analyses of clinopyroxenes are made, including determination of their $\text{Fe}^{3+}/\text{Fe}^{2+}$ ratios. Clinopyroxene-oxide equilibria using the MELTS models indicate that reactions involving esseneite will be useful for determining $f\text{O}_2$ of oxidized igneous rocks if the mixing models for esseneite are improved. There are very few experimental data in the literature for intermediate magma compositions equilibrated at high $f\text{O}_2$. Once incorporated in programs such as MELTS, the data included in this study can be used to improve the current mixing models for hematite, magnetite and clinopyroxene.

References

- Andersen, D. J., Lindsley, D. H., and Davidson, P. M., 1993, QUILF: a Pascal program to assess equilibria among Fe-Mg-Mn-Ti oxides, pyroxenes, olivine, and quartz: Computers & Geosciences, v. 19, p. 1333-1350.
- Bacon, C. R., and Hirschmann, M. M., 1988, Mg/Mn partitioning as a test for equilibrium between coexisting Fe-Ti oxides: American Mineralogist, v. 73, p. 57-61.
- Buddington, A. F., and Lindsley, D. H., 1964, Iron-titanium oxide minerals and synthetic equivalents: Journal of Petrology, v. 5, p. 310-357.
- Cornejo, P. C., and Mahood, G. A., 1997, Seeing past the effects of re-equilibration to reconstruct magmatic gradients in plutons: La Gloria Pluton, central Chilean Andes: Contributions to Mineralogy and Petrology, v. 127, p. 159-175.
- Dilles, J. H., 1987, Petrology of the Yerington Batholith, Nevada; evidence for evolution of porphyry copper ore fluids: Economic Geology, v. 82, p. 1750-1789.
- Ghiorso, M. S., Evans, B. W., Sauerzapf, U., Lattard, D., Scaillet, B., and Anonymous, 2003, A new calibration of the Fe-Ti, two-oxide geothermometer and oxygen barometer: Geological Society of America Abstracts with Programs, v. 35, p. 393.
- Ghiorso, M. S., and Sack, R. O., 1991, Fe-Ti oxide geothermometry; thermodynamic formulation and the estimation of intensive variables in silicic magmas: Contributions to Mineralogy and Petrology, v. 108, p. 485-510.
- Ghiorso, M. S., and Sack, R. O., 1995, Chemical mass transfer in magmatic processes. IV. A revised and internally consistent thermodynamic model for the interpolation and extrapolation of liquid-solid equilibria in magmatic systems at elevated temperatures and pressures: Contributions to Mineralogy and Petrology, v. 119, p. 197-212.
- Hattori, K., 1993, High-sulfur magma, a product of fluid discharge from underlying mafic magma: evidence from Mount Pinatubo, Philippines: Geology, v. 21, p. 1083-1086.

- Hattori, K., 1996, Occurrence and origin of sulfide and sulfate in the 1991 Mount Pinatubo eruption products.
- Housh, T. B., and Luhr, J. F., 1991, Plagioclase-melt equilibria in hydrous systems: *American Mineralogist*, v. 76, p. 477-492.
- Imai, A., Listanco, E. L., and Fujii, T., 1993, Petrologic and sulfur isotopic significance of highly oxidized and sulfur-rich magma of Mt. Pinatubo, Philippines: *Geology*, v. 21, p. 699-702.
- Kress, V. C., and Carmichael, I. S. E., 1991, The compressibility of silicate liquids containing Fe_2O_3 and the effect of composition, temperature, oxygen fugacity and pressure on their redox states: *Contributions to Mineralogy and Petrology*, v. 108, p. 82-92.
- Lattard, D., Sauerzapf, U., and Kasemann, M., 2003, Towards a new calibration of Fe-Ti, two-oxide geothermometer and oxygen barometer; experiments at 1 bar, 1000-1300 °C in the Fe-Ti-O system: *Geological Society of America Abstracts with Programs*, v. 35, p. 393.
- Luhr, J. F., 1990, Experimental phase relations of water- and sulfur-saturated arc magmas and the 1982 eruptions of El Chichon Volcano: *Journal of Petrology*, v. 31, p. 1071-1114.
- Moore, G., Vennemann, T., and Carmichael, I. S. E., 1998, An empirical model for the solubility of H_2O in magmas to 3 kilobars: *American Mineralogist*, v. 83, p. 36-42.
- Scaillet, B., and Evans, B. W., 1999, The 15 June 1991 eruption of Mount Pinatubo I: Phase equilibria and pre-eruption P-T- $f\text{O}_2$ - $f\text{H}_2\text{O}$ conditions of the dacite magmas: *Journal of Petrology*, v. 40, p. 381-411.

Chapter III

Oxygen Fugacity of Granitoids: Implications for Magma Source Regions and Genesis of Sulfur-Rich Magmas

Abstract

Mineral equilibria involving pyroxenes and oxides were applied to determine oxygen fugacity (fO_2) of granitoid intrusive rocks from Utah, Indonesia, British Columbia, and Chile. The calculated fO_2 for the intrusions ranges from -0.2 to +3.9 log units relative to the nickel-nickel oxide (NNO) oxygen buffer (Fig. 3.5). The most oxidized intrusions are alkaline magmas associated with mineralization at Copper Mountain, British Columbia, and the most reduced is the Clayton Peak stock in Utah. Measured fO_2 values are similar to previously measured values for arc andesites indicating that granitoid magmas are likely formed through direct partial melting of underplated basalts.

The wide range of fO_2 indicates that behavior of sulfur varied dramatically in these intrusions. The equation of Wallace et al. (1994) indicates that S^{6+}/S_{Tot} during crystallization was between 0.19 and 0.9998. The composition of a coexisting vapor phase would also be affected by fO_2 . At 800°C and 2 kbar total pressure at water saturation, the sulfur species in the fluid ranges from 99.8% H_2S to 99.99% SO_2 for the intrusions in this study. The intrusion associated with Batu Hijau, Indonesia crystallized at NNO +1.3, indicating that 88% of the sulfur in the vapor phase would be H_2S while the intrusion associated with Bingham, Utah crystallized at NNO +1.7, indicating that 5.5% of the sulfur would be H_2S . The intrusion associated with Copper Mountain is extremely oxidized and would have produced a fluid with only 0.01% of the sulfur as H_2S .

Intrusions associated with porphyry copper deposits (PCDs) have fO_2 from NNO

+1.3 to NNO +3.8 while barren intrusions have fO_2 from NNO -0.2 to NNO +2.3. The overlap of these values suggests that fO_2 is not the primary control on the ore-forming potential of a magma. However, within each district the most highly oxidized intrusion is associated with mineralization, indicating that increased fO_2 is providing a record of other processes affecting the ore-forming potential of a magma.

Introduction

Granitoids crystallize under variable oxygen fugacity (fO_2) conditions (Haggerty, 1976), and the classification of magnetite and ilmenite series granitoids is related to variations in oxidation state (Ishihara, 1981). This classification is an over-simplification because in each of these groups there is a large variation in fO_2 , and at high fO_2 the magnetite-series magmas become saturated with respect to hematite-rich ilmenite in addition to magnetite.

Oxygen fugacity of volcanic rocks is inherited from the magmatic source region, and characteristics of source regions should be reflected in magmas that are produced by partial melting (Carmichael, 1991; Carmichael et al., 1996; Lange and Carmichael, 1996). The initial fO_2 of granitoid magmas should reflect magmatic source regions but these magmas undergo complex processes such as degassing and subsolidus alteration that could change magmatic fO_2 .

In this study, redox reactions involving oxides and clinopyroxene were used to estimate magmatic fO_2 for a wide range of calc-alkaline granitoids. These data can be used to evaluate the controls on magmatic fO_2 of granitoids and to determine if fO_2 changes during crystallization. The fO_2 of a melt also plays an important role in the behavior of sulfur during crystallization by controlling valence and solubility of sulfur, stability of sulfide and sulfate phases, and impacting the composition of magmatic vapor phases. Magmatic fO_2 provides a means to evaluate the potential for a magma to generate a magmatic-hydrothermal ore deposit or sulfur-rich eruption. A method for determining relative fO_2 using zircon geochemistry that was proposed by Ballard et al. (2002) was also

evaluated.

fO₂ of Calc-Alkaline Magmas

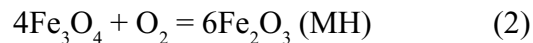
The fO₂ may be defined relative to a convenient redox reaction, e.g., NNO +3, which means the fO₂ is 3 log units above the Ni-NiO buffer. Studies of basalts erupted at subduction zones show that these magmas vary widely in bulk composition as well as oxygen fugacity, fO₂ (Carmichael and Ghiorso, 1990; Carmichael, 1991; Lange et al., 1993; Carmichael et al., 1996; Lange and Carmichael, 1996). These studies have shown that terrestrial magmas have fO₂ ranging from NNO -3 to +5, with andesites varying from NNO -0.5 to +2.5. Subduction-related alkaline basalts at Mascota, Mexico, have been shown to have fO₂ as high as NNO +5 (Carmichael et al., 1996). These values are significantly higher than those observed for OIB and MORB, which range from NNO -3 to -0.5. The high fO₂ observed for subduction zone magmas indicates that oxidized fluids from subducting slabs play an important role in the generation of calc-alkaline magmas (Carmichael, 1991).

The method most commonly used for calculating fO₂ of volcanic rocks is determination of Fe³⁺/Fe²⁺ ratio of the magma (Kress and Carmichael, 1991). This technique only works when applied to rocks that are equivalent in composition to the magmas that formed them. Granitoids no longer have the same chemistry as the magmas that formed them because they generally exsolve hydrothermal fluid and undergo subsolidus alteration. Calculating fO₂ in granitoids therefore requires the use of mineral equilibria.

Previous measurements of the oxygen fugacity of felsic intrusive rocks have been based on phase equilibria of coexisting Fe-Ti oxides using the reaction



to determine the temperature of the magma and the reaction:



to determine fO₂ at that temperature (Buddington and Lindsley, 1964; Ghiorso and Sack,

1991; Andersen et al., 1993). However, application of these reactions to felsic intrusive rocks produced temperatures well below possible magmatic conditions and unreasonably high fO_2 above the magnetite-hematite oxygen buffer (Dilles, 1987; Cornejo and Mahood, 1997). Low temperatures calculated for these intrusions are most likely due to the resetting of the Ti content of the magnetite. However, it was shown in *Chapter II* that this has little effect on the activity of the magnetite end-member. Therefore, if ilmenite is not altered and an independent temperature estimate is available, two oxides may be applied up to NNO +3.7 with an expected error of less than 0.3 log units if the MELTS activity models are used. In addition, other reactions that may be less susceptible to resetting can be used to estimate the fO_2 of calc-alkaline magmas.

Geologic Settings

Oxygen fugacity was determined for a wide range of samples from five districts in Utah, Indonesia, Chile, British Columbia, and Mexico. Additional areas were sampled but suitable samples were not found for this study (*Appendix V*). Districts were selected on the basis of having both ore-forming and barren intrusions, well-constrained petrology, and with access to fresh intrusive rocks. Intrusions were included that are associated with porphyry copper deposits (PCDs) and carbonate replacement deposits (CRDs). These are sulfide ore deposits that form from hydrothermal fluids that exsolved from crystallizing granitoid magmas.

Bingham-Park City belt, Utah

The Bingham-Park City belt consists of 15 granitoid intrusions and coeval volcanic rocks that crop out in an E-W trending belt. The BPCB magmas probably formed by partial melting of lower crustal equivalents of the amphibolites in the Little Willow Formation and were emplaced in an extensional tectonic regime (Vogel et al., 2001). The intrusions have varying depth of exposure and are associated with a range of alteration types (John, 1989). Samples of dike rocks in the region were also examined. Sample 950712-1a1b is from one such dike that cuts the Clayton Peak stock.

This belt includes the largest porphyry copper deposit (PCD) in North America at Bingham. The Bingham PCD formed between 37.5 and 37.0 Ma and is associated with a composite intrusion (Chesley et al., 1997; Deino and Keith, 1997; Parry et al., 2001). The first intrusive phases are the equigranular Last Chance and Bingham stocks and the Phoenix dike, which are 38.6 ± 0.2 Ma old and not associated with significant mineralization (Parry et al., 2001). This event was followed by emplacement of the quartz monzonite porphyry (QMP) that is associated with the majority of mineralization (Redmond, 2002). The QMP was followed by the quartz latite porphyry (QLP) and then the latite porphyry (LP) that appear to be directly associated with small amounts of mineralization (Redmond, 2002). The Ohio Copper dike is a post-mineral dike that cuts the Bingham PCD. New U-Pb ages for the porphyry intrusions are reported in this study.

Batu Hijau, Indonesia

The Batu Hijau igneous complex is located in the Indonesian Archipelago and is part of the Sunda-Banda magmatic arc (Meldrum et al., 1994; Irianto and Clark, 1995; Clode et al., 1999). The arc is related to subduction of the Indian Plate underneath the Philippine Sea and Caroline-Pacific Plates. The sub-arc crust in this region is oceanic and the intrusions range in composition from gabbro to tonalite. Volcanic and minor intrusive activity occurred in the region between 15 and 6 Ma. The main period of intrusive activity consisted of four magmatic episodes between 5.9 and 3.7 Ma (Garwin, 2000). This activity culminated in the formation of the Batu Hijau Au-rich PCD, which formed at 3.7 Ma and is associated with the young tonalite unit of Garwin (2000) (sample SBD69-137.6m).

El Teniente-Andina belt, Chile

The southern end of the central Andes contains a large number of felsic intrusions ranging in age from 2 to 20 Ma. Magmatism in the area is of calc-alkaline affinity and is the result of subduction of the Farallon Plate under the South American Plate. Magmas that formed these rocks are thought to have formed by partial melting of hornblende-

bearing mineral assemblages above shallow subduction zones (Kay et al., 1999; Kay and Mpodozis, 2002). The La Gloria intrusion, with a vertical exposure of about 1500 m, has been studied in detail (Cornejo and Mahood, 1997).

The major ore deposits in this region are the giant El Teniente and Rio Blanco-Los Bronces PCDs. These deposits are both the result of prolonged intrusive activity including several barren intrusions with mineralization occurring between 4.37 and 4.81 Ma at El Teniente (Serrano et al., 1996; Makshev et al., 2002) and between 4.2 and 4.6 Ma at Rio Blanco-Los Bronces (Serrano et al., 1996). New U-Pb ages are presented for the La Obra, San Gabriel, La Gloria, and San Francisco intrusions and for mineralized porphyries at El Teniente and Rio Blanco-Los Bronces.

Copper Mountain, British Columbia

The Copper Mountain intrusions are located in the Quesnel region of the Intermontane Belt in British Columbia. Magmatism in the Quesnel region was generated by subduction of the Cache Creek oceanic terrane and consists of coeval alkaline and calc-alkaline volcanic and intrusive rocks (Wernicke and Klepacki, 1988). The intrusions at Copper Mountain are hosted in the Jurassic Nicola volcanic units and have alkaline affinity rather than the calc-alkaline affinity that is commonly observed in the other arcs. The intrusions in the region formed between 190-200 Ma and include the Voigt, Smelter Lake, and Copper Mountain stocks (Sinclair and White, 1968; Preto et al., 1971; Fahrni et al., 1976). The Copper Mountain stock is associated with mineralization at the Copper Mountain and Ingerbelle PCDs.

Providencia-Concepcion del Oro district, Zacatecas, Mexico

The PCdO district is located in the central portion of the Sierra Madre Occidental. It consists of a belt of well-exposed mid-Tertiary granodiorites that intruded Jurassic and Cretaceous limestones. Some of the intrusions in the district have been dated using K-Ar and Rb-Sr techniques (Ohmoto et al., 1966). These intrusions have not been very well studied but are roughly coeval with volcanic rocks of the Sierra Madre Occidental

Volcanic Province, which are subduction related dacite-rhyolite volcanic rocks (McDowell and Keizer, 1977). The ore deposits in the district include the Providencia Pb-Zn CRD and the small Concepcion del Oro PCD (Buseck, 1966; Rye and Haffty, 1969). No detailed petrologic studies have been conducted on the intrusive rocks exposed in the district.

Analytical Methods

Electron Microprobe

The necessary phases in each sample were analyzed using the Cameca SX100 electron microprobe at the University of Michigan. Pyroxene, magnetite, ilmenite, and plagioclase were analyzed using 15 kV accelerating potential and sample currents of 15, 20, 20, and 10 nA respectively. All minerals were analyzed with a focused beam except plagioclase, which was analyzed with a 5 μm rastered beam in order to minimize beam damage. All analyses were corrected using the Cameca PAP program. The following standards were used for pyroxenes: Na and Fe on synthetic acmite (ACM), Ca, Si, and Mg on Irving diopside (PX69), Al on Tiburon jadeite (JADE), Ti on synthetic geikielite (GEIK), and Mn on Broken Hill rhodonite (BHRH). The following standards were used for magnetite and ilmenite: Fe on Elba hematite (HEMA), Ti on ilmenite (ILM), Al and Si on Ingamells almandine (IALM), Mg on synthetic MgTiO_3 (GEIK), Mn on synthetic MnFe_2O_4 (JACB) or Broken Hill rhodonite (BHRH), V on synthetic V_2O_5 (V2O5), Ca on Irving diopside (PX69), and Cr on synthetic Cr_2O_3 or synthetic uvarovite (UVAR). The following standards were used for plagioclase: Na on Tiburon albite (TAB), Ca and Al on Tanzania tanzanite (TANZ), K and Si on St. Gotthard microcline (GKFS), Fe on Ingamells almandine (IALM), Mg on synthetic MgTiO_3 (GEIK) and Ba on synthetic Ba-chlorapatite (BACL). The $\text{Fe}^{3+}/\text{Fe}^{2+}$ of pyroxene and oxide analyses were estimated using the method of Droop (1987).

SEM-EDS Analyses

Many of the oxide grains in these samples have exsolved to form intergrowths of magnetite-ilmenite, hematite-rutile, or hematite-ilmenite. Several methods to analyze these

were examined including reintegration of EMP analyses, broad-beam microprobe analyses, standardless broad-beam EDS analyses, and broad-beam EDS analyses with standards. The EMP analyses revealed that chemical gradients exist within hematite and ilmenite lamellae making reintegration with BSE images impossible. Magnetite grains often have small, erratic lamellae that cannot be analyzed individually with the EMP. The maximum beam size for EMP analysis is 20 μm , making it necessary to run time-consuming grids in order to analyze entire grains. Much larger beam sizes of up to 200 μm can be used for EDS analyses making it more effective for getting the composition of entire grains.

The EDS measurements can be obtained with both standardized and standardless analysis. Standardized analyses were attempted using FLAME and DTSA software packages on a Camebax EMP equipped with a Si-Li EDS detector and Voyager software on a Hitachi SEM with a Si-Li detector. Standardless analyses were applied using FLAME and DTSA on a Camebax EMP with a Si-Li detector, Roentec software on an SX100 EMP with a Si-drift detector, and Voyager software on a Hitachi SEM with a Si-Li detector. All software packages were tested on the ILM ilmenite standard, and unexpectedly, the best results were produced with standardless analysis using Voyager software on the SEM. Estimates of the ilmenite composition using this method are within 0.5 wt% on Ti, 0.5 wt% on Fe, and 1% on Mg for element wt %. EDS detectors on the EMPs have thicker windows leading to decreased signal on lower energy X-rays such as Mg and Al, and there are unresolved problems fitting the background at low energy. The latter leads to overestimation and false detection of light elements. In general, EDS detectors on the EMPs overestimated the Mg content of the ilmenite by more than 3 wt% and underestimated the Ti content by 0-4 wt%.

Laser ablation ICP-MS

Zircons were separated by density and magnetic separation using 300-1000 g samples. The separates were examined under a microscope and the most inclusion-free zircons were picked and mounted in epoxy. The mounts were polished to expose the

zircons and examined optically to select the best grains for analysis.

Zircons from intrusive rocks in Indonesia, Utah, and Chile were analyzed with the LA-ICP-MS at Australian National University using a method modified from Horn et al. (2000). Samples were ablated using a pulsed Lambda Physik LPX 1201 UV ArF excimer laser operated between 21 and 23 kV at 5 Hz and an approximate beam size of 30 μm . The ablated material was carried by He-Ar gas through a flow homogenizer to an Agilent 7500 ICP-MS. Approximately 40 grains of each sample were analyzed to provide a statistically significant dataset. Standards were analyzed every ten samples in order to monitor machine drift.

The Indonesian samples were also analyzed using LA-ICP-MS at Michigan State University for comparison. All samples were analyzed for REE concentrations and samples from Utah and Chile were also analyzed for U-Pb isotopes for geochronology. REE concentrations and ages were calculated using a MatLab program written by the author (*Appendix I*). All ages were corrected for common Pb using the method of Cumming and Richards (1975) using ^{207}Pb for correction and using the $^{206}\text{Pb}/^{238}\text{U}$ age as the initial age. $\text{Ce}^{4+}/\text{Ce}^{3+}$ ratios were calculated using the method of Ballard et al. (2002). REE whole rock data are not available for all samples so normalization of the REE concentrations was done assuming upper crustal rare earth element abundances.

Mineral Compositions

Samples in this study are granitoids with plagioclase, quartz, K-feldspar, apatite, magnetite, biotite, hornblende \pm clinopyroxene \pm orthopyroxene \pm ilmenite \pm sphene (Fig. 3.1). Compositions were determined for magnetite, ilmenite, clinopyroxene, and orthopyroxene for mineral equilibrium calculations. Several grains of each mineral were analyzed and average compositions were calculated (Tables 3.1-3.4). Grains were excluded from the average if the analytical total was less than 98.5 or greater than 101.5 oxide wt.%. Standardless EDS analyses of oxides were normalized to analytical totals of 100 wt %, and those analyses were excluded if monitored elements such as Ca and Si

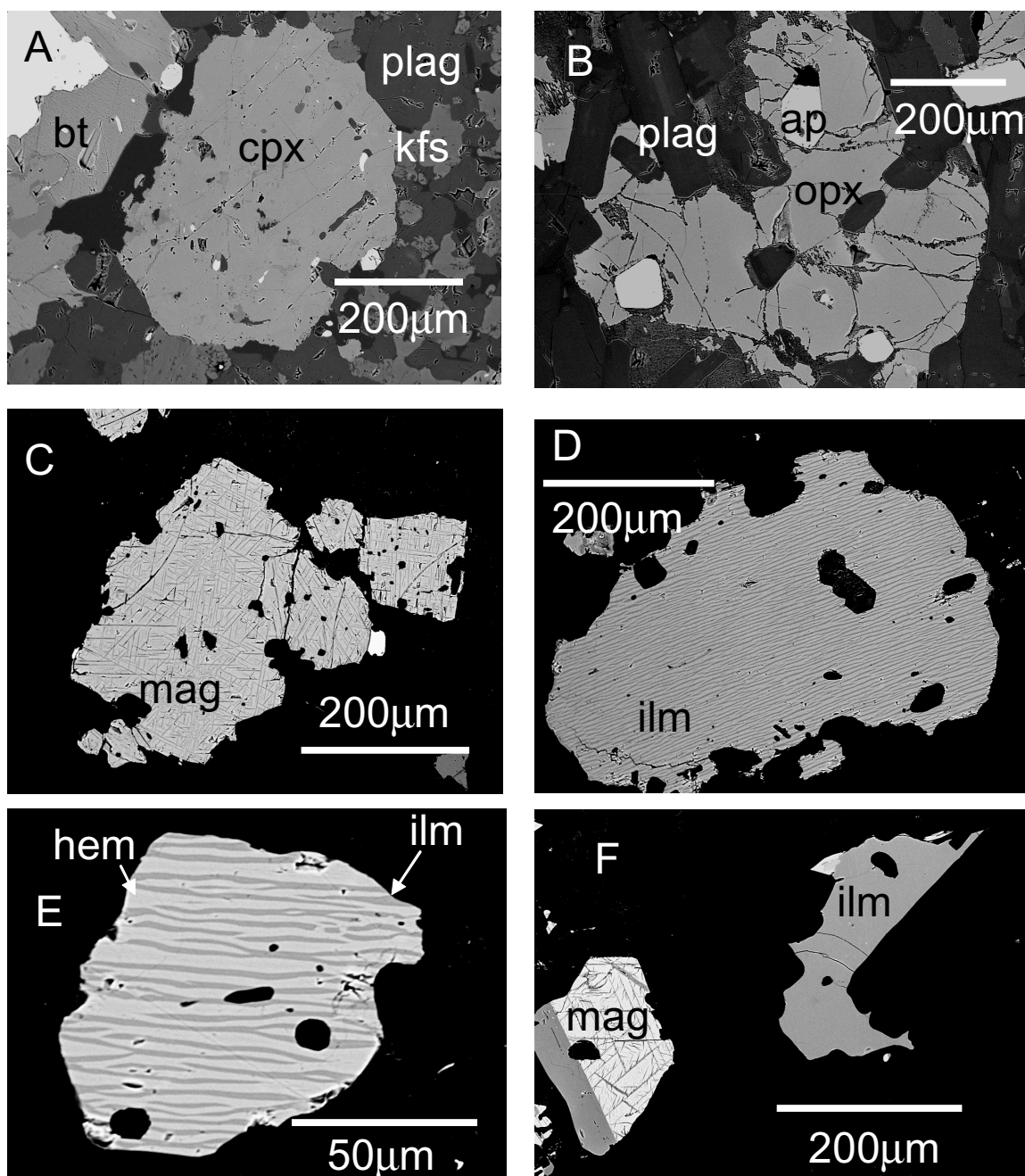


Figure 3.1. BSE images showing occurrence of silicate and oxide minerals. A. Clinopyroxene from LC7 with fine-grained groundmass of plagioclase and K-feldspar. B. Orthopyroxene from sample RTT190 showing anhedral orthopyroxene grain cut by veins of a low temperature alteration product. C. Magnetite from sample O11-4 showing fine exsolution of ilmenite in magnetite. D. Ilmenite from sample 98100801 showing fine exsolution lamellae. E. Ilmenite from sample LC7 showing ilmenite with coarser exsolution lamellae. EMPA analyses show that these lamellae are chemically zoned. F. Reset ilmenite and exsolved magnetite from RTT190. bt = biotite; cpx = clinopyroxene; plag = plagioclase; kfs = K-feldspar; ap = apatite; opx = orthopyroxene; mag = magnetite; ilm = ilmenite; hem = hematite.

were >1 wt.%. In some cases, all analyses from some samples had significant Ca and Si due to partial alteration of the oxides to sphene. These analyses were used to evaluate the effect of alteration on fO_2 calculations. Cores and rims of larger grains were analyzed and no consistent variation was observed. In general there was less than 5% compositional variation between grains in each sample.

Clinopyroxene

Clinopyroxene occurs in 25 samples in this study, usually as large subhedral to euhedral grains rimmed by late biotite or hornblende (Fig. 3.1A). The rims typically appear to be nucleation sites for the biotite or hornblende, not reaction rims. The clinopyroxene grains appear to be in equilibrium since the grain boundaries are still sharp and there are no embayments into the crystals. In samples RDA124, LC7, and RTT190 abundant clinopyroxene occurs in the fine-grained groundmass of the samples.

The clinopyroxene grains are magnesian, with Mg# ranging from 0.75 to 0.94. Variations in the Mg# do not correlate with bulk composition; both the highest and lowest Mg# occur in mafic samples with bulk SiO_2 of less than 60 wt %. The clinopyroxene grains from more felsic samples such as LG6 and SG4 have intermediate Mg#. The major components of the clinopyroxene in most samples are diopside, hedenbergite, and clinoenstatite with minor ferrosilite and esseneite (Fig. 3.2). All of the pyroxenes except sample SG4 have deficiencies in the M2 site with $Ca + Na < 1$ leading to significant activities for clinoenstatite and ferrosilite. The samples from British Columbia have significantly more Fe^{3+} than the other samples with 8.6-16.1% esseneite. This causes them to plot above the diopside-hedenbergite join on the clinopyroxene ternary despite having deficiencies in the M2 site.

Orthopyroxene

Orthopyroxene was found in six samples and is abundant only in 97100808b, SRD02320m, 950917-36 and CP92-6. In these samples, orthopyroxene is a phenocryst phase and is found as euhedral grains locally rimmed by late biotite. Orthopyroxene was

Table 3.1.1. Clinopyroxene compositions determined by EMPA.

N	18	21	22	18	2	4	4	2
Sample Location	BC2020	BC2032	BC2036	BC2042	981000301a	CP13-14	CP13-18	LC10
SiO ₂	BC	BC	BC	BC	Indonesia	Utah	Utah	Utah
TiO ₂	52.10	50.49	49.75	50.38	52.88	52.68	52.33	52.83
Al ₂ O ₃	0.23	0.28	0.60	0.52	0.35	0.22	0.28	0.38
Fe ₂ O ₃	1.28	2.91	3.09	3.15	1.28	1.02	1.09	1.58
FeO	3.47	4.71	5.72	5.78	2.93	1.47	2.22	1.97
MgO	4.68	3.27	2.80	1.54	5.03	8.48	7.56	6.45
MnO	14.68	13.68	13.00	14.64	16.11	14.07	14.87	15.96
CaO	0.69	0.48	0.61	0.40	0.30	0.51	0.36	0.26
Na ₂ O	22.61	23.48	22.84	23.09	21.63	21.70	21.09	20.75
Totals	0.43	0.52	0.90	0.67	0.38	0.28	0.30	0.38
	100.16	99.81	99.29	100.16	100.89	100.45	100.09	100.56
Si	1.933	1.881	1.867	1.861	1.936	1.961	1.948	1.942
Al (IV)	0.056	0.119	0.133	0.137	0.055	0.039	0.048	0.058
Ti	0.006	0.008	0.017	0.014	0.010	0.006	0.008	0.010
Al (VI)	0.000	0.009	0.003	0.000	0.000	0.006	0.000	0.010
Fe ³⁺	0.097	0.132	0.161	0.161	0.081	0.041	0.062	0.054
Fe ²⁺	0.145	0.102	0.088	0.048	0.154	0.264	0.235	0.198
Mg	0.812	0.760	0.727	0.806	0.879	0.781	0.825	0.874
Mn	0.022	0.015	0.019	0.012	0.009	0.016	0.011	0.008
Ca	0.898	0.937	0.918	0.914	0.849	0.866	0.841	0.817
Na	0.031	0.038	0.066	0.048	0.027	0.020	0.021	0.027
Mg#	0.848	0.882	0.892	0.944	0.851	0.747	0.778	0.815

Table 3.1. Clinopyroxene compositions determined by EMPA.

N	4	1	6	9	14	8	5	8	6
Sample	LC5	LC7	OC1	LC7X	O11-4	950712-1a1b	CP92-6	V950718-9	SC4
Location	Utah	Utah	Utah	Utah	Utah	Utah	Utah	Utah	Utah
SiO ₂	52.47	52.28	52.13	52.90	52.93	51.94	51.92	52.07	52.17
TiO ₂	0.38	0.25	0.24	0.30	0.19	0.20	0.35	0.30	0.14
Al ₂ O ₃	2.02	1.79	1.98	1.14	1.19	1.19	1.11	1.74	0.70
Fe ₂ O ₃	2.78	2.86	2.81	3.06	2.23	3.82	2.38	3.35	2.84
FeO	6.09	5.33	6.24	4.45	6.31	4.45	7.66	7.63	7.12
MgO	16.25	15.64	15.29	16.24	15.13	15.12	13.84	13.16	13.34
MnO	0.21	0.26	0.23	0.29	0.60	0.39	0.52	0.42	0.36
CaO	20.12	21.21	20.78	21.71	21.68	22.04	21.84	22.35	23.06
Na ₂ O	0.44	0.45	0.47	0.44	0.39	0.49	0.34	0.52	0.37
Totals	100.76	100.07	100.17	100.54	100.66	99.64	99.96	101.54	100.10
Si	1.923	1.931	1.928	1.940	1.952	1.932	1.944	1.926	1.954
Al	0.077	0.069	0.072	0.049	0.048	0.052	0.049	0.074	0.031
Ti	0.010	0.007	0.007	0.008	0.005	0.006	0.010	0.008	0.004
Al	0.011	0.008	0.014	0.000	0.003	0.000	0.000	0.001	0.000
Fe ³⁺	0.077	0.079	0.078	0.084	0.062	0.107	0.067	0.093	0.080
Fe ²⁺	0.187	0.165	0.193	0.137	0.195	0.138	0.240	0.236	0.223
Mg	0.887	0.861	0.843	0.888	0.832	0.839	0.773	0.725	0.744
Mn	0.006	0.008	0.007	0.009	0.019	0.012	0.016	0.013	0.011
Ca	0.790	0.839	0.824	0.853	0.857	0.879	0.876	0.886	0.925
Na	0.031	0.032	0.034	0.031	0.028	0.035	0.025	0.037	0.027
Mg#	0.826	0.840	0.814	0.867	0.810	0.858	0.763	0.754	0.770

Table 3.1. Clinopyroxene compositions determined by EMPA.

N	8	19	2	3	21	1	7
Sample	SC5	LG6	RDA124	RTT190	SG4	CDO6	ES6
Location	Utah	Chile	Chile	Chile	Chile	Mexico	Mexico
SiO ₂	53.96	52.61	53.62	51.44	52.47	52.20	51.06
TiO ₂	0.10	0.12	0.17	0.51	0.00	0.09	0.11
Al ₂ O ₃	0.62	0.58	0.63	1.47	0.21	0.62	0.81
Fe ₂ O ₃	1.97	1.60	0.70	3.46	1.59	2.63	3.10
FeO	5.01	5.57	6.14	6.71	4.63	5.44	6.09
MgO	15.46	14.38	14.86	15.48	14.30	14.39	12.59
MnO	0.29	0.58	0.40	0.32	0.43	0.96	1.08
CaO	23.41	23.00	22.83	20.16	24.80	22.66	23.17
Na ₂ O	0.38	0.38	0.43	0.33	0.09	0.31	0.40
Totals	101.21	98.81	99.78	99.88	98.52	99.29	98.41
Si	1.970	1.975	1.987	1.917	1.976	1.958	1.949
Al	0.027	0.025	0.013	0.065	0.009	0.028	0.036
Ti	0.003	0.003	0.005	0.014	0.000	0.002	0.003
Al	0.000	0.001	0.015	0.000	0.000	0.000	0.000
Fe ³⁺	0.054	0.045	0.019	0.097	0.045	0.074	0.089
Fe ²⁺	0.153	0.175	0.190	0.209	0.146	0.171	0.195
Mg	0.841	0.805	0.821	0.860	0.803	0.804	0.716
Mn	0.009	0.018	0.012	0.010	0.014	0.030	0.035
Ca	0.916	0.925	0.906	0.805	1.001	0.911	0.947
Na	0.027	0.028	0.031	0.024	0.006	0.022	0.029
Mg#	0.943	0.822	0.812	0.804	0.846	0.825	0.786

Table 3.2. Orthopyroxene compositions determined by EMPA.

N	9	4	13	8	2	3
Sample	97100808b	SRD02320m	950917-36	CP92-6	RDA124	RTT190
Location	Indonesia	Indonesia	Utah	Utah	Chile	Chile
SiO ₂	53.86	53.30	53.36	51.00	53.56	52.88
TiO ₂	0.14	0.21	0.18	0.27	0.10	0.29
Al ₂ O ₃	0.62	0.71	1.05	0.58	0.34	0.54
Fe ₂ O ₃	2.76	2.10	4.30	3.12	0.55	1.61
FeO	15.94	18.83	13.96	23.68	17.58	18.41
MgO	25.92	23.78	26.73	19.49	24.46	23.77
MnO	1.18	1.04	0.72	1.14	1.15	0.56
CaO	0.86	1.19	1.14	1.11	1.10	1.55
Na ₂ O	0.02	0.03	0.03	0.03	0.05	0.04
Totals	101.29	101.18	101.54	100.52	98.89	99.63
Si	1.946	1.951	1.915	1.936	1.985	1.959
Al	0.026	0.030	0.045	0.026	0.011	0.024
Ti	0.004	0.006	0.005	0.008	0.003	0.008
Al	0.000	0.000	0.000	0.000	0.004	0.000
Fe ³⁺	0.075	0.058	0.116	0.089	0.016	0.045
Fe ²⁺	0.482	0.576	0.419	0.752	0.545	0.571
Mg	1.396	1.297	1.430	1.103	1.351	1.313
Mn	0.036	0.032	0.022	0.037	0.036	0.017
Ca	0.033	0.047	0.044	0.045	0.044	0.061
Na	0.001	0.002	0.002	0.003	0.003	0.003
Mg#	0.743	0.692	0.773	0.595	0.713	0.697

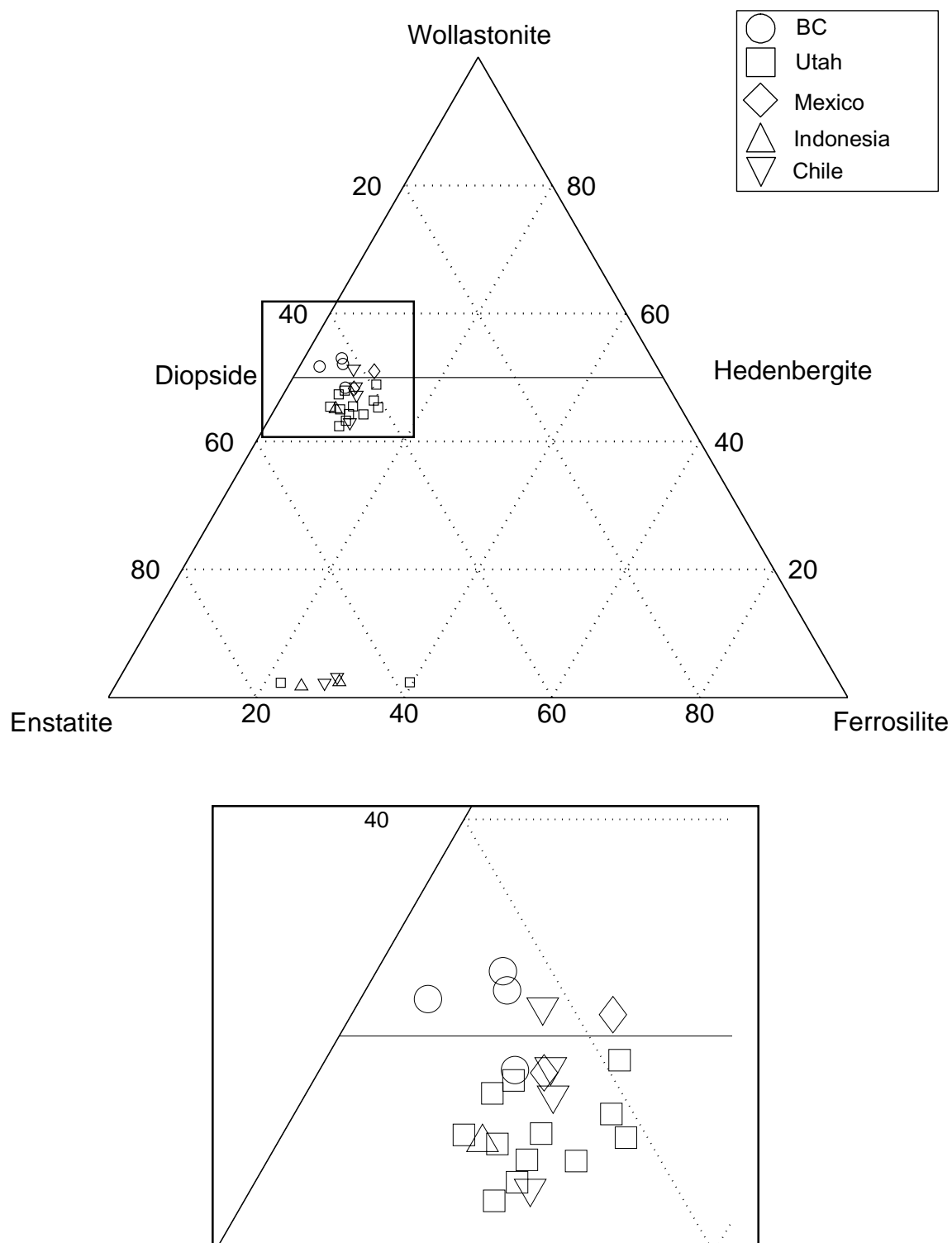


Figure 3.2. Ternary plot showing compositions of clinopyroxene and orthopyroxene. The clinopyroxene compositions are in the expanded part of the diagram.

found coexisting with clinopyroxene in samples RDA124, RTT190, and CP92-6. In samples RDA124 and RTT190 orthopyroxene is typically found in the cores of clinopyroxene or as anhedral and altered grains in the groundmass (Fig. 3.1B). In all samples the compositions of orthopyroxene are nearly binary solid solutions of enstatite and ferrosilite with only minor Ca, Al, Fe³⁺ and Ti substitution (Fig. 3.2). The Mg# for orthopyroxene ranges from 0.59-0.77 with lower Mg# than coexisting clinopyroxene. The Ca content of the orthopyroxene ranges from 0.9-1.5 wt% CaO, equivalent to 3.3-6.1% Ca in the M2 site. Most grains are deficient in Si, indicating minor substitution of Al and Fe³⁺ in the T site charge balanced by Fe³⁺ and/or Ti in the M1 site.

Magnetite

In most cases the magnetite grains have exsolved to form intergrowths of almost pure magnetite with lamellae of ilmenite or rutile (Fig. 3.1C). In other cases magnetite was found to be homogeneous without any evidence for exsolution. In most cases the magnetite has solid solution of ulvöspinel with minor spinel (Fig. 3.3). The composition of homogeneous magnetite in intrusive rocks is almost pure Fe₃O₄ with no major substitutions such as in samples ES6 or PR3 from Mexico. Exsolved grains also preserve significant solid solution containing up to 19% ulvöspinel and 5% spinel. In some cases, such as SC4 from Utah and BC2020 from British Columbia, exsolution lamellae in the magnetite grains contain minor sphene leading to high Ca and Si contents in the grains.

Ilmenite

As with magnetite, ilmenite has exsolved in some cases to intergrowths of ilmenite and hematite (Fig. 3.1D, E). In these cases the dominant solid solutions in ilmenite are ilmenite and hematite with minor pyrophanite and geikielite (Fig. 3.4). More commonly, the ilmenite is homogeneous and the major solid solutions are ilmenite, hematite, and pyrophanite and minor geikielite (Fig. 3.1F; Fig. 3.4). Many more samples contain ilmenite that has been partially reacted to mixtures of ilmenite, hematite, rutile and sphene. They are considered too altered to produce meaningful phase equilibrium results.

Table 3.3. Magnetite compositions determined by EDS.

N	4	4	6	4	5	2	3	3	5
Sample	BC2020	BC2032	BC2036	BC2042	97100808b	981000301	SBD69-137.6m	SRD02320m	950712-1a1b
Location	BC	BC	BC	BC	Indonesia	Indonesia	Indonesia	Indonesia	Utah
Analysis type	EDS	EDS	EDS	EDS	EDS	EDS	EDS	EDS	EDS
SiO ₂	1.00	0.42	0.54	1.08	0.40	0.61	0.39	0.54	0.31
TiO ₂	2.55	4.23	2.19	3.77	1.18	1.09	0.37	3.14	1.86
Al ₂ O ₃	1.08	1.40	1.43	1.31	2.24	1.19	1.21	0.66	0.63
V ₂ O ₃	0.76	0.92	1.06	0.73	0.54	1.19	0.38	0.49	0.64
Cr ₂ O ₃	0.00	0.02	0.01	0.03	0.04	0.03	0.15	0.04	0.26
Fe ₂ O ₃	59.86	57.40	60.90	57.12	62.81	63.00	65.44	60.48	63.06
FeO	33.74	33.82	31.70	34.66	31.42	32.45	31.77	33.29	32.89
MgO	0.12	0.22	0.30	0.33	0.32	0.34	0.08	0.17	0.11
MnO	0.27	1.30	1.78	0.64	0.59	0.08	0.16	0.90	0.19
CaO	0.62	0.27	0.09	0.34	0.47	0.03	0.06	0.29	0.04
Totals	100.00	100.00	100.00	100.00	100.00	100.00	100.00	100.00	100.00
Si	0.038	0.016	0.021	0.041	0.015	0.023	0.015	0.020	0.012
Ti	0.073	0.120	0.062	0.107	0.033	0.031	0.011	0.090	0.053
Al	0.048	0.063	0.064	0.059	0.100	0.053	0.054	0.030	0.028
V	0.023	0.028	0.032	0.022	0.016	0.036	0.012	0.015	0.020
Cr	0.000	0.001	0.000	0.001	0.001	0.001	0.004	0.001	0.008
Fe ³⁺	1.708	1.636	1.738	1.624	1.786	1.801	1.879	1.734	1.813
Fe ²⁺	1.070	1.071	1.005	1.095	0.993	1.031	1.014	1.060	1.051
Mg	0.007	0.013	0.017	0.019	0.018	0.019	0.004	0.009	0.006
Mn	0.009	0.042	0.057	0.021	0.019	0.003	0.005	0.029	0.006
Ca	0.025	0.011	0.004	0.014	0.019	0.001	0.003	0.012	0.002
Log(Mg/Mn)	-0.101	-0.519	-0.523	-0.042	-0.023	0.854	-0.066	-0.487	0.009

Table 3.3. Magnetite compositions determined by EDS.

N	5	5	4	5	3	3	3	5	5
Sample	950917-36	CP13-18	CP92-6	KV18-12	LC10	LC5	LC7	O11-4	OC1
Location	Utah	Utah	Utah	Utah	Utah	Utah	Utah	Utah	Utah
Analysis type	EDS	EDS	EDS	EDS	EDS	EDS	EDS	EDS	EDS
SiO ₂	0.46	0.56	0.32	0.57	0.41	0.48	0.35	0.42	0.37
TiO ₂	7.05	4.93	3.17	10.67	2.06	1.88	1.53	5.70	1.05
Al ₂ O ₃	2.80	1.18	0.94	2.61	0.37	0.87	0.48	1.10	0.34
V ₂ O ₃	0.57	0.78	0.92	0.63	0.71	0.81	0.76	0.52	0.76
Cr ₂ O ₃	0.11	0.13	0.04	0.11	0.24	0.11	0.26	0.05	0.14
Fe ₂ O ₃	51.06	55.96	60.09	43.76	62.69	62.34	63.69	55.24	64.84
FeO	36.03	35.74	33.86	39.80	33.17	33.07	32.38	35.44	31.99
MgO	1.33	0.14	0.04	0.90	0.06	0.13	0.07	0.11	0.03
MnO	0.43	0.39	0.36	0.76	0.28	0.16	0.06	1.05	0.14
CaO	0.16	0.21	0.26	0.21	0.03	0.13	0.40	0.36	0.33
Totals	100.00	100.00	100.00	100.00	100.00	100.00	100.00	100.00	100.00
Si	0.017	0.021	0.012	0.021	0.016	0.018	0.013	0.016	0.014
Ti	0.197	0.140	0.091	0.298	0.059	0.054	0.044	0.163	0.030
Al	0.123	0.052	0.042	0.114	0.017	0.039	0.022	0.049	0.016
V	0.017	0.024	0.028	0.019	0.022	0.025	0.023	0.016	0.023
Cr	0.003	0.004	0.001	0.003	0.007	0.003	0.008	0.001	0.004
Fe ³⁺	1.429	1.597	1.722	1.225	1.805	1.788	1.832	1.576	1.868
Fe ²⁺	1.120	1.133	1.079	1.238	1.061	1.054	1.035	1.124	1.024
Mg	0.074	0.008	0.002	0.049	0.003	0.008	0.004	0.006	0.002
Mn	0.013	0.012	0.012	0.024	0.009	0.005	0.002	0.034	0.004
Ca	0.007	0.008	0.010	0.008	0.001	0.005	0.017	0.015	0.014
Log(Mg/Mn)	0.738	-0.197	-0.725	0.317	-0.459	0.164	0.337	-0.752	-0.404

Table 3.3. Magnetite compositions determined by EMPA and EDS.

N	4	3	3	5	43	7	6	7	2
Sample	SC4	CP13-14	PC5_10	KV950718-9	LC7A	SC5	RDA124	RTT190	LG6
Location	Utah	Utah	Utah	Utah	Utah	Utah	Chile	Chile	Chile
Analysis type	EDS	EDS	EDS	EMPA	EMPA	EMPA	EDS	EDS	EDS
SiO ₂	1.89	0.92	0.29	0.12	0.06	0.11	0.44	0.52	0.61
TiO ₂	1.32	2.02	2.35	6.70	0.80	0.16	6.13	6.52	0.41
Al ₂ O ₃	0.84	1.31	1.18	3.13	0.42	0.27	0.47	1.81	0.35
V ₂ O ₃	0.48	0.87	0.32	0.50	0.48	0.42	0.71	1.36	0.55
Cr ₂ O ₃	0.40	0.04	0.07	0.00	0.30	0.00	0.21	0.21	0.30
Fe ₂ O ₃	60.60	60.57	62.18	53.28	65.45	67.90	54.93	51.82	65.59
FeO	32.08	33.80	32.61	33.69	31.36	30.77	36.57	36.24	31.63
MgO	0.17	0.18	0.37	2.26	0.05	0.04	0.31	0.63	0.07
MnO	0.17	0.18	0.58	0.58	0.09	0.12	0.16	0.76	0.21
CaO	2.05	0.11	0.05	0.10	0.03	0.18	0.08	0.14	0.29
Totals	100.00	100.00	100.00	100.60	99.17	100.19	100.00	100.00	100.00
Si	0.071	0.035	0.011	0.004	0.002	0.004	0.017	0.019	0.023
Ti	0.038	0.057	0.067	0.185	0.023	0.004	0.170	0.184	0.012
Al	0.037	0.058	0.053	0.135	0.019	0.012	0.021	0.080	0.016
V	0.015	0.026	0.010	0.015	0.015	0.013	0.022	0.041	0.017
Cr	0.012	0.001	0.002	0.000	0.009	0.000	0.006	0.006	0.009
Fe ³⁺	1.719	1.729	1.779	1.473	1.906	1.959	1.579	1.467	1.889
Fe ²⁺	1.011	1.072	1.037	1.035	1.015	0.987	1.157	1.138	1.012
Mg	0.010	0.010	0.021	0.124	0.003	0.002	0.017	0.035	0.004
Mn	0.005	0.006	0.019	0.018	0.003	0.004	0.005	0.024	0.007
Ca	0.082	0.005	0.002	0.004	0.001	0.007	0.003	0.006	0.012
Log(Mg/Mn)	0.249	0.229	0.049	0.839	-0.063	-0.237	0.547	0.160	-0.210

Table 3.3. Magnetite compositions determined by EMPA and EDS.

N	2	3	2	2
Sample	SG4	CDO6	ES6	PR3
Location	Chile	Mexico	Mexico	Mexico
Analysis type	EDS	EMPA	EMPA	EMPA
SiO ₂	0.57	0.04	0.04	0.04
TiO ₂	0.39	0.80	0.03	0.05
Al ₂ O ₃	0.40	0.61	0.05	0.08
V ₂ O ₃	0.58	0.35	0.30	0.36
Cr ₂ O ₃	0.10	0.00	0.00	0.00
Fe ₂ O ₃	65.78	65.73	67.83	67.94
FeO	31.77	31.07	30.02	30.77
MgO	0.10	0.15	0.00	0.00
MnO	0.25	0.18	0.40	0.10
CaO	0.06	0.10	0.17	0.05
Totals	100.00	99.11	98.88	99.41
Si	0.022	0.002	0.002	0.002
Ti	0.011	0.023	0.001	0.001
Al	0.018	0.028	0.002	0.004
V	0.018	0.011	0.009	0.011
Cr	0.003	0.000	0.000	0.000
Fe ³⁺	1.895	1.912	1.986	1.979
Fe ²⁺	1.017	1.004	0.977	0.996
Mg	0.006	0.009	0.000	0.000
Mn	0.008	0.006	0.013	0.003
Ca	0.003	0.004	0.007	0.002
Log(Mg/Mn)	-0.157	0.165	-	-

Table 3.4. Ilmenite compositions determined by EDS.

N	5	4	6	3	2	2	4	3	2
Sample	97100808b	98100301	SBD69-137.6m	SRD02320m	950712-1a1b	CP13-18	CP92-6	LC5	OC1
Location	Indonesia	Indonesia	Indonesia	Indonesia	Utah	Utah	Utah	Utah	Utah
Analysis type	EDS	EDS	EDS	EDS	EDS	EDS	EDS	EDS	EDS
SiO ₂	0.44	0.25	0.27	0.35	1.05	1.81	0.41	0.53	0.44
TiO ₂	27.37	35.83	26.40	28.99	42.62	46.80	47.64	43.62	45.65
Al ₂ O ₃	0.26	0.21	0.33	0.24	0.44	0.96	0.19	0.38	0.20
V ₂ O ₃	0.41	0.65	0.39	0.47	0.54	0.19	0.19	0.39	0.18
Cr ₂ O ₃	0.01	0.02	0.10	0.02	0.02	0.08	0.05	0.07	0.02
Fe ₂ O ₃	46.70	30.74	48.88	43.74	15.99	6.76	8.53	15.69	12.33
FeO	21.27	30.04	22.46	23.81	37.12	40.26	41.05	36.48	36.73
MgO	0.34	0.21	0.53	0.24	0.28	1.03	0.33	0.55	0.21
MnO	3.07	1.99	0.58	1.88	1.90	2.07	1.48	2.01	3.60
CaO	0.12	0.07	0.05	0.26	0.03	0.05	0.14	0.27	0.64
Totals	100.00	100.00	100.00	100.00	100.00	100.00	100.00	100.00	100.00
Si	0.011	0.006	0.007	0.009	0.026	0.044	0.010	0.013	0.011
Ti	0.529	0.688	0.510	0.560	0.809	0.876	0.904	0.828	0.867
Al	0.008	0.006	0.010	0.007	0.013	0.028	0.006	0.011	0.006
V	0.008	0.013	0.008	0.010	0.011	0.004	0.004	0.008	0.004
Cr	0.000	0.000	0.002	0.000	0.000	0.002	0.001	0.001	0.000
Fe ³⁺	0.903	0.591	0.945	0.845	0.304	0.127	0.162	0.298	0.234
Fe ²⁺	0.457	0.642	0.483	0.511	0.784	0.838	0.866	0.770	0.776
Mg	0.013	0.008	0.020	0.009	0.011	0.038	0.013	0.021	0.008
Mn	0.067	0.043	0.013	0.041	0.041	0.043	0.032	0.043	0.077
Ca	0.003	0.002	0.002	0.007	0.001	0.001	0.004	0.007	0.017
Log(Mg/Mn)	-0.716	-0.739	0.208	-0.645	-0.586	-0.061	-0.403	-0.315	-0.982

Table 3.4. Ilmenite compositions determined by EDS.

N	2	6	6	4	5	6	2	1
Sample	CP13-14	LC7	PC5-10	RTT190	LG6	RDA124	SG4	PR3
Location	Utah	Utah	Utah	Chile	Chile	Chile	Chile	Mexico
Analysis type	EDS	EDS	EDS	EDS	EDS	EDS	EDS	EMPA
SiO ₂	0.33	0.40	0.17	0.23	0.77	0.41	0.36	0.01
TiO ₂	48.17	28.84	27.25	47.08	43.28	29.66	41.72	46.48
Al ₂ O ₃	0.37	0.16	0.31	0.20	0.25	0.22	0.34	0.01
V ₂ O ₃	0.22	0.57	0.44	0.38	0.40	0.67	0.51	0.86
Cr ₂ O ₃	0.00	0.02	0.03	0.08	0.02	0.05	0.06	0.00
Fe ₂ O ₃	7.39	43.83	47.64	10.42	15.62	42.32	19.75	9.38
FeO	41.43	25.32	22.56	37.98	36.34	25.16	33.96	35.86
MgO	0.19	0.25	0.68	1.23	0.11	0.54	0.69	0.01
MnO	1.90	0.46	0.84	2.34	2.97	0.72	2.26	5.11
CaO	0.01	0.15	0.07	0.06	0.24	0.25	0.36	0.25
Totals	100.00	100.00	100.00	100.00	100.00	100.00	100.00	98.55
Si	0.008	0.010	0.004	0.006	0.020	0.011	0.009	0.000
Ti	0.914	0.557	0.526	0.888	0.824	0.571	0.792	0.901
Al	0.011	0.005	0.009	0.006	0.007	0.007	0.010	0.000
V	0.004	0.012	0.009	0.008	0.008	0.014	0.010	0.018
Cr	0.000	0.000	0.001	0.002	0.000	0.001	0.001	0.000
Fe ³⁺	0.140	0.848	0.920	0.197	0.298	0.815	0.376	0.182
Fe ²⁺	0.874	0.544	0.484	0.797	0.769	0.539	0.717	0.773
Mg	0.007	0.009	0.026	0.046	0.004	0.020	0.026	0.000
Mn	0.041	0.010	0.018	0.050	0.064	0.016	0.048	0.111
Ca	0.000	0.004	0.002	0.002	0.006	0.007	0.010	0.007
Log(Mg/Mn)	-0.746	-0.032	0.153	-0.035	-1.202	0.118	-0.272	-2.398

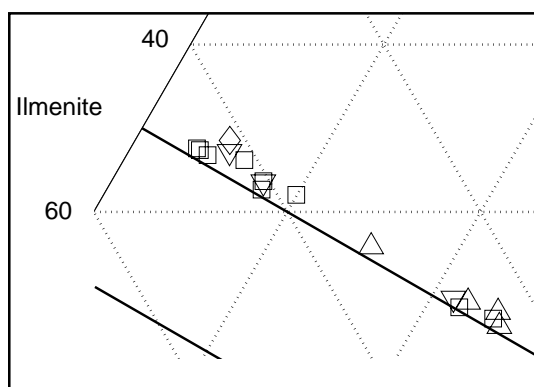
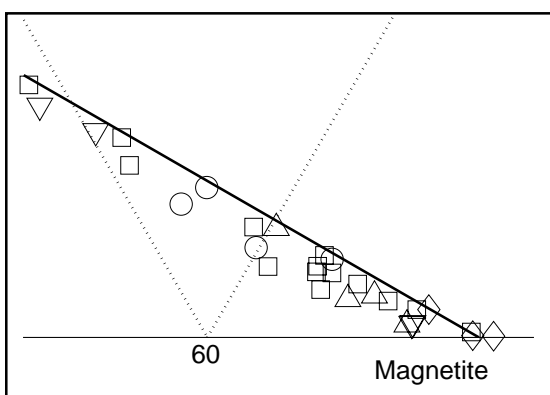
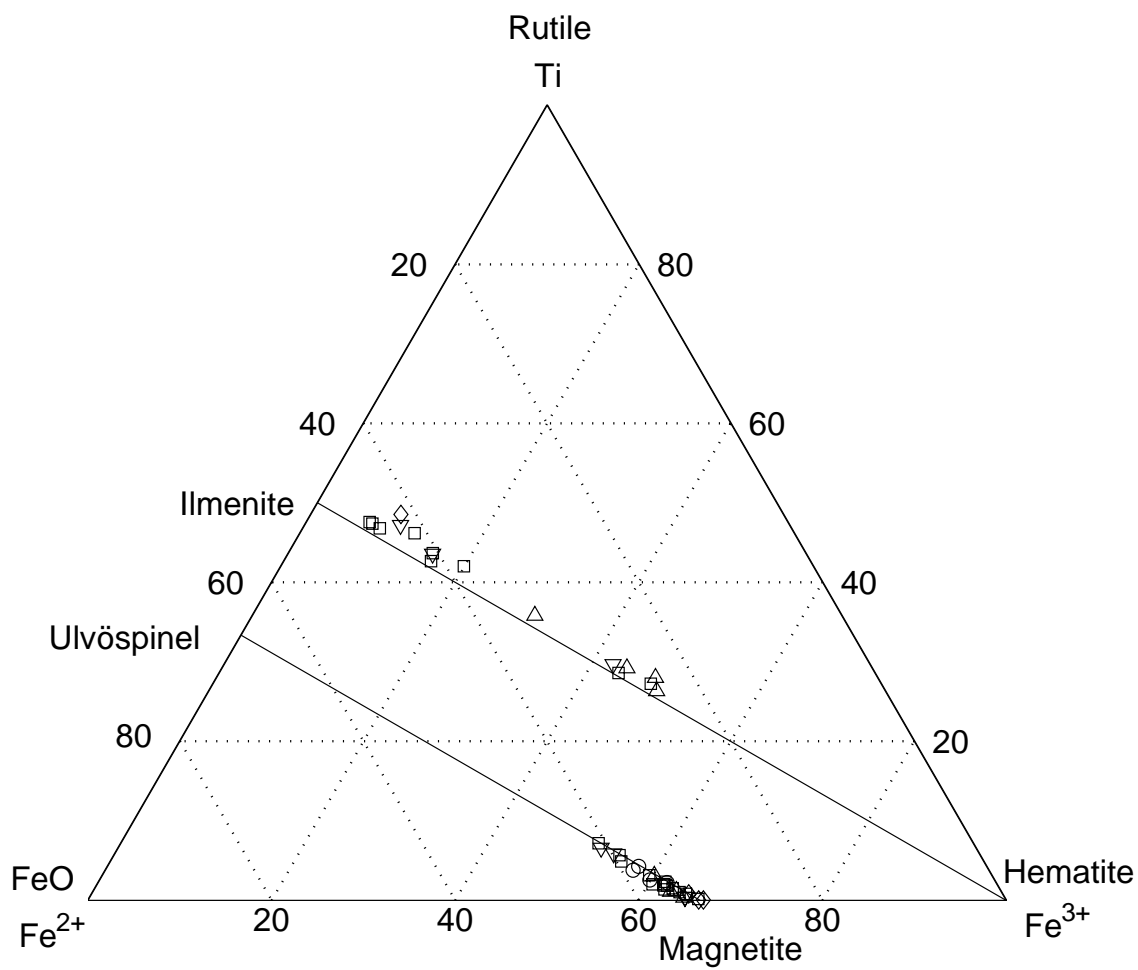


Figure 3.3. Ternary plot showing oxide compositions with the regions of interest blown up.

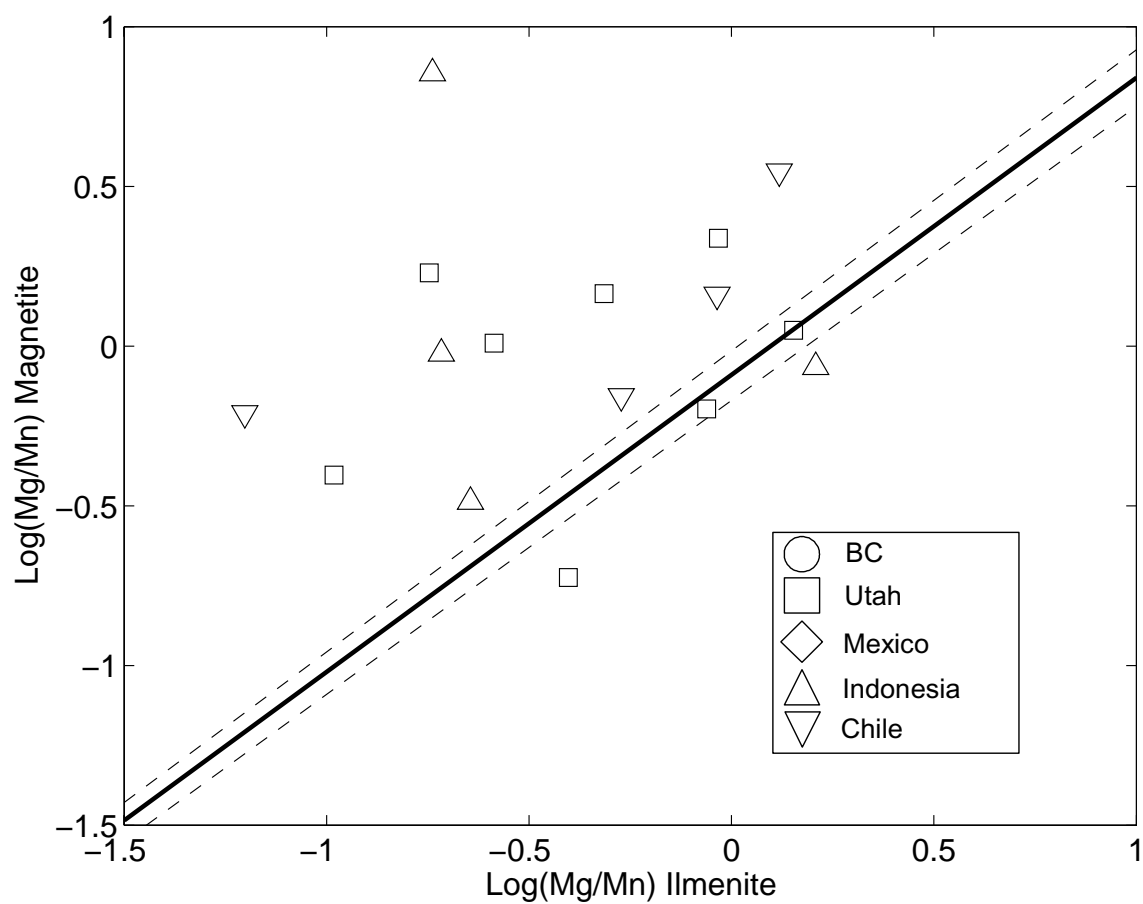


Figure 3.4. Mg/Mn plot of oxide composition. Line shows equilibrium determined by Bacon and Hirschmann (1988) with two-sigma error envelope (dotted lines).

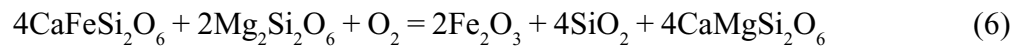
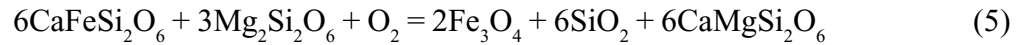
Sphene

Sphene was analyzed in only two samples to evaluate the degree of solid solution for activity calculations. In both cases, minor substitution of REE for Ca, Fe³⁺ and Al for Ti, and F and OH for O yields a mole fraction of 0.85-0.88 CaTiSiO₅. Using the mixing model of Tropper et al. (2002) the a_{sph} is approximately 0.9 for these compositions, and calculations were made with this value. This dilution corresponds to ca. 0.1 log unit change in the calculated log fO₂ and does not have a large effect on the fO₂ calculations.

fO₂ Calculations

Reactions for fO₂ Calculations

Reaction 2 can be applied to rocks that contain two oxides that have unaltered ilmenite. Oxidation reactions between ferromagnesian silicates and oxides can also be used to estimate fO₂. Several reactions can be written for the oxidation of pyroxene components:



Calculations of fO₂ were made using MELTS mixing models (Ghiorso and Sack, 1995; Ghiorso et al., 2003). Calculations made with QUILF for comparison averaged 0.5 log units higher than the MELTS calculations for silicate-oxide equilibria and 1.0 log units higher for two-oxide equilibria.

Oxygen fugacity calculations are nearly independent of P and T as long as the results are given relative to buffer curves. In this study, all fO₂ calculations are reported relative to NNO. Calculations were made at a temperature of 800°C and pressure of 2 kbars. A temperature of 800°C was selected because diffusion of Fe and Mg in cpx is

relatively slow, indicating that it likely retains compositions from 800°C or more (Dimanov and Sautter, 2000). Oxides are often included inside the pyroxenes, implying that they equilibrated together in the magmas. If the pressure is changed by 1 kbar, the fO_2 shifts by just 0.002 log units relative to the buffer curve. Pressure does not have significant bearing on the calculations.

Estimating $aSiO_2$

Reactions 3-8, those involving clinopyroxene to determine fO_2 , require knowledge of the activity of SiO_2 ($aSiO_2$) during the time the minerals equilibrated. The clinopyroxene crystallized early in the samples in this study and did not crystallize with quartz; therefore, the $aSiO_2$ was less than one. In order to evaluate the $aSiO_2$ it is necessary to know the melt composition at the time the oxides and silicates equilibrated. The $aSiO_2$ was estimated using experimental glass compositions with starting materials that are similar in bulk compositions to the intrusive rocks in this study that were equilibrated at or near 800°C and 2 kbars. Only two sets of experiments were found that used these conditions. The experiments of Luhr (1990) used a mildly alkaline trachyandesite with 57 wt% SiO_2 as a starting composition. Glass composition from run 149 of these experiments was used for samples from British Columbia, Clayton Peak in Utah, RTT190 in Chile, and 98100301 from Indonesia. For the remaining samples, the glass composition from run number 4 of Scaillet and Evans (1999) was used. These experiments used Pinatubo dacite with about 65 wt% SiO_2 as a starting material. The MELTS supplemental calculator was used to calculate $aSiO_2$ from the glass compositions assuming water content given by the model of Moore et al. (1998).

Results

In most samples, the fO_2 calculated using more than one reaction produced results with 2- σ errors of 0.4-0.5 log units. This was not the case in samples where the ilmenite had clearly been altered and reset. In these cases, the hematite component of the ilmenite was almost completely removed leading to low fO_2 estimates in all reactions involving

hematite. All hematite reactions from samples with altered ilmenite grains were excluded from the averages. The fO_2 of all samples was obtained by averaging the fO_2 for all reactions that included phases that appeared to be in equilibrium (Table 3.5).

The calculated fO_2 for the intrusions ranges from -0.2 to 3.9 log units relative to NNO (Fig. 3.5). The most oxidized intrusions are the alkaline magmas associated with mineralization at Copper Mountain, British Columbia, and the most reduced is the Clayton Peak stock in Utah. Measured fO_2 values are similar to previously measured values for arc andesites.

Zircon Analyses

The Ce^{4+}/Ce^{3+} measurements in zircon were undertaken to evaluate the fO_2 in samples that lack the appropriate mineral assemblage or have been altered (Table 3.6). Ballard et al. (2002) used this method to distinguish between barren and mineralized intrusions at the Chuquicamata PCD in Chile. The differences between ore-forming and barren samples was attributed to differences in oxygen fugacity leading to higher Ce^{4+} content of zircons in mineralized samples. Simultaneous U-Pb dating can be used to consider the evolution of magmatic systems.

For samples in this study, there is no correlation between the measured fO_2 and zircon Ce^{4+}/Ce^{3+} (Fig 3.6). There is a better correlation between Ce^{4+}/Ce^{3+} in zircon and bulk SiO_2 of the whole rock for most samples (Fig. 3.7). There is no relationship between Ce^{4+}/Ce^{3+} or fO_2 and age for samples from Utah or Chile. For Indonesian samples, both Ce^{4+}/Ce^{3+} and fO_2 increase with time, similar to the results observed at Chuquicamata by Ballard et al. (2002) (Fig. 3.8).

Discussion

Recording of fO_2

The initial fO_2 of a granitoid magma should reflect the oxidation state in the source region of the magma. However, the fO_2 recorded by an intrusive rock could change during crystallization, due to fractional crystallization or exsolution of a magmatic vapor phase.

Table 3.5. fO_2 calculated for all samples using MELTS activity models relative to NNO.

Samples	BC2020	BC2032	BC2036	BC2042	LG6	RDA124	RTT190	SG4
Region	BC	BC	BC	BC	Chile	Chile	Chile	Chile
Location	Smelter Lk.	Voigt	Copper Mt.	Copper Mt.	La Gloria	Cerro Littoria Quebrada	Castillo	San Gabriel
Age (Ma)	197±8 ¹	194±7 ¹	193±7 ¹	193±7 ¹	9.5±0.3 ²	~9	~10	10.6±0.8 ²
Reaction 2	-	-	-	-	-0.7	1.0	-1.5	-0.3
Reaction 3	-	-	-	-	-	0.6	0.1	-
Reaction 4	-	-	-	-	-	0.7	-0.4	-
Reaction 5	1.3	2.8	3.7	3.8	1.7	1.1	0.5	-
Reaction 6	-	-	-	-	0.9	1.1	-0.1	-
Reaction 7	-	-	-	-	1.5	1.4	-	-
Reaction 8	-	-	-	-	0.7	1.3	-	-
Sample fO_2	1.3	2.8	3.7	3.8	1.6	1.0	0.3	-
Samples	97100808b	98100301	SBD69-137.6mSRD02320m	CDO6	ES6	PR3	950712-1a1b	
Region	Indonesia	Indonesia	Indonesia	Indonesia	Mexico	Mexico	Utah	
Location	Katala	Concentrator	Batu Hijau	Arung Ara	Conc. del Oro	El Salvador	Clayton Peak	
Age (Ma)	15-7 ³	4.43±0.14 ³	3.74±0.14 ³	4.99±0.16 ³	-	-	<35.3±0.4	
Reaction 2	1.3	0.5	1.3	0.9	-	-	-2.7	-0.5
Reaction 3	0.9	-	-	0.6	-	-	-	-
Reaction 4	1.0	-	-	0.7	-	-	-	-
Reaction 5	-	-	-	-	1.4	2.6	-	1.8
Reaction 6	-	-	-	-	-	-	-	1.0
Reaction 7	-	-	-	-	-	-	-	2.1
Reaction 8	-	-	-	-	-	-	-	1.2
Sample fO_2	1.1	0.5	1.3	0.7	1.4	2.6	-	1.9

- = Not applicable. Necessary phase missing or not analyzed. Age data from: 1 Preto et al. (1971) K-Ar biotite; 2 This study LA-ICPMS U-Pb zircon; 3 Garwin (2000) SHRIMP U-Pb zircon. Errors on all ages are two standard errors of the mean.

Table 3.5 (cont'd). fO_2 calculated for all samples using MELTS activity models relative to NNO.

Samples	950917-36	CP13-14	CP13-18	CP92-6	LC10	LC5	LC7	LC7X
Region	Utah	Utah	Utah	Utah	Utah	Utah	Utah	Utah
Location	Park Premier	Clayton Peak	Clayton Peak	Clayton Peak	Last Chance	Last Chance	Last Chance	Last Chance
Age (Ma)	32.4 ± 0.5^4	35.3 ± 0.4^2	35.3 ± 0.4^2	35.3 ± 0.4^2	38.6 ± 0.2^5	38.6 ± 0.2^5	38.6 ± 0.2^5	38.6 ± 0.2^5
Reaction 2	-	-2.9	-2.2	-2.4	-	-0.7	0.8	-
Reaction 3	0.5	-	-	-0.3	-	-	-	-
Reaction 4	-	-	-	-1.0	-	-	-	-
Reaction 5	-	0.2	0.3	0.4	1.1	1.4	1.5	1.9
Reaction 6	-	-0.9	-0.5	-0.6	-	0.7	1.3	-
Reaction 7	-	-	-	-	-	2.1	2.3	-
Reaction 8	-	-	-	-	-	1.2	1.8	-
Sample fO_2	0.5	0.2	0.3	0.0	1.1	1.8	1.7	1.9

Samples	O11-4	OC1	PC5-10	SC4	SC5
Region	Utah	Utah	Utah	Utah	Utah
Location	Ontario	Ohio Copper	Pine Creek	Soldier Canyon	Soldier Canyon
Age (Ma)	33.7 ± 0.3^2	34 ± 1.4^2	41.3 ± 1.0^4	34.7 ± 1.4^2	34.7 ± 1.4^2
Reaction 2	-	-1.6	1.3	-	-
Reaction 3	-	-	-	-	-
Reaction 4	-	-	-	-	-
Reaction 5	0.9	1.3	-	1.4	1.8
Reaction 6	-	0.3	-	-	-
Reaction 7	-	-	-	-	-
Reaction 8	-	-	-	-	-
Sample fO_2	0.9	1.3	1.3	1.4	1.8

- = Not applicable. Necessary phase missing or not analyzed. Ages from: 2 This study LA-ICPMS U-Pb zircon; 4 John et al. (1997) Ar-Ar biotite; 5 Parry et al. (2001) U-Pb zircon. Errors on all ages are two standard errors of the mean.

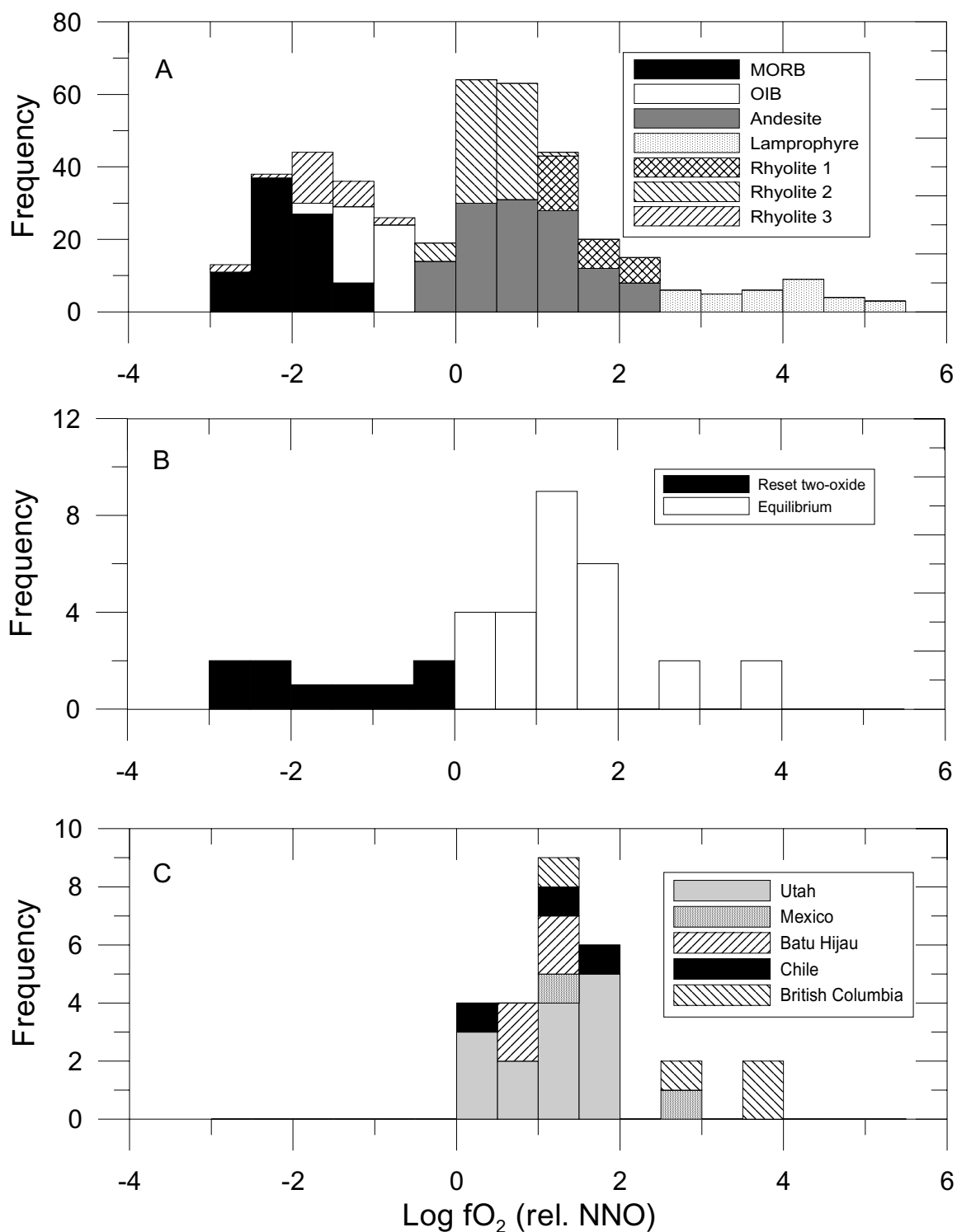


Figure 3.5. Histograms showing the distribution of calculated fO_2 . A. fO_2 determined for a wide range of volcanic rocks from previous studies (Carmichael and Ghiorso, 1991). B. Data from this study showing the effect of reequilibration of ilmenite on fO_2 calculations. C. Data from this study showing the variation of fO_2 within each locality. Rhyolite 1 has biotite-hornblende assemblage; Rhyolite 2 has quartz-ferrosilite assemblage; Rhyolite 3 has fayalite-quartz assemblage.

Table 3.6. Age and Ce^{4+}/Ce^{3+} for zircons determined by LA-ICPMS.

Sample	LO4	LB50	ET13	LB5	SG14	LG3	971713A	97101030
Region	Chile	Chile	Chile	Chile	Chile	Chile	Indonesia	Indonesia
Location	La Obra	Andina	El Teniente	San Francisco	San Gabriel	La Gloria	Sekongkang	Katala
Age	20.3±1.4	5.5±0.8	4.7±0.7	14.2±0.4	10.6±0.9	9.5±0.3	5.88±0.14 ¹	4.43±0.14 ¹
fO ₂	-	-	-	-	-	1.6	-	1.1
Ce ⁴⁺ /Ce ³⁺	130±40	140±50	85±30	15±2	90±40	190±70	65±20	90±30
Sample	97101143	SBD04-157m	97100808A	SKD01-276m	SBD41-414m	SBD12-2329	98112302	98040
Region	Indonesia	Indonesia	Indonesia	Indonesia	Indonesia	Indonesia	Indonesia	Utah
Location	Katala	Batu Hijau	Katala	Katala	Batu Hijau	Batu Hijau	Teluk Puna	QMP
Age	4.75±0.22 ¹	3.76±0.10 ¹	4.49±0.12 ¹	4.70±0.16 ¹	3.74±0.14 ¹	3.89±0.08 ¹	6.84±0.16 ¹	37.4±0.7
fO ₂	-	-	-	-	1.3	-	-	-
Ce ⁴⁺ /Ce ³⁺	170±40	190±20	130±40	190±40	340±70	340±60	160±40	120±30
Sample	99011	4890 2080L	OC1	SC6	O11-4	CP92-6	A9-11	LC8-12
Region	Utah	Utah	Utah	Utah	Utah	Utah	Utah	Utah
Location	LP	QLP	Ohio Copper	Soldier Canyon	Ontario	Clayton Peak	Alta	Little Cottonwood
Age	37.3±0.8	36.2±0.8	34.0±1.3	34.7±1.4	33.7±0.3	35.3±0.4	34.0±0.2	30.8±0.4
fO ₂	-	-	1.3	1.6	0.6	0.2	-	-
Ce ⁴⁺ /Ce ³⁺	150±40	480±110	13±4	50±20	140±60	12±4	320±60	460±80

- = Not determined; 1 Garwin (2003) SHRIMP U-Pb zircon ages. All other ages are LA-ICPMS U-Pb zircon ages from this study. Errors are two standard errors of the mean.

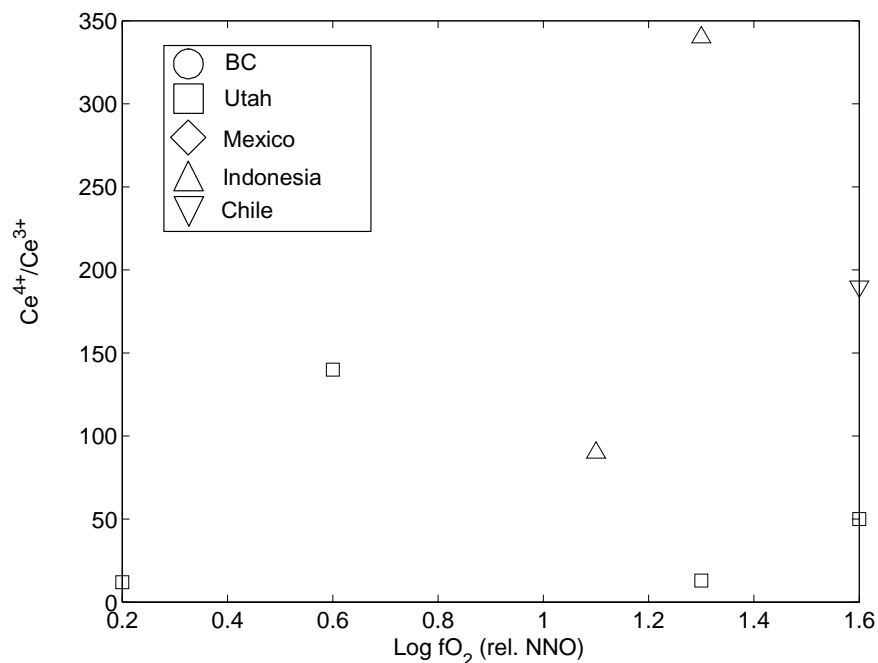


Figure 3.6. Plot showing calculated Ce^{4+}/Ce^{3+} of zircon vs. sample fO_2 . No correlation is observed, indicating that Ce^{4+}/Ce^{3+} ratios do not reflect variations in fO_2 .

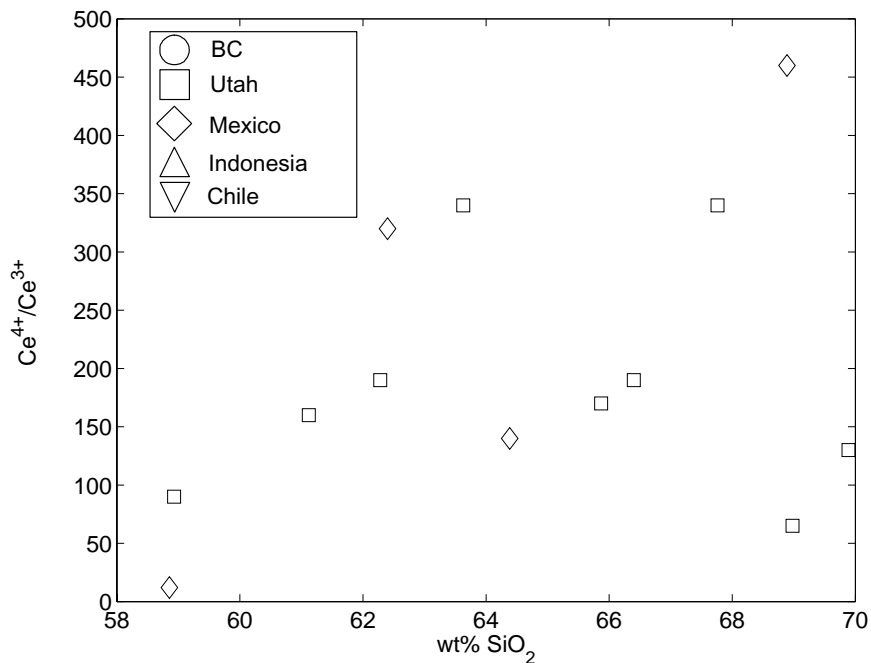


Figure 3.7. Plot showing calculated Ce^{4+}/Ce^{3+} in zircon vs. whole rock wt% SiO_2 . There is better correlation with SiO_2 than fO_2 , suggesting that bulk composition plays an important role in controlling Ce^{4+}/Ce^{3+} ratios in zircon.

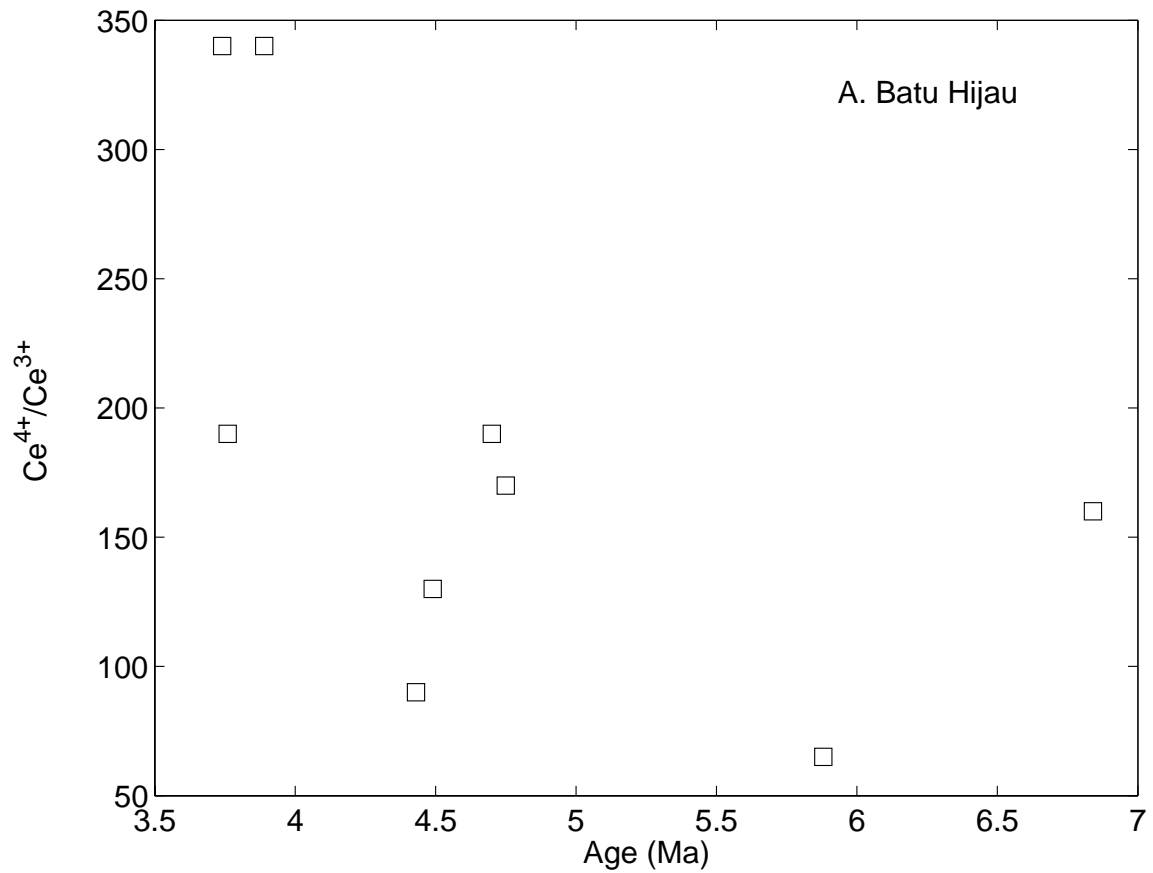


Figure 3.8. Calculated $\text{Ce}^{4+}/\text{Ce}^{3+}$ for zircon vs. U-Pb zircon ages for samples from Batu Hijau, Indonesia. The $\text{Ce}^{4+}/\text{Ce}^{3+}$ increases with time, similar to the results of Ballard et al. (2002).

The fO_2 recorded by a granitoid could also be changed during subsolidus alteration. Therefore, in order to understand how to interpret the fO_2 of granitoids it is necessary to determine when the fO_2 is fixed.

Probably the biggest concern when applying mineral equilibria to granitoids is the resetting of mineral compositions during subsolidus alteration. Bacon and Hirschmann (1988) showed that Mg-Mn partitioning between the oxides may be used to determine if oxides equilibrated at high temperature (Fig. 3.4). Several intrusions from this study plot very close to the equilibrium line with the remaining samples having Mn enrichment in the ilmenite. Although oxides that equilibrate at high temperature should plot on the equilibrium line, this method does not work very well for testing the suitability of oxides from granitoids for fO_2 calculations. Some samples that show clear resetting of the ilmenite, such as RTT190, plot very close to the equilibrium line described by Bacon and Hirschmann (1988) while other samples that have oxides that give apparently magmatic fO_2 , such as 97100808b, plot far away from the equilibrium line. This is because the Mg/Mn partitioning of oxides can be reset without greatly perturbing the hematite and magnetite activities.

Suitability of oxides is more dependent on whether the ilmenite exsolved during cooling. In samples where exsolution of ilmenite is preserved, Reaction 2 produces reasonable results for fO_2 calculations and samples with homogeneous ilmenite produced unreasonably low fO_2 . The magnetite chemistry does not affect fO_2 calculations very much. This is because there is rarely more than 10-15% dilution of the magnetite component in magnetites that crystallize from intermediate magmas above NNO. Therefore, even total loss of the minor components will only change the $\log a(Fe_3O_4)$ by approximately 0.15, leading to a maximum change of 0.6 log units using the two-oxide method and a 0.3 log unit shift using clinopyroxene-oxide-quartz equilibria.

The fO_2 calculated using Reactions 3-8 is largely dependent on the composition of silicate minerals rather than oxides. The components of silicates are often more diluted

than the components of oxides (e.g. $\text{Mg}_2\text{Si}_2\text{O}_6$ in clinopyroxene for Reactions 5 and 6), and the ratio between the coefficient of the oxide components and the coefficient of O_2 is smaller in the reactions that include silicates. Silicates are more likely to retain their compositions during cooling because of slower diffusion. Samples from Copper Mountain have between 10-16 mol% esseneite and have Mg# of around 0.9, indicating that equilibria such as those represented by Reactions 2-8 have progressed to the right leading to depletion of the ferrosilite, enstatite, and hedenbergite components of the pyroxenes. This is in contrast to the Clayton Peak stock, which has very little Fe^{3+} and has Mg# of 0.6 in the clinopyroxene. Silicate compositions are clearly recording the influence of magmatic $f\text{O}_2$ on mineral chemistry. Therefore, application of equilibria involving silicates yields improved $f\text{O}_2$ estimates if silicate-oxide equilibria can be applied.

The effects of re-equilibration of the oxides can be seen in the data for samples that contain ilmenite that reset during cooling and lost most of their Fe_2O_3 component. These grains are typically homogeneous and sometimes show alteration to complex mixtures of silicates and oxides. For example, in sample CP92-6, two-oxide equilibrium produces $f\text{O}_2$ of NNO -2.4, equilibria between silicates and hematite yield $f\text{O}_2$ of NNO -0.7, and silicate magnetite equilibria give $f\text{O}_2$ of NNO +0.0. Silicate-magnetite equilibria show the highest $f\text{O}_2$ and appear to have preserved the magmatic conditions. In the cases where no phases appear to be altered, $f\text{O}_2$ calculated using silicate-oxide reactions is in good agreement with that of the $f\text{O}_2$ calculated using two oxides. In these samples, the hematite and magnetite components of the oxides do not appear to have changed during cooling.

Other factors can lead to changes in $f\text{O}_2$ during crystallization of granitoids. Changes in $f\text{O}_2$ during fractional crystallization of layered mafic intrusions were found experimentally by Snyder et al. (1993). They showed that initial crystallization of olivine and Fe^{3+} -poor chromite led to oxidation of the magma at the Newark Island layered mafic intrusion. Oxidation continued until saturation with titanomagnetite led to reduction of the magma by removal of Fe^{3+} . Though fractional crystallization is common in large mafic

magma chambers, it is more difficult to fractionally crystallize granitoid magmas as a result of their higher viscosity. The stocks in this study do not show evidence of significant layering or the formation of large cumulates as are found in layered mafic intrusions. Therefore it is unlikely that fractional crystallization would affect a granitoid stock to the same extent as a layered mafic intrusion.

Exsolution of a vapor phase during crystallization of a granitoid magma is likely to occur and might affect the fO_2 . Sato and Wright (1966) showed that certain Hawaiian basalts experienced large increases in fO_2 during cooling. This occurred during the period where the magma has solidified to the point where H_2O is no longer able to diffuse through the magma but H_2 is still capable of leaving the magma. This leads to fO_2 conditions above the magnetite-hematite buffer and causes the olivine in the samples to become oxidized, leading to the formation of hematite. The oxidation occurred because H_2 and H_2O were separated. If degassing occurs under equilibrium conditions the vapor phase and the magma will have identical fO_2 leading to no change in magmatic fO_2 during degassing.

Degassing processes do not appear to have affected the granitoids in this study. The mafic silicates in the samples in this study are not altered indicating that they did not experience significant late stage oxidation. Pure hematite was not found in granitoid samples as those described in the oxidized Hawaiian basalts. Measurements of fO_2 for mineral inclusions and groundmass grains yields comparable results, indicating that late-stage processes did not significantly affect mineral compositions. Although degassing must have occurred at some point during crystallization of the granitoids, it had relatively little effect on the minerals that are being used to infer the oxidation state.

Magmatic source regions of granitoids

Intermediate calc-alkaline volcanic magmas are most likely generated by partial melting of gabbroic rocks that formed during ponding of basaltic magma at the mantle-crust interface (Lange and Carmichael, 1996). Granitoids are often thought of as the

intrusive equivalents of these magmas. Though geochemically similar to arc-volcanic rocks, granitoids often form at different periods during arc evolution than volcanic rocks. Usually the exposed granitoids in a region are younger than most of the volcanic rocks and intrude into them. This may just be a matter of preservation resulting from differential erosion of younger volcanic rocks during exposure of the granitoids. It may also indicate that granitoids have higher viscosity due to a lower water content and therefore are unable to erupt. There may also be a fundamental difference in source regions for volcanic and intrusive rocks that would be reflected in fO_2 calculations.

The fO_2 measurements of granitoids in this study generally overlap with previously determined fO_2 for andesites. This suggests that granitoids share a similar source region with calc-alkaline andesites. The source for calc-alkaline andesites is most likely direct partial melting of ponded mafic magmas at the crust mantle interface in subduction zones (Lange and Carmichael, 1996). This view contrasts with models producing intermediate magmas through fractional crystallization of basalts or mixing between basalts and more felsic magmas. The fractional crystallization model would lead to andesites having lower fO_2 than arc basalts due to the removal of titanomagnetite (Lange and Carmichael, 1996). However, arc basalts and andesites often have similar fO_2 relative to a buffer curve. If granitoid magmas formed through magma mixing there should be significant textural evidence that is typically lacking. It is also difficult to generate large volumes of intermediate magma by mixing felsic and mafic magmas due to large differences in temperature and viscosity. The few granitoids that have higher fO_2 than andesites are the peralkaline samples from British Columbia with fO_2 ranging from NNO +2.3 to +3.8. The highest fO_2 volcanic rocks known are alkaline minettes from Mexico, suggesting that the source regions for alkaline magmas in subduction zones are highly oxidized.

Behavior of sulfur in granitoids

The behavior of sulfur during the crystallization of calc-alkaline magmas is of great importance to understanding processes that lead to ore deposit formation and sulfur-rich

volcanic eruptions. The fO_2 of a magma plays an important role in the behavior of sulfur because it controls the valence of sulfur and impacts the stability of sulfur-bearing phases. Previous studies on natural and experimental samples have shown that sulfur valence in the magma varies systematically with magmatic fO_2 with sulfide (S^{2-}) dominating at low fO_2 and sulfate (S^{6+}) dominating at high fO_2 (Carroll and Rutherford, 1988; Wallace and Carmichael, 1994; Matthews et al., 1999). These studies agree that the transition from sulfate to sulfide occurs at approximately NNO +1. Recent XANES analyses of melt inclusions confirmed the presence of sulfite (S^{4+}) in subduction zone basalts that formed at NNO +0.5 to NNO +1.2 (Metrich et al., 2002).

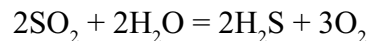
Using the equation of Wallace and Carmichael (1994) that relates S^{6+}/S_{Tot} to oxygen fugacity, it is possible to calculate sulfur valence in granitoids when fO_2 is known.

The equation used is:

$$\log\left(\frac{S^{6+}}{S^{2-}}\right) = 1.02 \log fO_2 + \frac{25410}{T} - 10.0$$

where $\log fO_2$ is the absolute value (not relative to a buffer curve) and T is in Kelvin. This equation does not account for the possibility of sulfite. This equation shows that intrusions in this study had S^{6+}/S_{Tot} during crystallization between 0.19 and 0.9998, suggesting that these magmas had varying behavior of sulfur (Fig. 3.9). More reduced intrusions are more likely to become saturated with respect to a sulfide phase, whereas anhydrite may form in the more oxidized intrusions.

Magmatic fO_2 also has an affect on the composition of a coexisting vapor phase (Giggenbach, 1987). Using the calculated fO_2 and an estimate for H_2O activity it is possible to calculate the sulfur species in an exsolved vapor phase in equilibrium with that magma using the reaction



At 800°C and 2 kbar total pressure at water saturation, the sulfur species in the fluid ranges from 99.8% H_2S to 99.99% SO_2 for the intrusions in this study. The transition between H_2S and SO_2 dominant fluids occurs between NNO +1 and NNO +2. The ore-

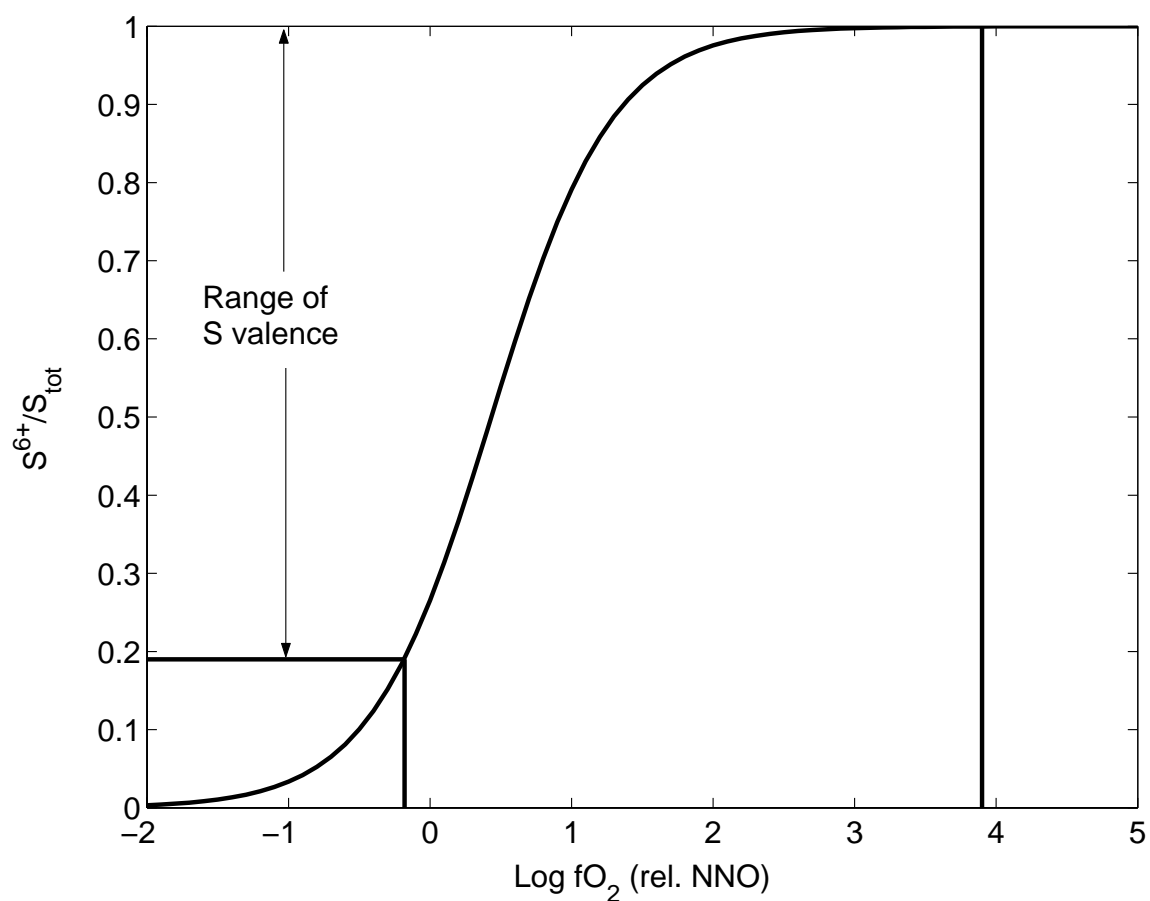


Figure 3.9. Valence of sulfur calculated using the equation of Wallace and Carmichael (1994) plotted against fO_2 . Range of sulfur valence expected for samples in this study is shown.

forming intrusions in this study show highly variable sulfur speciation in the vapor phase. The intrusion associated with Batu Hijau crystallized at NNO +1.3, indicating that 88% of the sulfur in the vapor phase would be H_2S while the intrusion associated with Bingham crystallized at NNO +1.7, such that 5.5% of the sulfur would be H_2S . The intrusion associated with Copper Mountain is extremely oxidized and would have produced a fluid with only 0.01% of the sulfur as H_2S .

The solubility of sulfur is important in evaluating the ore-forming potential of an intrusion and the possible environmental impact of an extrusive rock. Previous studies have suggested that sulfur solubility is dependent on the $f\text{O}_2$ of the magma with the sulfur solubility reaching a minimum at NNO +1 (Carroll and Rutherford, 1987, 1988; Carroll and Webster, 1994). This is the $f\text{O}_2$ of many sulfur-rich volcanic and intrusive rocks and is the $f\text{O}_2$ at which Metrich et al. (2002) detected S^{4+} in glass inclusions. They hypothesized that the minimum in sulfur solubility occurs because S^{4+} partitions strongly into the vapor phase and that magmas at NNO +1 would experience the most efficient scavenging of sulfur during the formation of a magmatic vapor phase. Under more oxidized conditions SO_4^{2-} is dissolved in the magma, whereas S^{2-} would be stable under more reduced conditions leading to reduced partitioning of sulfur into the vapor phase. Sulfur solubility is highest under high $f\text{O}_2$ conditions because S^{6+} does not partition as strongly into the vapor phase as S^{2-} or S^{4+} . Under volatile-undersaturated conditions, the solubility minimum should be less pronounced.

Evaluation of zircon oxybarometer

The use of zircon geochemistry as an oxybarometer is an appealing way to determine $f\text{O}_2$ of altered intrusive rocks. However, in this study, $f\text{O}_2$ and $\text{Ce}^{4+}/\text{Ce}^{3+}$ usually do not correlate, indicating that $\text{Ce}^{4+}/\text{Ce}^{3+}$ does not provide an accurate estimate of $f\text{O}_2$. The correlation of $\text{Ce}^{4+}/\text{Ce}^{3+}$ with bulk sample SiO_2 of several samples indicates that factors other than $f\text{O}_2$ might be affecting the $\text{Ce}^{4+}/\text{Ce}^{3+}$. Temperature and bulk composition are two likely variables that could affect the partitioning of Ce into zircon.

The $\text{Ce}^{4+}/\text{Ce}^{3+}$ ratio is largely dependent on the REE^{3+} pattern of the zircon that is used to estimate the Ce^{3+} content. The REE typically substitute into zircon as a coupled substitution involving P for Si, i.e., as xenotime-type solid solution. The correlation of $\text{Ce}^{4+}/\text{Ce}^{3+}$ with bulk SiO_2 may indicate that temperature affects these measurements, because more mafic magmas should in general be hotter. Bulk composition may play a role in other ways such as the availability of P for the coupled substitution. If magma has low P content, REE^{3+} may not substitute as readily into the zircon structure, whereas substitution of Ce^{4+} is not affected, leading to increased $\text{Ce}^{4+}/\text{Ce}^{3+}$ in zircon. For instance, Hanchar et al. (2001) showed that the presence of P can enhance Dy substitution into zircon by a factor of 5.

The role of other phases crystallizing from the magma must also be evaluated. Crystallization of apatite or allanite would lead to depletion in LREE in the magma. That would lead to a decrease in the amount of Ce^{3+} available for substitution into zircon. Therefore, zircons that coexist with apatite or allanite may have higher $\text{Ce}^{4+}/\text{Ce}^{3+}$ than those that do not. This may be responsible for some of the large within-sample variation typically observed in $\text{Ce}^{4+}/\text{Ce}^{3+}$ for most samples. Grains that crystallized before the magma was saturated with apatite may have lower $\text{Ce}^{4+}/\text{Ce}^{3+}$ than grains that formed after saturation with apatite. The effects could be evaluated by detailed *in situ* studies of zircons with known textural relationships with other phases.

Implications for formation of magmatic-hydrothermal ore deposits

Many previous studies have suggested that PCDs form from hydrothermal fluids exsolved from highly oxidized granitoids (e.g., Burnham and Ohmoto, 1980). These studies have shown that $f\text{O}_2$ of such granitoids is between NNO and NNO +4. This spans most of the range of $f\text{O}_2$ commonly observed for subduction zone magmatism, so it does not provide very much information on how $f\text{O}_2$ may affect the ore-forming process. In addition, there is evidence that some porphyry intrusions are associated with reduced magmas that crystallize at or below the fayalite-magnetite-quartz (FMQ) oxygen buffer

(Rowins, 2000).

In this study, intrusions associated with mineralization (fertile intrusions) have fO_2 from NNO +1.3 to NNO +3.8, whereas intrusions not associated with mineralization (barren intrusions) have fO_2 from NNO to NNO +2.8. There is considerable overlap between the barren and fertile intrusions, indicating that fO_2 alone is not controlling the ore-forming potential of a magma. For example, the fertile intrusion at Batu Hijau has fO_2 of NNO +1.3, which is lower than the fO_2 of nine of the barren intrusions from other districts. However, in British Columbia, Indonesia and Utah, where fO_2 of an intrusion closely associated with PCDs was determined, it was the most highly oxidized intrusion in the district (Figs. 3.10, 3.11). This may indicate that enrichment of the source regions in water, metals, and sulfur is accompanied by oxidation. In an arc setting such as Batu Hijau, this could be due to build up of slab derived components during subduction. Therefore, even though fO_2 is not controlling the ore-forming potential of a magma, it is recording the occurrence of other events that affect the mineralization process.

Magmatic fO_2 affects the solubility of sulfur in granitoid magmas and therefore may have an affect on the size of PCDs. The intrusions associated with Bingham and Batu Hijau crystallized at fO_2 conditions near the experimentally determined minimum for sulfur solubility under vapor-saturated conditions at NNO +1.0 (Carroll and Rutherford, 1987, 1988; Carroll and Webster, 1994). That solubility limit most likely does not exist when a magma is vapor undersaturated since S^{4+} could be dissolved in the magma. This indicates that the intrusion probably rose to a high level in the crust without separating a magmatic vapor phase, otherwise the intrusion would have lost its sulfur. Upon vapor saturation the sulfur would have been efficiently scavenged, resulting in the PCD. The intrusion associated with the much smaller Copper Mountain deposit crystallized at NNO +3.8 where sulfur solubility is significantly higher. It is possible that much of the sulfur in this magma remained in the melt upon exsolution of a vapor phase, leading to a smaller ore body.

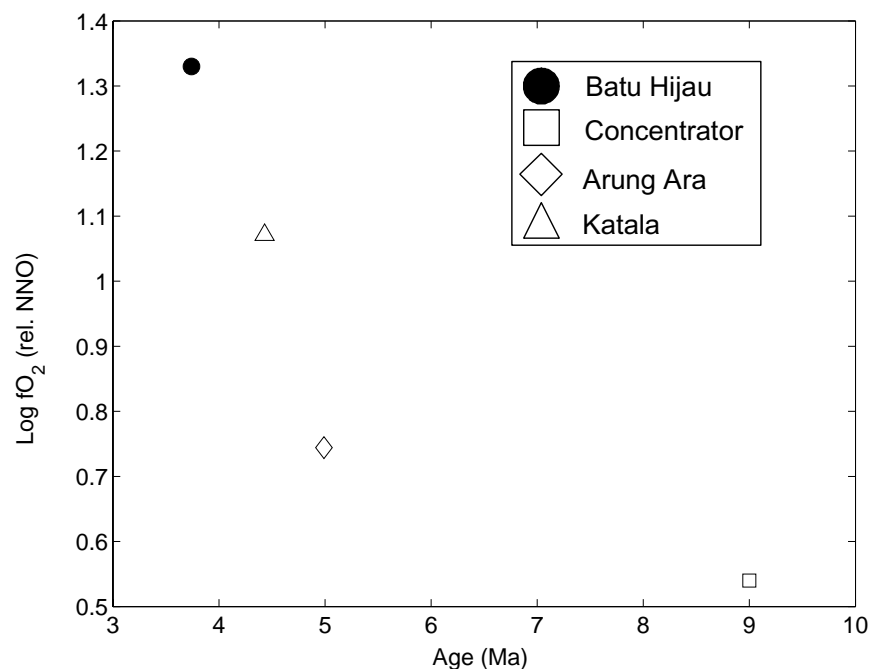


Figure 3.10. fO_2 vs. U-Pb zircon age for samples from Batu Hijau, Indonesia. The intrusion associated with mineralization is the youngest and most oxidized sample in the district.

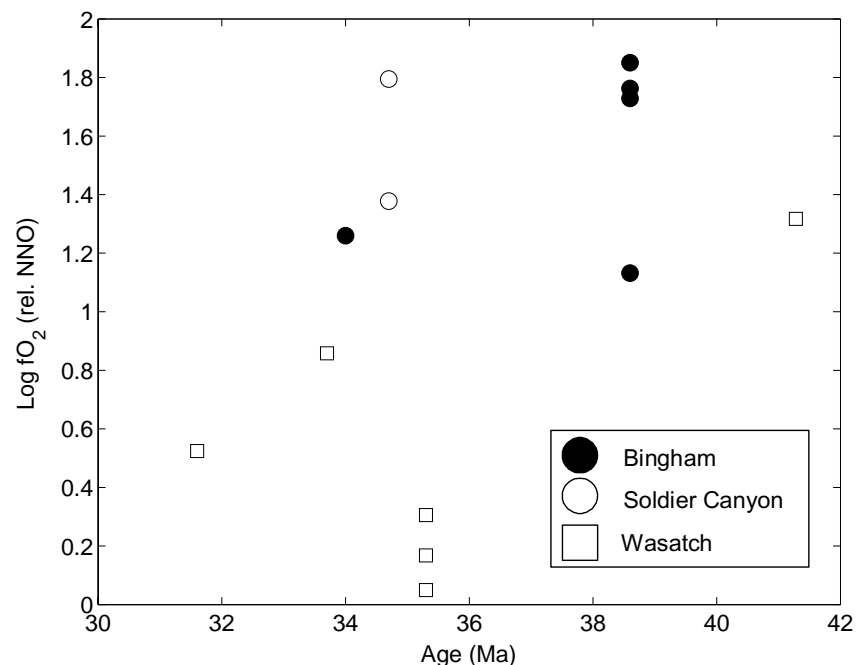


Figure 3.11. fO_2 vs. U-Pb zircon age for samples from Bingham-Park City belt in Utah. The intrusion associated with mineralization is one of the older intrusions in the region and is the most oxidized. Samples from the Oquirrh Range (Soldier Canyon, Last Chance, and Ohio Copper) are more oxidized than the remaining samples from the Wasatch range. The Ohio Copper dike is a 34 Ma post-mineralization dike that cuts the Bingham PCD.

References

- Andersen, D. J., Lindsley, D. H., and Davidson, P. M., 1993, QUILF: a Pascal program to assess equilibria among Fe-Mg-Mn-Ti oxides, pyroxenes, olivine, and quartz: *Computers & Geosciences*, v. 19, p. 1333-1350.
- Bacon, C. R., and Hirschmann, M. M., 1988, Mg/Mn partitioning as a test for equilibrium between coexisting Fe-Ti oxides: *American Mineralogist*, v. 73, p. 57-61.
- Ballard, J. R., Palin, J. M., and Campbell, I. H., 2002, Relative oxidation states of magmas inferred from Ce(IV)/Ce(III) in zircon: application to porphyry copper deposits of northern Chile: *Contributions to Mineralogy and Petrology*, v. 144, p. 347-364.
- Buddington, A. F., and Lindsley, D. H., 1964, Iron-titanium oxide minerals and synthetic equivalents: *Journal of Petrology*, v. 5, p. 310-357.
- Buseck, P. R., 1966, Contact metamorphism and ore deposition, Concepcion del Oro, Mexico: *Economic Geology*, v. 61, p. 97-136.
- Carmichael, I. S. E., 1991, The redox states of basic and silicic magmas: a reflection of their source regions?: *Contributions to Mineralogy and Petrology*, v. 106, p. 129-141.
- Carmichael, I. S. E., and Ghiorso, M. S., 1990, The effect of oxygen fugacity on the redox state of natural liquids and their crystallizing phases: *Reviews in Mineralogy*, v. 24, p. 191-212.
- Carmichael, I. S. E., Lange, R. A., and Luhr, J. F., 1996, Quaternary minettes and associated volcanic rocks of Mascota, western Mexico: a consequence of plate extension above a subduction modified mantle wedge: *Contributions to Mineralogy and Petrology*, v. 124, p. 302-333.
- Carroll, M. R., and Rutherford, M. J., 1987, The stability of igneous anhydrite: experimental results and implications for sulfur behaviour in the 1982 El Chichon trachyandesite and other evolved magmas: *Journal of Petrology*, v. 28, p. 781-801.
- Carroll, M. R., and Rutherford, M. J., 1988, Sulfur speciation in hydrous experimental

- glasses of varying oxidation state; results from measured wavelength shifts of sulfur X-rays: *American Mineralogist*, v. 73, p. 845-849.
- Carroll, M. R., and Webster, J. D., 1994, Solubilities of sulfur, noble gases, nitrogen, chlorine, and fluorine in magmas: *Reviews in Mineralogy*, v. 30, p. 231-279.
- Chesley, J. T., and Ruiz, J., 1997, Preliminary geochronology on molybdenite mineralization from the Bingham Canyon ore deposit, Utah: *Geological Society of America Abstracts with Programs*, v. 29, p. 282.
- Clode, C., Proffett, J., Mitchell, P., and Munajat, I., 1999, Relationships of intrusion, wall-rock alteration and mineralisation in the Batu Hijau copper-gold porphyry deposit: *Australasian Institute of Mining and Metallurgy Publication Series*, v. 4-99, p. 485-498.
- Cornejo, P. C., and Mahood, G. A., 1997, Seeing past the effects of re-equilibration to reconstruct magmatic gradients in plutons; La Gloria Pluton, central Chilean Andes: *Contributions to Mineralogy and Petrology*, v. 127, p. 159-175.
- Deino, A., and Keith, J. D., 1997, Ages of volcanic and intrusive rocks in the Bingham mining district, Utah: *Society of Economic Geologists Guidebook Series*, v. 29, p. 91-100.
- Dilles, J. H., 1987, Petrology of the Yerington Batholith, Nevada: evidence for evolution of porphyry copper ore fluids: *Economic Geology*, v. 82, p. 1750-1789.
- Dimanov, A., and Sautter, V., 2000, "Average" interdiffusion of (Fe,Mn)-Mg in natural diopside: *European Journal of Mineralogy*, v. 12, p. 749-760.
- Fahrni, K. C., Macauley, T. N., and Preto, V. A., 1976, Copper Mountain and Ingerbelle, *in* Brown, A. S., ed., *Porphyry Deposits of the Canadian Cordillera: CIM Special Volume*, p. 368-375.
- Garwin, S., 2000, The Setting, Geometry, and Timing of Intrusion-Related Hydrothermal Systems in the Vicinity of the Batu Hijau Porphyry Copper-Gold Deposit, Sumbawa, Indonesia [Ph.D. thesis]: University of Western Australia, 320 p.

- Ghiorso, M. S., Evans, B. W., Sauerzapf, U., Lattard, D., and Scaillet, B., 2003, A new calibration of the Fe-Ti, two-oxide geothermometer and oxygen barometer: Geological Society of America Abstracts with Programs, v. 35, p. 393.
- Ghiorso, M. S., and Sack, R. O., 1991, Fe-Ti oxide geothermometry; thermodynamic formulation and the estimation of intensive variables in silicic magmas: Contributions to Mineralogy and Petrology, v. 108, p. 485-510.
- Ghiorso, M. S., and Sack, R. O., 1995, Chemical mass transfer in magmatic processes IV: A revised and internally consistent thermodynamic model for the interpolation and extrapolation of liquid-solid equilibria in magmatic systems at elevated temperatures and pressures: Contributions to Mineralogy and Petrology, v. 119, p. 197-212.
- Giggenbach, W. F., 1987, Redox processes governing the chemistry of fumarolic gas discharges from White Island, New Zealand: Applied Geochemistry, v. 2, p. 143-161.
- Haggerty, S. E., 1976, Opaque mineral oxides in terrestrial igneous rocks, *in* D. Rumble, III., ed., Oxide Minerals: Reviews in Mineralogy, p. 1-177.
- Hanchar, J. M., Finch, R. J., Hoskin, W. O., Watson, E. B., Cherniak, D. J., and Mariano, A. N., 2001, Rare earth elements in synthetic zircon. Part 1. synthesis, and rare earth element and phosphorus doping: American Mineralogist, v. 86, p. 667-680.
- Horn, I., Rudnick, R. L., and McDonough, W. F., 2000, Precise elemental and isotope ratio determination by simultaneous solution nebulization and laser ablation-ICP-MS: application to U-Pb geochronology: Chemical Geology, v. 164, p. 281-301.
- Irianto, B., and Clark, G. H., 1995, The Batu Hijau porphyry copper-gold deposit, Sumbawa Island, Indonesia: Australasian Institute of Mining and Metallurgy Publication Series, v. 9/95, p. 299-304.
- Ishihara, S., 1981, The granitoid series and mineralization, *in* Skinner, B., ed., Economic Geology 75th Anniversary Volume: Economic Geology Publishing Company,

- Lancaster, PA, p. 458-484.
- John, D. A., 1989, Geologic setting, depths of emplacement, and regional distribution of fluid inclusions in intrusions of the central Wasatch Mountains, Utah: *Economic Geology*, v. 84, p. 386-409.
- Kay, S. M., and Mpodozis, C., 2002, Magmatism as a probe to the Neogene shallowing of the Nazca Plate beneath the modern Chilean flat-slab: *Journal of South American Earth Sciences*, v. 15, p. 39-57.
- Kay, S. M., Mpodozis, C., and Coira, B., 1999, Neogene magmatism, tectonism, and mineral deposits of the Central Andes (22° to 33° S latitude): *Society of Economic Geologists Special Publication*, v. 7, p. 27-59.
- Kress, V. C., and Carmichael, I. S. E., 1991, The compressibility of silicate liquids containing Fe_2O_3 and the effect of composition, temperature, oxygen fugacity and pressure on their redox states: *Contributions to Mineralogy and Petrology*, v. 108, p. 82-92.
- Lange, R. A., and Carmichael, I. S. E., 1996, The Aurora volcanic field, California-Nevada: oxygen fugacity constraints on the development of andesitic magma: *Contributions to Mineralogy and Petrology*, v. 125, p. 167-185.
- Lange, R. A., Carmichael, I. S. E., and Renne, P. R., 1993, Potassic volcanism near Mono Basin, California: evidence for high water and oxygen fugacities inherited from subduction: *Geology*, v. 21, p. 949-952.
- Luhr, J. F., 1990, Experimental phase relations of water- and sulfur-saturated arc magmas and the 1982 eruptions of El Chichon Volcano: *Journal of Petrology*, v. 31, p. 1071-1114.
- Maksaev, V., Munizaga, F., McWilliams, M., Fanning, M., Mathur, R., Ruiz, J., and Thiele, K., 2002, El Teniente porphyry copper deposit in the Chilean Andes: New geochronological timeframe and duration of hydrothermal activity: *Geological Society of America Abstracts with Programs*, v. 34, p. 336.

- Matthews, S. J., Moncrieff, D. H. S., and Carroll, M. R., 1999, Empirical calibration of the sulphur valence oxygen barometer from natural and experimental glasses; method and applications: *Mineralogical Magazine*, v. 63, p. 421-431.
- McDowell, F. W., and Keizer, R. P., 1977, Timing of mid-Tertiary volcanism in the Sierra Madre Occidental between Durango City and Mazatlan, Mexico: *Geological Society of America Bulletin*, v. 88, p. 1479-1487.
- Meldrum, S. J., Aquino, R. S., Gonzales, R. I., Burke, R. J., Suyadi, A., Irianto, B., and Clarke, D. S., 1994, The Batu Hijau porphyry copper-gold deposit, Sumbawa Island, Indonesia: *Journal of Geochemical Exploration*, v. 50, p. 203-220.
- Metrich, N., Bonnin-Mosbah, M., Susini, J., Menez, B., and Galois, L., 2002, Presence of sulfite (S^{IV}) in arc magmas: implications for volcanic sulfur emissions: *Geophysical Research Letters*, v. 29, p. no.11, 4.
- Moore, G., Vennemann, T., and Carmichael, I. S. E., 1998, An empirical model for the solubility of H_2O in magmas to 3 kilobars: *American Mineralogist*, v. 83, p. 36-42.
- Ohmoto, H., Hart, S. R., and Holland, H. D., 1966, Studies in the Providencia area, Mexico. 2. K-Ar and Rb-Sr ages of intrusive rocks and hydrothermal minerals: *Economic Geology and the Bulletin of the Society of Economic Geologists*, v. 61, p. 1205-1213.
- Parry, W. T., Wilson, P. N., Moser, D., and Heizler, M. T., 2001, U-Pb dating of zircon and $^{40}Ar/^{39}Ar$ dating of biotite at Bingham, Utah: *Economic Geology*, v. 96, p. 1671-1683.
- Preto, V. A. G., White, W. H., and Harakal, J. E., 1971, Further potassium-argon age dating at Copper mountain, B.C: *Canadian Mining and Metallurgical Bulletin*, v. 64, p. 58-61.
- Redmond, P. B., 2002, Magmatic-hydrothermal fluids and copper-gold ore formation at Bingham Canyon, Utah [Ph.D. thesis]: Stanford, University, 228 p.
- Rye, R. O., and Haffty, J., 1969, Chemical composition of the hydrothermal fluids

- responsible for the lead-zinc deposits at Providencia, Zacatecas, Mexico: *Economic Geology*, v. 64, p. 629-643.
- Sato, M., and Wright, T. L., 1966, Oxygen fugacities directly measured in magmatic gases: *Science*, v. 153, p. 1103-1105.
- Scaillet, B., and Evans, B. W., 1999, The 15 June 1991 eruption of Mount Pinatubo I: Phase equilibria and pre-eruption P-T-fO₂-fH₂O conditions of the dacite magmas: *Journal of Petrology*, v. 40, p. 381-411.
- Serrano, L., Vargas, R., Stambuck, V., Aguilar, C., Galeb, M., Holmgren, C., Contreras, A., Godoy, S., Vela, I., Skewes, M. A., and Stern, C. R., 1996, The later Miocene to early Pliocene Rio Blanco-Los Bronces copper deposit, central Chilean Andes, *in* Camus, F., Sillitoe, R. H., and Petersen, R., eds., *Andean copper deposits: new discoveries, mineralization, styles, and metallogeny*: Society of Economic Geologists Special Publication, p. 119-130.
- Sinclair, A. J., and White, W. H., 1968, Age of mineralization and post-ore hydrothermal alteration at Copper Mountain, B.C: *Canadian Mining and Metallurgical Bulletin*, v. 61, p. 633-636.
- Snyder, D., Carmichael, I. S. E., and Wiebe, R. A., 1993, Experimental study of liquid evolution in a Fe-rich, layered mafic intrusion; constraints of Fe-Ti oxide precipitation on the T-fO₂ and T-p paths of tholeiitic magmas: *Contributions to Mineralogy and Petrology*, v. 113, p. 73-86.
- Tropper, P., Manning, C. E., and Essene, E. J., 2002, The substitution of Al and F in titanite at high pressure and temperature: experimental constraints on phase relations and solid solution properties: *Journal of Petrology*, v. 43, p. 1787-1814.
- Vogel, T. A., Cambray, F. W., and Constenius, K. N., 2001, Origin and emplacement of igneous rocks in the central Wasatch Mountains, Utah: *Rocky Mountain Geology*, v. 36, p. 119-162.
- Wallace, P. J., and Carmichael, I. S. E., 1994, S speciation in submarine basaltic glasses as

determined by measurements of S K- α X-ray wavelength shifts: *American Mineralogist*, v. 79, p. 161-167.

Wernicke, B. P., and Klepacki, D. W., 1988, Escape hypothesis for the Stikine Block: *Geology*, v. 16, p. 461-464.

Chapter IV

Thermodynamic Properties of Sulfatian Apatite: Constraints on the Behavior of Sulfur in Calc-Alkaline Systems

Abstract

The free energy of hydroxyllestadite $[\text{Ca}_{10}(\text{SiO}_4)_3(\text{SO}_4)_3(\text{OH})_2]$ is estimated using mineral equilibria applied to the experimental charges of Luhr (1990). Estimations were made using an ideal mixing model for apatite and MELTS mixing models for all other phases. Free energy data of Robie and Hemingway (1995) were used for all calculations. The estimated ΔG_{298}° for hydroxyllestadite is given by:

$$\Delta G_{298}^\circ (\text{kJ/mol}) = 2.817T(^{\circ}\text{C}) - 11831$$

The entropy calculated is $1944 \text{ Jmol}^{-1}\text{K}^{-1}$ at 800°C and $2151 \text{ Jmol}^{-1}\text{K}^{-1}$ at 950°C .

Independent estimation of entropy using the method of Robinson and Haas (1983) are within 5% of this value. These data are used to show that sulfur zoning observed in apatite from granitoids reflects a drop in the $f\text{S}_2$ by more than 1 log unit and records the removal of a magmatic vapor phase.

Introduction

Sulfur is an important element in calc-alkaline igneous systems. Calc-alkaline magmas are associated with sulfur-rich volcanic eruptions that may have a global climatic impact following the release of SO_2 aerosols (Handler, 1989). Similar magmas are associated with large ore deposits that are enriched in sulfur (Hattori and Keith, 2001). In order to understand the processes that lead to sulfur-rich volcanic eruptions and ore deposits it is necessary to understand the behavior of sulfur in calc-alkaline systems. The behavior of sulfur is largely controlled by variations in oxygen and sulfur fugacities during

crystallization of the magma. The oxygen fugacity of a magma is indicated by silicate-oxide equilibria as described in *Chapters II* and *III*. Determining the sulfur fugacity of rocks typically requires the presence of anhydrite or sulfides. However, in oxidized rocks sulfides are likely to be unstable, and both sulfides and anhydrite can easily be dissolved during low temperature alteration. Therefore, it is necessary to find another mineral that contains sulfur for use as a sulfur barometer.

Sulfur substitutes for P in the structure of apatite as a coupled substitution with Si (Rouse and Dunn, 1982). Apatite is a ubiquitous accessory mineral in most metamorphic and igneous rocks. The composition of apatite has been used to constrain the fugacities of volatile components such as Cl and F (Piccoli and Candela, 1992; Piccoli et al., 1999), although the possibility that Cl and F contents are easily reset by late exchange has been raised (Brenan, 1993). Substitution of sulfate in apatite should also record the oxidation state of sulfur during its formation. In order to use apatite chemistry to estimate fS_2 it is first necessary to determine the free energy of sulfatian apatite.

Synthetic calc-alkaline rocks produced by Luhr (1990) contained sulfur-rich apatite that was analyzed by Peng et al. (1997). The apatites in these experimental products were shown to have a strong correlation between Si and S suggesting that the major substitution mechanism for sulfur in these apatites is $S^{6+}Si^{4+} = 2 P^{5+}$, or $(SO_4)^{2-}(SiO_4)^{4-} = 2(PO_4)^{3-}$. The mineral hydroxyllestadite is the sulfate-bearing end-member of this substitution and has the formula $Ca_{10}(SiO_4)_3(SO_4)_3(OH)_2$ (Rouse and Dunn, 1982). In this study, the data from Peng et al. (1997) are combined with the data from Luhr (1990) and *Chapter III* to calculate the free energy and entropy of hydroxyllestadite. Reactions that control the sulfur content of apatite are examined to determine the constraints on the sulfur content of apatite and to evaluate the usefulness of data on sulfur content and zoning of sulfate in apatite from calc-alkaline volcanic and intrusive rocks

Experimental Technique

Details of the experimental technique are presented in Luhr (1990). Starting

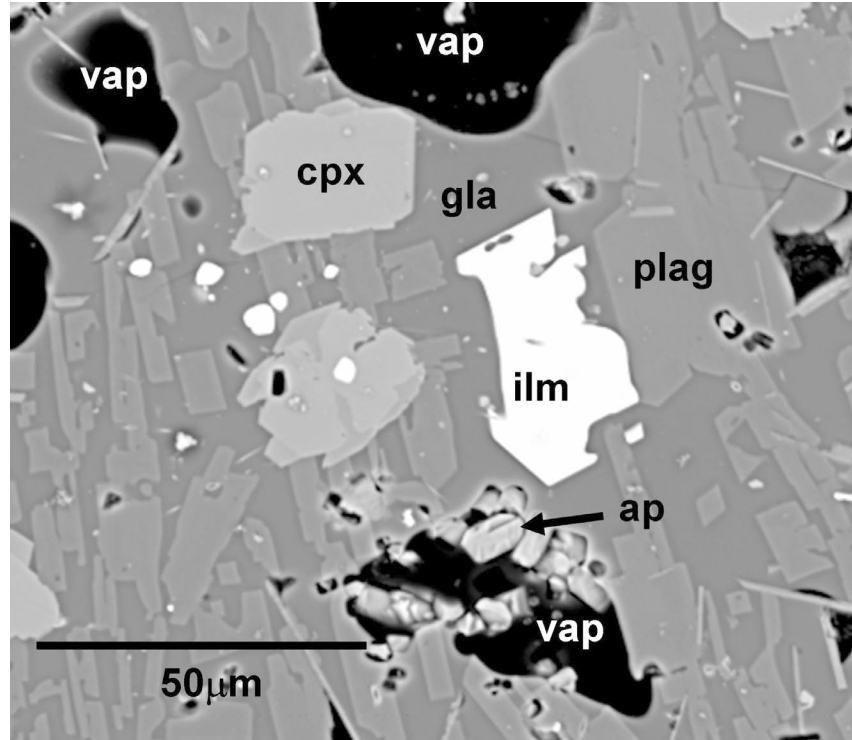
material for experiments that were used in this study was El Chichon trachyandesite doped with anhydrite. The experiments were run at temperatures of 800, 850, 900, and 950°C and pressures of 2, 2.5, and 4 kbars in an internally heated pressure vessel. All experiments were run under volatile saturated conditions as evidenced by the presence of voids in the glass (Fig. 4.1). The oxygen fugacity of the charges was buffered using solid oxygen buffers in double-gold capsules at the manganosite-hausmanite (MnH) or magnetite-hematite (MH) buffers. The experiments were not reversed, so mineralogical and chemical evidence must be used to test whether equilibrium was approached. Luhr (1990) demonstrated systematic changes in mineralogy and glass compositions of the charges with changing fO_2 , T, and P. Housh and Luhr (1991) showed changes in plagioclase composition with T and P. In Chapter II it was shown that the experimental oxides have equilibrium compositions according to the test of Bacon and Hirschmann (1988), and the composition of mafic silicates varies with T and fO_2 . This study required electron microprobe analysis of the apatite, glass, clinopyroxene, and oxides from the experimental charges. The analytical techniques used for these phases are described in Peng et al. (1997) for apatite, Luhr (1990) for glass, and Chapter II for all other phases.

Occurrence of Apatite in Experimental Charges

The charges are coarse-grained with euhedral grains of clinopyroxene, plagioclase, magnetite, apatite, anhydrite, \pm hematite \pm biotite \pm hornblende in a glass groundmass (Fig 4.1). The textures of the silicates and oxides are described in detail in Chapter II. The apatite grains are typically small ($<10\ \mu\text{m}$ wide) and euhedral occurring mostly within the glass or in vesicles. In some cases, apatite is included in plagioclase, magnetite, hornblende and/or clinopyroxene.

The chemistry of the apatite was shown to vary systematically with fO_2 and T. In general, the sulfur content of apatite increases with fO_2 ; apatite in FMQ charges has S below detection limit, and apatite in MnH and MH charges has 1 to 3 wt% SO_3 . In some cases, charges run at MH have less S than charges run at MnH with the same P-T

A



B

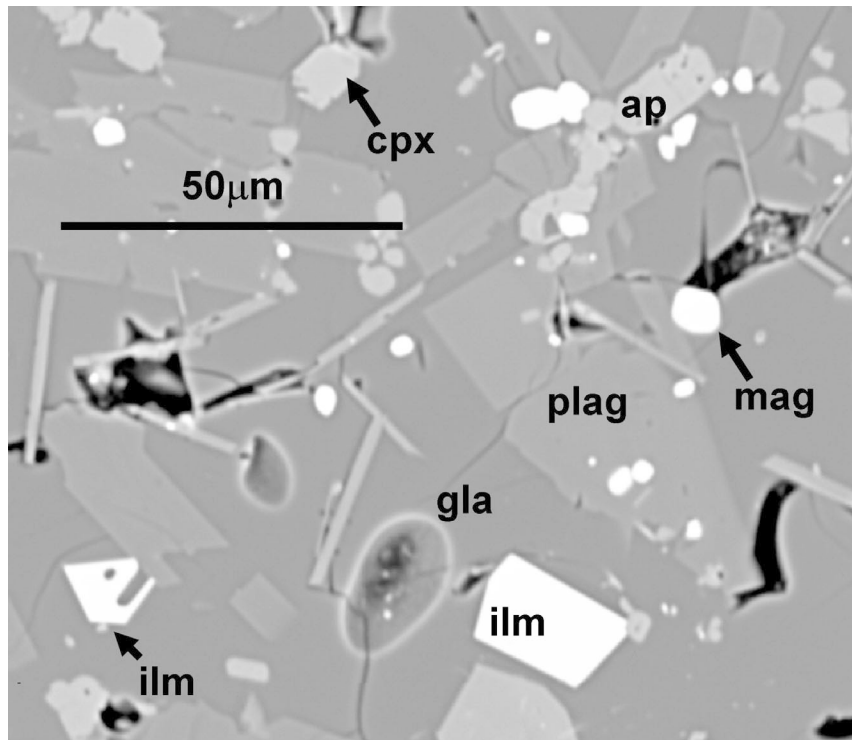


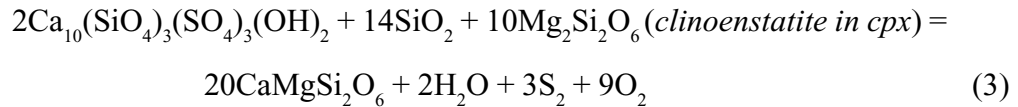
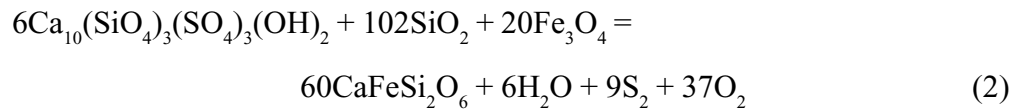
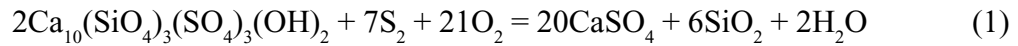
Figure 4.1. A. BSE image showing euhedral grains in a glassy matrix. The vapor bubbles demonstrate that the charge was vapor-saturated. The image also shows the occurrence of apatite in the vapor bubbles. B. BSE image showing euhedral oxides and plagioclase in glassy matrix. Apatite occurs as a euhedral grain with plagioclase. gla = glass; ilm = ilmenite; mag = magnetite; ap = apatite; cpx = clinopyroxene; vap = vapor; plag = plagioclase.

conditions.

In most cases, the sulfur content of the apatite increases with decreasing temperature. The exceptions to this are the experiments at MH and 2 kbar, which have constant S content of apatite across the entire temperature range. In all cases the sulfur content of the glass decreases with decreasing temperature, indicating that partitioning of sulfur into apatite increases with decreasing temperature.

Free Energy Calculations

The free energy of hydroxyllestadite was calculated using reactions between apatite and other phases present in the experimental charges. For all reactions hydroxyllestadite $[\text{Ca}_{10}(\text{SiO}_4)_3(\text{SO}_4)_3(\text{OH})_2]$ was used for the end-member composition. The following reactions were selected because they use phases present in the charges for which thermodynamic data are well known.



These reactions were used to calculate ΔG of $\text{Ca}_{10}(\text{SiO}_4)_3(\text{SO}_4)_3(\text{OH})_2$ using the experimental temperature and pressure. The activity of hydroxyllestadite,

$a[\text{Ca}_{10}(\text{SiO}_4)_3(\text{SO}_4)_3(\text{OH})_2]$, in apatite was approximated with an ideal mixing model:

$$a[\text{Ca}_{10}(\text{SiO}_4)_3(\text{SO}_4)_3(\text{OH})_2] = \frac{X_{\text{Ca}}^{10} X_{\text{Si}}^3 X_{\text{S}}^3 X_{\text{OH}}^2}{0.5^3 0.5^3} \quad (4)$$

Application of this relation gives activities between 2.1×10^{-4} and 1.7×10^{-9} . The low value suggests that the $a[\text{Ca}_{10}(\text{SiO}_4)_3(\text{SO}_4)_3(\text{OH})_2]$ is in the Henry's Law region where a constant activity coefficient (γ) is expected. We have no way of determining γ but will assume it is constant in the thermodynamic calculations.

Near end-member hydroxyllestadite was described by Harada et al. (1971), and

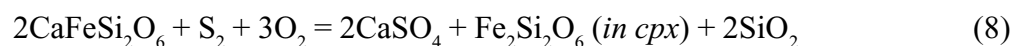
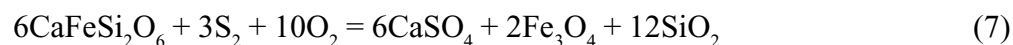
its volume was determined to be 271.20 cm³/mol using the formula with 10 Ca. This volume was used for the small pressure correction in the calculations. Because there are no free energy or entropy data available for hydroxyllestadite, the entropy was estimated and a fictive free energy derived. This value might require modification once the activity coefficient is measured or calculated.

Activities for all other phases were determined using the MELTS mixing models (Ghiorso and Sack, 1995). These activities were then used with the free energy data of Robie and Hemingway (1995). This was necessitated by the absence of anhydrite in the MELTS thermodynamic database, which would prevent the application of Reaction 1. The thermodynamic data for anhydrite in Robie and Hemingway (1995) only extends to 1000 K so data had to be extrapolated for the calculations. This was done by plotting ΔG vs. T for the existing data and obtaining a best-fit line through the points given by the equation

$$\Delta G = 0.38875T(K) - 1438.71, \quad (5)$$

which has an R² value of 0.9997 indicating an excellent fit.

The fH₂O was estimated by assuming that P(fluid) = P(total) and that the fluid was pure H₂O. The pressure was then converted to fugacity using a modified Redlich-Kwong equation of state (Holloway and Blank, 1994). The fO₂ of the charges was calculated at the appropriate buffer (MnH or MH) for the given charge using thermodynamic data from Robie and Hemingway (1995). The fS₂ was estimated using the following reactions:



The fS₂ was calculated using MELTS mixing models and thermodynamic data from Robie and Hemingway (1995).

The a(SiO₂) in the experimental runs needed to be estimated for both the fS₂ and ΔG calculations. The charges are all undersaturated with respect to quartz so the composition of the glass was used to determine the a(SiO₂). This was obtained from the

MELTS models for liquid compositions, which determines the $a(\text{SiO}_2)$ relative to pure SiO_2 glass. The $a(\text{SiO}_2)$ is affected significantly by the water content of the glasses. The water content of the glasses has not been directly analyzed, so calculations were made using estimated water content. The calculations used renormalized data from Luhr (1990) assuming that the water content of the glass was the difference between the total of the original microprobe analysis of the glass and 100. This is thought to be the maximum water content of the glass and actually exceeds what is thought to be the solubility at the experimental temperature and pressure. Using water content at solubility does not significantly affect the calculations.

The calculated ΔG of formation for hydroxyllestadite from these reactions shows a linear correlation with temperature (Fig. 4.2). The best-fit line through the data is given by the equation:

$$\Delta G_{298}^{\circ} (\text{kJ/mol}) = 2.817T(^{\circ}\text{C}) - 11831 \quad R^2 = 0.9581 \quad (10)$$

The slope of the ΔG vs T defines the ΔS of formation of hydroxyllestadite from the elements. The addition of the entropy for each element at each T provides an estimate of the entropy of hydroxyllestadite. The entropy calculated is $1944 \text{ Jmol}^{-1}\text{K}^{-1}$ at 800°C and $2151 \text{ Jmol}^{-1}\text{K}^{-1}$ at 950°C . It is also possible to estimate entropy by other independent means to determine if this result is reasonable.

Independent Estimation of Entropy

The ΔS of formation of a phase is the slope of the curve produced by plotting ΔG of formation vs. temperature. Thus, independent knowledge of the entropy provides an additional constraint on the best-fit curve through the free energy calculations. Knowledge of the entropy over a wide range of T also allows better extrapolation of ΔG estimations to low temperature. Entropy was estimated using two different types of calculations. The first estimate was made using the procedures given by Robinson and Haas (1983), which allows calculation of entropy as the sum of the contribution to entropy from the components of that compound. The contribution of the SO_3 component was estimated by

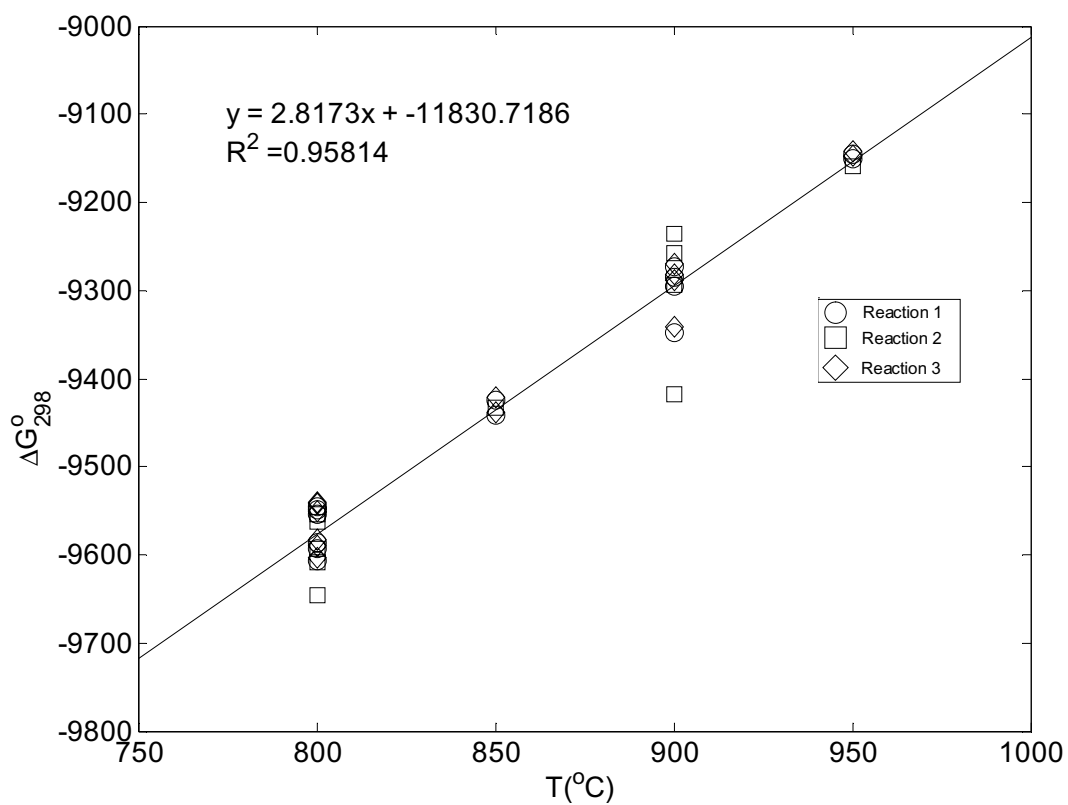


Figure 4.2 ΔG vs T diagram for $\text{Ca}_{10}(\text{SiO}_4)_3(\text{SO}_4)_3(\text{OH})_2$ using Reactions 1-3. The equation of the best fit line and R^2 value are shown. The slope of the line is the ΔS of formation from the elements.

subtracting the contribution for MgO in 8-fold coordination from the measured entropy of MgSO_4 from Robie and Hemingway (1995). This was calculated at the points where data were available and the best-fit curve was determined using the form of equations in Robinson and Haas (1983). This gives the sulfate component of entropy in $\text{Jmol}^{-1}\text{K}^{-1}$ as:

$$S_{\text{SO}_3} = 58.8275 \ln T + 0.463T - \frac{2.4948 \times 10^5}{T^2} - 298.6261 + 1.4403 \times 10^{-7} T^2 - \frac{32.8519}{\sqrt{T}} \quad (11)$$

Subtracting the elemental components of hydroxyllestadite gives an equation for entropy at any given temperature:

$$S_{\tau}^{\circ} = 1599 \ln T + 0.0389T - \frac{2.2092 \times 10^6}{T^2} - 9933.4 + 4.3200 \times 10^{-7} T^2 + \frac{-27309}{\sqrt{T}} \quad (12)$$

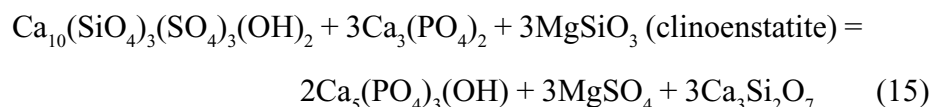
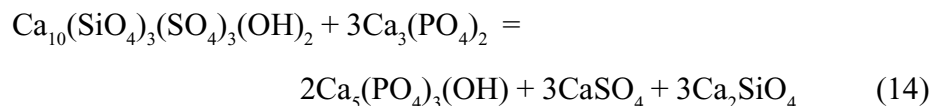
These data can also be used to calculate the entropy of anhydrite at higher T, which is given by:

$$S_T^{\circ} = 142.44 \ln T + 0.0404T - \frac{2.6914 \times 10^5}{T^2} - 813.793 + 1.4402 \times 10^{-7} T^2 + \frac{-1400.0}{\sqrt{T}} \quad (13)$$

This estimate is not very good at low temperature with an 18% difference between the actual and estimated S_{298}° for anhydrite (Robie and Hemingway, 1995). For temperatures above 800 K the estimate is within 5% of the actual entropy value of anhydrite and the estimate at 1000 K is within 4% of the measured value. This indicates that the estimates of entropy for hydroxyllestadite using the sulfate component derived from MgSO_4 improve with increasing temperature.

Entropy can also be estimated using solid-solid reactions because the ΔS of solid-solid reactions is often close to zero. The entropy of a phase can therefore be estimated if a solid-solid reaction can be written using the unknown phase along with phases for which

the entropy is known. This approximation is best if the reaction is isostructural (Fyfe et al., 1958; Helgeson et al., 1978). Two reactions were used to approximate the entropy of hydroxyllestadite:



For reaction 14, the entropy used for anhydrite at high T was estimated using equation 13.

The ΔS of formation from the elements is the slope of the ΔG vs. T curve. Over the range of temperatures covered by the experiments the entropy constrained by these methods produces average ΔS of formation from the elements of 2678 Jmol⁻¹K⁻¹ for the component method, 2807 Jmol⁻¹K⁻¹ for reaction 14, and 2816 Jmol⁻¹K⁻¹ for reaction 15. All of the estimated values are within 5 % of the slope of the ΔG vs. T curve, which is 2817 Jmol⁻¹K⁻¹. The two values calculated using reactions 14 and 15 were within 0.6% of the slope of the ΔG vs. T curve. This suggests that the variation of the ΔG data with temperature is acceptable and can therefore be extrapolated to lower and higher T than the experimental range with reasonable confidence.

The calculated estimate for ΔS using the component calculation differs the most from the slope of the ΔG vs. T curve. This calculation requires knowledge of the coordination of all the elements in the compound. The apatite structure of hydroxyllestadite has Ca in two sites with coordination numbers of 9 and 8 (Hughes and Rakovan, 2002). There are no data in Robinson and Haas (1983) for Ca in 9-fold coordination so it was assumed that all Ca is in 8-fold coordination, which may have led to errors in this calculation.

Discussion

Controls on sulfur content of apatite

It has been proposed that sulfur can also enter the apatite structure through

coupled substitution of Na-S for Ca-P (Liu and Comodi, 1993). Apatite compositions in intermediate igneous rocks typically show that both Si and S than Na and S substitutions are important (Peng et al., 1997; Streck and Dilles, 1998). One could also consider the exchange of $\text{Ca}(\text{SO}_4) = \text{REE}(\text{PO}_4)$ in apatite, which is a combination of the more commonly recognized exchanges $\text{REE}(\text{SiO}_4) = \text{Ca}(\text{PO}_4)$ and $(\text{SO}_4)(\text{SiO}_4) = 2(\text{PO}_4)$. The REE are typically far less abundant than sulfur in sulfate-rich apatite and sulfur, and they do not typically correlate indicating that this substitution is not significant in controlling the sulfate content of apatite.

The level of hydroxylapatite solid solution in apatite is controlled by many reactions involving calc-silicate and sulfate minerals. Reactions 1-3 show that $f\text{O}_2$ - $f\text{S}_2$ conditions, $a(\text{SiO}_2)$, and the compositions of coexisting silicates affect the stability of hydroxylapatite and substitution of SO_4 in apatite. These variables will fix or provide a limit for the activity of hydroxylapatite. All three reactions show that the stability of hydroxylapatite is dependent on $f\text{O}_2$ - $f\text{S}_2$ conditions (Fig. 4.3). This is also demonstrated by the correlation between $f\text{O}_2$ and sulfate content of apatite established by Peng et al. (1997). In addition to the other variables mentioned above, temperature and pressure affect the stability of hydroxylapatite. Hydroxylapatite is on the low temperature/high pressure side of these dehydration reactions.

Reactions 1-3 have different effects on the stability of hydroxylapatite depending on the presence of anhydrite in the system. Reaction 1 is directly applicable to buffer the sulfate content of apatite in anhydrite saturated granitic magmas, whereas reactions 2 and 3 are applicable under the more common anhydrite undersaturated conditions. These reactions can be used to understand the trends observed in the composition of hydroxylapatite from the experimental charges. The increase in sulfur content with decreasing temperature could be due to two factors. Hydroxylapatite is on the low temperature side of reactions 1-3 if $f\text{O}_2$, $f\text{S}_2$, and $f(\text{H}_2\text{O})$ are held constant, and therefore the activity of hydroxylapatite in apatite is expected to increase with

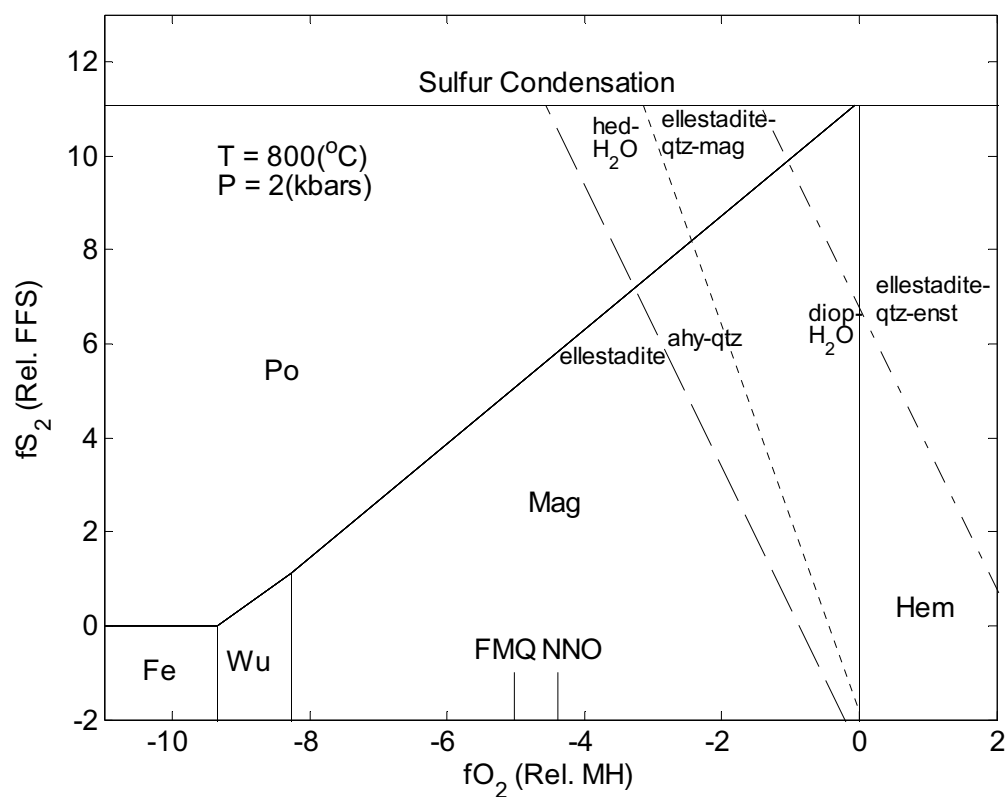


Figure 4.3. fO_2 - fS_2 diagram showing the locus of reactions 1-3. Common fO_2 buffers are shown as is sulfur condensation. All calculations were made at 800°C and 2 kbars pressure, assuming fluid pressure is equal to total pressure and the fluid is pure water.

decreasing T. The other major factor that could influence the sulfate content of the apatite is the $a(\text{SiO}_2)$. Experimental charges equilibrated at lower T have much higher SiO_2 in the glass, corresponding to a higher $a(\text{SiO}_2)$ and thus higher $a[\text{Ca}_{10}(\text{SiO}_4)_3(\text{SO}_4)_3(\text{OH})_2]$ in the apatite if Reaction 1 controls the sulfur content of apatite.

The observed increase in the sulfate content with temperature is in contrast to experiments by Parat and Holtz (2004) that show a decrease in sulfate content of apatite with decreasing temperature. They suggested that the differences observed by Peng et al. (1997) are due problems reaching equilibrium in the experiments of Luhr (1990). They argued that the high S apatite crystallized at high T and then persisted at lower T. This does not appear to be the case because the thermodynamic calculations in this study produce reasonable estimates for ΔG of hydroxylapatite and its variation with temperature. The experiments of Luhr (1990) were run under different conditions with different starting materials. Luhr (1990) added 1.2 wt% S (3 wt% SO_3) in the form of anhydrite to the experimental charges, whereas Parat and Holtz (2004) added 0.5 wt% S as elemental S. The lower sulfur content of their runs would potentially lead to different $f\text{S}_2$. Their use of native sulfur instead of anhydrite would affect the $a(\text{CaSO}_4)$ in the experiments. Most of the experiments by Parat and Holtz (2004) were under-saturated in anhydrite indicating that the sulfur content of apatite will be buffered by reactions like 2 and 3. Increasing $a(\text{SiO}_2)$ with decreasing temperature thus would decrease the sulfate content of apatite.

Implications for sulfur zoning in apatite

Previous studies have shown that apatite grains in some plutonic and volcanic igneous rocks are zoned with respect to sulfur (Peng et al., 1997; Streck and Dilles, 1998). Apatite in intrusive rocks typically shows high sulfate cores with very low sulfate rims (Streck and Dilles, 1998). Different types of sulfate zoning can be found in apatite from volcanic rocks, with sulfur increasing toward the rim in some cases, or decreasing toward the rim in others (Peng et al., 1997). The reactions shown above can provide

information on the causes of such zoning in sulfate-rich apatite.

Streck and Dilles (1998) described apatites from the Yerington batholith, Nevada, with cores containing up to 1.2 wt% SO_3 and rims containing as little as 0.07 wt% SO_3 . Similar zoning was found in this study in the Ruby Star granodiorite, Arizona and the Tyrone laccolith, New Mexico (Fig. 4.4). Streck and Dilles (1998) suggested that crystallization of anhydrite was the cause of this type of zoning, whereas Streck and Dilles (1997) suggested the zoning was due to magmatic degassing. Reaction 1 shows that the activity of hydroxylapatite will be highest in the presence of anhydrite (i.e. $a(\text{CaSO}_4)$ is unity). Therefore it seems unlikely that the crystallization of anhydrite would decrease the sulfur content of apatite unless the anhydrite is somehow fractionated out of the system. This is not likely to occur in a viscous granitoid magma. The observed decrease of almost approximately 6 log units in $a[\text{Ca}_{10}(\text{SiO}_4)_3(\text{SO}_4)_3(\text{OH})_2]$ from core to rim would require a change of -0.6 log units in $a(\text{CaSO}_4)$ using reaction 1, indicating that anhydrite must be destabilized.

Instead, it is more likely that crystallization took place at anhydrite under-saturated conditions as no magmatic anhydrite has been found at Yerington. Then the observed zoning would require changes of +0.35 log units in $a(\text{SiO}_2)$, -6 log units in $f(\text{H}_2\text{O})$, -1.0 log units in $f\text{O}_2$, or -1.0 log unit in $f\text{S}_2$ or some combination of these. Since the zoning is extremely sharp, the change appears to have happened abruptly. The most likely event that could cause an abrupt change in these controlling variables is the removal of a vapor phase from the magma. Degassing would cause water to exsolve from the magma leading to an increase in $a(\text{SiO}_2)$ and decrease in $f(\text{H}_2\text{O})$. However, these changes will not be enough to affect the $a_{\text{H}_2\text{O}}$ significantly. Exsolution of a vapor phase will not have a strong affect on the magmatic $f\text{O}_2$ (*Chapter III*). Sulfur partitions strongly into magmatic vapor phases so removal of a vapor phase from the magma would lead to a significant drop in the $f\text{S}_2$ and sulfur content of the magma. Such a decrease would lead to lower sulfate in any apatite that crystallized after removal of the fluid.

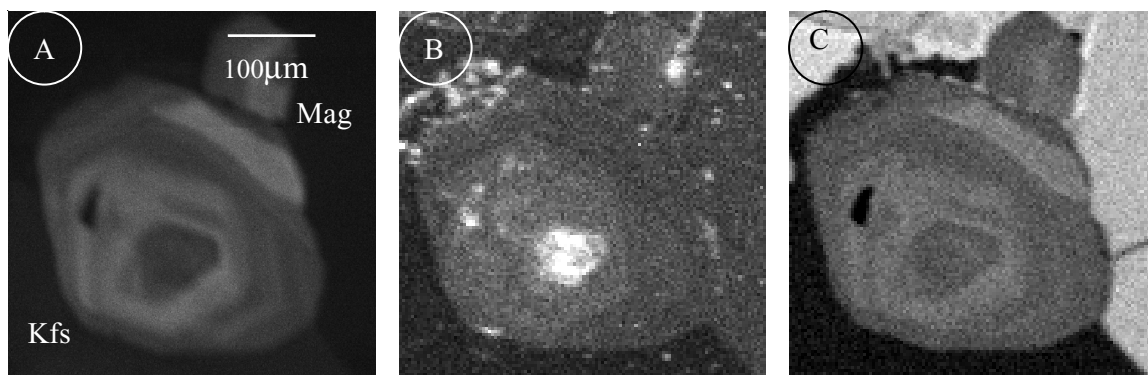


Figure 4.4. A. Cathodoluminescence image of apatite from the Ruby Star granodiorite, Arizona. B. Element map of sulfur $K\alpha$ peak made using an electron microprobe. The core is enriched in sulfur, followed by an intermediate zone, and a depleted rim. C. Element map of the Ce $L\alpha$ peak showing that the distribution of REE is identical to the cathodoluminescence.

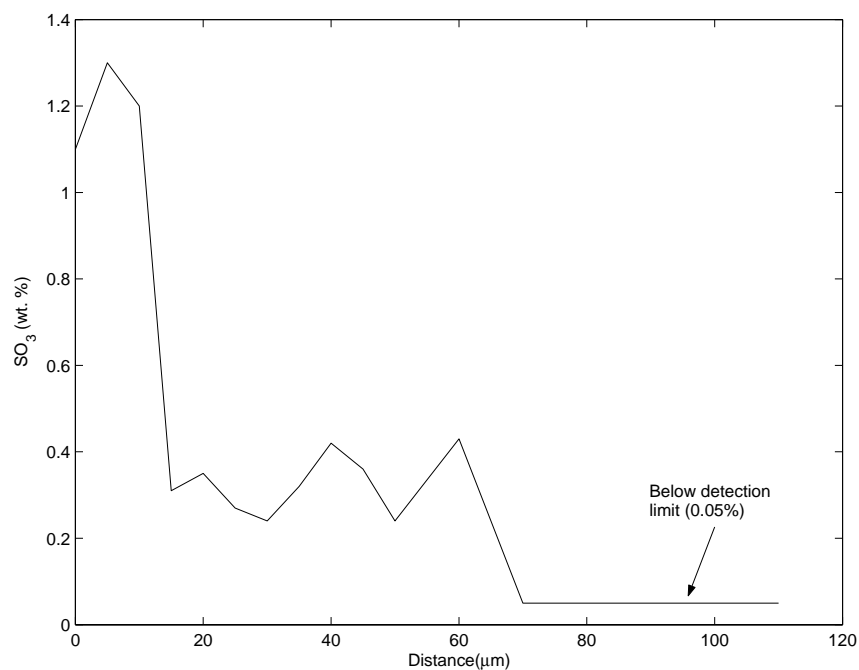


Figure 4.5. Core to rim traverse of grain shown above showing variations in sulfur content. There are three distinct zones with the first zone averaging about 1.2% SO_3 followed by a zone with 0.37% SO_3 and the last zone with sulfur below the detection limit of 0.05% SO_3 .

Streck and Dilles (1998) ruled out the removal of a vapor phase as a cause of the zoning. Using the method of Piccoli and Candela (1994) they calculated that the magma would have saturated with apatite at a very high temperature and most of the apatite would have crystallized prior to the formation of a vapor phase. However, Parat and Holtz (2004) showed that apatite solubility increases with increasing sulfur content in the magma due to the formation of CaSO_4 complexes in the magma, reducing the activity of hydroxyapatite, $a[\text{Ca}_5(\text{PO}_4)_3\text{OH}]$. This increase in apatite solubility was not observed in Luhr's (1990) experiments because sulfur was added as CaSO_4 . Therefore, none of the existing Ca in the glass would have formed complexes with the sulfur that was added preventing a decrease in the $a[\text{Ca}_5(\text{PO}_4)_3\text{OH}]$. If the magmas that crystallize these zoned apatites were sufficiently sulfate-rich without being enriched in Ca, the temperature at which apatite crystallized could have been depressed significantly. Removal of a vapor phase would almost completely remove sulfur from the magma. This would lead to a drop in the apatite solubility leading to crystallization of sulfur-poor apatite.

Conclusions

The $f\text{S}_2$ of igneous and metamorphic rocks has largely been overlooked as an important variable. Along with $f\text{O}_2$, $f\text{S}_2$ plays a major role in determining the stability of various silicate, oxide, sulfate and sulfide minerals. This is of particular importance in understanding the behavior of sulfur in intermediate calc-alkaline magmas that are associated with ore deposits and sulfur-rich eruptions.

The rocks that crystallize from calc-alkaline magmas retain little or no magmatic sulfide and anhydrite because these phases are often destroyed during degassing or weathering, making it difficult to reconstruct the history of their sulfur. However, apatite is ubiquitous in calc-alkaline igneous rocks and in many cases resists alteration and weathering. The current work indicates the utility of apatite in evaluating $f\text{O}_2$ - $f\text{S}_2$ conditions during crystallization of magmas. The possibility of using apatite to determine the $f\text{O}_2$ - $f\text{S}_2$ conditions of other igneous and metamorphic rocks is also implicit in this

work. A careful study of more oxidized metamorphic rocks that contain transition metals of higher valence such as Fe^{3+} in hematite, Mn^{3+} and Mn^{4+} in silicates and oxides, and As^{5+} as well as V^{5+} in apatite would be useful in understanding the controls on sulfate content of apatite. Solid solutions of these elements indicate unusually oxidizing conditions and should be accompanied by sulfatian apatite if S is available in the rock.

The current work demonstrates that zoning of sulfur in apatite from intrusive rocks records the removal of a vapor phase from the magma. Removal of sulfur from magmas by hydrothermal fluids is important to ore forming processes and sulfur-rich volcanic eruptions. Zoned apatite has been found in intrusive rocks closely associated with porphyry copper deposits. The apatite from these samples might record the removal of ore-forming solutions from the magma, providing information on the timing of exsolution of ore-forming solutions during crystallization.

Studies of apatites in volcanic rocks should provide better information on sulfate-rich eruptions. Peng et al. (1997) attempted this by evaluating the composition of apatite without knowledge of all the controls on the sulfate content of apatite. By calculating $f\text{S}_2$ using reactions involving sulfatian apatite it would be possible to provide better constraints on the behavior of sulfur in the magmas. In many cases, sulfur-rich magmas erupt with a coexisting vapor phase that contains the major of the sulfur. Evaluation of zoning could be used to determine if a sulfur-rich vapor phase exsolved during crystallization. If a vapor phase exsolved in the presence of anhydrite, the sulfur content of apatite would increase, whereas in the absence of anhydrite the sulfur content of apatite should decrease follow vapor exsolution. In addition to evaluating sulfur-rich calc-alkaline eruptions it should also be possible to evaluate the oxidation and sulfidation states of flood basalts such as the K-T flood basalts in India and the Parana basalts in Brazil.

References

- Bacon, C. R., and Hirschmann, M. M., 1988, Mg/Mn partitioning as a test for equilibrium between coexisting Fe-Ti oxides: *American Mineralogist*, v. 73, p. 57-61.
- Brenan, J., 1993, Kinetics of fluorine, chlorine and hydroxyl exchange in fluorapatite: *Chemical Geology*, v. 110, p. 195-210.
- Fyfe, W. S., Turner, F. J., and Verhoogen, J., 1958, Metamorphic reactions and metamorphic facies: *Geological Society of America Memoir*, v. 73, p. no.6, 259.
- Ghiorso, M. S., and Sack, R. O., 1995, Chemical mass transfer in magmatic processes. IV. A revised and internally consistent thermodynamic model for the interpolation and extrapolation of liquid-solid equilibria in magmatic systems at elevated temperatures and pressures: *Contributions to Mineralogy and Petrology*, v. 119, p. 197-212.
- Handler, P., 1989, The effect of volcanic aerosols on global climate: *Journal of Volcanology and Geothermal Research*, v. 37, p. 233-249.
- Harada, K., Nagashima, K., Nakao, K., and Kato, A., 1971, Hydroxyllellestadite, a new apatite from Chichibu Mine, Saitama Prefecture, Japan: *American Mineralogist*, v. 56, p. 1507-1518.
- Hattori, K. H., and Keith, J. D., 2001, Contribution of mafic melt to porphyry copper mineralization: evidence from Mount Pinatubo, Philippines and Bingham Canyon, Utah, USA: *Mineralium Deposita*, v. 36, p. 799-806.
- Helgeson, H. C., Delany, J. M., Nesbitt, H. W., and Bird, D. K., 1978, Summary and critique of the thermodynamic properties of rock-forming minerals: *American Journal of Science*, v. 278-A, p. 1-229.
- Holloway, J. R., and Blank, J. G., 1994, Application of experimental results to C-O-H species in natural melts: *Reviews in Mineralogy*, v. 30, p. 187-230.
- Housh, T. B., and Luhr, J. F., 1991, Plagioclase-melt equilibria in hydrous systems: *American Mineralogist*, v. 76, p. 477-492.

- Hughes, J. M., and Rakovan, J., 2002, The crystal structure of apatite, $\text{Ca}_5(\text{PO}_4)_3(\text{F},\text{OH},\text{Cl})$: Reviews in Mineralogy and Geochemistry, v. 48, p. 1-12.
- Liu, Y., and Comodi, P., 1993, Some aspects of the crystal-chemistry of apatites: Mineralogical Magazine, v. 57, p. 709-719.
- Luhr, J. F., 1990, Experimental phase relations of water- and sulfur-saturated arc magmas and the 1982 eruptions of El Chichon Volcano: Journal of Petrology, v. 31, p. 1071-1114.
- Parat, F., and Holtz, F., 2004, Sulfur partitioning between apatite and melt and effect of sulfur on apatite solubility at oxidizing conditions: Contributions to Mineralogy and Petrology, v. 147, p. 201-212.
- Peng, G., Luhr, J. F., and McGee, J. J., 1997, Factors controlling sulfur concentrations in volcanic apatite: American Mineralogist, v. 82, p. 1210-1224.
- Piccoli, P., and Candela, P., 1994, Apatite in felsic rocks: a model for the estimation of initial halogen concentrations in the Bishop Tuff (Long Valley) and Tuolumne Intrusive Suite (Sierra Nevada Batholith) magmas: American Journal of Science, v. 294, p. 92-135.
- Piccoli, P. M., and Candela, P. A., 1992, Interpretation of the chemistry of the mineral apatite from granitic rocks: a preliminary model calculation for the estimation of initial halogen contents in the Tuolumne Intrusive Suite, Sierra Nevada Batholith, California: Geological Society of America Special Paper, v. 272, p. 496.
- Piccoli, P. M., Candela, P. A., and Williams, T. J., 1999, Estimation of aqueous HCl and Cl concentrations in felsic systems: Lithos, v. 46, p. 591-604.
- Robie, R. A., and Hemingway, B. S., 1995, Thermodynamic properties of minerals and related substances at 298.15 K and 1 bar pressure and at higher temperatures, United States Geological Survey Bulletin 2131, 461 p.
- Robinson, G. R., Jr., and Haas, J. L., Jr., 1983, Heat capacity, relative enthalpy, and calorimetric entropy of silicate minerals: an empirical method of prediction:

- American Mineralogist, v. 68, p. 541-553.
- Rouse, R. C., and Dunn, P. J., 1982, A contribution to the crystal chemistry of ellettadite and the silicate sulfate apatites: American Mineralogist, v. 67, p. 90-96.
- Streck, M., and Dilles, J. H., 1997, Sulfur content of apatite from the Yerington Batholith, Nevada: a record of porphyry copper magma degassing: Geological Society of America Abstracts with Programs, v. 29, p. 445-446.
- Streck, M. J., and Dilles, J. H., 1998, Sulfur evolution of oxidized arc magmas as recorded in apatite from a porphyry copper batholith: Geology, v. 26, p. 523-526.

Chapter V

Cu-rich Source Region for Giant Porphyry Copper Deposits:

Last Chance Stock, Bingham, Utah

Abstract

Copper-rich mafic enclaves containing 5% bornite and 0.5% chalcopyrite were found in the Last Chance stock at Bingham. Mineral compositions and pressure estimates indicate that the enclaves are autoliths consisting of the earliest phases to crystallize from the stock. Early crystallization of chalcopyrite and bornite suggest that the magma was enriched with respect to Cu early during its crystallization history. Early Cu enrichment also suggests that the source region of the magma may have contained a mixture of Cu-Fe sulfides. Other enclaves from the Bingham-Park City belt indicate that the Cu enrichment in the source region is localized indicating heterogeneity in Cu content of the lower crust. Copper-rich rocks that have undergone partial melting with similar mineralogy to the enclaves are exposed at Curaca Valley, Brazil and Okiep, South Africa. Similar Cu enrichment may occur during cumulate formation at subduction zones. Enrichment of Cu in the source regions of granitoid magmas may be a necessary step in the formation of giant porphyry copper deposits.

Introduction

Granitoid stocks, with volumes of about 50 km³, are thought to contain enough copper and water to form typical porphyry copper deposits (PCDs) containing 250 Mt of ore with an average grade of 0.75% Cu, larger deposits such as Bingham, which contain an order of magnitude more copper, present major problems to simple orthomagmatic models for porphyry copper genesis. Although these larger amounts of copper might be

derived from larger parent intrusive bodies with average copper contents (Cloos, 2002), it is also possible that the parent intrusions were enriched in copper. Newly discovered sulfide-rich enclaves in the Last Chance stock at Bingham, which are described here, suggest that magmas that form unusually large PCDs were derived from anomalously copper-rich source regions. Evidence from enclaves in nearby intrusions suggests that the copper enrichment reflects a small-scale heterogeneity in the lower crust, possibly a pre-existing ore deposit.

Geologic Setting of the Sulfide-rich Enclaves

The Bingham PCD is part of the Bingham-Park City belt (BPCB), an east-west trending belt of intrusive and associated volcanic rocks in north-central Utah (Fig. 5.1). Igneous activity in the BPCB occurred between 39.8 Ma and 30.5 Ma, with igneous activity in the Bingham district occurring between 39.8 and 37.6 Ma (Warnaars et al., 1978; Deino and Keith, 1997; Vogel et al., 2001). The first intrusive phases at Bingham are the pre-mineralization Last Chance and Bingham stocks and the Phoenix dike, which have a U-Pb zircon age of 38.6 ± 0.2 Ma (Parry et al., 2001) (Fig. 5.2). These were followed by the syn-mineralization quartz monzonite porphyry (QMP), which has zircons with a LA-ICP-MS U-Pb age of 37.3 ± 0.3 Ma (*Chapter III*). This age is within error of the $^{40}\text{Ar}/^{39}\text{Ar}$ age of 37.6 ± 0.1 Ma on hydrothermal biotite in the QMP (Parry et al., 2001). Three later porphyries are associated with minor Cu mineralization, and Mo mineralization post-dates emplacement of all exposed intrusive rocks (Redmond, 2002). Molybdenite mineralization has a Re-Os age of 37.0 ± 0.3 Ma confirming that it post-dates the major Cu mineralizing event (Chesley and Ruiz, 1997). The difference in age between the earliest Cu mineralization and the molybdenite mineralization suggests that mineralization at Bingham was completed within a period of approximately 0.6 Ma.

Sulfide-rich enclaves that have been discovered recently in drill core from the Last Chance stock consist dominantly of clinopyroxene, biotite, magnetite, ilmenite, and plagioclase, with bornite, talnakhite, chalcopyrite and minor galena (Figs. 5.3, 5.4).

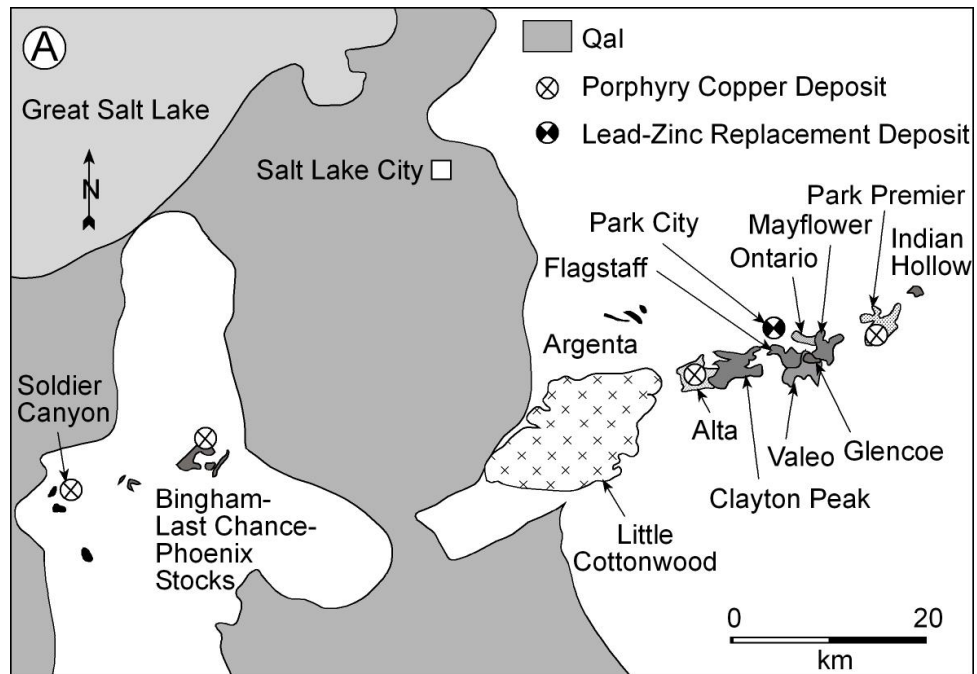


Figure 5.1. Geological map of the Bingham Park City Belt showing location of major intrusions.

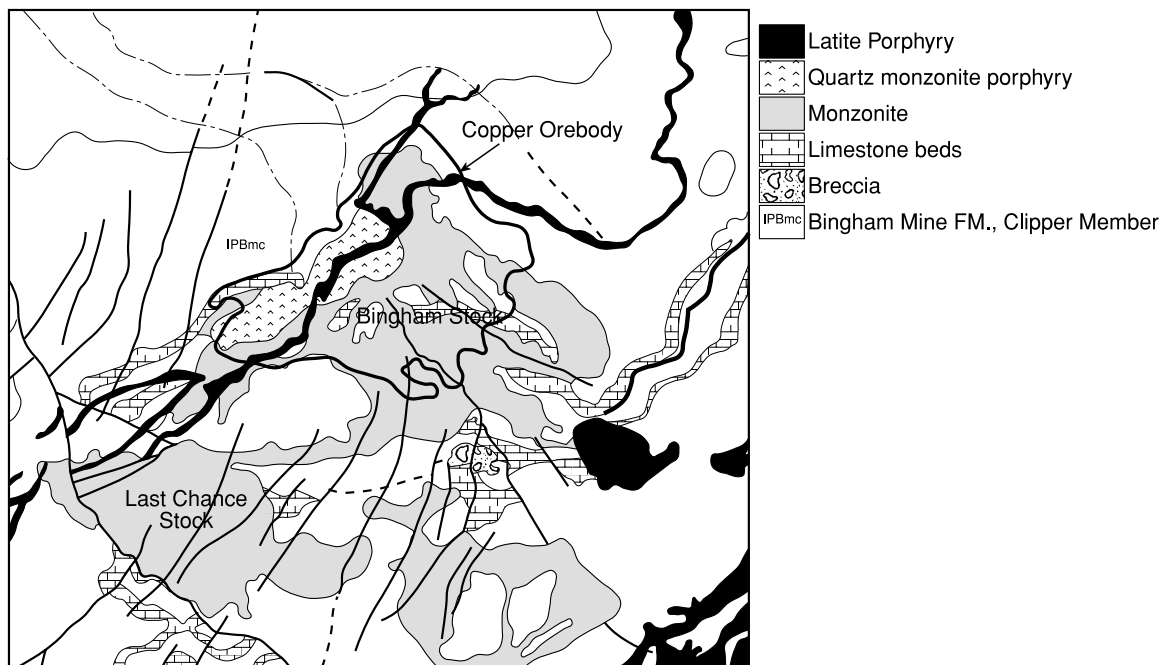


Figure 5.2. Geological map of the Bingham district showing major intrusions and dikes (After Phillips et al., 1997).

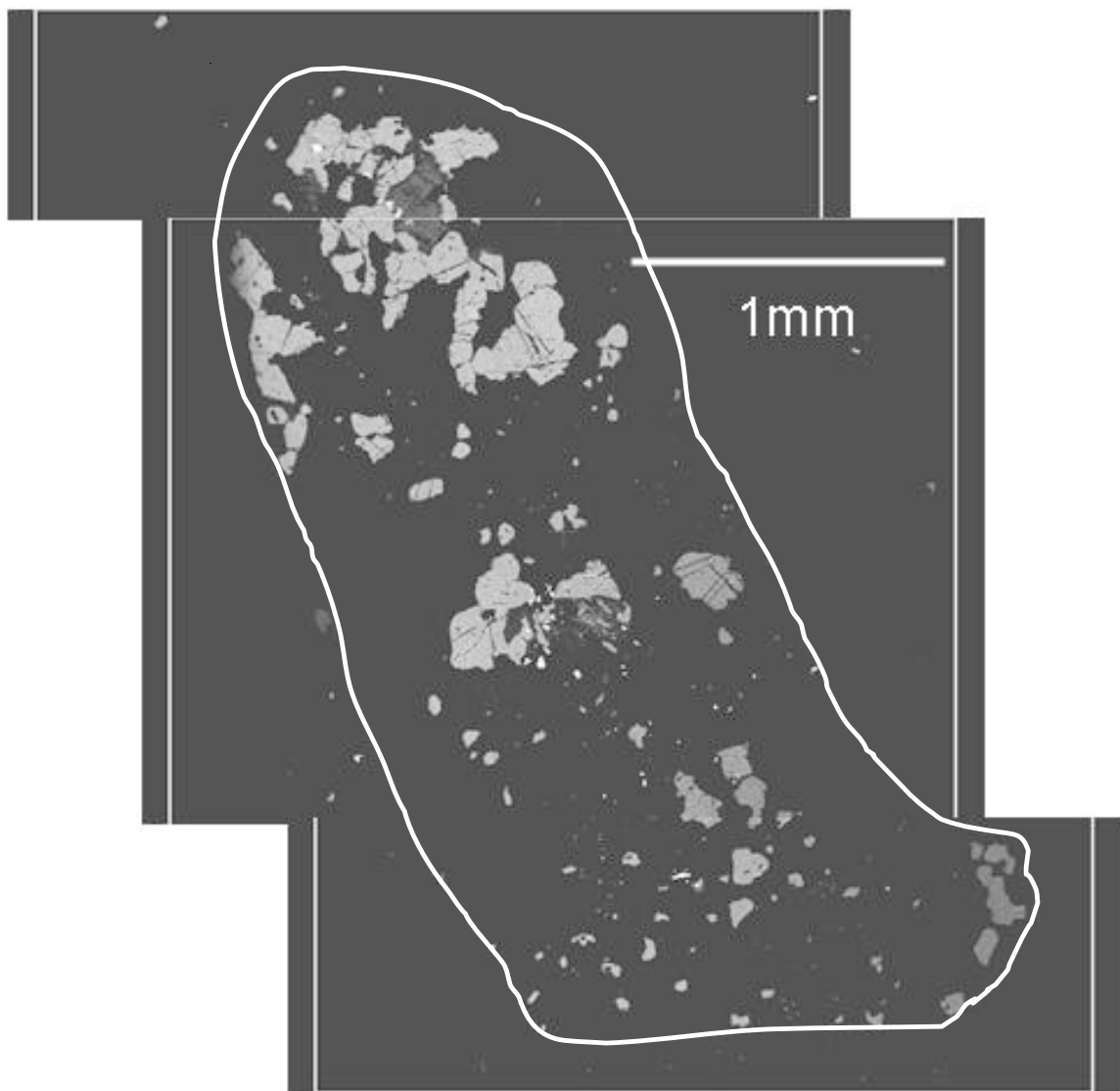


Figure 5.3. View of the largest enclave showing abundant oxide and sulfide grains. The magnetite has ilmenite lamellae and the ilmenite has exsolution of hematite. The white line shows the outline of the enclave.

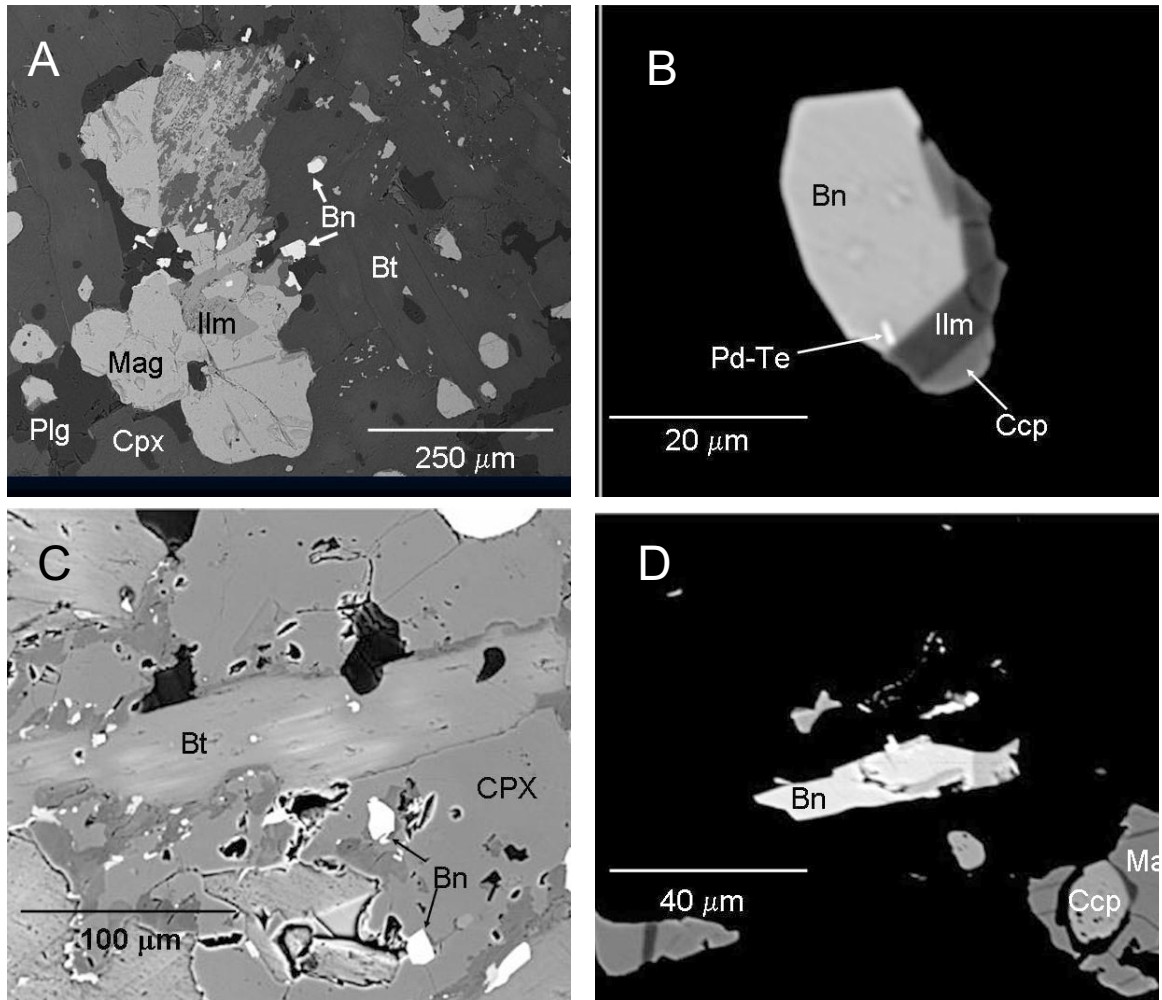


Figure 5.4. BSE images showing textures in the enclaves from the Last Chance stock. A. Exsolved magnetite and ilmenite with biotite and clinopyroxene near the edge of the enclave. Bornite near and included in the oxides. B. Bornite grain with ilmenite and chalcopyrite with inclusion of a Pd-Te grain. C. Primary biotite grain in enclave with Ba zoning indicated by brighter zones in the BSE image. D. Bornite grain with exsolved chalcopyrite on the right side of the grain. Also a chalcopyrite grain included in an exsolved magnetite. Cpx = clinopyroxene; Bt = biotite; Mag = magnetite; Ilm = ilmenite; Plg = plagioclase; Bn = bornite; Ccp = chalcopyrite; Pd-Te = palladium telluride.

Estimates of the abundance of sulfides in the enclaves were made using image analysis with BSE images. These estimates indicate that the enclaves contain approximately 5% bornite and 0.5% chalcopyrite raising the possibility that they represent a previously unrecognized stage in the enrichment of Cu to form the giant Bingham PCD.

The mineral assemblage in the enclaves is the same as that observed for the phenocryst assemblage in the Last Chance stock. Relative abundances of the various minerals are also similar with the exception of sulfides, which are present at the percent level in the enclave, whereas magmatic sulfides reach levels of only a few parts per million in unaltered Last Chance stock (Borrok et al., 1999). Furthermore, compositions of clinopyroxene, plagioclase, and oxide phenocrysts in the enclave are identical to those in the Last Chance stock (Table 5.1). Pyroxenes in the enclave are Al-poor with very little CaTs or jadeite components.

Microprobe analyses of the sulfides show enrichment of Au, Ag and Se with Se/S ratios of 1000-1250 (Table 5.2). One inclusion of a Pd-telluride mineral seen in bornite from the enclave is too small for quantitative analysis but the Pd/Te ratio is approximately one indicating that the mineral is merenskeyite. These observations indicate that the inclusion is enriched in Au, Ag, and Pd, all of which are produced at Bingham.

Discussion

Source of enclaves

The sulfide-bearing enclaves could represent: autoliths that formed during crystallization of the Last Chance magma, xenoliths that were incorporated into the magma during its ascent, or restites or residue left behind during partial melting that formed the Last Chance magma. Xenoliths would have mineral compositions different from those in the Last Chance stock and should show evidence of extensive reaction with the magma. Compositional similarity between minerals in the sulfide-rich enclaves and those in the surrounding Last Chance stock, along with minor reaction rims, suggests that the enclaves are autoliths or restites rather than xenoliths. Because they form at greater

Table 5.1. Mineral compositions of mafic silicates in the enclaves and adjacent Last Chance stock showing that the compositions are similar.

Mineral	Plagioclase	Plagioclase	Clinopyroxene	Clinopyroxene	Magnetite	Magnetite
N	5	4	9	4	43	3
Type	Enclave	Groundmass	Enclave	Groundmass	Enclave	Groundmass
SiO ₂	60.00	61.69	52.90	52.28	0.06	0.35
TiO ₂	0.07	0.03	0.30	0.25	0.80	1.53
Al ₂ O ₃	24.06	23.10	1.14	1.79	0.42	0.48
V ₂ O ₃	-	-	-	-	0.48	0.76
Cr ₂ O ₃	-	-	-	-	0.30	0.26
Fe ₂ O ₃	0.69	0.46	3.06	2.86	65.45	63.69
FeO	-	-	4.45	5.33	31.36	32.38
MgO	0.01	0.01	16.24	15.64	0.05	0.07
MnO	0.01	0.01	0.29	0.26	0.09	0.06
BaO	0.05	0.06	-	-	-	-
CaO	5.82	4.71	21.71	21.21	0.03	0.40
Na ₂ O	8.15	8.69	0.44	0.45	-	-
K ₂ O	0.26	0.36	-	-	-	-
Totals	99.12	99.15	100.54	100.07	99.17	100.00
Si	2.700	2.764	1.940	1.931	0.002	0.013
Al	1.276	1.220	0.049	0.069	0.019	0.022
Ti	0.002	0.001	0.008	0.007	0.023	0.044
Al(VI)	-	-	0.000	0.008	-	-
V	-	-	-	-	0.015	0.023
Cr	-	-	-	-	0.009	0.008
Fe ³⁺	0.023	0.015	0.084	0.079	1.906	1.832
Fe ²⁺	-	-	0.137	0.165	1.015	1.035
Mg	0.001	0.001	0.888	0.861	0.003	0.004
Mn	0.000	0.000	0.009	0.008	0.003	0.002
Ba	0.001	0.001	-	-	-	-
Ca	0.281	0.226	0.853	0.839	0.001	0.017
Na	0.712	0.755	0.031	0.032	-	-
K	0.015	0.021	-	-	-	-

- = Not analyzed.

Table 5.2. Analyses of sulfides from enclaves in the Last Chance stock.

Mineral	Bornite	Bornite	Bornite	Talnakhite ¹	Chalcopyrite ¹	Bornite ²
Si	0.02	0.05	0.04	0.14	0.42	0.04
S	26.00	25.59	25.82	32.82	34.34	24.73
Mn	0.01	0.02	0.03	0.01	0.01	0.05
Fe	10.46	14.53	11.97	27.91	28.86	10.82
Ni	bd	0.01	bd	0.01	bd	bd
Cu	63.28	59.85	61.75	36.28	32.91	59.15
Zn	bd	bd	bd	bd	bd	bd
As	bd	bd	bd	bd	bd	0.00
Se	0.03	0.02	0.04	0.04	bd	0.03
Pd	bd	bd	0.01	bd	bd	1.69
Ag	0.10	bd	bd	0.03	0.08	0.13
Sb	bd	bd	bd	bd	bd	0.01
Au	bd	bd	0.01	bd	bd	0.08
Pb	bd	bd	bd	bd	bd	bd
Bi	bd	bd	bd	bd	bd	0.09
Te	bd	bd	bd	bd	bd	1.26
Total	99.89	100.07	99.67	97.24	96.63	98.07
Si	0.003	0.008	0.008	0.077	0.225	0.007
S	4.066	3.989	4.042	16.096	16.200	3.995
Mn	0.001	0.002	0.003	0.002	0.003	0.004
Fe	0.939	1.300	1.075	7.858	7.816	1.004
Ni	bd	0.001	bd	0.001	bd	bd
Cu	4.993	4.708	4.877	8.977	7.833	4.821
Zn	bd	bd	bd	bd	bd	bd
As	bd	bd	bd	bd	bd	0.000
Se	0.002	0.001	0.003	0.007	bd	0.002
Pd	bd	bd	0.000	bd	bd	0.082
Ag	0.005	bd	bd	0.004	0.012	0.006
Sb	bd	bd	bd	bd	bd	0.001
Au	bd	bd	0.000	bd	bd	0.002
Pb	bd	bd	bd	bd	bd	bd
Bi	bd	bd	bd	bd	bd	0.002
Te	bd	bd	bd	bd	bd	0.073

bd = below detection. 1 = Talnakhite and chalcopyrite grains are small making it difficult to get acceptable analytical totals. 2 = Bornite with small merenskyite inclusion.

depth in the magma source region, restites should record a higher pressure than the phases that crystallized from the shallow level intrusion. Pressure estimates for the enclave using pyroxene-plagioclase-quartz with the activity model of Anovitz (1991). These calculations indicate maximum pressure of 3 kbars assuming $a(\text{SiO}_2)$ is unity. Quartz is not present in the enclave so the actual pressure would be less than 3 kbars. Similar estimates are obtained for pyroxene-plagioclase pairs in the matrix. Thus, the enclaves formed at low pressure and are probably autoliths consisting of the first phases to crystallize from the Last Chance magma. This indicates that bornite and ISS (the high-temperature equivalent of chalcopyrite) were among the first phases to crystallize from the Last Chance magma.

Cu-rich source region for Bingham magmas

Early crystallization of bornite and ISS indicates that the Last Chance stock was enriched in Cu and S early in its history. This, in turn, requires that the source region of the magma was also enriched in Cu and S. Furthermore, the early crystallization of bornite and chalcopyrite in the Last Chance stock means that the magma formed at or near saturation with respect to bornite and chalcopyrite, and therefore that the source region contained a mixture of Cu and Fe sulfides, probably bornite and ISS.

The BPCB magmas are thought to have formed by partial melting of lower crustal equivalents of the amphibolites similar to those in the Little Willow Formation and were emplaced in an extensional tectonic regime (Vogel et al., 2001). The Little Willow formation is not significantly enriched in Cu, suggesting most of the BPCB magmas had a relatively Cu-poor source region. The distribution and mineralogy of autoliths in other intrusions in the BPCB was determined in order to provide information on the scale of the proposed lower crustal Cu-rich zone that might have formed Bingham.

Autoliths composed of clinopyroxene, magnetite, and plagioclase were found in the Clayton Peak stock and autoliths of hornblende, magnetite, and plagioclase were found in the Alta stock. There is no sulfide present in the Clayton Peak autoliths and the Alta autoliths contain minor pyrrhotite. Autoliths from both stocks lack bornite and

chalcopyrite. This suggests that the Clayton Peak and Alta stocks were less enriched in Cu and S than the Last Chance stock, which is consistent with the lack of large associated Cu deposits. Therefore, they appear to have formed from a source that is lower in Cu and S. This suggests further that the lower and middle crust is heterogeneous with respect to the distribution of Cu and S on a small scale. Therefore, the Cu-enriched source region for the Last Chance stock was most likely a relatively small, localized sulfide-rich part of the lower crust.

Possible examples of Cu-rich source rocks of the type that could have melted to form the Bingham magmas are exposed at present in the Okiep district in South Africa and the Curaca Valley in Brazil. Mineral deposits in the Okiep district commonly consist of clinopyroxene, magnetite, bornite, and chalcopyrite, an assemblage similar to that seen in the Last Chance autoliths. Mineral assemblages in granulites in the Okiep terrain record maximum P-T conditions of 5-7 kbars and 750-900°C (Clifford et al., 1981; Raith and Prochaska, 1995). These rocks have undergone anatexis with migration and loss of melts (Kisters et al., 1998). The Curaca Valley deposits of Brazil are also rich in magnetite, bornite, and chalcopyrite but contain orthopyroxene instead of clinopyroxene. The deposits were interpreted by Maier and Barnes (1999) to be examples of restites from norites that partially melted to produce intermediate magmas.

Trace element compositions of the Last Chance autoliths also resemble those of the Okiep and Curaca Valley sulfide occurrences. The most distinctive element is Se, which is relatively rare in most sulfide ore deposits. Microprobe analyses of sulfides in the autoliths, however, which have S/Se weight ratios of 1040-1280, which are similar to ranges of 700-1400 and 350-100 for Okiep and Curaca, respectively (Maier, 2000). These data suggest that the source region for the Bingham magmas is chemically similar to the Okiep and Curaca rocks.

Genesis of Cu-rich source regions

The Okiep and Curaca districts contain examples of Cu-rich source rocks that

formed in the mid to upper crust and were then buried tectonically and partially melted during high grade metamorphism. Though this model would be possible for source rocks in the Bingham district, it is unlikely to occur in other regions with giant PCDs such as Chile and Batu Hijau where more typical arc processes occur. In these areas, magmatism is likely associated with partial melting of mafic magmas ponded in the lower crust during subduction.

Recent studies suggest that cumulates form during the ponding of mafic magmas at the crust-mantle interface (Downes et al., 2001; Féménias et al., 2003). As the ponded magmas crystallize at the base of the crust, it would be possible to form immiscible sulfide melts that could deposit a metal-rich layer in the magma chamber. Some xenoliths from lower crustal cumulates have accessory pyrrhotite and pentlandite (Féménias et al., 2003). A sulfur-rich underplated magma would likely form large amounts of sulfide that could be pyrrhotite, pentlandite, ISS, or bornite depending on the prevailing fO_2 - fS_2 conditions and the Cu content of the melt. Partial melting of these sulfide deposits would lead to the generation of magmas enriched in metals and sulfur.

Analysis of factors that could influence the Cu and S content of underplated magmas may provide a better understanding of the distribution of porphyry copper deposits at subduction zones. Areas where large amounts of underplating have occurred may produce larger accumulation of sulfide-rich cumulates. Subduction of more sulfur-rich oceanic crust could also impact the distribution of sulfur-rich magmas. Additionally, the possible occurrence of anhydrite in the lower crust should be evaluated as a source of sulfur in calc-alkaline systems. Sulfur contributed by dissolution of anhydrite in source rocks may provide the high sulfur/metal ratio observed in many ore deposits associated with granitoid magmas.

References

- Anovitz, L. M., 1991, Al zoning in pyroxene and plagioclase; window on late prograde to early retrograde P-T paths in granulite terranes: *American Mineralogist*, v. 76, p. 1328-1343.
- Borrok, D., Kesler, S. E., and Vogel, T. A., 1999, Sulfide mineral in intrusive and volcanic rocks of the Bingham-Park City Belt, Utah: *Economic Geology*, v. 94, p. 1213-1230.
- Chesley, J. T., and Ruiz, J., 1997, Preliminary Re-Os dating on molybdenite mineralization from the Bingham Canyon porphyry copper deposit, Utah, *in* John, D. A., and Ballantyne, G. H., eds., *Geology and ore deposits of the Oquirrh and Wasatch Mountains, Utah: Society of Economic Geologists Guidebook Series*, p. 165-169.
- Clifford, T. N., Stumpfl, E. F., Burger, A. J., MacCarthy, T. S., and Rex, D. C., 1981, Mineral-chemical and isotopic studies of Namaqualand granulites, South Africa; a Grenville analogue: *Contributions to Mineralogy Petrology*, v. 77, p. 225-250.
- Cloos, M., 2002, Bubbling magma chambers, cupolas, and porphyry copper deposits: *International Book Series*, v. 6, p. 191-217.
- Deino, A., and Keith, J. D., 1997, Ages of volcanic and intrusive rocks in the Bingham mining district, Utah, *in* John, D. A., and Ballantyne, G. H., eds., *Geology and ore deposits of the Oquirrh and Wasatch Mountains, Utah: Society of Economic Geologists Guidebook Series*, p. 91-100.
- Downes, H., Upton, B. G. J., Handisyde, E., and Thirlwall, M. F., 2001, Geochemistry of mafic and ultramafic xenoliths from Fidra (Southern Uplands, Scotland); implications for lithospheric processes in Permo-Carboniferous times: *Lithos*, v. 58, p. 105-124.
- Féménias, O., Coussaert, N., Bingen, B., Whitehouse, M. J., Mercier, J.-C. C., and Demaiffe, D., 2003, A Permian underplating event in late- to post-orogenic tectonic setting; evidence from the mafic-ultramafic layered xenoliths from Beaunit

- (French Massif Central): *Chemical Geology*, v. 199, p. 293-315.
- Kisters, A. F. M., Gibson, R. L., Charlesworth, E. G., and Anhaeusser, C. R., 1998, The role of strain localization in the segregation and ascent of anatectic melts, Namaqualand, South Africa: *Journal of Structural Geology*, v. 20, p. 229-242.
- Maier, W. D., 2000, Platinum-group elements in Cu-sulphide ores at Carolusberg and East Okiep, Namaqualand, South Africa: *Mineralium Deposita*, v. 35, p. 422-429.
- Maier, W. D., and Barnes, S. J., 1999, The origin of Cu sulfide deposits in the Curaca Valley, Bahia, Brazil; evidence from Cu, Ni, Se, and platinum-group element concentrations: *Economic Geology*, v. 94, p. 165-183.
- Parry, W. T., Wilson, P. N., Moser, D., and Heizler, M. T., 2001, U-Pb dating of zircon and $^{40}\text{Ar}/^{39}\text{Ar}$ dating of biotite at Bingham, Utah: *Economic Geology*, v. 96, p. 1671-1683.
- Raith, J. G., and Prochaska, W., 1995, Tungsten deposits in the Wolfram Schist, Namaqualand, South Africa: strata-bound versus granite-related genetic concepts: *Economic Geology*, v. 90, p. 1934-1954.
- Redmond, P. B., 2002, Magmatic-hydrothermal fluids and copper-gold ore formation at Bingham Canyon, Utah [Ph.D. thesis]: Stanford University, 228 p.
- Vogel, T. A., Cambray, F. W., and Constenius, K. N., 2001, Origin and emplacement of igneous rocks in the central Wasatch Mountains, Utah: *Rocky Mountain Geology*, v. 36, p. 119-162.
- Warnaars, F. W., Smith, W. H., Bray, R. E., Lanier, G., and Shafiqullah, M., 1978, Geochronology of igneous intrusions and porphyry copper mineralization at Bingham, Utah: *Economic Geology*, v. 73, p. 1242-1249.

Chapter VI

Conclusions

Introduction

The methods discussed in the earlier chapters of this dissertation allow for the calculation of $f\text{O}_2$ - $f\text{S}_2$ conditions of a wide range of metamorphic and igneous rocks. Estimating these parameters in a variety of geological environments will provide a framework for understanding the behavior of sulfur in the crust. This will lead to a better understanding of ore-forming processes in metamorphic and igneous environments. These methods can also be used to gain a better understanding of the sulfur contribution of various igneous rocks to the global sulfur cycle. In this chapter, an example of such an application is present with an evaluation of what can be learned about the importance of sulfides in calc-alkaline magmas using magmatic $f\text{O}_2$ - $f\text{S}_2$ conditions. The implications for the composition of magmatic source regions are discussed. A method is also discussed for using the sulfur content of biotite as a sulfur barometer making it possible to estimate the $f\text{S}_2$ of a wide range of reduced rocks.

Role of sulfides in magmatic processes

One of the biggest controversies concerning the formation of porphyry copper deposits is the role that magmatic sulfides play. Halter et al. (2002) and Keith et al. (1997) have suggested that Cu is depleted in a magma by the crystallization of a sulfide phase. They suggested that these magmatic sulfides are then destroyed during degassing and the metals leached by hydrothermal solutions and redeposited as PCDs. In general, intermediate intrusive rocks contain a few ppm of magmatic sulfide, suggesting that magmatic sulfides would not have a large effect on metal behavior during crystallization

(Borrok et al., 1999). An alternative model is that sulfides in the source region could affect the behavior of metals during the formation of granitoid magmas. Sulfides in the source region may strongly affect metal behavior while generating magmas that contain crystallize relatively small amounts of sulfide.

Experimental data show that Cu sulfides such as ISS and bornite accommodate much larger amounts of Au than pyrrhotite at magmatic temperatures and, as a result, Cu-sulfides can strip Au from a melt, whereas pyrrhotite has a much smaller effect (Jugo et al., 1999; Simon et al., 2000). Jugo et al. (1999) also showed that chalcopyrite and bornite buffer Cu content of magmas at a high level, whereas pyrrhotite depletes magmas in Cu. Similar relationships would be expected during partial melting if sulfides are not completely removed from the source rocks. Pyrrhotite would retain Cu in the source region while bornite and chalcopyrite would retain Au.

The presence of ISS and bornite in the source region at Bingham would have led to relatively high Cu/Au ratios in the magmas and related PCDs. This is supported by the high Cu/Au ratios observed at Bingham (Kesler et al., 2002). If the deposit was formed by redissolution of magmatic sulfide, it would likely have had a lower Au/Cu ratio because the chalcopyrite and bornite would have sequestered the Au that was present in the intrusion.

In contrast, intrusions associated with the Au-rich Bajo de Alumbrera porphyry copper deposit contain magmatic pyrrhotite (Halter et al., 2002). This indicates that the source region likely contained pyrrhotite as well. Pyrrhotite in the source region would have retained Cu upon melting, leading to a low Cu/Au ratio in the magma (Jugo et al., 1999). This is consistent with the relatively low Cu/Au ratio observed at Bajo de Alumbrera deposit (Kesler et al., 2001). This hypothesis also provides insights into the formation of “porphyry gold” deposits such as those at Fort Knox, Alaska and 17 Mile Hill, Australia, which are closely associated with strongly reduced, ilmenite series intrusions (Rowins, 2000). Even at moderate fS_2 , the source regions for these intrusions

would be saturated with respect to pyrrhotite, which would remove Cu but not Au from the melt, leading to the very low Cu/Au ratios observed in these deposits.

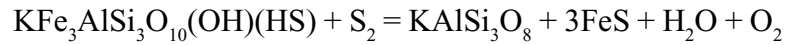
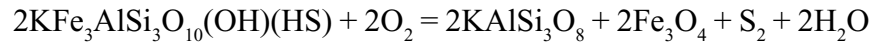
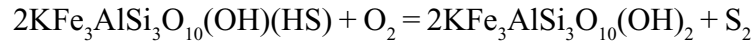
Variations in prevailing fO_2 - fS_2 conditions in arc settings could lead to different sulfide assemblages in the lower crust. More reducing conditions would lead to the generation of pyrrhotite-rich source rocks, whereas bornite and chalcopyrite are stable to much higher fO_2 . Moreover, under highly oxidized conditions, sulfates could form instead of, or in addition to, sulfides. This could strongly affect the distribution of metals and sulfur in the lower crust and change the availability of metals and sulfur to melts that are generated through partial melting.

Formation of magmatic sulfides is not a critical step in the formation of PCDs, as suggested by Keith et al. (1997) and Halter et al. (2002). Instead, pyrrhotite and Cu-sulfides in the lower crustal source regions of PCD forming magmas probably sequester metals during partial melting. Variations in prevailing fO_2 - fS_2 conditions in arc settings could lead to different sulfide assemblages in the lower crust. More reducing conditions would lead to the generation of pyrrhotite-rich source rocks while bornite and chalcopyrite are stable to much higher fO_2 . Moreover, under highly oxidized conditions, sulfates could form instead of, or in addition to, sulfides. This could strongly affect the distribution of metals and sulfur in the lower crust and change the availability of metals and sulfur to melts that are generated through partial melting.

Biotite as a sulfur barometer

Sulfur substitutes into the biotite structure as sulfide with the end-member formulae of $KFe_3AlSi_3O_{10}(OH)(HS)$ and $BaFe_3AlSi_3O_{10}(OH)(S)$. Previous analyses of sulfur in biotite from granitoids range from 0.06 to 0.2 wt.% S (Vikre, 2000). Samples included in this study from the Bingham-Park City belt and Mexico contain up to 0.1 wt% S. This indicates that biotite can be a significant host of sulfur in calc-alkaline rocks and likely records the behavior of sulfur. Since sulfur substitutes as sulfide in biotite, sulfur contents will most likely be highest under reducing conditions. Reactions that could

control the sulfide content of biotite are:



These reactions can be used to gain an understanding of $f\text{O}_2$ - $f\text{S}_2$ conditions in granitoids.

Under sulfide-undersaturated conditions the sulfur content of biotite will go up with $f\text{S}_2$ and down with $f\text{O}_2$. The opposite effect is observed in the presence of pyrrhotite. If free energy data were available for sulfide biotite, it would be possible to use these reactions to uniquely determine $f\text{S}_2$ at a given $f\text{O}_2$.

References

- Borrok, D., Kesler, S. E., and Vogel, T. A., 1999, Sulfide mineral in intrusive and volcanic rocks of the Bingham-Park City Belt, Utah: *Economic Geology*, v. 94, p. 1213-1230.
- Halter, W. E., Pettke, T., and Heinrich, C. A., 2002, The origin of Cu/Au ratios in porphyry-type ore deposits: *Science*, v. 296, p. 1844-1846.
- Jugo, P. J., Candela, P. A., and Piccoli, P. M., 1999, Magmatic sulfides and Au:Cu ratios in porphyry deposits: an experimental study of copper and gold partitioning at 850°C, 100 MPa in a haplogranitic melt-pyrrhotite-intermediate solid solution-gold metal assemblage, at gas saturation: *Lithos*, v. 46, p. 573-589.
- Keith, J. D., Whitney, J. A., Hattori, K., Ballantyne, G. H., Christiansen, E. H., Barr, D. L., Cannan, T. M., and Hook, C. J., 1997, The role of magnetic sulfides and mafic alkaline magmas in the Bingham and Tintic mining districts, Utah: *Journal of Petrology*, v. 38, p. 1679-1690.
- Kesler, S. E., Chryssoulis, S., and Simon, G., 2001, Gold in porphyry copper deposits: its abundance and fate: *Ore Geology Reviews*, v. 21, p. 103-124.
- Simon, G., Kesler, S. E., Essene, E. J., and Chryssoulis, S. L., 2000, Gold in porphyry copper deposits: experimental determination of the distribution of gold in the Cu-Fe-S system at 400° to 700° C: *Economic Geology*, v. 95, p. 259-270.
- Vikre, P. G., 2000, Subjacent crustal sources of sulfur and lead in eastern Great Basin metal deposits: *Geological Society of America Bulletin*, v. 112, p. 764-782.

APPENDICES

Appendix I

Source Code for Zircon U-Pb Age Dating and REE Chemistry

Introduction

The following is a description of and source code for a data reduction program for zircon U-Pb and trace element data collected in the ICP-MS Lab at the Australian National University. The major reason for writing this program was to speed up the data reduction process and to reduce the amount of space taken up by data. The method previously used at the ANU required the user to copy and paste data from the text files produced by the ICP-MS into large (~5 MB) Excel spreadsheets. Each grain had its own spreadsheet leading to a days worth of analyses taking up ~700 MB of disk space. The data reduction process was also cumbersome taking up to two days to reduce one day of analytical data. The program presented below generates approximately 10 MB of data for a days worth of analysis and it takes approximately 1-1.5 hours to reduce that data.

The program is written in MatLab 13.0 and was run on a Dell Inspiron 4000 laptop computer with an 800 MHz Intel Celeron processor and 512 MB of RAM running Windows 2000 operating system. The program takes as input, raw data files for zircon standards, glass standards, and unknown zircons produced by the software running an Agilent 7500 ICP-MS (Table A1.1). Each set of files are then placed in separate folders and must have the extension “.csv”. The program is started by selecting run under the debug menu after the source code has been opened. When the program is started, a graphic user interface begins with five options: load data, standard calculations, sample start/end, age and geochemistry calculations with drift correction, and Ce anomaly calculation (Fig. A1.1). These options should be followed sequentially for reducing a set

Table A1.1. File format for input into zircon data reduction

1\1\DATA\ancore\030324\001LB5.D																		
Intensity Vs Time		Counts																
Time [Sec]		P31	Zr91	La139	Ce140	Nd146	Sm147	Eu153	Dy163	Lu175	Hf177	Pb206	Pb207	Pb208	Th232	U235	U238	
0.394	350.49	27	0	0	0	0	0	0	0	1	0	1	1	0	1	1	0	
0.778	277.3	40.01	0	0	0	0	0	0	0	0	0	1	1	1	1	0	0	
1.162	281.31	31	0	0	0	0	0	0	0	0	0	1	0	2	0	1	0	
1.546	269.29	24	1	0	0	1	0	0	0	0	0	0	1	0	0	0	1	
1.93	428.73	49.01	0	0	0	0	0	0	0	0	0	0	0	2	0	2	0	
2.314	258.26	32	0	0	0	0	0	0	0	1	0	1	0	0	1	0	1	
2.698	275.3	37.01	0	0	0	0	0	0	0	0	0	0	0	1	0	1	0	
3.082	282.32	32	0	0	0	0	0	0	0	0	0	1	1	2	1	0	0	
3.466	260.27	27	0	0	0	0	0	0	0	0	0	0	0	3	1	0	1	
3.85	281.31	36.01	0	0	0	0	0	0	0	0	0	0	1	0	0	0	3	
4.235	264.28	35	0	0	0	0	0	0	0	0	0	1	0	2	0	2	1	
4.619	283.32	39.01	1	0	0	0	0	0	0	0	0	0	0	1	0	1	0	
5.003	282.32	40.01	0	0	0	0	0	0	0	0	0	1	1	0	1	0	1	
5.387	349.48	45.01	0	0	0	0	0	0	0	0	0	0	1	1	1	1	0	
5.771	380.57	40.01	0	0	0	0	0	0	0	0	0	2	2	0	0	0	0	
6.155	282.32	26	0	1	0	0	0	1	0	0	0	0	2	1	0	0	0	
6.539	289.33	48.01	0	0	0	0	0	0	0	0	0	1	0	1	1	1	0	
6.923	272.29	40.01	0	0	0	0	0	0	0	0	1	1	0	0	0	1	1	
7.307	258.26	28	0	0	0	0	0	0	0	0	0	0	0	1	0	0	1	
7.691	270.29	43.01	0	0	0	0	0	0	0	0	1	2	0	0	0	2	0	
8.075	255.26	41.01	0	0	0	0	0	0	0	0	0	0	3	2	0	1	0	
8.459	360.51	30	0	0	0	0	0	0	0	0	0	0	0	0	0	1	0	
8.843	364.53	31	0	0	0	0	0	0	1	0	0	0	0	3	0	1	0	
9.227	374.56	35	0	0	0	0	0	0	0	0	0	1	0	0	1	0	3	
9.611	244.24	32	0	0	0	0	0	0	0	0	0	1	2	0	0	1	0	
9.995	256.26	28	0	1	0	0	0	0	0	0	0	1	0	2	2	0	0	
10.379	246.24	33	0	0	0	0	0	0	0	0	0	0	1	0	0	0	0	
10.763	239.23	40.01	0	1	2	0	0	0	0	0	0	1	1	4	1	0	2	
11.147	298.35	30	0	0	0	0	0	0	0	0	1	0	1	0	0	0	0	
11.531	278.31	30	0	0	0	0	0	0	0	0	0	0	0	2	0	0	0	
11.915	269.29	39.01	0	0	0	1	0	0	0	0	0	0	0	0	0	0	2	
12.299	332.44	33	0	0	0	0	0	0	0	1	0	1	0	2	0	0	1	
12.683	284.32	40.01	0	0	0	0	0	0	0	0	0	3	0	0	2	1	0	

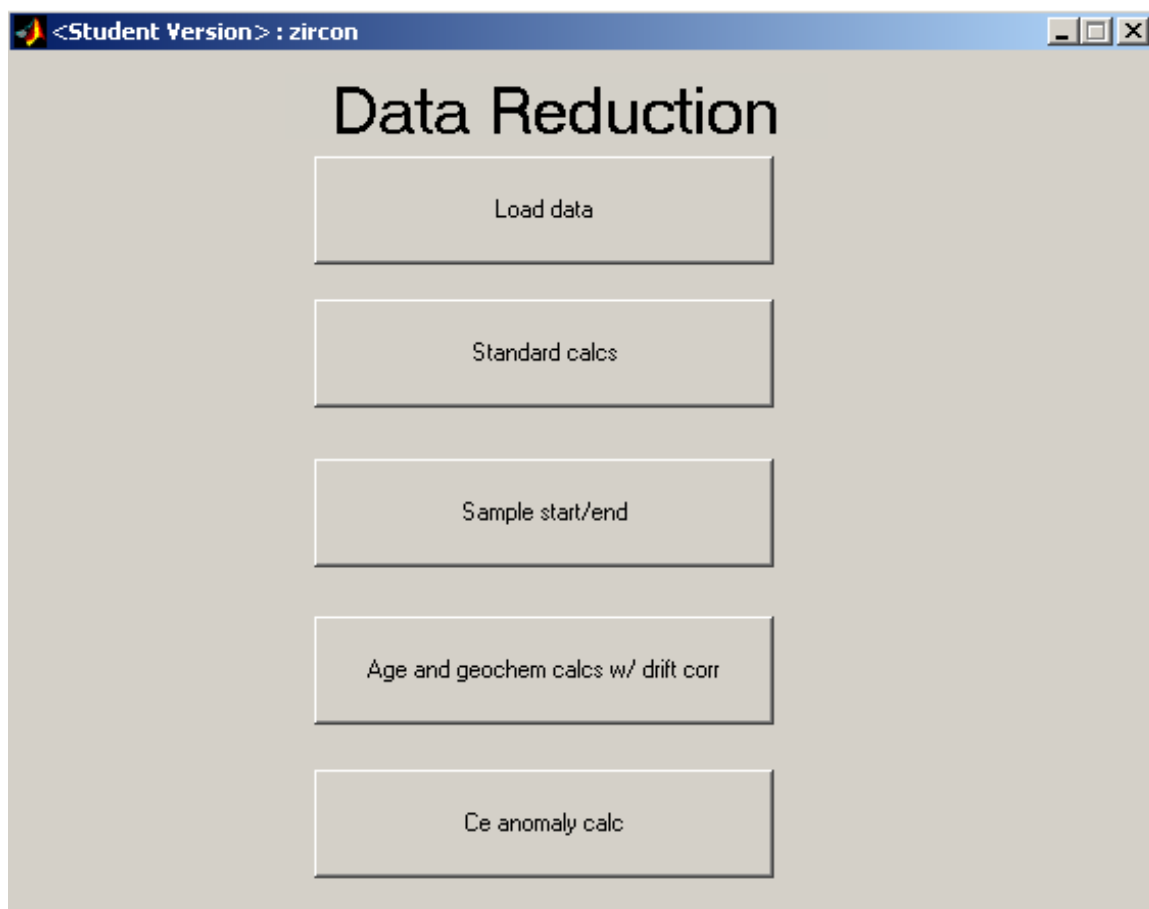


Figure A1.1. User interface for zircon data reduction showing the program options.

of data. If files are transferred via ftp prior to data reduction, the files should first be archived to make sure that the time stamp on the files does not get reset. The time stamp on the file is used to name the output files and to do the drift correction.

Load data

This step loads all of the data from a days worth of analyses into a single matlab variable (.mat) file. The user is prompted to select the folders that contain the standard data and the unknowns. The header of the files is read to determine the elements analyzed and all the data are placed into three dimensional matrices with the following size: number of samples \times sampling depths \times isotopes analyzed. The user is prompted to select the appropriate standard composition files for the glass (.comp file) and standard (.age file) (Table A1.2). Variables are defined that associate a given isotope with the appropriate location in the data matrices. For example Si29 recalls the appropriate column containing data for Si. The variables are saved in a file called raw_zricon_data_(analysis data).mat

Standard calculations

This step does background subtraction and ratio calculation for the glass and zircon standards. First the user selects a raw data file produced by the previous step. The user is prompted to enter the elements that are used to determine when analyses start, usually the first six elements on the list and includes P, Si, Zr, La, Ce, and Nd. The program then determines the start of the analysis as occurring four time steps after and the end of the background as occurring four times step before:

$$(P + 1) \times (Si + 1) \times (Zr + 1) + (La + 1) \times (Ce + 1) \times (Nd + 1) > 100,000$$

The user is then prompted to enter the dwell times for each isotope so that counts per second can be calculated. Typical values are 40ms for all elements used for dating and 10ms for remaining elements. The user is then asked if the default analyses start and end should be used or if the user wants to enter new start and stop times. If the user chooses to enter new times graphs are brought up for ratios and raw counts for each of the

Table A1.2. Format for comma delimited standard composition file 610.comp.

NIST610,Allen (2001)*Hinton's (1999) factors
Si29,U238,P31,Zr91,Hf177,La139,Ce140,Nd146,Sm147,Eu153,Dy163,Lu175,Th232
69.47,471.63,410.42,497.95,470.15,468.68,460.41,443,481.92,467.46,460.98,481.95,480.449481

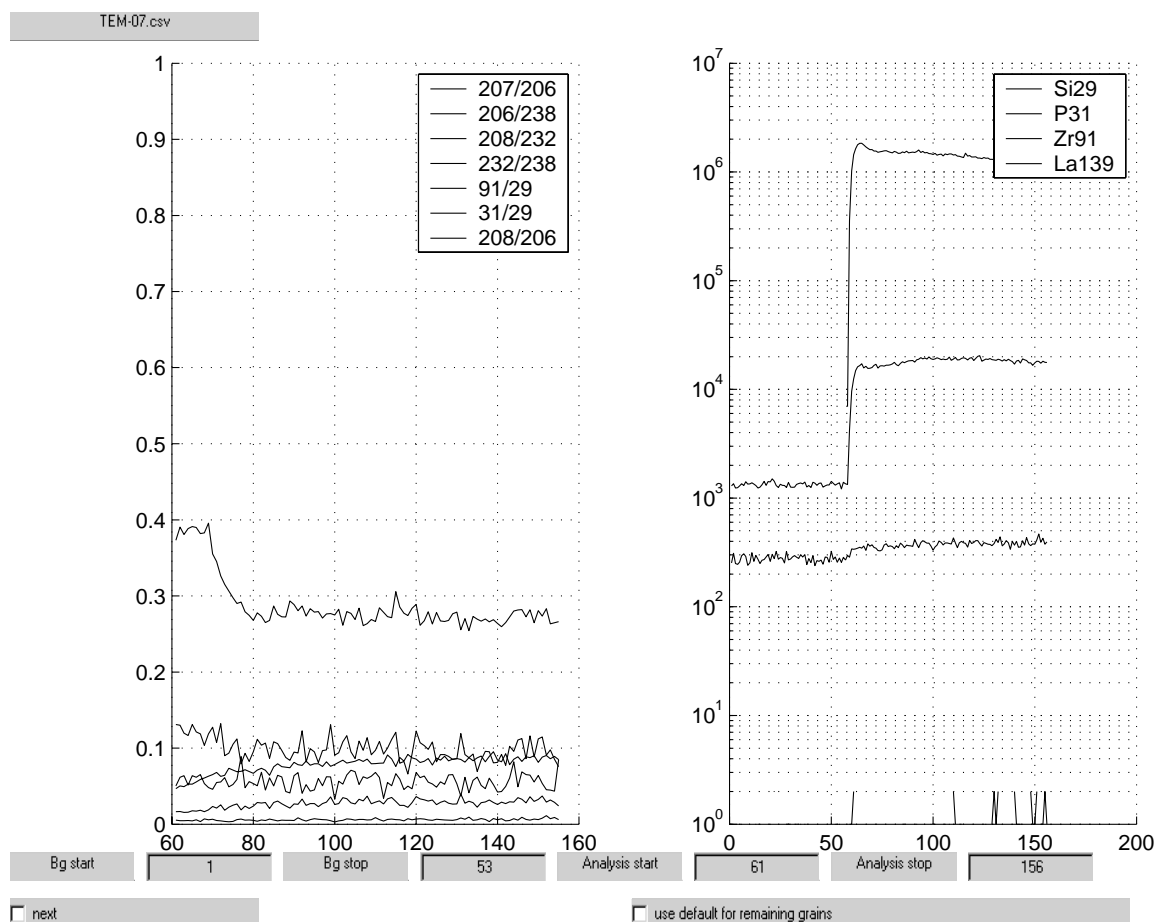


Figure A1.2. Screen shot of analysis start and end selection. The different curves are differentiated by color in the program.

standard grains analyzed so the user can determine if any inclusions were analyzed or if any grains were drilled through (Fig. A2). After the start and end times are entered new ratios are calculated. The user is then asked if drift correction should be applied. If yes, then the program shows graphs of the ratios used for geochemistry and dating plotted against time (Fig. A1.3). The user has the option of selecting no fit (the average of all values are used) or can choose from linear, quadratic or logarithmic fits. It is possible to look at every time slice for each zircon so that multiple types of fitting can be applied or one type of fitting can be applied to all time slices. The data from this step are then saved to a file called “standard_data_(run date).mat”.

Sample Start/End

This step is uses the standard data file created in the previous step as input. This step is used to determine the start and end of sample analyses. The default start is determined as in the previous section and then the user is prompted if they want to change the default values. Many grains have inclusions or get drilled through so it is usually best to change the default times. This can take up to an hour for a set of 150 zircons. At any time, the user can select an option to apply the default value to the remaining samples in order to exit the data entry. The output from this step is stored in a file called “data_for_date_gc_calc_(run date).mat”.

Age and geochemistry calculations with drift correction

This step uses the file created by the previous step as input. First the user is asked to select the type of common Pb correction to be applied. The options are Cumming and Richards (1975), Broken Hill, custom, or none. Cumming and Richards (1975) used a time dependent model for the isotopic composition of common Pb that also requires the user to select an initial age. This is usually a $^{206}\text{Pb}/^{238}\text{U}$ age for young zircons (<100Ma) and a $^{207}\text{Pb}/^{206}\text{Pb}$ age for older zircons. The approach of Cumming and Richards (1975) is best if one believes that the common Pb is in the structure of the zircon and has been trapped since the zircon formed. If the common Pb is thought to be a surface effect, it

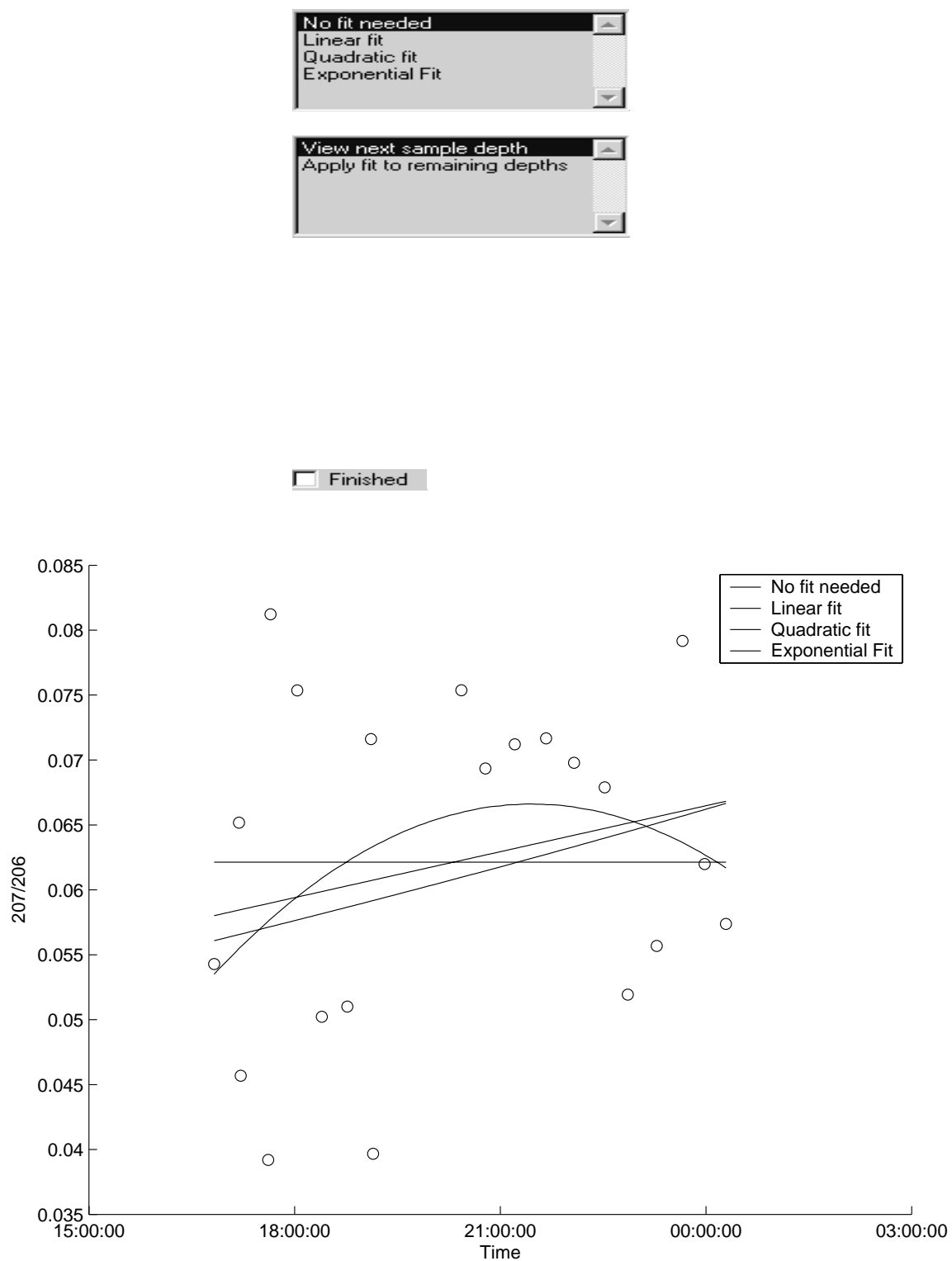


Figure A1.3. Screen shot of user interface for drift correction.

would be more appropriate to enter the common Pb isotopic ratios now. The Broken Hill correction uses the Pb isotope composition of broken hill ore to represent common Pb.

After selecting the common Pb correction there is no more user interaction in this step. The program does corrections for drift and depth of drilling for all isotope ratios and then the ages and geochemistry are calculated. These steps can take up to 20 minutes to run but do not require any user input. The output file is the same format as the ANU summary Excel spreadsheet. This allows the data produced by this program to be input into existing spreadsheets for evaluating grain populations and making graphs. There is an additional geochemistry file that is produced for calculating the Ce^{4+}/Ce^{3+} ratio for the zircons using the next step.

Ce anomaly calculation

This step calculated Ce^{4+}/Ce^{3+} using the method of Ballard et al. (2002) with REE normalized to average crustal values. Ce^{3+} is calculated using a linear fit through the log of the other REE $^{3+}$ concentrations plotted against their associated strain factors in zircon. Results are saved in a file called “REE_data.xls”.

Source Code

Any code follow the symbol “%” is for comment only and is not compiled when the program is run. Any lines of code that extend to the following line are followed by “...”. The program uses functions called `uigetfolder_win32` and `xlswrite` that are available from the Mathworks File Exchange. All other functions are either defined below or are include din MatLab version 13.

Main function: zircon_ANU.m

```
function varargout = zircon_ANU(varargin)
% ZIRCON M-file for zircon_ANU.fig
%   ZIRCON, by itself, creates a new ZIRCON or raises the existing
%   singleton*.
%
%   H = ZIRCON returns the handle to a new ZIRCON or the handle to
%   the existing singleton*.
%
```



```

% ZIRCON('CALLBACK',hObject,eventData,handles,...) calls the local
% function named CALLBACK in ZIRCON.M with the given input arguments.
%
% ZIRCON('Property','Value',...) creates a new ZIRCON or raises the
% existing singleton*. Starting from the left, property value pairs are
% applied to the GUI before zircon_OpeningFunction gets called. An
% unrecognized property name or invalid value makes property application
% stop. All inputs are passed to zircon_OpeningFcn via varargin.
%
% *See GUI Options on GUIDE's Tools menu. Choose "GUI allows only one
% instance to run (singleton)".
%
% See also: GUIDE, GUIDATA, GUIHANDLES

% Edit the above text to modify the response to help zircon

% Last Modified by GUIDE v2.5 09-Jun-2004 16:18:04

% Begin initialization code - DO NOT EDIT
gui_Singleton = 1;
gui_State = struct('gui_Name',    mfilename, ...
    'gui_Singleton', gui_Singleton, ...
    'gui_OpeningFcn', @zircon_OpeningFcn, ...
    'gui_OutputFcn', @zircon_OutputFcn, ...
    'gui_LayoutFcn', [] , ...
    'gui_Callback', []);
if nargin & isstr(varargin{1})
    gui_State.gui_Callback = str2func(varargin{1});
end

if nargout
    [varargout{1:nargout}] = gui_mainfcn(gui_State, varargin{:});
else
    gui_mainfcn(gui_State, varargin{:});
end
% End initialization code - DO NOT EDIT

% — Executes just before zircon is made visible.
function zircon_OpeningFcn(hObject, eventdata, handles, varargin)
% This function has no output args, see OutputFcn.
% hObject    handle to figure
% eventdata  reserved - to be defined in a future version of MATLAB
% handles     structure with handles and user data (see GUIDATA)
% varargin    command line arguments to zircon (see VARARGIN)

```

```

% Choose default command line output for zircon
handles.output = hObject;

% Update handles structure
guidata(hObject, handles);

% UIWAIT makes zircon wait for user response (see UIRESUME)
% uiwait(handles.figure1);

% — Outputs from this function are returned to the command line.
function varargout = zircon_OutputFcn(hObject, eventdata, handles)
% varargout cell array for returning output args (see VARARGOUT);
% hObject handle to figure
% eventdata reserved - to be defined in a future version of MATLAB
% handles structure with handles and user data (see GUIDATA)

% Get default command line output from handles structure
varargout{1} = handles.output;

% — Executes on button press in pushbutton1.
function pushbutton1_Callback(hObject, eventdata, handles)
% hObject handle to pushbutton1 (see GCBO)
% eventdata reserved - to be defined in a future version of MATLAB
% handles structure with handles and user data (see GUIDATA)
%Loads all .csv files from zircon standard, glass standard, and sample
%folders and loads them into matrices. Also retrieves standard info,
%concordia data, etc...

clear all;
%Get data folder that has subfolders zircon_std, glass_std, and samples
%that contain necessary data
path = uigetfolder_win32('Pick zircon standard folder','C:\ANU_zircon');
zircon_std_path = [path '\'];
path = uigetfolder_win32('Pick glass standard folder','C:\ANU_zircon');
glass_std_path = [path '\'];
path = uigetfolder_win32('Pick sample folder','C:\ANU_zircon');
samples_path = [path '\'];
paths={zircon_std_path;glass_std_path;samples_path};
%Set counter for number of files
counter = 0;
%Go to the folders and retrieve the data
h = waitbar(0,'Processing folders');

```

```

for j=1:size(paths);
    folder = paths{j};
    samples = dir([folder '*.csv']);
    %store filenames in variables
    if j==1;
        zircon_standard_files = samples;
        zircon_files = {samples.name};
    elseif j==2;
        glass_standard_files = samples;
        glass_files = {samples.name};
    else
        sample_list_files = samples;
    end
    sample_files = {samples.name};
    last_file = size(samples,1);
    %Cycle through files in each folder retrieving the data and storing it
    %in the variable data
    for i=1:last_file;
        waitbar((counter+i)/(size(dir(paths{1}),1)+size(dir(paths{2}),1)+...
            size(dir(paths{3}),1)-6));
        filename=[paths{j} sample_files{i}];
        if j+i==2;
            % Retrieve line of data with masses measured
            fid = fopen(filename);
            fgetl(fid);
            fgetl(fid);
            elements = fgetl(fid);
            fclose(fid);
            elements = strread(elements,'%q','delimiter',' ');
        end
        data_temp=textread(filename,'%f','headerlines',3,'delimiter',' ');
        data(j,i,:,:)=[reshape(data_temp,length(elements),length(data_temp)/...
            length(elements))];
    end
    clear data_temp;
    counter = counter + last_file;
end
close(h);
dates = {samples.date};
run_date = dates{1};
%separate the zircon standard, glass standard, and sample data
zircon_std_data = data(1,1:size(dir([paths{1} '*.csv']),1),:,:);
zircon_std_data = squeeze(zircon_std_data);

glass_std_data = data(2,1:size(dir([paths{2} '*.csv']),1),:,:);

```

```

glass_std_data = squeeze(glass_std_data);

sample_data = data(3,1:size(dir([paths{3} '*.csv']),1),:,:);
sample_data = squeeze(sample_data);

clear data;

%Get the file containing concordia data for use in plotting
[concordia_file concordia_path]=uigetfile('*.csv','Pick concordia file');
concordia_filename = [concordia_path concordia_file];
fid = fopen(concordia_filename);
concordia_header = fgetl(fid);
fclose(fid);
concordia_header = strread(concordia_header,'%q','delimiter',' ');

concordia_data = textread(concordia_filename,'%f','headerlines',1,'delimiter',' ');
concordia_data =
[reshape(concordia_data,length(concordia_header),length(concordia_data)/...
length(concordia_header))];

%Define the decay constants for each isotope of Th and U
lambdas = {'Th232','U235','U238'};
lambdas(:,2) = {1000000*4.9475*(10^-11);1000000*9.8485*(10^-
10);1000000*1.55125*(10^-10)};

%Get standard compositions/ages
[zircon_std_age_file zircon_std_age_path]=uigetfile('*.age','Pick zircon standard...
composition file');
[glass_std_comp_file glass_std_comp_path]=uigetfile('*.comp','Pick glass standard...
composition file');

std_age = textread([zircon_std_age_path zircon_std_age_file],'%f');

fid = fopen([glass_std_comp_path glass_std_comp_file]);
fgetl(fid);
glass_header = fgetl(fid);
glass_comp = fgetl(fid);
fclose(fid);
glass_header = strread(glass_header,'%q','delimiter',' ');
glass_comp = strread(glass_comp,'%f','delimiter',' ');

%Define the masses as variables
time = strmatch('Time',elements);
Si29 = strmatch('Si29',elements);
P31 = strmatch('P31',elements);

```

```

Zr91 = strmatch('Zr91',elements);
La139 = strmatch('La139',elements);
Ce140 = strmatch('Ce140',elements);
Nd146 = strmatch('Nd146',elements);
Sm147 = strmatch('Sm147',elements);
Eu153 = strmatch('Eu153',elements);
Dy163 = strmatch('Dy163',elements);
Lu175 = strmatch('Lu175',elements);
Hf177 = strmatch('Hf177',elements);
Pb206 = strmatch('Pb206',elements);
Pb207 = strmatch('Pb207',elements);
Pb208 = strmatch('Pb208',elements);
Th232 = strmatch('Th232',elements);
U235 = strmatch('U235',elements);
U238 = strmatch('U238',elements);

%Save data to file
save(['raw_zircon_data_' run_date(1:11) '.mat']);

% — Executes on button press in pushbutton2.
function pushbutton2_Callback(hObject, eventdata, handles)
% hObject    handle to pushbutton2 (see GCBO)
% eventdata  reserved - to be defined in a future version of MATLAB
% handles    structure with handles and user data (see GUIDATA)
%Calculates background subtracted ratios for all the zircons in a run
clear all;
%Get data file created by previous steo
[data_file data_path]=uigetfile('*.mat','Pick raw data file');
filename = [data_path data_file];
%Loads all variables included in the previous program
load(filename);

%Get default times for analysis
%Creat graphical interface for selecting the masses to use for determining
%default times
needed_elements = checkbox_list(elements,'Pick elements for determining analysis...
    start/stop',2:7);

%Find the start/stop of the zircon std analyses
[zirc_std_start,zirc_std_stop,zirc_std_background_start,zirc_std_background_stop]=...
    find_start(zircon_std_data,needed_elements);
[glass_std_start,glass_std_stop,glass_std_background_start,...
    glass_std_background_stop] = find_start(glass_std_data,needed_elements);

%Find the data necessary for background subtraction and ratio calculations

```

```

%Also change the matrices so the data all start at 1 and pad the end with zeros
%Finally, calculate and subtract the background
zircon_calc_data =
background_subtraction(zircon_std_data,zirc_std_start,zirc_std_stop,...
    zirc_std_background_start,zirc_std_background_stop);
glass_calc_data = background_subtraction(glass_std_data,glass_std_start,...
    glass_std_stop,glass_std_background_start,glass_std_background_stop);

%Get dwell times
dwell_times_str = textbox_list(elements,'Enter dwell times',10,...
    'Pb, U, and Th typically 40 everything else 10');
for i=1:length(dwell_times_str);
    dwell_times(i)=(str2num(dwell_times_str{i}))/1000;
end
dwell_times(1)=1;
zirc_dwell_times_matrix = ...
    repmat(dwell_times,[size(zircon_calc_data,1) 1 size(zircon_calc_data,3)]);
glass_dwell_times_matrix = ...
    repmat(dwell_times,[size(glass_calc_data,1) 1 size(glass_calc_data,3)]);

zircon_calc_data = zircon_calc_data./zirc_dwell_times_matrix;
glass_calc_data = glass_calc_data./glass_dwell_times_matrix;

%Find where the different standards have counts > 0
for i=1:size(zircon_calc_data,3)
    valid_zirc_stds(i) = {find(zircon_calc_data(:,2,i))};
end
for i=1:size(glass_calc_data,3)
    valid_glass_stds(i) = {find(glass_calc_data(:,2,i))};
end

%Calculate standard ratios for age dating
%Eliminate times where there are not at least 4 measurements
for i=1:size(zircon_calc_data,3)
    if size(valid_zirc_stds{i},1)>=4
        zircon_calc_data(:,i)=zircon_calc_data(:,i);
    else
        zircon_calc_data(:,i:size(zircon_calc_data,3))=[];
        break
    end
end

for i=1:size(glass_calc_data,3)
    if size(valid_glass_stds{i},1)>=4
        glass_calc_data(:,i)=glass_calc_data(:,i);
    end
end

```

```

else
    glass_calc_data(:,i:size(glass_calc_data,3))=[];
    break
end
end

%Get time and header info
dating_ratios_header = {'Time(seconds)', 'Scan
    number', '207/206', '206/238', '208/232', '232/238', '91/29', '31/29', '208/206'};

%calculate U,Pb ratios plus Zr/Si and P/Si
zircon_date_ratios = date_ratio_calc(zircon_calc_data,elements,zirc_std_start);
glass_date_ratios = date_ratio_calc(glass_calc_data,elements,glass_std_start);

%User interface for entering new analysis starts and finish for all
%standards
figure;
h2.listbox1=uicontrol('Style','listbox','String',{'no','yes'},'Units',...
    'normalized','Position',[0,.4,0.3,.2]);
h2.textbox1=uicontrol('Style','text','String','Enter new analysis start/end positions?',...
    'Units','normalized','Position',[0,.75,0.4,.05]);
%Stop program until user selects the finished box in the graphical interface
h2.checkbox1=uicontrol('Style','checkbox','String','finished','Units','normalized','Position',[0,0,0.2,0.04]);
waitfor(h2.checkbox1,'Value',1);
yes_or_no = get(h2.listbox1,'Value');
close;

ui_elements = {'Si29','P31','Zr91','La139'};
ui_data_loc = [Si29;P31;Zr91;La139];

if yes_or_no == 2;

    zircon_ui_data = zircon_std_data(:,ui_data_loc,:);
    glass_ui_data = glass_std_data(:,ui_data_loc,:);
    [zirc_std_start,zirc_std_stop,zirc_std_background_start,zirc_std_background_stop]...
        =user_entered_start(zircon_files,zircon_date_ratios,zircon_ui_data,...
            dating_ratios_header,zirc_std_start,zirc_std_stop,zirc_std_background_start,...
            zirc_std_background_stop,ui_elements);

    [glass_std_start,glass_std_stop,glass_std_background_start,...
        glass_std_background_stop]=user_entered_start(glass_files,glass_date_ratios,...
            glass_ui_data,dating_ratios_header,glass_std_start,glass_std_stop,...
            glass_std_background_start,glass_std_background_stop,ui_elements);
%Clear any variables that will change with the new start and end times
clear zircon_calc_data glass_calc_data zircon_date_ratios glass_date_ratios;

```

```

clear valid_zirc_stds valid_glass_stds;
%Rerun the background subtraction
zircon_calc_data = background_subtraction(zircon_std_data,zirc_std_start,...
    zirc_std_stop,zirc_std_background_start,zirc_std_background_stop);
glass_calc_data = background_subtraction(glass_std_data,glass_std_start,...
    glass_std_stop,glass_std_background_start,glass_std_background_stop);

for i=1:size(zircon_calc_data,3)
    valid_zirc_stds(i) = {find(zircon_calc_data(:,2,i))};
end

for i=1:size(glass_calc_data,3)
    valid_glass_stds(i) = {find(glass_calc_data(:,2,i))};
end

for i=1:size(zircon_calc_data,3)
    if size(valid_zirc_stds{i},1)>=4
        zircon_calc_data(:,i)=zircon_calc_data(:,i);
    else
        zircon_calc_data(:,i:size(zircon_calc_data,3))=[];
        break
    end
end

for i=1:size(glass_calc_data,3)
    if size(valid_glass_stds{i},1)>=4
        glass_calc_data(:,i)=glass_calc_data(:,i);
    else
        glass_calc_data(:,i:size(glass_calc_data,3))=[];
        break
    end
end

%calculate U,Pb ratios plus Zr/Si and P/Si
zircon_date_ratios = date_ratio_calc(zircon_calc_data,elements,zirc_std_start);
glass_date_ratios = date_ratio_calc(glass_calc_data,elements,glass_std_start);

end

%Calculate glass ratios for geochemistry
glass_Si29 = squeeze(glass_calc_data(:,Si29,:))';
glass_Si29 = repmat(glass_Si29,[1 1 size(glass_calc_data,2)]);
glass_Si29 = shiftdim(glass_Si29,1);
glass_Si29(:,1,:)=1;
glass_gc_ratios = glass_calc_data./glass_Si29;

%Make header for glass GC ratios

```



```

for i=2:size(elements,1);
    if i==1; glass_std_ratios_header(1,1) = {'T(seconds)'}; end;
    gc_ratios_header(1,i)=[elements{i} '/Si29'];
end

%Plot ratios versus time to get curve fit for machine drift
%User interface for entering drift curve fits
figure;
h2.listbox1=uicontrol('Style','listbox','String',{'no';'yes'},'Units','normalized',...
    'Position',[0,4,0.3,.2]);
h2.textbox1=uicontrol('Style','text','String','Select drift corrections for each ratio?',...
    'Units','normalized','Position',[0,.75,0.4,.05]);
%Stop program until user selects the finished box in the graphical interface
h2.checkbox1=uicontrol('Style','checkbox','String','finished','Units','normalized',...
    'Position',[0,0,0.2,0.04]);
waitfor(h2.checkbox1,'Value',1);
yes_or_no = get(h2.listbox1,'Value');
close;

if yes_or_no == 2;
    %Allows user to enter the type of fit for drift correction (plots of
    %each type of fit are shown)
    [zircon_drift_type,zircon_drift_correction] = drift_plot(zircon_date_ratios,...
        zircon_standard_files,dating_ratios_header,valid_zirc_stds);
    [glass_drift_type,glass_drift_correction] = drift_plot(glass_gc_ratios,...
        glass_standard_files,gc_ratios_header,valid_glass_stds);
    [glass_date_drift_type,glass_date_drift_correction] = drift_plot(glass_date_ratios,...
        glass_standard_files,dating_ratios_header,valid_glass_stds);
else
    %Applies no drift correction
    [zircon_drift_type,zircon_drift_correction] = drift_plot_fixed(zircon_date_ratios,...
        zircon_standard_files,dating_ratios_header,valid_zirc_stds);
    [glass_drift_type,glass_drift_correction] = drift_plot_fixed(glass_gc_ratios,...
        glass_standard_files,gc_ratios_header,valid_glass_stds);
    [glass_date_drift_type,glass_date_drift_correction] = drift_plot_fixed...
        (glass_date_ratios,glass_standard_files,dating_ratios_header,valid_glass_stds);
end

zirc_std_ratios_header = {'Scan number','Number of standards','207/206','206/238',...
    '208/232','232/238','91/29','31/29','208/206','Std dev 207/206','Std dev 206/238',...
    'Std dev 208/232','Std dev 232/238','Std dev 91/29','Std dev 31/29','Std dev 208/
    206'};

%Calculate average and std dev for the age ratios for both the zircon and
%glass stds

```

```

zircon_ratios = age_ratio_calc(zircon_calc_data,valid_zirc_stds,elements);
glass_age_ratios = age_ratio_calc(glass_calc_data,valid_glass_stds,elements);

%%%%Calculates mean at each sample depth for glass analyses averaging over
%%%%the valid standards. This is no longer needed for determining
%%%%concentration but is still necessary for calculating the standard error
%%%%on the concentration
%Make header and calculate the average and std deviation of the glass
%geochem ratios
for j=1:size(glass_gc_ratios,3);
    glass_ratios(1,j) = size(valid_glass_stds{j},1);
    if j==1; glass_std_ratios_header(1,1) = {'Number of standards'}; end;
    for i=2:size(glass_gc_ratios,2)
        glass_ratios(i,j) = mean(squeeze(glass_gc_ratios(valid_glass_stds{j},i,j)),1);
        if j==1;glass_std_ratios_header(1,i)=[elements{i} ' /Si29'];end;
    end
    for i=(size(glass_gc_ratios,2)+1):(2*size(glass_gc_ratios,2)-1)
        glass_ratios(i,j) = std(squeeze(glass_gc_ratios(valid_glass_stds{j},i-
size(glass_gc_ratios,2)+1,j)),1);
        if j==1;glass_std_ratios_header(1,i)=[ 'std dev ' elements{i-
size(glass_gc_ratios,2)+1} ' /Si29'];end;
    end
end

%Calculate the standard ratios necessary for dating
std_207_206 = (exp(lambdas{strmatch('U235',lambdas(:,1)),2}*std_age)-1)*(1/137.88)/
(exp(lambdas{strmatch('U238',lambdas(:,1)),2}*std_age)-1);
std_206_238 = (exp(lambdas{strmatch('U238',lambdas(:,1)),2}*std_age)-1);
std_208_232 = (exp(lambdas{strmatch('Th232',lambdas(:,1)),2}*std_age)-1);

std_232 = glass_comp(strmatch('Th232',glass_header));
std_238 = glass_comp(strmatch('U238',glass_header));
std_232_238 = std_232/std_238;
std_208_206 = 2.169006;

save(['standard_data_' run_date(1:11)]);

% — Executes on button press in pushbutton3.
function pushbutton3_Callback(hObject, eventdata, handles)
% hObject    handle to pushbutton3 (see GCBO)
% eventdata  reserved - to be defined in a future version of MATLAB
% handles    structure with handles and user data (see GUIDATA)
% Allows user to manually enter start/end of analyses and does the drift
% correction

```

```

clear all;
%Get standard data file created by previous step. This file also contains
%all the sample raw data
[data_file data_path]=uigetfile('*.mat','Pick standard data file');
filename = [data_path data_file];
%Loads all variables included in the previous program
load(filename);

[sample_start,sample_stop,sample_background_start,sample_background_stop]=...
    find_start(sample_data,needed_elements);
sample_calc_data = background_subtraction(sample_data,sample_start,sample_stop,...
    sample_background_start,sample_background_stop);
sample_dwelling_times_matrix = repmat(dwelling_times,...
    [size(sample_calc_data,1) 1 size(sample_calc_data,3)]);
sample_counts_data = sample_calc_data;
sample_calc_data = sample_calc_data.*sample_dwelling_times_matrix;
sample_date_ratios = date_ratio_calc(sample_calc_data,elements,sample_start);

%User interface for entering new analysis starts and finish for all and samples
figure;
h2.listbox1=uicontrol('Style','listbox','String',{'no';'yes'},'Position',[0,.4,0.3,.2],...
    'Units','normalized');
h2.textbox1=uicontrol('Style','text','String','Enter new analysis start/end positions?',...
    'Units','normalized','Position',[0,.75,0.4,.05]);
%Stop program until user selects the finished box in the graphical interface
h2.checkbox1=uicontrol('Style','checkbox','String','finished','Position',[0,0,0.2,0.04],...
    'Units','normalized');
waitfor(h2.checkbox1,'Value',1);
yes_or_no = get(h2.listbox1,'Value');
close;

if yes_or_no == 2;
    data_change = 1;
    sample_ui_data = sample_data(:,ui_data_loc,:);
    [sample_start,sample_stop,sample_background_start,sample_background_stop]=...
        user_entered_start(sample_files,sample_date_ratios,sample_ui_data,...
            dating_ratios_header,sample_start,sample_stop,sample_background_start,...
            sample_background_stop,ui_elements);
    %Clear any variables that will change with the new start and end times
    clear sample_calc_data sample_date_ratios;
    %Rerun the background subtraction
else
    data_change = 0;
end

```

```

save(['data_for_date_gc_calc_' run_date(1:11)]);

% — Executes on button press in pushbutton4.
function pushbutton4_Callback(hObject, eventdata, handles)
% hObject    handle to pushbutton4 (see GCBO)
% eventdata  reserved - to be defined in a future version of MATLAB
% handles    structure with handles and user data (see GUIDATA)
% Does the age and geochem calculations with drift correction

clear all;

%Get standard data file created by previous step. This file also contains
%all the sample raw data
[data_file data_path]=uigetfile('*.mat','Pick data file for age/gc calc');
filename = [data_path data_file];
%Loads all variables included in the previous program
load(filename);

%User interface for selecting type of common Pb correction
common_Pb_list = {'Cumming and Richard';'Broken Hill';'Custom';'None'};
figure;
h2.listbox1=uicontrol('Style','listbox','String',common_Pb_list,'Units','normalized',...
    'Position',[0,4,0.3,2]);
h2.textbox1=uicontrol('Style','text','String','Which type of common Pb correction?',...
    'Units','normalized','Position',[0,.75,0.4,.05]);
%Stop program until user selects the finished box in the graphical interface
h2.checkbox1=uicontrol('Style','checkbox','String','finished','Units','normalized',...
    'Position',[0,0,0.2,0.04]);
waitfor(h2.checkbox1,'Value',1);
common_Pb_number = get(h2.listbox1,'Value');
common_Pb_type = common_Pb_list{common_Pb_number};
close;

if common_Pb_number == 3;
    figure;
    h1.textedit1=uicontrol('Style','edit','String','0.0625','Units','normalized',...
        'Position',[.45,2,0.2,.05]);
    h1.text1=uicontrol('Style','text','String','Common 204/206','Units','normalized',...
        'Position',[0.2,2,0.2,.05]);
    h1.textedit2=uicontrol('Style','edit','String','0.962','Units','normalized',...
        'Position',[.45,4,0.2,.05]);
    h1.text2=uicontrol('Style','text','String','Common 207/206','Units','normalized',...
        'Position',[0.2,0.4,0.2,.05]);
    h1.textedit3=uicontrol('Style','edit','String','2.23','Units','normalized',...

```

```

        'Position',[.45,.6,0.2,.05]);
h1.text3=uicontrol('Style','text','String','Common 208/206','Units','normalized',...
    'Position',[0.2,0.6,0.2,.05]);
h1.checkbox1=uicontrol('Style','checkbox','String','Finished','Units','normalized',...
    'Position',[0,0,0.2,0.05]);
waitfor(h1.checkbox1,'Value',1);
common_204_206 = str2num(get(h1.textedit1,'String'));
common_207_206 = str2num(get(h1.textedit2,'String'));
common_208_206 = str2num(get(h1.textedit3,'String'));
close;
end
%User interface for selecting start date for 208 correction. 207 correction
%always uses 206/238 age
if common_Pb_number == 4;
    %DO NOTHING...
else
    age_list = {'207/206';'206/238'};
    figure;
    h2.listbox1=uicontrol('Style','listbox','String',age_list,'Units','normalized',...
        'Position',[0,.4,0.3,.2]);
    h2.textbox1=uicontrol('Style','text','String','Enter start date for 208
correction?',...
        'Units','normalized','Position',[0,.75,0.4,.05]);
    %Stop program until user selects the finished box in the graphical interface

h2.checkbox1=uicontrol('Style','checkbox','String','finished','Units','normalized',...
    'Position',[0,0,0.2,0.04]);
waitfor(h2.checkbox1,'Value',1);
age_type_number = get(h2.listbox1,'Value');
age_type_208 = age_list{age_type_number};
close;
end
age_type_207 = '206/238';

if data_change == 1;
    sample_calc_data = background_subtraction(sample_data,sample_start,sample_stop,...
        sample_background_start,sample_background_stop);
    sample_counts_data = sample_calc_data;
    sample_calc_data = sample_calc_data.*sample_dwell_times_matrix;
    sample_date_ratios = date_ratio_calc(sample_calc_data,elements,sample_start);
end

%Calculate sample ratios for geochemistry

```

```

sample_Si29 = squeeze(sample_calc_data(:,Si29,:));
sample_Si29 = repmat(sample_Si29,[1 1 size(sample_calc_data,2)]);
sample_Si29 = shiftdim(sample_Si29,1);
sample_Si29(:,1,:)=1;
sample_gc_ratios = sample_calc_data./sample_Si29;

%Start drift correction
clear data_temp;
%Retrieve the time stamp of the files
sample_file_dates={sample_list_files.date};
%Convert time stamp into a number that MatLab can plot
for i=1:size(sample_file_dates,2);
    data_temp(i)=datenum(sample_file_dates{i});
end
sample_file_numbers = data_temp';

drift_ratios = {'207/206','206/238','208/232','232/238','208/206'};
standard_ratios = [std_207_206,std_206_238,std_208_232,std_232_238,std_208_206];

h = waitbar(0,'Doing drift/depth correction for age data');

for i=1:size(sample_date_ratios,1)
    waitbar(i/size(sample_date_ratios,1));
    [corr_sample_ratios(i,:),sample_date_corr_factor(i,:)] = depth_drift_correction...
        (sample_date_ratios(i,:),zircon_drift_type,zircon_drift_correction,...
        sample_start(i),sample_stop(i),dating_ratios_header,...
        sample_file_numbers(i),drift_ratios,standard_ratios,glass_date_drift_type,...
        glass_date_drift_correction);
end
close(h)
corr_sample_ratios = squeeze(corr_sample_ratios);
corr_sample_ratios_header = {'207/206','206/238','208/232','232/238','208/206','207/235'};

%calculate average ratios and s.e. for age calculation ratios
for j=1:size(corr_sample_ratios,1)
    for i=1:size(corr_sample_ratios,2)
        ratio_data = corr_sample_ratios{j,i};
        corr_factor = sample_date_corr_factor{j,i};
        average_date_corr_factor(j,i) = mean(corr_factor);
        average_corr_sample_ratios(j,i) = mean(ratio_data);
    end
end
end

```

```

for j=1:size(corr_sample_ratios,1)
    for i=1:size(corr_sample_ratios,2)
        ratio_data = corr_sample_ratios{j,i};
        corr_factor = sample_date_corr_factor{j,i};
        std_average_date_corr_factor(j,i) = std(corr_factor);
        se_corr_sample_ratios(j,i) = std(ratio_data)/sqrt(size(corr_sample_ratios{j},2));
    end
end

```

%calculate ages for average ratios (this is the reported data!) Per time
 %slice data is stored in a separate file

```

% This gets all of the elements that are included in the header for the
% glass standard composition
for i = 1:size(elements,1)
    if strmatch(elements{i},glass_header) > 0
        element_index(i) = 1;
    else
        element_index(i) = 0;
    end
end

```

```

%Retrieve the masses of interest
needed_elements = find(element_index);

```

```

%create header for the geochem report file
numbers = {'0','1','2','3','4','5','6','7','8','9'};
element_names(1) = {'Sample name'};
for j=1:size(needed_elements,2)
    for i=1:size(elements{needed_elements(j)},2)
        clear flag location;
        flag = ismember(elements{needed_elements(j)}(i),numbers);
        if flag==1
            element_names(j+1) = {'ppm 'elements{needed_elements(j)}...
                (1:(i-1))}];
            element_names(size(needed_elements,2)+1+j) = ...
                {'std error ' elements{needed_elements(j)}(1:(i-1))}];
        break
    end
end
end

```

```

%Change Si from ppm to %

```

```

Si=strmatch('ppm Si',element_names);
if Si>0
    element_names(Si)={'% Si'};
end

glass_known_ratios=(glass_comp./glass_comp(1));

% Make appropriate headers for searching when doing drift correction
for i = 1:size(needed_elements,2)
    drift_gc_ratios(i) = {[elements{needed_elements(i)} 'Si29']}';
    drift_known_ratios(i) =
glass_known_ratios(strmatch(elements{needed_elements(i)},glass_header));
end
gc_ratios_header(1) = {' '};

% Correct ratios for drift, drilling depth, and standard composition
h = waitbar(0,'Doing drift/depth correction for geochem data');
for i=1:size(sample_date_ratios,1)
    waitbar(i/size(sample_date_ratios,1));
    [corr_sample_gc_ratios(i,:),sample_gc_corr_factor(i,:)] = ...
        depth_drift_correction_glass(sample_gc_ratios(i,:),glass_drift_type,...
        glass_drift_correction,...
        sample_start(i),sample_stop(i),gc_ratios_header,sample_file_numbers(i),...
        drift_gc_ratios,drift_known_ratios);
end
close(h)
corr_sample_gc_ratios = squeeze(corr_sample_gc_ratios);
corr_sample_gc_header = drift_gc_ratios;

for i=1:size(corr_sample_gc_ratios,1)
    for j = 1:size(corr_sample_gc_ratios,2)
        average_sample_gc_ratios(i,j) = mean(corr_sample_gc_ratios{i,j});
    end
end

for i=1:size(sample_gc_ratios,1)
    for j = 1:size(corr_sample_gc_ratios,2)
        se_sample_gc_ratios(i,j) = std(corr_sample_gc_ratios{i,j})./
size(corr_sample_gc_ratios{i,j},2);
    end
end

% Needed for calculating the standard error on the concentration
average_glass_gc_ratios = (mean(glass_ratios(1:size(sample_gc_ratios,2),:),2))';

```



```

se_glass_gc_ratios = (std(glass_ratios(1:size(sample_gc_ratios,2),:),0,2)/...
    sqrt(size(glass_ratios,2)))';

%Multiply by $SiO2 in zircon
for j=1:size(average_sample_gc_ratios,1)
    final_geochem_ppm(j,1)={sample_files{j}};
    for i=1:size(needed_elements,2)
        final_geochem_ppm(j,i+1) = ...
            {average_sample_gc_ratios(j,i)*37.22};%SiO2 in zircon
    end
end

%Calculate standard error
for j=1:size(average_sample_gc_ratios,1)
    for i=1:size(needed_elements,2)
        final_geochem_ppm(j,size(needed_elements,2)+1+i) = ...
            {final_geochem_ppm{j,i+1}*...
            ((se_sample_gc_ratios(j,i)/...
            average_sample_gc_ratios(j,i))^2+...
            (se_glass_gc_ratios(needed_elements(i))/...
            average_glass_gc_ratios(needed_elements(i)))^2)^(1/2)};
    end
end

export_file_name = [pwd '\geochem_data_' run_date(1:11) '.xls'];
header = 'zircon geochemical data';
xlswrite(final_geochem_ppm,header,element_names,export_file_name);

h = waitbar(0,'Processing ages');
%Calculate age at each time slice for depth profile.
for i=1:size(sample_date_ratios,1)
    waitbar(i/size(sample_date_ratios,1));
    raw_ages_per_time_slice(i)={age_calc(corr_sample_ratios(i,:),lambdas,...
        corr_sample_ratios_header)};
end
close(h);
age_header={'206/238','207/235','208/232','207/206'};
save(['depth_age_data_' run_date(1:11) '.mat'],'raw_ages_per_time_slice');

raw_average_ages(:,1) = log(...
    average_corr_sample_ratios(:,strmatch('206/238',corr_sample_ratios_header))+1)/...
    lambdas{strmatch('U238',lambdas(:,1)),2};

```

```

raw_average_ages(:,2) = log(...
    average_corr_sample_ratios(:,strmatch('207/235',corr_sample_ratios_header))+1)./...
    lambdas{strmatch('U235',lambdas(:,1)),2};
raw_average_ages(:,3) = log(...
    average_corr_sample_ratios(:,strmatch('208/232',corr_sample_ratios_header))+1)./...
    lambdas{strmatch('Th232',lambdas(:,1)),2};

U_ratio = 137.88;
lambda_238 = lambdas{strmatch('U238',lambdas(:,1)),2};
lambda_235 = lambdas{strmatch('U235',lambdas(:,1)),2};
lambda_232 = lambdas{strmatch('Th232',lambdas(:,1)),2};
for i=1:size(average_corr_sample_ratios,1);
    tinit=raw_average_ages(i,1);
    ratio_temp = average_corr_sample_ratios(i,strmatch('207/
206',corr_sample_ratios_header));
    t1=log(U_ratio*ratio_temp*(exp(lambda_238*tinit)-1)+1)/lambda_235;
    t2=log(U_ratio*ratio_temp*(exp(lambda_238*t1)-1)+1)/lambda_235;
    delta_t = abs(t1-t2);
    while delta_t > 0.1
        t1=log(U_ratio*ratio_temp*(exp(lambda_238*t2)-1)+1)/lambda_235;
        t2=log(U_ratio*ratio_temp*(exp(lambda_238*t1)-1)+1)/lambda_235;
        delta_t = abs(t1-t2);
    end
    raw_average_ages(i,4)=t1;
end

raw_average_ages(:,5) =
    se_corr_sample_ratios(:,strmatch('206/238',corr_sample_ratios_header))./...
    ((average_corr_sample_ratios(:,strmatch('206/238',...
    corr_sample_ratios_header))+1)*lambda_238);
raw_average_ages(:,6) =
    se_corr_sample_ratios(:,strmatch('207/235',corr_sample_ratios_header))./...
    ((average_corr_sample_ratios(:,strmatch('207/
235',corr_sample_ratios_header))...+1)*lambda_235);
raw_average_ages(:,7) =
    se_corr_sample_ratios(:,strmatch('208/232',corr_sample_ratios_header))./...
    ((average_corr_sample_ratios(:,strmatch('208/
232',corr_sample_ratios_header))...+1)*lambda_232);
raw_average_ages(:,8) =
    se_corr_sample_ratios(:,strmatch('207/206',corr_sample_ratios_header))./...
    (lambda_235*(1./(U_ratio.*(exp(raw_average_ages(:,4).*lambda_238)-1))+...
    average_corr_sample_ratios(:,strmatch('207/206',corr_sample_ratios_header))));

raw_average_age_header = {'206/238','207/235','208/232','207/206','se 206/238',...
    'se 207/235','se 208/232','se 207/206'};

```

```

raw_ages_cell = num2cell(raw_average_ages);
sample_names = sample_files';
raw_age_export_data = [sample_names raw_ages_cell];
raw_age_header = 'U-Pb ages not corrected for common Pb but corrected for...
    machine drift';
raw_age_columns = {'Sample names','Pb206/U238 age (Ma)','Pb207/U235 age
(Ma)',...
    'Pb208/Th232 age (Ma)','Pb207/Pb206 age (Ma)','s.e. Pb206/U238 age (Ma)',...
    's.e. Pb207/U235 age (Ma)','s.e. Pb208/Th232 age (Ma)',...
    's.e. Pb207/Pb206 age (Ma)'};
raw_age_filename = [pwd '\raw_ages_' run_date(1:11) '.xls'];
xlswrite(raw_age_export_data,raw_age_header,raw_age_columns,raw_age_filename);

```

```

%Define headers for output data from the common Pb corrections
common_Pb_header_208 = {'206/238','207/206','207/235','238/206','208/206','232/
238'};
common_Pb_header_207 = {'206/238','208/232','238/206','207/206'};

```

```

if common_Pb_number == 1
    %Needs to be recursive so put in a loop that calculates ratios then
    %calculates the correction and loops
    age_earth = 4550;
    age_init_207 =
raw_average_ages(:,strmatch(age_type_207,raw_average_age_header));
    age_init_208 =
raw_average_ages(:,strmatch(age_type_208,raw_average_age_header));
    h = waitbar(0,'Doing common Pb correction');
    for i = 1:size(raw_average_ages,1)
        waitbar(i/size(raw_average_ages,1));
        counter = 1;
        t_diff = 10;
        while t_diff > 0.05
            if counter == 1
                age_1 = age_init_207(i);
            else
                age_1 = age_2;
            end
            common_204_206 = 1/(9.307 + 8.8*exp(lambda_238*age_earth)-
                exp(lambda_238*age_1));
            common_207_206 = common_204_206*(10.294 +
                (8.8/U_ratio)*(exp(lambda_235*age_earth)-exp(lambda_235*age_1)));
            common_208_206 = common_204_206*(29.476 +

```

```

        (3.8*8.8)*(exp(lambda_232*age_earth)-exp(lambda_232*age_1));
    if counter == 1
        [pb_corr_ratios_207(i,:),pb_corr_ages_207(i,:),...
         pb_corr_ratios_se_207(i,:),pb_corr_ages_se_207(i,:),...
         est_204_206_207(i),est_204_206_se_207(i),f_207(i),...
         f_207_se(i)]=common_pb_corr_207(raw_average_ages(i,:),...
         raw_average_age_header,average_corr_sample_ratios(i,:),...
         corr_sample_ratios_header,common_Pb_header_207,age_1,...
         common_204_206,common_207_206,common_208_206,...
         lambda_232,lambda_235,lambda_238,se_corr_sample_ratios(i,:));
    else

        [pb_corr_ratios_207(i,:),pb_corr_ages_207(i,:),...
         pb_corr_ratios_se_207(i,:),pb_corr_ages_se_207(i,:),...
         est_204_206_207(i),est_204_206_se_207(i),f_207(i),...
         f_207_se(i)]=common_pb_corr_207(pb_corr_ages_207(i,:),...
         common_Pb_header_207,pb_corr_ratios_207(i,:),...
         common_Pb_header_207,common_Pb_header_207,age_1,...
         common_204_206,common_207_206,common_208_206,...
         lambda_232,lambda_235,lambda_238,pb_corr_ratios_se_207(i,:));
    end

    age_2 = pb_corr_ages_207(i,strmatch(age_type_207,common_Pb_header_207));
    t_diff = abs(age_1-age_2);
    counter = counter + 1;
    if counter > 20
        break
    end
end
counter = 1;
t_diff = 10;
while t_diff > 0.05
    if counter == 1
        age_1 = age_init_208(i);
    else
        age_1 = age_2;
    end
    common_204_206 = 1/(9.307 + 8.8*exp(lambda_238*age_earth)-...
        exp(lambda_238*age_1));
    common_207_206 = common_204_206*(10.294 +...
        (8.8/U_ratio)*(exp(lambda_235*age_earth)-exp(lambda_235*age_1)));
    common_208_206 = common_204_206*(29.476 +...
        (3.8*8.8)*(exp(lambda_232*age_earth)-exp(lambda_232*age_1)));

    if counter == 1

```

```

        [pb_corr_ratios_208(i,:),pb_corr_ages_208(i,:),...
         pb_corr_ratios_se_208(i,:),pb_corr_ages_se_208(i,:),...
         est_204_206_208(i),est_204_206_se_208(i),f_208(i),...
         f_208_se(i)] = common_pb_corr_208(raw_average_ages(i,:),...
         raw_average_age_header, average_corr_sample_ratios(i,:),...
         corr_sample_ratios_header,common_Pb_header_208,age_1,...
         common_204_206,common_207_206,common_208_206,...
         lambda_232,lambda_235,lambda_238,se_corr_sample_ratios(i,:));
    else
        [pb_corr_ratios_208(i,:),pb_corr_ages_208(i,:),...
         pb_corr_ratios_se_208(i,:),pb_corr_ages_se_208(i,:),...
         est_204_206_208(i),est_204_206_se_208(i),f_208(i),f_208_se(i)]
        =.common_pb_corr_208(pb_corr_ages_208(i,:),...
        common_Pb_header_208,pb_corr_ratios_208(i,:),...
        common_Pb_header_208,common_Pb_header_208,age_1,...
        common_204_206,common_207_206,common_208_206,...
        lambda_232,lambda_235,lambda_238,pb_corr_ratios_se_208(i,:));
    end

    age_2 = pb_corr_ages_208(i,strmatch(age_type_208,common_Pb_header_208));
    t_diff = abs(age_1-age_2);
    counter = counter + 1;
    if counter > 20
        break
    end
end
end
close(h);

elseif common_Pb_number == 2
    common_204_206 = 0.0625;
    common_207_206 = 0.962;
    common_208_206 = 2.23;
    age_207 = raw_average_ages(:,strmatch(age_type_207,raw_average_age_header));
    age_208 = raw_average_ages(:,strmatch(age_type_208,raw_average_age_header));
    h = waitbar(0,'Doing common Pb correction');
    for i = 1:size(raw_average_ages,1)
        waitbar(i/size(raw_average_ages,1));
        [pb_corr_ratios_207(i,:),pb_corr_ages_207(i,:),pb_corr_ratios_se_207(i,:),...
         pb_corr_ages_se_207(i,:),est_204_206_207(i),est_204_206_se_207(i),...
         f_207(i), f_207_se(i)] = common_pb_corr_207(raw_average_ages(i,:),...
         raw_average_age_header,average_corr_sample_ratios(i,:),...
         corr_sample_ratios_header,common_Pb_header_207,age_207(i),...
         common_204_206,common_207_206,common_208_206,...

```

```

        lambda_232,lambda_235,lambda_238,se_corr_sample_ratios(i,:));
    [pb_corr_ratios_208(i,:),pb_corr_ages_208(i,:),pb_corr_ratios_se_208(i,:),...
     pb_corr_ages_se_208(i,:),est_204_206_208(i),est_204_206_se_208(i),...
     f_208(i),f_208_se(i)] = common_pb_corr_208(raw_average_ages(i,:),...
     raw_average_age_header,average_corr_sample_ratios(i,:),...
     corr_sample_ratios_header,common_Pb_header_208,age_208(i),...
     common_204_206,common_207_206,common_208_206,...
     lambda_232,lambda_235,lambda_238,se_corr_sample_ratios(i,:));
end
close(h);
elseif common_Pb_number == 3
%uicontrol to enter the needed ratio

    age_207 = raw_average_ages(:,strmatch(age_type_207,...
        raw_average_age_header));
    age_208 = raw_average_ages(:,strmatch(age_type_208,...
        raw_average_age_header));

    h = waitbar(0,'Doing common Pb correction');
    for i = 1:size(raw_average_ages,1)
        waitbar(i/size(raw_average_ages,1));

        [pb_corr_ratios_207(i,:),pb_corr_ages_207(i,:),pb_corr_ratios_se_207(i,:),...
         pb_corr_ages_se_207(i,:),est_204_206_207(i),est_204_206_se_207(i),...
         f_207(i),f_207_se(i)] = common_pb_corr_207(raw_average_ages(i,:),...
         raw_average_age_header, average_corr_sample_ratios(i,:),...
         corr_sample_ratios_header,common_Pb_header_207,age_207(i),...
         common_204_206,common_207_206,common_208_206,lambda_232,...
         lambda_235,lambda_238,se_corr_sample_ratios(i,:));

        [pb_corr_ratios_208(i,:),pb_corr_ages_208(i,:),pb_corr_ratios_se_208(i,:),...
         pb_corr_ages_se_208(i,:),est_204_206_208(i),est_204_206_se_208(i),...
         f_208(i),f_208_se(i)] = common_pb_corr_208(raw_average_ages(i,:),...
         raw_average_age_header,average_corr_sample_ratios(i,:),...
         corr_sample_ratios_header,common_Pb_header_208,age_208(i),...
         common_204_206,common_207_206,common_208_206,lambda_232,...
         lambda_235,lambda_238,se_corr_sample_ratios(i,:));
    end
    close(h);
end

%GENERATE ANU STYLE REPORT

```

```

%First have to calculate some new numbers for the export. These are the
%expected standard errors and MSWDs (both expected and actual)
%Expected SE's
counts_206 = sum(sample_counts_data(:,strmatch('Pb206',elements),:),3);
counts_238 = sum(sample_counts_data(:,strmatch('U238',elements),:),3);
ratio_206_238 = average_corr_sample_ratios(:,strmatch('206/238',...
    corr_sample_ratios_header));
expected_se_206_238 = (sqrt(1./counts_206 + 1./counts_238).*ratio_206_238)./...
    ((1+ratio_206_238)*lambda_238);

counts_208 = sum(sample_counts_data(:,strmatch('Pb208',elements),:),3);
counts_232 = sum(sample_counts_data(:,strmatch('Th232',elements),:),3);
ratio_208_232 = average_corr_sample_ratios(:,strmatch('208/232',...
    corr_sample_ratios_header));
expected_se_208_232 = (sqrt(1./counts_208 + 1./counts_232).*ratio_208_232)./...
    ((1+ratio_208_232)*lambda_232);

counts_207 = sum(sample_counts_data(:,strmatch('Pb207',elements),:),3);
ratio_207_206 = average_corr_sample_ratios(:,strmatch('207/206',...
    corr_sample_ratios_header));
age_207_206 = raw_average_ages(:,4);
factor_207_206 = 1./(U_ratio.*(exp(lambda_238*age_207_206) - 1) + ratio_207_206);
expected_se_207_206 = (sqrt(1./counts_207 + 1./counts_206).*ratio_207_206)./...
    (lambda_235*factor_207_206);

expected_se_207_235 = ratio_206_238.*ratio_207_206.*U_ratio.*...
    sqrt(1./counts_207 + 1./counts_206 + 1./counts_206 + 1./counts_238)./...
    (lambda_235*(1+ratio_206_238.*ratio_207_206.*U_ratio));

%Expected MSWD
N_1 = sample_stop - sample_start;
exp_mswd = 1 + 2*sqrt(2./N_1);

%MSWDs

%Strat with theor +/- per time slice
theor_err_206_time = 1./sqrt(sample_counts_data(:,strmatch('Pb206',elements),:));
theor_err_207_time = 1./sqrt(sample_counts_data(:,strmatch('Pb207',elements),:));
theor_err_238_time = 1./sqrt(sample_counts_data(:,strmatch('U238',elements),:));

theor_err_206_time = squeeze(theor_err_206_time);
theor_err_207_time = squeeze(theor_err_207_time);
theor_err_238_time = squeeze(theor_err_238_time);

```

```

%theor_err_206_time(1,1:(sample_stop(1)-sample_start(1)))
%Now get the ratios at each time slice
ratio_206_238_time =
    corr_sample_ratios(:,strmatch('206/238',corr_sample_ratios_header));
ratio_207_206_time =
    corr_sample_ratios(:,strmatch('207/206',corr_sample_ratios_header));

for i = 1:size(corr_sample_ratios,1);
    %Now calculate the weighted averages and e^2
    e_2_206_238(i) = {(1./(ratio_206_238_time{i}.*...
        sqrt(theor_err_206_time(i,1:(sample_stop(i)-sample_start(i))).^2...
        + theor_err_238_time(i,1:(sample_stop(i)-sample_start(i))).^2))).^2};
    x_e_2_206_238(i) = {ratio_206_238_time{i}.*e_2_206_238{i}};
    wtd_avg_num_206_238(i) = sum(x_e_2_206_238{i});
    wtd_avg_den_206_238(i) = sum(e_2_206_238{i});
    wtd_avg_206_238(i) = wtd_avg_num_206_238(i)/wtd_avg_den_206_238(i);
    delta_y_2_206_238(i) = {(ratio_206_238_time{i} - wtd_avg_206_238(i)).^2};
    delta_y_2_e_2_206_238(i) = {e_2_206_238{i}.*delta_y_2_206_238{i}};
    mswd_num(i) = sum(delta_y_2_e_2_206_238{i});
    mswd_206_238(i) = mswd_num(i)/(sample_stop(i)-sample_start(i));
    e_2_207_206(i) = {(1./(ratio_207_206_time{i}.*...
        sqrt(theor_err_206_time(i,1:(sample_stop(i)-sample_start(i))).^2 +
        theor_err_207_time(i,1:(sample_stop(i)-sample_start(i))).^2))).^2};
    x_e_2_207_206(i) = {ratio_207_206_time{i}.*e_2_207_206{i}};
    wtd_avg_num_207_206(i) = sum(x_e_2_207_206{i});
    wtd_avg_den_207_206(i) = sum(e_2_207_206{i});
    wtd_avg_207_206(i) = wtd_avg_num_207_206(i)/wtd_avg_den_207_206(i);
    delta_y_2_207_206(i) = {(ratio_207_206_time{i} - wtd_avg_207_206(i)).^2};
    delta_y_2_e_2_207_206(i) = {e_2_207_206{i}.*delta_y_2_207_206{i}};
    mswd_num(i) = sum(delta_y_2_e_2_207_206{i});
    mswd_207_206(i) = mswd_num(i)/(sample_stop(i)-sample_start(i));

end

%Now extract the variables needed for export into a cell matrix

%num2cell
output_data(1:size(corr_sample_ratios),1) = {'c'};
output_data(1:size(corr_sample_ratios),2) = sample_names;
output_data(1:size(corr_sample_ratios),3) =
    {zircon_std_age_file((1:size(zircon_std_age_file,2)-4))};
output_data(1:size(corr_sample_ratios),4) =
    num2cell(pb_corr_ages_207(:,strmatch('206/238',common_Pb_header_207)));
output_data(1:size(corr_sample_ratios),5) =

```



```

        num2cell(pb_corr_ages_se_207(:,strmatch('206/
238',common_Pb_header_207)));
output_data(1:size(corr_sample_ratios),6) = num2cell(expected_se_206_238);
output_data(1:size(corr_sample_ratios),7) = num2cell(f_207);
output_data(1:size(corr_sample_ratios),8) = num2cell(f_207_se);
output_data(1:size(corr_sample_ratios),9) = num2cell(f_208);
output_data(1:size(corr_sample_ratios),10) = num2cell(f_208_se);
output_data(1:size(corr_sample_ratios),11) = num2cell(average_corr_sample_ratios(:,...
    strmatch('206/238',corr_sample_ratios_header)));
output_data(1:size(corr_sample_ratios),12) = num2cell(se_corr_sample_ratios(:,...
    strmatch('206/238',corr_sample_ratios_header)));
output_data(1:size(corr_sample_ratios),13) = num2cell(average_corr_sample_ratios(:,...
    strmatch('207/235',corr_sample_ratios_header)));
output_data(1:size(corr_sample_ratios),14) = num2cell(se_corr_sample_ratios(:,...
    strmatch('207/235',corr_sample_ratios_header)));
output_data(1:size(corr_sample_ratios),15) = num2cell(average_corr_sample_ratios(:,...
    strmatch('207/206',corr_sample_ratios_header)));
output_data(1:size(corr_sample_ratios),16) = num2cell(se_corr_sample_ratios(:,...
    strmatch('207/206',corr_sample_ratios_header)));
output_data(1:size(corr_sample_ratios),17) = num2cell(1./...
    average_corr_sample_ratios(:,strmatch('206/238',corr_sample_ratios_header)));
output_data(1:size(corr_sample_ratios),18) = num2cell(se_corr_sample_ratios(:,...
    strmatch('206/238',corr_sample_ratios_header))./
average_corr_sample_ratios(:,...
    strmatch('206/238',corr_sample_ratios_header)).^2);
output_data(1:size(corr_sample_ratios),19) = num2cell(average_corr_sample_ratios(:,...
    strmatch('208/232',corr_sample_ratios_header)));
output_data(1:size(corr_sample_ratios),20) = num2cell(se_corr_sample_ratios(:,...
    strmatch('208/232',corr_sample_ratios_header)));
output_data(1:size(corr_sample_ratios),21) = num2cell(average_corr_sample_ratios(:,...
    strmatch('232/238',corr_sample_ratios_header)));
output_data(1:size(corr_sample_ratios),22) = num2cell(se_corr_sample_ratios(:,...
    strmatch('232/238',corr_sample_ratios_header)));
output_data(1:size(corr_sample_ratios),23) = num2cell(1./average_sample_gc_ratios(:,...
    strmatch('Zr91/Si29',corr_sample_gc_header)));
output_data(1:size(corr_sample_ratios),24) = num2cell(sample_start);
output_data(1:size(corr_sample_ratios),25) = num2cell(sample_stop);
output_data(1:size(corr_sample_ratios),26) = {'yes'};
output_data(1:size(corr_sample_ratios),27) = num2cell(raw_average_ages(:,...
    strmatch('206/238',raw_average_age_header)));
output_data(1:size(corr_sample_ratios),28) = num2cell(raw_average_ages(:,...
    strmatch('se 206/238',raw_average_age_header)));
output_data(1:size(corr_sample_ratios),29) = num2cell(expected_se_206_238);
output_data(1:size(corr_sample_ratios),30) = num2cell(raw_average_ages(:,...
    strmatch('207/235',raw_average_age_header)));

```

```

output_data(1:size(corr_sample_ratios),31) = num2cell(raw_average_ages(:,...
    strmatch('se 207/235',raw_average_age_header)));
output_data(1:size(corr_sample_ratios),32) = num2cell(expected_se_207_235);
output_data(1:size(corr_sample_ratios),33) = num2cell(raw_average_ages(:,...
    strmatch('207/206',raw_average_age_header)));
output_data(1:size(corr_sample_ratios),34) = num2cell(raw_average_ages(:,...
    strmatch('se 207/206',raw_average_age_header)));
output_data(1:size(corr_sample_ratios),35) = num2cell(expected_se_207_206);
output_data(1:size(corr_sample_ratios),36) = num2cell(raw_average_ages(:,...
    strmatch('208/232',raw_average_age_header)));
output_data(1:size(corr_sample_ratios),37) = num2cell(raw_average_ages(:,...
    strmatch('se 208/232',raw_average_age_header)));
output_data(1:size(corr_sample_ratios),38) = num2cell(expected_se_208_232);
output_data(1:size(corr_sample_ratios),39) = {common_Pb_type};
output_data(1:size(corr_sample_ratios),40) = num2cell(pb_corr_ages_208(:,...
    strmatch('206/238',common_Pb_header_208)));
output_data(1:size(corr_sample_ratios),41) = num2cell(pb_corr_ages_se_208(:,...
    strmatch('206/238',common_Pb_header_208)));
output_data(1:size(corr_sample_ratios),42) = num2cell(pb_corr_ages_208(:,...
    strmatch('207/235',common_Pb_header_208)));
output_data(1:size(corr_sample_ratios),43) = num2cell(pb_corr_ages_se_208(:,...
    strmatch('207/235',common_Pb_header_208)));
output_data(1:size(corr_sample_ratios),44) = num2cell(pb_corr_ages_208(:,...
    strmatch('207/206',common_Pb_header_208)));
output_data(1:size(corr_sample_ratios),45) = num2cell(pb_corr_ages_se_208(:,...
    strmatch('207/206',common_Pb_header_208)));
output_data(1:size(corr_sample_ratios),46) = num2cell(pb_corr_ages_207(:,...
    strmatch('206/238',common_Pb_header_207)));
output_data(1:size(corr_sample_ratios),47) = num2cell(pb_corr_ages_se_207(:,...
    strmatch('206/238',common_Pb_header_207)));
output_data(1:size(corr_sample_ratios),48) = num2cell(pb_corr_ages_207(:,...
    strmatch('208/232',common_Pb_header_207)));
output_data(1:size(corr_sample_ratios),49) = num2cell(pb_corr_ages_se_207(:,...
    strmatch('208/232',common_Pb_header_207)));
output_data(1:size(corr_sample_ratios),50) = num2cell(est_204_206_207);
output_data(1:size(corr_sample_ratios),51) = num2cell(est_204_206_se_207);
output_data(1:size(corr_sample_ratios),52) = ...
    final_geochem_ppm(:,strmatch('ppm U',element_names));
output_data(1:size(corr_sample_ratios),53) = ...
    final_geochem_ppm(:,strmatch('std error U',element_names));
output_data(1:size(corr_sample_ratios),54) = ...
    final_geochem_ppm(:,strmatch('ppm Th',element_names));
output_data(1:size(corr_sample_ratios),55) = ...
    final_geochem_ppm(:,strmatch('std error Th',element_names));
output_data(1:size(corr_sample_ratios),56) = ...

```

```

        final_geochem_ppm(:,strmatch('ppm P',element_names));
output_data(1:size(corr_sample_ratios),57) = ...
        final_geochem_ppm(:,strmatch('std error P',element_names));
output_data(1:size(corr_sample_ratios),58) =
        num2cell(cell2mat(final_geochem_ppm(:,...
        strmatch('ppm Hf',element_names)))./10000);
output_data(1:size(corr_sample_ratios),59) =
        num2cell(cell2mat(final_geochem_ppm(:,...
        strmatch('std error Hf',element_names)))./10000);
output_data(1:size(corr_sample_ratios),60) = num2cell(mswd_206_238);
output_data(1:size(corr_sample_ratios),61) = num2cell(exp_mswd);
output_data(1:size(corr_sample_ratios),62) = num2cell(mswd_207_206);
output_data(1:size(corr_sample_ratios),63) = {'no'};
output_data(1:size(corr_sample_ratios),64) = ...
        final_geochem_ppm(:,strmatch('ppm La',element_names));
output_data(1:size(corr_sample_ratios),65) = ...
        final_geochem_ppm(:,strmatch('ppm Ce',element_names));
output_data(1:size(corr_sample_ratios),66) = ...
        final_geochem_ppm(:,strmatch('ppm Nd',element_names));
output_data(1:size(corr_sample_ratios),67) = ...
        final_geochem_ppm(:,strmatch('ppm Sm',element_names));
output_data(1:size(corr_sample_ratios),68) = ...
        final_geochem_ppm(:,strmatch('ppm Eu',element_names));
output_data(1:size(corr_sample_ratios),69) = ...
        final_geochem_ppm(:,strmatch('ppm Dy',element_names));
output_data(1:size(corr_sample_ratios),70) = ...
        final_geochem_ppm(:,strmatch('ppm Lu',element_names));
output_data(1:size(corr_sample_ratios),71) = num2cell(pb_corr_ratios_208(:,...
        strmatch('206/238',common_Pb_header_208)));
output_data(1:size(corr_sample_ratios),72) = num2cell(pb_corr_ratios_se_208(:,...
        strmatch('206/238',common_Pb_header_208)));
output_data(1:size(corr_sample_ratios),73) = num2cell(pb_corr_ratios_208(:,...
        strmatch('207/235',common_Pb_header_208)));
output_data(1:size(corr_sample_ratios),74) = num2cell(pb_corr_ratios_se_208(:,...
        strmatch('207/235',common_Pb_header_208)));
output_data(1:size(corr_sample_ratios),75) = num2cell(pb_corr_ratios_208(:,...
        strmatch('207/206',common_Pb_header_208)));
output_data(1:size(corr_sample_ratios),76) = num2cell(pb_corr_ratios_se_208(:,...
        strmatch('207/206',common_Pb_header_208)));
output_data(1:size(corr_sample_ratios),77) = num2cell(pb_corr_ratios_207(:,...
        strmatch('206/238',common_Pb_header_207)));
output_data(1:size(corr_sample_ratios),78) = num2cell(pb_corr_ratios_se_207(:,...
        strmatch('206/238',common_Pb_header_207)));
output_data(1:size(corr_sample_ratios),79) = num2cell(pb_corr_ratios_207(:,...
        strmatch('208/232',common_Pb_header_207)));

```

```

output_data(1:size(corr_sample_ratios),80) = num2cell(pb_corr_ratios_se_207(:,...
    strmatch('208/232',common_Pb_header_207)));
output_data(1:size(corr_sample_ratios),81) = num2cell(average_date_corr_factor(:,...
    strmatch('207/206',corr_sample_ratios_header)));
output_data(1:size(corr_sample_ratios),82) = num2cell(std_average_date_corr_factor...
    (:,strmatch('207/206',corr_sample_ratios_header)));
output_data(1:size(corr_sample_ratios),83) = num2cell(average_date_corr_factor(:,...
    strmatch('206/238',corr_sample_ratios_header)));
output_data(1:size(corr_sample_ratios),84) =
num2cell(std_average_date_corr_factor(:,...
    strmatch('206/238',corr_sample_ratios_header)));
output_data(1:size(corr_sample_ratios),85) = num2cell(average_date_corr_factor(:,...
    strmatch('208/232',corr_sample_ratios_header)));
output_data(1:size(corr_sample_ratios),86) = num2cell...
    (std_average_date_corr_factor(:,strmatch('208/
232',corr_sample_ratios_header)));
output_data(1:size(corr_sample_ratios),87) = num2cell(average_date_corr_factor(:,...
    strmatch('232/238',corr_sample_ratios_header)));
output_data(1:size(corr_sample_ratios),88) = num2cell...
    (std_average_date_corr_factor(:,strmatch('232/
238',corr_sample_ratios_header)));
output_data(1:size(corr_sample_ratios),89) = num2cell(mswd_206_238);
output_data(1:size(corr_sample_ratios),90) = num2cell(exp_mswd);
output_data(1:size(corr_sample_ratios),91) = num2cell(mswd_207_206);
output_data(1:size(corr_sample_ratios),92) = num2cell(exp_mswd);

```

```

header_filename = 'anu_report_header.csv';
fid = fopen(header_filename);
output_header_string = fgetl(fid);
fclose(fid);
output_columns = strread(output_header_string,'%q','delimiter',' ','');
output_columns = output_columns';

```

```

output_header = 'Final data ready to import into the ANU summary Excel sheet';

```

```

output_filename = [pwd 'final_data_' run_date(1:11) '.xls'];

```

```

xlswrite(output_data,output_header,output_columns,output_filename);

```

```

% — Executes on button press in pushbutton9.
function pushbutton9_Callback(hObject, eventdata, handles)
% hObject    handle to pushbutton9 (see GCBO)
% eventdata  reserved - to be defined in a future version of MATLAB

```

```

% handles    structure with handles and user data (see GUIDATA)
clear all

[filename,num_data,col_names,samples] = xls_parse_zircon('Pick file with zircon data
created by previous step');
samples(1) = [];

if strmatch('La139',col_names) > 0;
    La_col = strmatch('La139',col_names);
    Ce_col = strmatch('Ce140',col_names);
    Nd_col = strmatch('Nd146',col_names);
    Sm_col = strmatch('Sm147',col_names);
    Eu_col = strmatch('Eu153',col_names);
    Dy_col = strmatch('Dy163',col_names);
    Lu_col = strmatch('Lu175',col_names);
else
    La_col = strmatch('ppm La',col_names);
    Ce_col = strmatch('ppm Ce',col_names);
    Nd_col = strmatch('ppm Nd',col_names);
    Sm_col = strmatch('ppm Sm',col_names);
    Eu_col = strmatch('ppm Eu',col_names);
    Dy_col = strmatch('ppm Dy',col_names);
    Lu_col = strmatch('ppm Lu',col_names);
end

REE = {'La','Ce','Nd','Sm','Eu','Dy','Lu'};
La = strmatch('La',REE);
Ce = strmatch('Ce',REE);
Nd = strmatch('Nd',REE);
Sm = strmatch('Sm',REE);
Eu = strmatch('Eu',REE);
Dy = strmatch('Dy',REE);
Lu = strmatch('Lu',REE);

crust(La) = 16;
crust(Ce) = 33;
crust(Nd) = 16;
crust(Sm) = 3.5;
crust(Eu) = 1.1;
crust(Dy) = 3.7;
crust(Lu) = 0.3;
crust_mat = repmat(crust,size(samples,1),1);

strain_fact(La) = 0.05393;

```

```

strain_fact(Ce) = 0.04783;
strain_fact(Nd) = 0.03688;
strain_fact(Sm) = 0.02854;
strain_fact(Eu) = 0.02530;
strain_fact(Dy) = 0.016867;
strain_fact(Lu) = 0.0087401;

comp(:,La) = num_data(:,La_col);
comp(:,Ce) = num_data(:,Ce_col);
comp(:,Nd) = num_data(:,Nd_col);
comp(:,Sm) = num_data(:,Sm_col);
comp(:,Eu) = num_data(:,Eu_col);
comp(:,Dy) = num_data(:,Dy_col);
comp(:,Lu) = num_data(:,Lu_col);

comp_norm = comp./crust_mat;

strain_vect = [strain_fact(Lu),strain_fact(Dy),strain_fact(Sm)];
strain_vect_b = [strain_fact(Lu),strain_fact(Dy),strain_fact(Nd)];
%strain_vect_c = [strain_fact(Lu),strain_fact(Sm)];
comp_mat = [comp_norm(:,Lu),comp_norm(:,Dy),comp_norm(:,Sm)];
comp_mat_b = [comp_norm(:,Lu),comp_norm(:,Dy),comp_norm(:,Nd)];
%comp_mat_c = [comp_norm(:,Lu),comp_norm(:,Sm)];
strain_mat = repmat(strain_vect,size(comp_mat,1),1);

for i = 1:size(comp_mat,1)
    if comp(i,Sm) > 0;
        p(i,:) = polyfit(strain_vect,log(comp_mat(i,:)),1);
    else;
        p(i,:) = polyfit(strain_vect_b,log(comp_mat_b(i,:)),1);
    end
    Ce_three(i) = exp(polyval(p(i,:),strain_fact(Ce)));
end

Ce_four = comp_norm(:,Ce)';

Ce_ratio = Ce_four./Ce_three;
Ce_ratio = Ce_ratio';

col_1 = {'Sample'};
last_col = {'Ce4+/Ce3+'};
export_col_names = horzcat(col_1,REE,last_col);
export_data = horzcat(samples,num2cell(comp),num2cell(Ce_ratio));

export_header = 'REE data with Ce4+/Ce3+ relative to average crust';

```

```
export_filename = [pwd '\REE_data.xls'];
```

```
xlswrite(export_data,export_header,export_col_names,export_filename);
```

User interaction control : text_box_list.m

```
function needed_data = checkbox_list(list,title,suggested_default)
```

```
%Makes a list of checkboxes and returns the checked boxes
```

```
figure('Name',title);
```

```
for i=1:length(list);
```

```
    position_index = 1-i*(1./((length(list))+1));
```

```
    if ismember(i,suggested_default)==1;
```

```
        h(i)=uicontrol('Style','checkbox','Value',1,'String',list{i},...  
            'Units','normalized','Position',[0,position_index,0.2,0.04]);
```

```
    else
```

```
        h(i)=uicontrol('Style','checkbox','String',list{i},...  
            'Units','normalized','Position',[0,position_index,0.2,0.04]);
```

```
    end
```

```
end
```

```
%Stop program until user selects the finished box in the graphical interface
```

```
h(i+1)=uicontrol('Style','checkbox','String','finished','Units','normalized','...  
    Position',[0,0,0.2,0.04]);
```

```
waitfor(h(i+1),'Value',1);
```

```
%Retrieve the results of the checkboxes
```

```
for i=1:length(list);
```

```
    list_index(i) = get(h(i),'Value');
```

```
end
```

```
%close the figure
```

```
close
```

```
%Retrieve the masses of interest
```

```
needed_data = find(list_index);
```

Find analysis start/end: find_start.m

```
function [an_start,an_stop,bg_start,bg_stop] = find_start(data,needed_elements)
```

```
clear data_temp;
```

```

data_temp = data + 1;
prod1 = prod(data_temp(:,needed_elements,:),2);
prod1=squeeze(prod1);
ratio = (prod1(:,3:size(prod1,2))./prod1(:,1:(size(prod1,2)-2)))';
[start_x start_y] = find(ratio>=100000);
clear data_temp;

for j=1:size(data,1)
    needed_x = start_x(find(start_y==j));
    an_start(j) = needed_x(1) + 4;
    counter = 1;
    for i=an_start(j):(size(data,3)-2)
        if prod1(j,(an_start(j)))./prod1(j,i)>10000
            test_data(j,i)=prod1(j,(an_start(j)))./prod1(j,i);
            counter = counter + 1;
            if counter > 5
                an_stop(j) = i-5;
                break
            end
        else
            an_stop(j)=size(data,3);
        end
    end
    bg_start(j) = 1;
    bg_stop(j) = needed_x(1) - 4;
    clear needed_x;
end

```

Subtract background: background_subtract.m

```
function calc_data = background_subtraction(data,an_start,an_stop,bg_start,bg_stop)
```

```

max_time = max(an_stop-an_start);
time = an_stop-an_start;
for j=1:size(data,1)
    for i=an_start(j):(an_start(j)+max_time)
        if i < an_start(j)+time(j)
            calc_data(j,:,i+1-an_start(j)) = data(j,:,i);
        else
            calc_data(j,:,i+1-an_start(j)) = 0;
        end
    end
end
end
save calc.mat calc_data
for i=1:size(data,1)

```



```

    bg(i,:) = squeeze(mean(data(i,:,bg_start(i):bg_stop(i)),3));
end

```

```

bg = repmat(bg,[1 1 size(calc_data,3)]);
bg(:,1,:)=0;

```

```

calc_data = calc_data - bg;
calc_data=calc_data.*(calc_data>0);

```

User interaction control: text_box_list.m

```

function needed_data_str = textbox_list(list,title,suggested_default,comments)
%associates number values to a list of text values

```

```

figure('Name',title);
for i=1:length(list);
    h1.text1(i)=uicontrol('Style','text','String',list(i),'Units','normalized',...
        'Position',[.05,1-i/(length(list)+1),0.1,.04]);
    h2.edit1(i)=uicontrol('Style','edit','String',suggested_default,'Units','normalized',...
        'Position',[.16,1-i/(length(list)+1),0.1,.04]);
end
h1.checkbox1=uicontrol('Style','checkbox','String','finished','Units','normalized',...
    'Position',[0,0,0.2,0.04]);
h1.text2 = uicontrol('Style','text','String',comments,'Units','normalized',...
    'Position',[0.5,0.5,0.4,.04]);
waitfor(h1.checkbox1,'Value',1);
needed_data_str=get(h2.edit1,'String');
close;

```

Calculate ratios for age calculation: date_ratios_calc.m

```

function ratios = date_ratio_calc(data,elements,start_analysis)

```

```

%Define the masses as variables
time = strmatch('Time',elements);
Si29 = strmatch('Si29',elements);
P31 = strmatch('P31',elements);
Zr91 = strmatch('Zr91',elements);
Pb206 = strmatch('Pb206',elements);
Pb207 = strmatch('Pb207',elements);
Pb208 = strmatch('Pb208',elements);
Th232 = strmatch('Th232',elements);
U235 = strmatch('U235',elements);
U238 = strmatch('U238',elements);

```

```

for i=1:size(data,1)
    scan_numbers(i,:)= start_analysis(i):(start_analysis(i)+size(data,3)-1);
end

%Calculate standard ratios
ratios(:,1,:)= squeeze(data(:,1,:));
ratios(:,2,:)= scan_numbers;
ratios(:,3,:)= squeeze(data(:,Pb207,:)./data(:,Pb206,:));
ratios(:,4,:)= squeeze(data(:,Pb206,:)./data(:,U238,:));
ratios(:,5,:)= squeeze(data(:,Pb208,:)./data(:,Th232,:));
ratios(:,6,:)= squeeze(data(:,Th232,:)./data(:,U238,:));
ratios(:,7,:)= squeeze(data(:,Zr91,:)./data(:,Si29,:));
ratios(:,8,:)= squeeze(data(:,P31,:)./data(:,Si29,:));
ratios(:,9,:)= squeeze(data(:,Pb208,:)./data(:,Pb206,:));

User interface for selecting new analysis start/end: user_entered_start.m
function [an_start,an_stop,bg_start,bg_stop]=user_entered_start(file_names,...
    ratios,data,dating_ratios_header,def_an_start,def_an_stop,def_bg_start,...
    def_bg_stop,elements)

colors={'r','g','b','c','m','y','k'};

for j=1:size(ratios,1)
    figure;
    set(gcf,'Units','normalized','Position',[0,-.05,1,1]);
    subplot(1,2,1);
    hold on
    grid on
    for i=3:size(ratios,2)
        plot(squeeze(ratios(j,2,:)),squeeze(ratios(j,i,:)),colors{i-2})
        ylim([0 1])
    end
    legend(dating_ratios_header{3:size(ratios,2)})
    subplot(1,2,2);
    hold on
    grid on
    for k=1:4
        plot(squeeze(data(j,k,:)),colors{k})
    end
    set(gca,'YScale','log')
    legend(elements{1:4})

    h1.textedit1=uicontrol('Style','edit','String',def_bg_start(j),'Units','normalized',...

```

```

        'Position',[.11,.05,0.1,.03]);
h1.text1=icontrol('Style','text','String','Bg start','Units','normalized',...
    'Position',[0,.05,0.1,.03]);
h1.textedit2=icontrol('Style','edit','String',def_bg_stop(j),'Units','normalized',...
    'Position',[.33,.05,0.1,.03]);
h1.text2=icontrol('Style','text','String','Bg stop','Units','normalized',...
    'Position',[.22,0.05,0.1,.03]);
h1.textedit3=icontrol('Style','edit','String',def_an_start(j),'Units',...
    'normalized','Position',[.55,.05,0.1,.03]);
h1.text3=icontrol('Style','text','String','Analysis start','Units','normalized',...
    'Position',[.44,0.05,0.1,.03]);
h1.textedit4=icontrol('Style','edit','String',def_an_stop(j),'Units','normalized',...
    'Position',[.77,.05,0.1,.03]);
h1.text4=icontrol('Style','text','String','Analysis stop','Units','normalized',...
    'Position',[0.66,0.05,0.1,.03]);
h1.checkbox1=icontrol('Style','checkbox','String','next','Units','normalized',...
    'Position',[0,0,0.2,0.03]);
h1.checkbox2=icontrol('Style','checkbox','String','use default for remaining
grains',...
    'Units','normalized','Position',[.5,0,0.4,0.03]);
h1.text5=icontrol('Style','text','String',file_names{j},'Units','normalized',...
    'Position',[0,0.95,0.2,.03]);
waitfor(h1.checkbox1,'Value',1);
bg_start(j) = str2num(get(h1.textedit1,'String'));
bg_stop(j) = str2num(get(h1.textedit2,'String'));
an_start(j) = str2num(get(h1.textedit3,'String'));
an_stop(j) = str2num(get(h1.textedit4,'String'));
cont_enter = get(h1.checkbox2,'Value');
close;
if cont_enter == 1
    bg_start(j+1:size(ratios,1)) = def_bg_start(j+1:size(ratios,1));
    bg_stop(j+1:size(ratios,1)) = bg_stop(j+1:size(ratios,1));
    an_start(j+1:size(ratios,1)) = an_start(j+1:size(ratios,1));
    an_stop(j+1:size(ratios,1)) = an_stop(j+1:size(ratios,1));
    break
end
end
end

```

Selecting fit for drift and depth correction: drift_plot.m

```
function [corr_type,corr_factor] = drift_plot(ratios,files,header,valid_data)
```

```

clear data_temp;
%Retrieve the time stamp of the files
file_dates={files.date};

```

```

%Convert time stamp into a number that MatLab can plot
for i=1:size(file_dates,2);
    data_temp(i)=datenum(file_dates{i});
end
file_numbers = data_temp';
needed_data = [];

for j=3:size(ratios,2)
    start_loop = 0;
    clear data_temp;
    i=1;
    % Determine where there are 4 or more standards with valid data
    for i=1:size(ratios,3)
        if size(valid_data{i},1)>=4
            needed_data(i) = 1;
        else
            break;
        end
    end
end
needed_size = size(needed_data,2);
% Loop through where there are 4 or more standards plotting the data
% and allowing the user to choose the fit. There is the option to apply
% a single fit to all depths or to change the fit with depth.
for i = 1:needed_size;
    plot_ratio = ratios(valid_data{i},j,i);
    x=file_numbers(valid_data{i});
    y=plot_ratio;
    % Average (ie linear fit forcing the slope to be 0)
    fit_1 = polyfit(x,y,0);
    % Linear fit
    fit_2 = polyfit(x,y,1);
    % Parabolic fit
    fit_3 = polyfit(x,y,2);
    % Exponential fit
    fit_4 = polyfit(x,log10(y),1);
    % Makes xx have 100 steps to make a continuous curve for the graph of the fit
    xx = min(x):((max(x)-min(x))/100):max(x);
    yy1 = polyval(fit_1,xx);
    yy2 = polyval(fit_2,xx);
    yy3 = polyval(fit_3,xx);
    yy4 = 10.^polyval(fit_4,xx);
    fit_types = {'No fit needed';'Linear fit';'Quadratic fit';'Exponential Fit'};
    %Sets up figure with GUI allowing user to pick fit and whether to
    %apply to all depths or just the current one
    figure(1);

```

```

set(1,'Units','normalized','Position',[0.0234,0.3594,0.4004,0.4010]);
h1.listbox1=uicontrol('Style','listbox','String',fit_types,'Units',...
    'normalized','Position',[0,.75,0.5,0.2]);
h1.listbox2=uicontrol('Style','listbox','String',...
    {'View next sample depth';'Apply fit to remaining depths'},'Units',...
    'normalized','Position',[0,0.5,0.5,0.2]);
h1.checkbox1=uicontrol('Style','checkbox','String','Finished','Units',...
    'normalized','Position',[0,0,0.2,0.04]);
%Creates figure with the fits plotted
figure(2);
set(2,'Units','normalized','Position',[0.4404,0.2747,0.5469,0.5469]);
scatter(x,y)
datetick('x',13)
hold on
%Add curve fits of the data onto the graph
plot(xx,yy1,'-r');
plot(xx,yy2,'-g');
plot(xx,yy3,'-b');
plot(xx,yy4,'-c');
legend(fit_types);

xlabel('Time')
ylabel(header{j});

waitfor(h1.checkbox1,'Value',1);
close(2);
%Gets the fit type
type = get(h1.listbox1,'Value');
%Has a value of 1 if the user wants to continue viewing the data or
%2 to apply the fit to all depths
cont_enter = get(h1.listbox2,'Value');
%Breaks loop if the user selects apply value to all depths
if cont_enter == 2;
start_loop = i+1;
close(1);
break;
else;
corr_type(i,j) = {fit_types{type}};
corr_factor(i,j) = {eval(['fit_' num2str(type)])};
close(1);
end

end
if start_loop > 0;

```

```

    for k = start_loop:needed_size
        corr_type(k,j) = {fit_types{type}};
        plot_ratio = ratios(valid_data{k},j,k);
        x=file_numbers(valid_data{k});
        y=plot_ratio;
        % Average (ie linear fit forcing the slope to be 0)
        if type == 1;
            % Average (ie linear fit forcing the slope to be 0)
            fit_1 = polyfit(x,y,0);
        elseif type == 2;
            % Linear fit
            fit_2 = polyfit(x,y,1);
        elseif type == 3;
            % Parabolic fit
            fit_3 = polyfit(x,y,2);
        elseif type == 4;
            % Exponential fit
            fit_4 = polyfit(x,log10(y),1);
        end
        corr_factor(k,j) = {eval(['fit_' num2str(type)])};
    end
end
end

```

Depth correction w/o drift correction: drift_plot_fixed.m

```

function [corr_type,corr_factor] = drift_plot_fixed(ratios,files,header,valid_data)
warning off MATLAB:polyfit:RepeatedPointsOrRescale
clear data_temp;
%Retrieve the time stamp of the files
file_dates={files.date};
%Convert time stamp into a number that MatLab can plot
for i=1:size(file_dates,2);
    data_temp(i)=datenum(file_dates{i});
end
file_numbers = data_temp';

```

```

for j=3:size(ratios,2)
    clear data_temp;
    i=1;
    %Setup a loop that will curve fit the ratios at all depths in the
    %zircon as long as there are 4 or more standards with valid data
    while size(valid_data{i},1) >= 4;
        plot_ratio = ratios(valid_data{i},j,i);
    end
end

```

```

        x=file_numbers(valid_data{i});
        y=plot_ratio;
        fit_1 = polyfit(x,y,0);
        fit_types = {'No fit needed'};

        corr_type(i,j) = {fit_types{1}};
        corr_factor(i,j) = {fit_1};
        i = i+1;
    end
end

```

Depth and drift correction for age data: depth_drift_correction.m

```

function [corr_ratios,corr_factor] = depth_drift_correction(uncorr_ratios,...
    zircon_drift_type,zircon_drift_correction,an_start,an_stop,header,file_number,...
    ratios,standard_ratios,glass_drift_type,glass_drift_correction);

```

```

warning off MATLAB:polyfit:RepeatedPointsOrRescale
uncorr_ratios = squeeze(uncorr_ratios);

```

```

scan_numbers = 1:(an_stop-an_start);

```

```

% BUILD CORRECTION VECTOR FOR GIVEN SAMPLE

```

```

%for loop through the drift correction evaluating at current file number

```

```

for i = 1:size(zircon_drift_correction,1)

```

```

    for j = 1:size(ratios,2)

```

```

        check_1 = strcmp('232/238',ratios{j});

```

```

        check_2 = strcmp('208/206',ratios{j});

```

```

        if check_1 || check_2;

```

```

            %do nothing

```

```

        else

```

```

            if strcmp(glass_drift_type,'Exponential Fit') == 1;

```

```

                std_depth_profile_zircon(i,j) = 10.^polyval(zircon_drift_correction...
                    {i,strmatch(ratios{j},header)},file_number);

```

```

            else

```

```

                std_depth_profile_zircon(i,j) = polyval(zircon_drift_correction...
                    {i,strmatch(ratios{j},header)},file_number);

```

```

            end

```

```

        end

```

```

    end

```

```

end

```

```

for i = 1:size(glass_drift_correction,1)

```

```

    for j = 1:size(ratios,2)

```

```

        check_1 = strcmp('232/238',ratios{j});

```

```

check_2 = strcmp('208/206',ratios{j});
if check_1 || check_2;
    if strcmp(glass_drift_type,'Exponential Fit') == 1;
        std_depth_profile_glass(i,j) = 10.^polyval(glass_drift_correction...
            {i,strmatch(ratios{j},header)},file_number);
    else
        std_depth_profile_glass(i,j) = polyval(glass_drift_correction...
            {i,strmatch(ratios{j},header)},file_number);
    end
end
else
    end
end
end

%curve fit the results of the evaluations from the previous step
for j = 1:size(ratios,2)
    check_1 = strcmp('232/238',ratios{j});
    check_2 = strcmp('208/206',ratios{j});
    if check_1 || check_2
        y = squeeze(std_depth_profile_glass(:,j));
        x = 1:size(y,1);
        x=x';
        n = 4;
        poly = polyfit(x,y,n);
        corr_ratios(:,j) = {uncorr_ratios(strmatch(ratios{j},header),...
            1:(an_stop-an_start))*standard_ratios(j)./...
            polyval(poly,scan_numbers)};
        corr_factor(:,j) = {standard_ratios(j)./polyval(poly,scan_numbers)};
    else
        y = squeeze(std_depth_profile_zircon(:,j));
        x = 1:size(y,1);
        x=x';
        n = 4;
        poly = polyfit(x,y,n);
        corr_ratios(:,j) = {uncorr_ratios(strmatch(ratios{j},header),...
            1:(an_stop-an_start))*standard_ratios(j)./polyval(poly,scan_numbers)};
        corr_factor(:,j) = {standard_ratios(j)./polyval(poly,scan_numbers)};
    end
end

%Correction factors
corr_ratios(:,(size(ratios,2)+1)) = {(corr_ratios{:,1}.*corr_ratios{:,2})*137.88};
corr_factor(:,(size(ratios,2)+1)) = {(corr_factor{:,1}.*corr_factor{:,2})};
%divide the uncorrected ratios by the evaluation of the curve fir from the

```


%previous step

Depth and drift correction for geochemistry data: depth_drift_correction_glass.m

```
function [corr_ratios,corr_factor] = depth_drift_correction_glass(uncorr_ratios,...  
    drift_type,drift_correction,an_start,an_stop,header,file_number,ratios,...  
    standard_ratios);
```

warning off MATLAB:polyfit:RepeatedPointsOrRescale

```
uncorr_ratios = squeeze(uncorr_ratios);
```

```
scan_numbers = 1:(an_stop-an_start);
```

%START WITH BUILDING CORRECTION VECTOR FOR GIVEN SAMPLE

%for loop through the drift correction evaluating at current file number

```
for i = 1:size(drift_correction,1)  
    for j = 1:size(ratios,2)  
        if strcmp(ratios{j},'Si29/Si29') == 1  
            std_depth_profile(i,j) = 1;  
        elseif strcmp(drift_type,'Exponential Fit') == 1;  
            std_depth_profile(i,j) = 10.^polyval(drift_correction...  
                {i,strmatch(ratios{j},header)},file_number);  
        else  
            std_depth_profile(i,j) = polyval(drift_correction...  
                {i,strmatch(ratios{j},header)},file_number);  
        end  
    end  
end
```

```
save test.mat std_depth_profile;
```

%curve fit the results of the evaluations from the previous step

```
for j = 1:size(ratios,2)  
    y = squeeze(std_depth_profile(:,j));  
    x = 1:size(y,1);  
    x=x';  
    n = 4;  
    poly = polyfit(x,y,n);  
    corr_ratios(:,j) = {uncorr_ratios(strmatch(ratios{j},header),...  
        1:(an_stop-an_start))*standard_ratios(j)./polyval(poly,scan_numbers)};  
    corr_factor(:,j) = {standard_ratios(j)./polyval(poly,scan_numbers)};  
end
```

Calculate ages at each time slice: age_calc.m

```
function ages=age_calc(ratios,lambdas,header);
```

```

ratios=squeeze(ratios);

rat_206_238 = ratios{1,strmatch('206/238',header)};
rat_207_235 = ratios{1,strmatch('207/235',header)};
rat_208_232 = ratios{1,strmatch('208/232',header)};
rat_207_206 = ratios{1,strmatch('207/206',header)};

ages(:,1) = log(rat_206_238' + 1)./lambdas{strmatch('U238',lambdas(:,1)),2};
ages(:,2) = log(rat_207_235' + 1)./lambdas{strmatch('U235',lambdas(:,1)),2};
ages(:,3) = log(rat_208_232' + 1)./lambdas{strmatch('Th232',lambdas(:,1)),2};

U_ratio = 137.88;
lambda_238 = lambdas{strmatch('U238',lambdas(:,1)),2};
lambda_235 = lambdas{strmatch('U235',lambdas(:,1)),2};

for i=1:size(rat_207_206,2);
    tinit=ages(i,1);
    ratio_temp = rat_207_206(i);

    t1=log(U_ratio*ratio_temp*(exp(lambda_238*tinit)-1)+1)/lambda_235;
    t2=log(U_ratio*ratio_temp*(exp(lambda_238*t1)-1)+1)/lambda_235;
    delta_t = abs(t1-t2);
    while delta_t > 0.1
        t1=log(U_ratio*ratio_temp*(exp(lambda_238*t2)-1)+1)/lambda_235;
        t2=log(U_ratio*ratio_temp*(exp(lambda_238*t1)-1)+1)/lambda_235;
        delta_t = abs(t1-t2);
    end
    ages(i,4)=t1;
end

Common Pb correction using 207Pb: common_pb_corr_207.mat
function
[corr_ratios,corr_ages,corr_ratios_se,corr_ages_se,est_204_206,est_204_206_se,...
    correction_ratio,correction_ratio_se] = common_pb_corr_207(uncorr_ages,...
    uncorr_age_header,... uncorr_ratios,uncorr_ratios_header,corr_header_207,...
    age,common_204_206,common_207_206,common_208_206,...
    lambda_232,lambda_235,lambda_238,se_uncorr_ratios)

%%Function for calculating common Pb corrected ratios and ages using Pb
%%207

U_ratio = 137.88;

exp_rad_207_206 = (1/U_ratio)*(exp(lambda_235*age)-1)/(exp(lambda_238*age)-1);

```

```

%the variable corr_ratio is (measured ratio-expected)/(common-expected)
correction_ratio = (uncorr_ratios(strmatch('207/206',uncorr_ratios_header))...
    -exp_rad_207_206)/(common_207_206-exp_rad_207_206);
%Set correction ratio to zero if it is negative
pos_check = correction_ratio > 0;
correction_ratio = correction_ratio * pos_check;

correction_ratio_se = sqrt((common_207_206-exp_rad_207_206)^2 *
se_uncorr_ratios(strmatch('207/206',uncorr_ratios_header))^2)/...
    (common_207_206 - exp_rad_207_206)^2;

%Correct the ratios for common Pb and calculate standard errors
corr_ratios(strmatch('206/238',corr_header_207)) = (1-correction_ratio)*...
    uncorr_ratios(strmatch('206/238',uncorr_ratios_header));
corr_ratios(strmatch('208/232',corr_header_207)) = (1-correction_ratio)*...
    uncorr_ratios(strmatch('208/232',uncorr_ratios_header));
corr_ratios(strmatch('238/206',corr_header_207)) =
    1/corr_ratios(strmatch('206/238',corr_header_207));
corr_ratios(strmatch('207/206',corr_header_207)) =
    uncorr_ratios(strmatch('207/206',uncorr_ratios_header));

corr_ratios_se(strmatch('206/238',corr_header_207)) = sqrt((1-correction_ratio^2)*...
    se_uncorr_ratios(strmatch('206/238',uncorr_ratios_header))^2+...
    uncorr_ratios(strmatch('206/238',uncorr_ratios_header))^2*...
    correction_ratio_se^2);
corr_ratios_se(strmatch('208/232',corr_header_207)) = sqrt((1-correction_ratio^2)*...
    se_uncorr_ratios(strmatch('208/232',uncorr_ratios_header))^2+...
    uncorr_ratios(strmatch('208/232',uncorr_ratios_header))^2*...
    correction_ratio_se^2);
corr_ratios_se(strmatch('238/206',corr_header_207)) = ...
    corr_ratios_se(strmatch('206/238',corr_header_207))/...
    corr_ratios(strmatch('206/238',corr_header_207))^2;
corr_ratios_se(strmatch('207/206',corr_header_207)) =...
    se_uncorr_ratios(strmatch('207/206',uncorr_ratios_header));

%Calculate ages using corrected ratios and calculate standard errors
corr_ages(strmatch('206/238',corr_header_207)) = ...
    log(1+corr_ratios(strmatch('206/238',corr_header_207)))/lambda_238;
corr_ages(strmatch('208/232',corr_header_207)) = ...
    log(1+corr_ratios(strmatch('208/232',corr_header_207)))/lambda_232;

corr_ages_se(strmatch('206/238',corr_header_207)) =...
    corr_ratios_se(strmatch('206/238',corr_header_207))/...

```

```

        ((1+corr_ratios(strmatch('206/238',corr_header_207)))*lambda_238);
corr_ages_se(strmatch('208/232',corr_header_207))=...
    corr_ratios_se(strmatch('208/232',corr_header_207))/...
    ((1+corr_ratios(strmatch('208/232',corr_header_207)))*lambda_232);

```

```

% Estimate the percentage of common Pb and calculate standard errors
percent_common(strmatch('206/238',corr_header_207))=...
    (uncorr_ratios(strmatch('206/238',uncorr_ratios_header))/...
    corr_ratios(strmatch('206/238',corr_header_207)) - 1);
percent_common(strmatch('208/232',corr_header_207))=...
    (uncorr_ratios(strmatch('208/232',uncorr_ratios_header))/...
    corr_ratios(strmatch('208/232',corr_header_207)) - 1);

```

```

percent_common_se(strmatch('206/238',corr_header_207)) = ...
    percent_common(strmatch('206/238',corr_header_207))*...
    sqrt((corr_ratios_se(strmatch('206/238',corr_header_207))/...
    corr_ratios(strmatch('206/238',corr_header_207)))^2+...

```

```

    (se_uncorr_ratios(strmatch('206/238',uncorr_ratios_header))/...
    uncorr_ratios(strmatch('206/238',uncorr_ratios_header)))^2);
percent_common_se(strmatch('208/232',corr_header_207)) = ...
    percent_common(strmatch('208/232',corr_header_207))*...
    sqrt((corr_ratios_se(strmatch('208/232',corr_header_207))/...
    corr_ratios(strmatch('208/232',corr_header_207)))^2+...
    (se_uncorr_ratios(strmatch('208/232',uncorr_ratios_header))/...
    uncorr_ratios(strmatch('208/232',uncorr_ratios_header)))^2);

```

```

% Estimate the 204/206 ratio and calculate a standard error
est_204_206 = common_204_206*...
    percent_common(strmatch('206/238',corr_header_207));
est_204_206_se = est_204_206*...
    percent_common_se(strmatch('206/238',corr_header_207))/...
    percent_common(strmatch('206/238',corr_header_207));

```

```

Common Pb correction using 208Pb: common_Pb_corr_208.m
function [corr_ratios,corr_ages,corr_ratios_se,corr_ages_se,est_204_206,...
    est_204_206_se,correction_ratio,correction_ratio_se] = ...
    common_pb_corr_208(uncorr_ages,uncorr_age_header,...
    uncorr_ratios,uncorr_ratios_header,corr_header_208,age,...
    common_204_206,common_207_206,common_208_206,...
    lambda_232,lambda_235,lambda_238,se_uncorr_ratios)

```

```

%%Function for calculating common Pb corrected ratios and ages using Pb208

```

```

%Headers for reference during programming:
%common_Pb_header_208 = {'206/238','207/206','207/235','238/206'};
% age_list = {'207/206';'206/238'}
U_ratio = 137.88;

exp_rad_208_206 = uncorr_ratios(strmatch('232/238',uncorr_ratios_header))*...
    (exp(lambda_232*age)-1)/(exp(lambda_238*age)-1);

%the variable corr_ratio is (measured ratio-expected)/(common-expected)
correction_ratio = (uncorr_ratios(strmatch('208/206',uncorr_ratios_header))-...
    exp_rad_208_206)/(common_208_206-exp_rad_208_206);
%Set correction ratio to zero if it is negative
pos_check = correction_ratio > 0;
correction_ratio = correction_ratio * pos_check;

correction_ratio_se = sqrt((common_208_206-exp_rad_208_206)^2 *
se_uncorr_ratios(strmatch('208/206',uncorr_ratios_header))^2)/...
    (common_208_206 - exp_rad_208_206)^2;

%Correct the ratios for common Pb and calculate standard errors
corr_ratios(strmatch('206/238',corr_header_208)) = ...
    (1-correction_ratio)*uncorr_ratios(strmatch('206/238',uncorr_ratios_header));
corr_ratios(strmatch('207/206',corr_header_208)) =...
    (uncorr_ratios(strmatch('207/206',uncorr_ratios_header))-...
    correction_ratio*common_207_206)/(1-correction_ratio);
corr_ratios(strmatch('207/235',corr_header_208)) = ...
    corr_ratios(strmatch('206/238',corr_header_208))*...
    corr_ratios(strmatch('207/206',corr_header_208))*U_ratio;
corr_ratios(strmatch('238/206',corr_header_208)) = ...
    1/corr_ratios(strmatch('206/238',corr_header_208));
corr_ratios(strmatch('208/206',corr_header_208)) = ...    uncorr_ratios(strmatch('208/
206',uncorr_ratios_header));
corr_ratios(strmatch('232/238',corr_header_208)) =...
    uncorr_ratios(strmatch('232/238',uncorr_ratios_header));

corr_ratios_se(strmatch('206/238',corr_header_208)) = ...
    sqrt((1-correction_ratio^2)*se_uncorr_ratios(strmatch('206/238',...
    uncorr_ratios_header))^2+uncorr_ratios(strmatch('206/238',...
    uncorr_ratios_header))^2*correction_ratio_se^2);
corr_ratios_se(strmatch('207/206',corr_header_208)) = ...
    sqrt((1-correction_ratio^2)*se_uncorr_ratios...
    (strmatch('207/206',uncorr_ratios_header))^2+...
    (uncorr_ratios(strmatch('207/206',uncorr_ratios_header))-...
    common_207_206)^2*correction_ratio_se^2)/(1-correction_ratio)^2;
corr_ratios_se(strmatch('207/235',corr_header_208)) =...

```

```

corr_ratios(strmatch('207/235',corr_header_208))*...
sqrt((corr_ratios_se(strmatch('206/238',corr_header_208))/...
corr_ratios(strmatch('206/238',corr_header_208)))^2+...
(corr_ratios_se(strmatch('207/206',corr_header_208))/...
corr_ratios(strmatch('207/206',corr_header_208)))^2);
corr_ratios_se(strmatch('238/206',corr_header_208))=...
corr_ratios_se(strmatch('206/238',corr_header_208))/...
corr_ratios(strmatch('206/238',corr_header_208))^2;
corr_ratios_se(strmatch('208/206',corr_header_208))=...
se_uncorr_ratios(strmatch('208/206',uncorr_ratios_header));
corr_ratios_se(strmatch('232/238',corr_header_208))=...
se_uncorr_ratios(strmatch('232/238',uncorr_ratios_header));

%Calculate ages using corrected ratios and calculate standard errors
corr_ages(strmatch('206/238',corr_header_208)) = ...
    log(1 + corr_ratios(strmatch('206/238',corr_header_208)))/lambda_238;
corr_ages(strmatch('207/235',corr_header_208)) = ...
    log(1 + corr_ratios(strmatch('207/235',corr_header_208)))/lambda_235;

% Iterative 207/206 age calculation
tinit=age;
ratio_temp = corr_ratios(strmatch('207/206',corr_header_208));

t1=log(U_ratio*ratio_temp*(exp(lambda_238*tinit)-1)+1)/lambda_235;
t2=log(U_ratio*ratio_temp*(exp(lambda_238*t1)-1)+1)/lambda_235;
delta_t = abs(t1-t2);

count = 1;
while delta_t > 0.1
    t1=log(U_ratio*ratio_temp*(exp(lambda_238*t2)-1)+1)/lambda_235;
    t2=log(U_ratio*ratio_temp*(exp(lambda_238*t1)-1)+1)/lambda_235;
    delta_t = abs(t1-t2);
    count = count + 1;
    if count > 20;
        break
    end
end
corr_ages(strmatch('207/206',corr_header_208))=t1;

corr_ages_se(strmatch('206/238',corr_header_208)) = ...
    corr_ratios_se(strmatch('206/238',corr_header_208))/...
    ((1+corr_ratios(strmatch('206/238',corr_header_208)))*lambda_238);
corr_ages_se(strmatch('207/206',corr_header_208))=...
    corr_ratios_se(strmatch('207/206',corr_header_208))/...

```

```

(lambda_235*(1/(U_ratio*(exp(lambda_238*...
corr_ages(strmatch('207/206',corr_header_208))-1))+...
corr_ratios(strmatch('207/206',corr_header_208))));
corr_ages_se(strmatch('207/235',corr_header_208))=...
corr_ratios_se(strmatch('207/235',corr_header_208))/...
((1+corr_ratios(strmatch('207/235',corr_header_208)))*lambda_235);

% Estimate the percentage of common Pb and calculate standard errors
percent_common(strmatch('206/238',corr_header_208))=
(uncorr_ratios(strmatch('206/238',uncorr_ratios_header))/...
corr_ratios(strmatch('206/238',corr_header_208)) - 1);

percent_common_se(strmatch('206/238',corr_header_208))=...
percent_common(strmatch('206/238',corr_header_208))*...
sqrt((corr_ratios_se(strmatch('206/238',corr_header_208))/...
corr_ratios(strmatch('206/238',corr_header_208))^2+...
(se_uncorr_ratios(strmatch('206/238',uncorr_ratios_header)))/...
uncorr_ratios(strmatch('206/238',uncorr_ratios_header))^2);

% Estimate the 204/206 ratio and calculate a standard error
est_204_206 = common_204_206*...
percent_common(strmatch('206/238',corr_header_208));
est_204_206_se = est_204_206*...
percent_common_se(strmatch('206/238',corr_header_208))/...
percent_common(strmatch('206/238',corr_header_208));

```

Read in Excel file for Ce anomaly calculation: xls_pars_zircon

```
function [filename,num_data,col_names,row_names] = xls_parse_zircon(title)
```

```
headerlines = 1;
```

```
[data_file,data_path]=uigetfile('*.xls',title);
```

```
filename = [data_path data_file];
```

```
[num_data,text_data] = xlsread(filename);
```

```
if headerlines > 0;
```

```
    text_data(1:headerlines,:) = [];
```

```
end
```

```
if strmatch('c',text_data(:,1),'exact') > 1
```

```
    row_names = text_data(:,2);
```

```
    text_data(:,1:3) = [];
```

```
else
```

```
    row_names = text_data(:,1);  
    text_data(:,1) = [];  
end
```

```
col_names = text_data(1,:);
```

References

Cumming, G. L., and Richards, J. R., 1975, Ore lead isotope ratios in a continuously changing Earth: *Earth and Planetary Science Letters*, v. 28, no. 2, p. 155-171.

Appendix II

Source Code for MELTS fO_2 Calculations

Introduction

The following source code is for calculating fO_2 using the MELTS activity models starting with a file with weight percents oxides for mineral and glass analyses. The first part of the source code sends mineral compositional data to the MELTS website and retrieves mole fraction, activity and ΔG for all the components. An example is shown for plagioclase and similar codes were written for other minerals. The second part of the code calculates oxygen fugacity for a variety of reactions using the downloaded ΔG data and activities from MELTS. The initial file format requires rows called T, P, and each of the weight percents appropriate for the mineral (Table A2.1). The first row of data must be numerical and is typically the number of grains used to calculate the average composition.

Retrieval of MELTS thermodynamic data

MELTS batch processing: melts_batch.m

This program requires the MatLab variable file ghiorso_vars.mat, which contains the forms (Table A2.2) and websites such as:

<http://ctserver.uchicago.edu/cgi-bin/mineral.cgi?feldspar>

for submitting data for processing by MELTS.

```
function melts_batch
clear all;
load ghiorso_vars.mat;
[file_name file_path] = uigetfile('*.xls');

[num_data,text_data] = xlsread([file_path file_name]);

col_names = text_data(3,:);
```

Table A2.1. Format of Excel file for submitting data to MELTS website for feldspars.

Average data for experimental feldspars																
N	15	10	10	10	15	12	10	10	11	12	14	203	14	7	12	268
Sample	104	105	105	114	119	139	165	169	195	195	203	263	263	263	268	268
Mineral	plag	plag	plag	plag	plag	plag	plag	plag	plag	plag	plag	plag	plag	plag	plag	plag
fO2 buffer	MnH	MH	MH	MH	MH	MH	MnH	MnH	MH	MH	MnH	MnH	MnH	MnH	MH	MH
Absolute fO2	-7.30213	-9.45675	-7.34543	-6.41923	-8.3541	-9.005	-8.11728	-9.4223	-9.83354	-9.93997	-9.44814					
fO2 rel MH	-0.8829	0	0	0	0	0	-0.6509	-0.77185	0	-0.41124	-0.49183	0				
fO2 rel MnH	0	0.51869	0.77185	0.8829	0.6509	0	0	0	0.4112	0	0	0	0	0	0.49183	
fO2 rel NNO	3.76335	4.38614	4.56694	4.64625	4.48056	3.82966	3.79509	4.3353	3.92406	3.8816	4.37343					
fO2 rel FMQ	4.37387	5.02141	5.18501	5.25677	5.10685	4.45595	4.41316	4.8789	4.46768	4.49396	4.98579					
T	950	800	800	900	950	850	850	900	800	800	800	800	800	800	800	800
P	2000	2000	2000	2000	2000	2000	2000	2000	4000	4000	4000	2500	2500	2500	2500	2500
X	-14805.7	-9816.5	16139.8	16647.3	15565.9	-10865.7	-10639.7	15222.3	-2921.86	-16182	-1468.83					
y	24796.8	-22407.8	22918.5	23903.1	24649.2	24269.1	23117.3	-26190.3	-23416.1	-24551.7	30854.9					
Z	155.2	18.4	189.7	119.667	169.417	153.2	97.4545	-13.8333	14044.5	-9.57143	132.667					
SiO2	49.0634	56.5268	51.8545	49.3833	54.8747	54.5783	52.1735	55.2885	54.5635	55.9727	56.4782					
Al2O3	31.0561	26.3622	29.2101	30.5808	27.4587	27.7813	29.3695	27.5952	27.8496	26.5464	26.753					
FeO	1.163	0.5702	0.8905	1.3206	0.67825	0.6533	0.80845	0.50433	0.43286	0.46243	0.57008					
MgO	0.0808	0.0608	0.0707	0.10367	0.04575	0.0557	0.06518	0.0295	0.02414	0.03257	0.07892					
BaO	0.03413	0.0973	0.0366	0.02653	0.08575	0.0448	0.02627	0.03042	0.01864	0.08229	0.0615					
CaO	14.5615	8.6732	12.1883	14.2924	9.89275	10.1199	12.0104	9.74375	10.2096	8.85229	8.88725					
Na2O	2.9668	5.9486	4.262	3.04653	5.51233	5.3183	4.33509	5.61942	5.42371	5.80557	5.93892					
K2O	0.15613	0.8528	0.2745	0.22027	0.50125	0.4584	0.28127	0.43842	0.24314	0.78929	0.68083					
Totals	99.0819	99.0919	98.7872	98.9741	99.0494	99.01	99.0697	99.2495	98.7651	98.5436	99.4488					
Si	2.26812	2.56888	2.38632	2.28521	2.50245	2.48927	2.39133	2.51088	2.49079	2.55729	2.55621					
Al	1.69205	1.41194	1.58422	1.66747	1.4759	1.49343	1.58654	1.47705	1.49836	1.42955	1.42718					
Fe	0.04046	0.0195	0.03084	0.04601	0.02327	0.02243	0.02788	0.01724	0.01487	0.01589	0.01942					
Mg	0.00557	0.00414	0.00485	0.00717	0.00311	0.00379	0.00445	0.002	0.00164	0.00222	0.0053					
Ba	0.00065	0.00182	0.00078	0.00058	0.00155	0.00082	0.00059	0.00057	0.00047	0.00147	0.00112					
Ca	0.72123	0.42233	0.60093	0.70842	0.48343	0.49461	0.58983	0.47414	0.49936	0.43344	0.43105					
Na	0.26593	0.52408	0.38031	0.27334	0.48735	0.47027	0.38523	0.49478	0.48005	0.51424	0.52112					
K	0.00921	0.04948	0.01612	0.01305	0.02916	0.02666	0.01644	0.0254	0.01416	0.04602	0.03931					

Table A2.1. Blank form for submitting data to MELTS website for plagioclase compositions.

type	
0	
sio2	
0	
al2o3	
0	
cao	
0	
na2o	
0	
k2o	
0	
albite	
0	
anorthite	
0	
sanidine	
0	
t	
0	
p	
0	

```

text_data(1,:) = [];
row_names = text_data(:,1);
text_data(:,1) = [];

mineral_names = {'feldspar';'pyroxene';'rh_m_oxide';'spinel';...
    'liquid wt per';'opx';'quartz';'liquid mole fracs'};

figure;
h2.listbox1=uicontrol('Style','listbox','String',mineral_names,'Units','normalized',...
    'Position',[0,2,0.4,.6]);
h2.textbox1=uicontrol('Style','text','String','Which field should samples be grouped by
...
    for average?','Units','normalized','Position',[0,.9,0.4,.05]);
%Stop program until user selects the finished box in the graphical interface
h2.checkbox1=uicontrol('Style','checkbox','String','finished','Units','normalized',...
    'Position',[0,0,0.2,0.04]);
waitfor(h2.checkbox1,'Value',1);
mineral_num = get(h2.listbox1,'Value');
close;

if mineral_num == 1;
    [components,thermo_data,variable,mole_data] = ...
        melts_batch_fs(num_data,row_names,feldspar_ws,pd_blank_fs);
elseif mineral_num == 2;
    [components,thermo_data,variable,mole_data] = ...
        melts_batch_cpx(num_data,row_names,cpx_ws,pd_blank_cpx);
elseif mineral_num == 3;
    [components,thermo_data,variable,mole_data] = ...
        melts_batch_ilm(num_data,row_names,rh_m_oxide_ws,pd_blank_rh_m_oxide);
elseif mineral_num == 4;
    [components,thermo_data,variable,mole_data] = ...
        melts_batch_mag(num_data,row_names,spinel_ws,pd_blank_spinel);
elseif mineral_num == 5;
    [components,thermo_data,variable,mole_data] = ...
        melts_batch_glass(num_data,row_names,glass_ws,pd_blank_glass);
elseif mineral_num == 6;
    [components,thermo_data,variable,mole_data] = ...
        melts_batch_opx(num_data,row_names,opx_ws,pd_blank_opx);
elseif mineral_num == 7;
    [components,thermo_data,variable] = ...
        melts_batch_qtz(num_data,row_names,qtz_ws,pd_blank_qtz);
elseif mineral_num == 8;
    [components,thermo_data,variable,mole_data] = ...
        melts_batch_glass_moles2wt(num_data,row_names,glass_ws,pd_blank_glass);
end

```

```

if mineral_num == 7
    export_row_names = vertcat(row_names,variable);
else
    for i = 1:size(components,1)
        dgs_temp(i) = {'DG' components{i}};
    end
    dgs = dgs_temp';
    export_row_names = vertcat(row_names,variable,components,dgs);
end

for i = 1:size(text_data,1);
    for j = 1:size(text_data,2);
        if isnan(num_data(i,j)) == 1;
            all_data(i,j) = {text_data{i,j}};
            text_rows(i) = i;
            num_rows(i) = 0;
        else;
            all_data(i,j) = {num_data(i,j)};
            text_rows(i) = 0;
            num_rows(i) = i;
        end
    end
end
end

if mineral_num == 7
    export_data = vertcat(all_data,thermo_data);
else
    export_data = vertcat(all_data,mole_data,thermo_data);
end
export_matrix = horzcat(export_row_names,export_data);

xlswrite(export_matrix,'Average data and activities','',...
    [file_path 'thermo_data_' mineral_names{mineral_num}]);

```

Mineral specific submission/retrieval of data: melts_batch_cpx.m

```

function [components,thermo_data,variable,mole_fracs] = ...
    melts_batch_cpx(num_data,row_names,website,post_data_blank);

post_data_blank(2) = {'WtToMoles'};
post_data = repmat(post_data_blank,1,size(num_data,2));

for i = 2:((size(post_data,1)+1)/2)

```

```

check = strmatch(post_data{2*i-1},lower(row_names),'exact');
if check > 0;
    for j = 1:size(post_data,2);
        post_data(2*i,j) = {num2str(num_data(check,j))};
    end
else
    post_data(2*i,:) = {'0'};
end
end

h = waitbar(0,'Posting data for weight to moles conversion');
for i = 1:size(post_data,2);
    waitbar(i/size(post_data,2));
    post_it = post_data(:,i);
    s(i) = {urlread(website,'post',post_it)};
end
close(h);

for i = 1:size(s,2);
    [variable,data(i,:)] = melts_parse_moles(s{i});
end
mole_fracs = data';

post_data(2,:) = {'MolesToThermo'};

diopside = 20;
clinoenstatite = diopside + 2;
hedenbergite = diopside + 4;
alumino_buffonite = diopside + 6;
buffonite = diopside + 8;
esseneite = diopside + 10;
jadeite = diopside + 12;

post_data(diopside,:) = mole_fracs(strmatch('Diopside',variable),:);
post_data(clinoenstatite,:) = mole_fracs(strmatch('Clinoenstatite',variable),:);
post_data(hedenbergite,:) = mole_fracs(strmatch('Hedenbergite',variable),:);
post_data(alumino_buffonite,:) = mole_fracs(strmatch('Alumino-buffonite',variable),:);
post_data(buffonite,:) = mole_fracs(strmatch('Buffonite',variable),:);
post_data(esseneite,:) = mole_fracs(strmatch('Essenite',variable),:);
post_data(jadeite,:) = mole_fracs(strmatch('Jadeite',variable),:);

h = waitbar(0,'Posting data for moles to thermodynamic conversion');
for i = 1:size(post_data,2);
    waitbar(i/size(post_data,2));
    post_it = post_data(:,i);

```

```

    s2(i) = {urlwrite(website,['thermo_data' num2str(i) '.txt'],'post',post_it)};
end
close(h);

components = {'CaMgSi2O6';'Mg2Si2O6';'CaFeSi2O6';...
    'CaTi0.5Mg0.5AlSiO6';'CaTi0.5Mg0.5FeSiO6';'CaFeAlSiO6';'NaAlSi2O6'};

[thermo_data] = melts_parse_activity(post_data,components);

```

Function for retrieving mole fractions: melts_parse_moles.m

```

function [variable,data] = melts_parse_moles(s);

r = findstr('right',s);
r_plus = 6;
l = findstr('left',s);
l_plus = 5;
less_than = findstr('<',s);

for i = 1:size(l,2);
    start_string = l(i) + l_plus;
    next_less = find(less_than > start_string);
    end_string = less_than(next_less(1))-1;
    variable(i) = {s(start_string:end_string)};
end
variable = variable';

for i = 1:size(r,2);
    start_string = r(i) + r_plus;
    next_less = find(less_than > start_string);
    end_string = less_than(next_less(1))-1;
    data(i) = {s(start_string:end_string)};
end

```

Function for retrieving activity and ΔG : melts_parse_activity.m

```

function [thermo_data] = melts_parse_activity(post_data,components);

l_plus = 5;
r_plus = 6;
for i = 1:size(post_data,2);
    fid = fopen(['thermo_data' num2str(i) '.txt']);

```

```

thermo_string = fgetl(fid);
fclose(fid);
table_start = strfind(thermo_string,'Component');
s_parse = thermo_string(table_start:size(thermo_string,2));
less_than = findstr('<',s_parse);
r = findstr('right',s_parse);
    l = findstr('left',s_parse);
for j = 1:size(components,1);
    comp_start = findstr(components{j},s_parse);
    if comp_start > 0;
        % Get activities
        next_right = find(r > comp_start);
        start_string_a = r(next_right(2)) + r_plus;
        next_less_a = find(less_than > start_string_a);
        end_string_a = less_than(next_less_a(1))-1;
        thermo_data_temp(j,i) = {s_parse(start_string_a:end_string_a)};
        % Get free energies
        next_right = find(r > comp_start);
        start_string_g = r(next_right(3)) + r_plus;
        next_less_g = find(less_than > start_string_g);
        end_string_g = less_than(next_less_g(1))-1;
        thermo_data_temp(size(components,1)+j,i) =
{s_parse(start_string_g:end_string_g)};
    else
        thermo_data_temp(j,i) = {'0'};
        thermo_data_temp(size(components,1)+j,i) = {'0'};
    end
end
end
thermo_data = thermo_data_temp;

```

Calculation of fO₂ using downloaded MELTS thermodynamic data

Main function: buffer_calc_auto.m

This program contains many different functions that are similar to the following. They all take as input the file format produced by the previous step and a reaction file with a “.mat” extension (Table A2.3). This is the file used to calculate fO₂ relative to FMQ, NNO, MH, and MnH and all are reported in Excel files.

```
clear all;
```

```
[minerals formulas DG1000 DG1100 DG1200 DG1300] =...
```


Table A2.3A. Format for phases involved in the reactions used in Chapter II.

mag	fesi	fesi	hede	hede	hede	hede
O2	O2	O2	clen	clen	an	an
hem	mag	hem	O2	O2	mag	hem
	qtz	qtz	mag	hem	O2	O2
			diop	diop	ess	ess
			qtz	qtz	qtz	qtz

Table A2.3B. Format for coefficients of the phases in the reactions from Chapter II.

-4	-3	-2	-6	-4	-3	-4
-1	-1	-1	-3	-2	-3	-4
6	2	2	-1	-1	-1	-2
0	6	4	2	2	-1	-1
0	0	0	6	4	6	8
0	0	0	6	4	6	8

Table A2.3C. Format for reaction names for the reactions in Chapter II.

Reaction 2
Reaction 3
Reaction 4
Reaction 5
Reaction 6
Reaction 7
Reaction 8

```

textread('free_energies_comps.csv','%q %q %f%f%f%f','delimiter',',');

[vol_minerals vol_formulas volumes] = ...
    textread('volumes_comps.csv','%q %q %f','delimiter',',');

[filename_cpx,num_data_cpx,text_data_cpx,row_names_cpx] = ...
    xls_parse('Pick file with cpx compositions');
[filename_opx,num_data_opx,text_data_opx,row_names_opx] = ...
    xls_parse('Pick file with opx compositions');
[filename_sph,num_data_sph,text_data_sph,row_names_sph] = ...
    xls_parse('Pick file with sphene compositions');
[filename_mag,num_data_mag,text_data_mag,row_names_mag] = ...
    xls_parse('Pick file with magnetite compositions');
[filename_ilm,num_data_ilm,text_data_ilm,row_names_ilm] = ...
    xls_parse('Pick file with ilmenite compositions');
[filename_glass,num_data_glass,text_data_glass,row_names_glass] = ...
    xls_parse('Pick file with glass compositions');

common_row_names = intersect(intersect(intersect(row_names_cpx,row_names_sph),...
    row_names_mag),intersect(intersect(row_names_ilm,row_names_glass),...
    row_names_opx));

figure;
h2.listbox1=uicontrol('Style','listbox','String',common_row_names,'Units',...
    'normalized','Position',[0,.2,0.4,.6]);
h2.textbox1=uicontrol('Style','text','String','Pick field to group minerals by ...
    (typically sample name/number)?','Units','normalized','Position',[0,.9,0.4,.05]);
%Stop program until user selects the finished box in the graphical interface
h2.checkbox1=uicontrol('Style','checkbox','String','finished','Units','normalized',...
    'Position',[0,0,0.2,0.04]);
waitfor(h2.checkbox1,'Value',1);
sample_row = get(h2.listbox1,'Value');
close;

cpx_row = strmatch(common_row_names{sample_row},row_names_cpx);
opx_row = strmatch(common_row_names{sample_row},row_names_opx);
sph_row = strmatch(common_row_names{sample_row},row_names_sph);
mag_row = strmatch(common_row_names{sample_row},row_names_mag);
ilm_row = strmatch(common_row_names{sample_row},row_names_ilm);
glass_row = strmatch(common_row_names{sample_row},row_names_glass);

cpx_samples = sample_text(cpx_row,num_data_cpx,text_data_cpx);
opx_samples = sample_text(opx_row,num_data_opx,text_data_opx);
sph_samples = sample_text(sph_row,num_data_sph,text_data_sph);
mag_samples = sample_text(mag_row,num_data_mag,text_data_mag);

```

```

ilm_samples = sample_text(ilm_row,num_data_ilm,text_data_ilm);
glass_samples = sample_text(glass_row,num_data_glass,text_data_glass);

all_samples = union(union(union(cpx_samples,sph_samples),...
    mag_samples),union(union(ilm_samples,glass_samples),opx_samples));

activity_names = {'Fe2Si2O6','CaFeSi2O6','CaFeAlSiO6','NaAlSi2O6','Fe3O4',...
    'a_ro_Fe2O3','FeTiO3','aSiO2','NaAlSi3O8','CaAl2Si2O8','CaTiSiO5',...
    'O2','Fe2TiO4','CaMgSi2O6','Mg2Si2O6'};
dg_names = {'DGF2Si2O6','DGCFeSi2O6','DGCFeAlSiO6','DGNAlSi2O6',...
    'DGF3O4','DGF2O3','DGF2TiO3','DGSiO2','DGNAlSi3O8',...
    'DGCAl2Si2O8','DGCATiSiO5','DGO2','DGF2TiO4','DGCAMgSi2O6',...
    'DGMg2Si2O6'};
mineral_names = {'fesi','hede','ess','jade','mag','hem','ilm','qtz','alb',...
    'an','sph','O2','us','diop','clen'};

for i = 1:size(activity_names,2);
    flag = 0;
    %q_flag = 0;
    if strmatch(activity_names{i},row_names_cpx) > 0;
        input_data = num_data_cpx;
        input_row_names = row_names_cpx;
        input_samples = cpx_samples;
    elseif strmatch(activity_names{i},row_names_opx) > 0;
        input_data = num_data_opx;
        input_row_names = row_names_opx;
        input_samples = opx_samples;
    elseif strmatch(activity_names{i},row_names_mag) > 0;
        input_data = num_data_mag;
        input_row_names = row_names_mag;
        input_samples = mag_samples;
    elseif strmatch(activity_names{i},row_names_ilm) > 0;
        input_data = num_data_ilm;
        input_row_names = row_names_ilm;
        input_samples = ilm_samples;
    elseif strmatch(activity_names{i},row_names_glass) > 0;
        input_data = num_data_glass;
        input_row_names = row_names_glass;
        input_samples = glass_samples;
    elseif strmatch(activity_names{i},row_names_sph) > 0;
        input_data = num_data_sph;
        input_row_names = row_names_sph;
        input_samples = sph_samples;
    else flag = 1;
end

```

```

if flag == 1;
    activities(i,1:size(all_samples,2)) = 0;
    dgs(i,1:size(all_samples,2)) = 0;
else
    activities(i,1:size(all_samples,2)) = get_activities(all_samples,input_data,...
        input_row_names,input_samples,activity_names{i});
    dgs(i,1:size(all_samples,2)) = get_activities(all_samples,input_data,...
        input_row_names,input_samples,dg_names{i});
end

end

[TC,Pbars] = get_conditions_nat(all_samples,cpx_samples,sph_samples,...
    mag_samples,ilm_samples,glass_samples,num_data_cpx,num_data_sph,...
    num_data_mag,num_data_ilm,num_data_glass,row_names_cpx,...
    row_names_sph,row_names_mag,row_names_ilm,...
    row_names_glass,text_data_cpx,text_data_sph,text_data_mag,text_data_ilm,text_data_glass);

TK = TC + 273.15;
P = Pbars./1000;

load nat_rxns.mat;
rxn_types = textread('nat_rxn_types.csv','%q','delimiter',' ');

free_energies = horzcat(DG1000,DG1100,DG1200,DG1300);

for i = 2:size(free_energies,1);
    p_temp(i,:) = polyfit(free_energies(1,:),free_energies(i,:),1);
end

p = p_temp;

row_names = {'Buffer','Absolute fO2','fO2 rel MH','fO2 rel MnH',...
    'fO2 rel NNO','fO2 rel FMQ'};
for i = 1:size(all_samples,2);
    mh = fO2_calc(TK(i),P(i),p,minerals,vol_minerals,volumes,[4;1;-6],...
        {'mag','O2','hem'});
    mnH = fO2_calc(TK(i),P(i),p,minerals,vol_minerals,volumes,[6;1;-2],...
        {'mno','O2','mn3o4'});
    nno = fO2_calc(TK(i),P(i),p,minerals,vol_minerals,volumes,[2;1;-2],{'ni','O2','nio'});
    fmQ = fO2_calc(TK(i),P(i),p,minerals,vol_minerals,volumes,[3;1;-2;-3],...
        {'fay','O2','mag','qtz'});
    for j = 1:size(rxn_names,1);
        needed_data = find(rxn_coef(:,j));
    end
end

```

```

coef = rxn_coef(needed_data,j);
names = rxn(needed_data,j);
if strcmp('fO2',rxn_types{j}) == 1;
    melts_fo2(j,i) = a_cor_fO2_calc_melts(TK(i),P(i),dgs(:,i),mineral_names,...
        coef,names,'O2',activities(:,i));
elseif strcmp('P',rxn_types{j}) == 1;
    melts_fo2(j,i) = 0;%a_cor_P_calc_melts(TK(i),dgs,minerals,vol_minerals,...
        volumes,coef,names,mineral_names,activities(:,i),formulas);
end
end
melts_fo2_mh(:,i) = melts_fo2(:,i) - mh;
melts_fo2_mnh(:,i) = melts_fo2(:,i) - mnh;
melts_fo2_nno(:,i) = melts_fo2(:,i) - nno;
melts_fo2_fmqs(:,i) = melts_fo2(:,i) - fmqs;
end
TC_cell = num2cell(TC);
P_cell = num2cell(P);
export_row_names = vertcat({'Samples';'T';'P'},rxn_names);
melts_fo2_cell = horzcat(export_row_names,vertcat(all_samples,...
    TC_cell,P_cell,num2cell(melts_fo2)));
melts_fo2_mh_cell = horzcat(export_row_names,vertcat(all_samples,...
    TC_cell,P_cell,num2cell(melts_fo2_mh)));
melts_fo2_mnh_cell = horzcat(export_row_names,vertcat(all_samples,...
    TC_cell,P_cell,num2cell(melts_fo2_mnh)));
melts_fo2_nno_cell = horzcat(export_row_names,vertcat(all_samples,...
    TC_cell,P_cell,num2cell(melts_fo2_nno)));
melts_fo2_fmqs_cell = horzcat(export_row_names,vertcat(all_samples,...
    TC_cell,P_cell,num2cell(melts_fo2_fmqs)));

calc_type_list = {'experimental';'natural'};

figure;
h2.listbox1=uicontrol('Style','listbox','String',calc_type_list,'Units','normalized',...
    'Position',[0,2,0.4,6]);
h2.textbox1=uicontrol('Style','text','String','Pick field to group minerals by ...
    (typically sample name/number)?','Units','normalized','Position',[0,9,0.4,.05]);
%Stop program until user selects the finished box in the graphical interface
h2.checkbox1=uicontrol('Style','checkbox','String','finished','Units','normalized',...
    'Position',[0,0,0.2,0.04]);
waitfor(h2.checkbox1,'Value',1);
calc_loc = get(h2.listbox1,'Value');
close;

calc_type = calc_type_list{calc_loc};

```

```

xlswrite(melts_fo2_cell,"",[pwd '\melts_fO2_abs_' calc_type '.xls']);
xlswrite(melts_fo2_mh_cell,"",[pwd '\melts_fO2_mh_' calc_type '.xls']);
xlswrite(melts_fo2_mnh_cell,"",[pwd '\melts_fO2_mnh_' calc_type '.xls']);
xlswrite(melts_fo2_nno_cell,"",[pwd '\melts_fO2_nno_' calc_type '.xls']);
xlswrite(melts_fo2_fmqs_cell,"",[pwd '\melts_fO2_fmqs_' calc_type '.xls']);

```

Parse input Excel files: xls_parse.m

```

function [filename,num_data,text_data,row_names] = xls_parse(title)

```

```

headerlines = 1;

```

```

[data_file,data_path]=uigetfile('*.xls',title);
filename = [data_path data_file];
[num_data,text_data] = xlsread(filename);

```

```

if headerlines > 0;
    text_data(1:headerlines,:) = [];
end
row_names = text_data(:,1);
text_data(:,1) = [];

```

Get activity values from input data: get_activities.m

```

function activities = get_activities(all_samples,input_data,input_row_names,...
    input_samples,activity_name);

```

```

for i = 1:size(all_samples,2);
    sample_loc = strmatch(all_samples{i},input_samples,'exact');
    if sample_loc > 0;
        activity_loc = strmatch(activity_name,input_row_names);
        activities(i) = squeeze(input_data(activity_loc,sample_loc));
    else
        activities(i) = 0;
    end
end
end

```

Get P, T conditions for all possible samples: get_conditions.m

```

function [TC,Pbars,buffer] = get_conditions(all_samples,cpx_samples,plag_samples,...
    mag_samples,ilm_samples,glass_samples,num_data_cpx,num_data_plag,...
    num_data_mag,num_data_ilm,num_data_glass,row_names_cpx,...
    row_names_plag,row_names_mag,row_names_ilm,row_names_glass,...

```

```

        text_data_cpx,text_data_plag,text_data_mag,text_data_ilm,text_data_glass)

for i = 1:size(all_samples,2);
    if strcmp(all_samples{i},cpx_samples) > 0;
        TC(i) = num_data_cpx(strcmp('T',row_names_cpx,'exact'),...
            strcmp(all_samples{i},cpx_samples));
        Pbars(i) = num_data_cpx(strcmp('P',row_names_cpx,'exact'),...
            strcmp(all_samples{i},cpx_samples));
        buffer(i) = text_data_cpx(strcmp('fO2 buffer',row_names_cpx,'exact'),...
            strcmp(all_samples{i},cpx_samples));
    elseif strcmp(all_samples{i},plag_samples) > 0;
        TC(i) = num_data_plag(strcmp('T',row_names_plag,'exact'),...
            strcmp(all_samples{i},plag_samples));
        Pbars(i) = num_data_plag(strcmp('P',row_names_plag,'exact'),...
            strcmp(all_samples{i},plag_samples));
        buffer(i) = text_data_plag(strcmp('fO2 buffer',row_names_plag,'exact'),...
            strcmp(all_samples{i},plag_samples));
    elseif strcmp(all_samples{i},mag_samples) > 0;
        TC(i) = num_data_mag(strcmp('T',row_names_mag,'exact'),...
            strcmp(all_samples{i},mag_samples));
        Pbars(i) = num_data_mag(strcmp('P',row_names_mag,'exact'),...
            strcmp(all_samples{i},mag_samples));
        buffer(i) = text_data_mag(strcmp('fO2 buffer',row_names_mag,'exact'),...
            strcmp(all_samples{i},mag_samples));
    elseif strcmp(all_samples{i},ilm_samples) > 0;
        TC(i) = num_data_ilm(strcmp('T',row_names_ilm,'exact'),...
            strcmp(all_samples{i},ilm_samples));
        Pbars(i) = num_data_ilm(strcmp('P',row_names_ilm,'exact'),...
            strcmp(all_samples{i},ilm_samples));
        buffer(i) = text_data_ilm(strcmp('fO2 buffer',row_names_ilm,'exact'),...
            strcmp(all_samples{i},ilm_samples));
    elseif strcmp(all_samples{i},glass_samples) > 0;
        TC(i) = num_data_glass(strcmp('T',row_names_glass,'exact'),...
            strcmp(all_samples{i},glass_samples));
        Pbars(i) = num_data_glass(strcmp('P',row_names_glass,'exact'),...
            strcmp(all_samples{i},glass_samples));
        buffer(i) = text_data_glass(strcmp('fO2 buffer',row_names_glass,'exact'),...
            strcmp(all_samples{i},glass_samples));
    else
        TC(i) = 0;
        Pbars(i) = 0;
        buffer(i) = {'0'};
    end
end

end

```

Calculation of oxygen buffer: fO2_calc.m

```
function log_fo2 = fO2_calc(TK,P,p,minerals,vol_minerals,volumes,...
    rxn_coefficients,rxn_minerals);
clear G V;

R = 8.3144/1000;
log_convert = 2.303;

for i = 1:size(rxn_minerals,2);
    min_pos_G = strmatch(rxn_minerals{i},minerals,'exact');
    min_pos_V = strmatch(rxn_minerals{i},vol_minerals,'exact');
    G(i) = rxn_coefficients(i)*polyval(p(min_pos_G,:),TK);
    V(i) = rxn_coefficients(i)*volumes(min_pos_V);
end
save test.mat G
DG = sum(G);
DV = P*sum(V);

log_fo2 = (-DG-DV)/...
    (R*TK*log_convert*rxn_coefficients(strmatch('O2',rxn_minerals))));
```

Calculation of sample fO_2 with activity correction:

```
function logfo2 = a_cor_fO2_calc_melts(TK,P,dgs,mineral_names,...
    rxn_coefficients,rxn_minerals,unk_min,activities);
clear G V loga;

R = 8.3144/1000;
log_convert = 2.303;

rxn_minerals = rxn_minerals';
rxn_coefficients = rxn_coefficients';
for i = 1:size(rxn_minerals,2);

    if strmatch(rxn_minerals{i},unk_min,'exact')==1;
        min_pos_a = strmatch(rxn_minerals{i},mineral_names);
        loga(i) = 0;
        G(i) = rxn_coefficients(i)*dgs(min_pos_a);
    else
```



```

        min_pos_a = strmatch(rxn_minerals{i},mineral_names);
        loga(i) = rxn_coefficients(i)*log10(activities(min_pos_a));
        G(i) = rxn_coefficients(i)*dgs(min_pos_a);
    end
end
save test.mat G loga
DG = sum(G);
DV = 0;%MELTS DG and a account for volume change
save test.mat
logfo2 = (-DG-DV)/...
    (R*TK*log_convert*rxn_coefficients(strmatch(unk_min,rxn_minerals))) - ...
    sum(loga,2)/rxn_coefficients(strmatch(unk_min,rxn_minerals));

```

Appendix III

Sulfur Isotopic Composition of Sulfide and Sulfate in Granitoids

Introduction

Sulfur is one of the few elements that show isotopic fractionation at magmatic temperature in granitoids. Analyses of sulfide and sulfate isotopes in anhydrite-bearing volcanic rocks show that this fractionation is approximately 7.5 per mil. Previous studies on the sulfur isotopic composition of granitoids focused on the bulk $\delta^{34}\text{S}$ of the samples (Sasaki and Ishihara, 1979; Ishihara and Sasaki, 1989). These studies show a deviation from the mantle value of 1.3 per mil with values of +1.6 to +12.5 per mil for magnetite series intrusions and -3.7 to -5.3 per mil for ilmenite series intrusions. The goal of this study is to determine the sulfide and sulfate isotopic composition of intrusions from the western United States. Therefore, it is possible to evaluate the fractionation between sulfide and sulfate and to examine other factors that might affect the sulfur isotopic composition of granitoids.

The analysis of sulfide and sulfate isotopes from natural rock and sediment samples requires the use of chemical reactions to extract the sulfur. This creates a pure sulfur-bearing phase that can then be analyzed for sulfur isotopes. Current techniques are not adequate for extracting sulfide and sulfate from granitoids. This paper presents a technique that can be used to extract sulfide and sulfate from various types of rock and is especially useful for extracting small amounts of sulfate from large samples as is necessary for granitoids.

Sulfur Geochemistry

Sulfur can occur in many forms in natural samples, including organically bound sulfur, inorganic sulfate, native sulfur and sulfide. Sulfite and thiosulfate can also be important transient species but are not often preserved in rocks. In rocks that form at high temperature, organic and native sulfur are not commonly present. Therefore in such samples it is most useful to be able to extract sulfide and sulfate (SO_4). There are two different types of sulfides that are of concern. Monosulfides such as sphalerite, pyrrhotite, and mackinawite are soluble in HCl and are often referred to as acid volatile sulfides (AVS). Disulfides such as pyrite do not readily react in HCl and require the use of a reductant such as chromous chloride in order to recover sulfur. Disulfides are often referred as chromium reduced sulfides (CRS) (Canfield et al., 1986)..

Previous Techniques

The most frequently used method for extracting sulfur from granitoids is reaction of the sample with dehydrated phosphoric acid and stannous chloride known as Kiba reagent (Sasaki et al., 1979). This method recovers all sulfur in a single step so information about the different sulfur species is lost. Ueda and Sakai (1983) presented a method for recovering sulfate and sulfide using a modified Kiba reagent, but this technique requires heating to 280°C in a vacuum making it difficult and costly to apply.

The most commonly used methods for looking at the different species of sulfur in rock samples is that of Canfield et al. (1986) and Tuttle et al. (1986) and later modified by Rice et al. (1993) and Hall et al. (1988). These techniques provide a method for recovering elemental sulfur, inorganic sulfate, AVS, CRS, and organically bound sulfur. Most of these methods use chromous chloride as a reductant to recover pyrite sulfur, whereas the method of Hall et al. (1988) used lithium aluminum hydride in tetrahydrofuran. In these methods AVS and CRS are reacted to produce H_2S and recovered as CdS or ZnS precipitated from a cadmium or zinc acetate solution. The precipitate is then converted to Ag_2S by reacting it with AgNO_3 solution. Sulfate recovery

requires filtration of the solution containing the rock powder or sediment followed by precipitation of BaSO_4 from the solution. This step can be time consuming when large samples are used and requires filtering large amounts of a highly acidic solution.

Sulfate recovery is also problematic when working with samples that have high phosphorous content relative to sulfur, such as granitoids. When phosphorous is much more abundant than sulfur, large amounts of Ba-phosphate precipitate in addition to BaSO_4 . The Ba-phosphate precipitate is gel-like and clogs filters. There is typically between 1-2 % sulfur in the precipitate and it is not suitable for isotopic analysis.

An alternative method for sulfate recovery is direct reduction of sulfate to sulfide using Thode solution (Thode et al., 1961). They used a mixture of 32% HI, 52% HCl and 16% H_3PO_2 to quantitatively reduce barite. Below is a method for extracting low levels of sulfur from granitoid samples by modifying the AVS and CRS steps of Rice et al. (1993) and the sulfate recovery of Thode et al. (1961).

Reagent Mixtures

The AVS step is conducted using 6 N HCl with approximately 0.15 M SnCl_2 . The SnCl_2 may be mixed with the HCl in advance or added to the dry sample prior to the extraction. The amount of reagents varies depending on the size of the samples being analyzed with samples larger than 20 g requiring 150 mL of 6N HCl and samples that are only a few grams requiring only 35 mL of 6N HCl. Large samples also require stirring, which is unnecessary for small samples.

The CrCl_2 solution used to recover CRS is 0.1 M CrCl_2 dissolved in 0.1 N HCl. The solution is made by passing a solution of CrCl_3 through a column of amalgamated Zn reducing Cr^{3+} to Cr^{2+} . The HI mixture is similar to that used by Thode et al., (1961) for sulfate reduction. The solution was modified to account for the presence of HCl already in the reaction vessel. A mixture of 65% HI, 25% hypophosphorous acid (H_3PO_2), and 10% HCl is mixed up and boiled for 2 hours under a nitrogen atmosphere. Boiling is necessary to remove sulfate that is present as a contaminant in the HI and H_3PO_2 . The solution is

allowed to cool under the N_2 atmosphere and then placed in dark glass bottles for storage since light can oxidize HI.

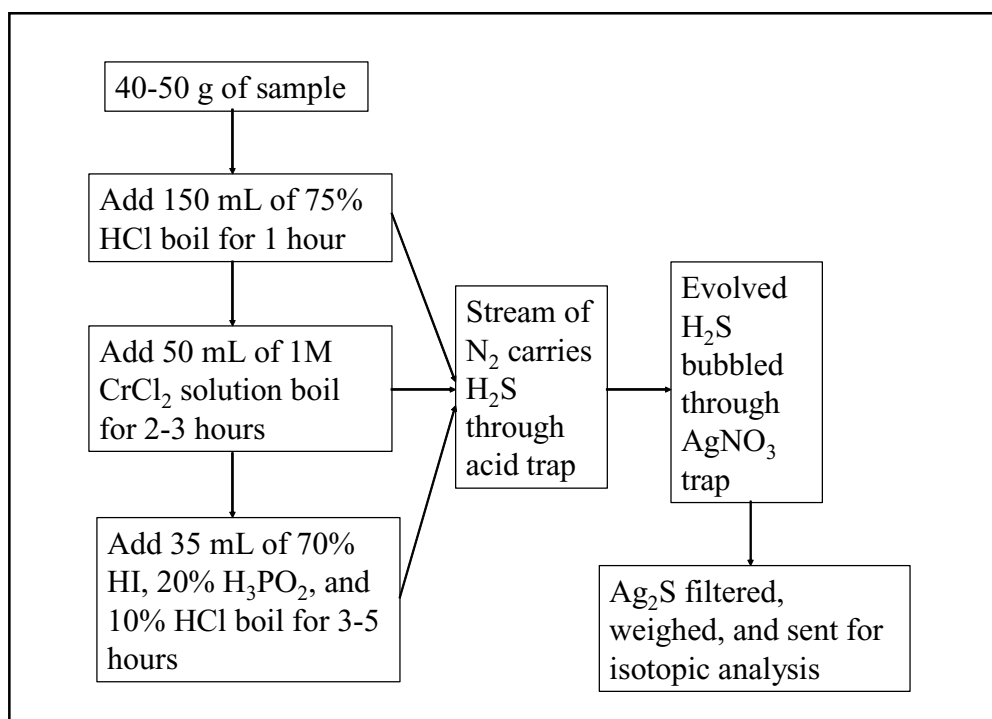
The H_2S produced during the extractions is trapped using 0.1 M $AgNO_3$ solution that contains 10% ammonium hydroxide. The ammonium hydroxide suppresses the precipitation of $AgCl$ and AgI that would result from HCl or HI vapors reaching the $AgNO_3$ trap.

Extraction Setup

All standards were stored in a desiccator to prevent oxidation of the sulfides and adsorption of water. The standards were crushed to a fine powder using an agate mortar and pestle immediately prior to sulfur extraction. Mixtures of known amounts of standards were used to test recovery. Granitoid samples were crushed using a jaw crusher and then powdered in a shatter box to a size of 50 μm . The samples were then placed in an oven overnight at 80-90°C to remove adsorbed water so that an accurate weight could be obtained. Whole rock samples were stored in a desiccator prior to extraction. About half the samples used the $BaSO_4$ precipitation method for sulfate recovery while the other half used direct reduction of sulfate using hydriodic acid.

The steps of the extraction method are shown in Figure A3.1. The setup has a reaction vessel where the sample and reactants are mixed together. The reaction vessel has one input for N_2 gas to be bubbled through the solution and one for reagents to be introduced via a syringe. There is one output from the vessel that carries H_2S produced by the reactions in N_2 carrier gas. These gases first pass through a condensing tube and then into an acid trap that contains 100 ml of very dilute HCl (pH of ~5). This traps HCl and HI vapors while allowing H_2S to pass through. The gas is then bubbled through 30-35 ml of $AgNO_3$ solution in a centrifuge tube leading to precipitation of Ag_2S .

For standard extractions 10-30 mg of the standard materials were used, and for whole rock extraction 40-60 g of powder were used. If the whole rock contains more sulfur, less of the sample should be used. The extraction of monosulfides, or acid volatile

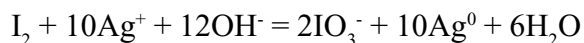


FigureA3.1. Flow chart showing the steps of the sulfur extraction procedure.

sulfur (AVS), is done similarly to the technique of Rice et al. (1993). The sample and HCl mixture is allowed to stay at room temperature for five minutes and then is heated for approximately 15 minutes to boiling. Samples are allowed to boil for five minutes and then the heat is reduced to keep the samples just below boiling for 30 minutes. The heat is then turned off and the samples allowed to cool and the AgNO₃ trap is changed prior to the next step.

Then 35-40 ml of CrCl₂ solution is injected in the reaction vessel to recover CRS, similar to the method described by Canfield et al. (1986) and Tuttle et al. (1986). The solution is heated to boiling and then heat reduced slightly. The reaction is allowed to proceed until the AgNO₃ solution again turns clear and stops precipitating Ag₂S. The AgNO₃ traps should be changed again prior to the next step.

After completion of the CRS step, 35 ml of hydriodic acid (HI) mixture is injected into the reaction vessel using a syringe. The solution in the reaction vessel should not be boiling at the time the HI mixture is injected because this can lead to a sudden decrease in pressure in the system, causing the AgNO₃ solution to be sucked into the acid trap or even the reaction vessel. After injecting the HI mixture, the solution in the reaction vessel is boiled and then the heat reduced slightly. The reaction is allowed to continue for approximately 2-3 hours until the AgNO₃ solution turns clear or light gray. The trap sometimes turns gray due to the formation of native Ag by the reaction:



This occurs when I₂ gas produced during the oxidation of HI in the reaction vessel reaches the AgNO₃ trap. Typically, small amounts of I₂ are produced during the reduction of sulfate but large amounts may form if oxygen enters the reaction vessel due to a leak in the system or if extremely oxidized samples are being used. The iodine gas can be prevented from reaching the AgNO₃ solution by using a cold trap in line that is cooled with ice water. The cold trap tested in this study is a coil of 1/4 inch glass tubing with a coil diameter of 6 cm and a path length of 0.5 m that was submerged in a small tub of ice

water. However, in general the production of native Ag is minimal and accounts for less than 2% of the precipitate. This is not enough to affect the isotopic analysis so the cold trap is not typically necessary.

The Ag_2S precipitates are then filtered, dried and weighed to determine the yield of AVS, CRS and sulfate. Significant fractionation of sulfur isotopes occurs during the runs so it is necessary to homogenize the precipitates prior to analyzing for sulfur isotopes. This is done by gently grinding the samples with an agate mortar and pestle.

Sample Descriptions

The technique was tested by extracting sulfur from mixtures of standards and then was applied to granitoids. The standard materials used were NBS 127 (barite from sea water sulfate), NBS 123 (sphalerite from Balmat), and Park City pyrite. Whole rock samples of granitoids from the Hanover-Fierro stock, New Mexico and several intrusions from the Bingham Park-City Belt, Utah were also run to test the technique.

Hanover-Fierro, New Mexico

The 61 Ma Hanover-Fierro granodiorite is located in the Grant Co. mining district, southwestern New Mexico (Fig. A3.2). It intrudes Precambrian gneisses and a sequence of Paleozoic sedimentary rocks consisting of limestones and clastic rocks but no evaporites. The stock is mainly porphyritic with a small exposure of an equigranular phase to the southwest. The porphyritic phase is associated with mineralization at the Continental Cu skarn.

The Hanover-Fierro stock is contemporaneous with the intrusion associated with mineralization at the Chino porphyry Cu deposit, which has a K-Ar age of 63 Ma (Rose and Baltosser, 1966). These intrusions formed during a period of subduction zone magmatism in Arizona and New Mexico from 52 to 72 Ma that led to the formation of approximately 50 porphyry copper deposits (Titley, 1993).

Samples for this study were collected from surface outcrops and drill core of the porphyritic phase of the Hanover-Fierro stock in the vicinity of the Continental Mine.

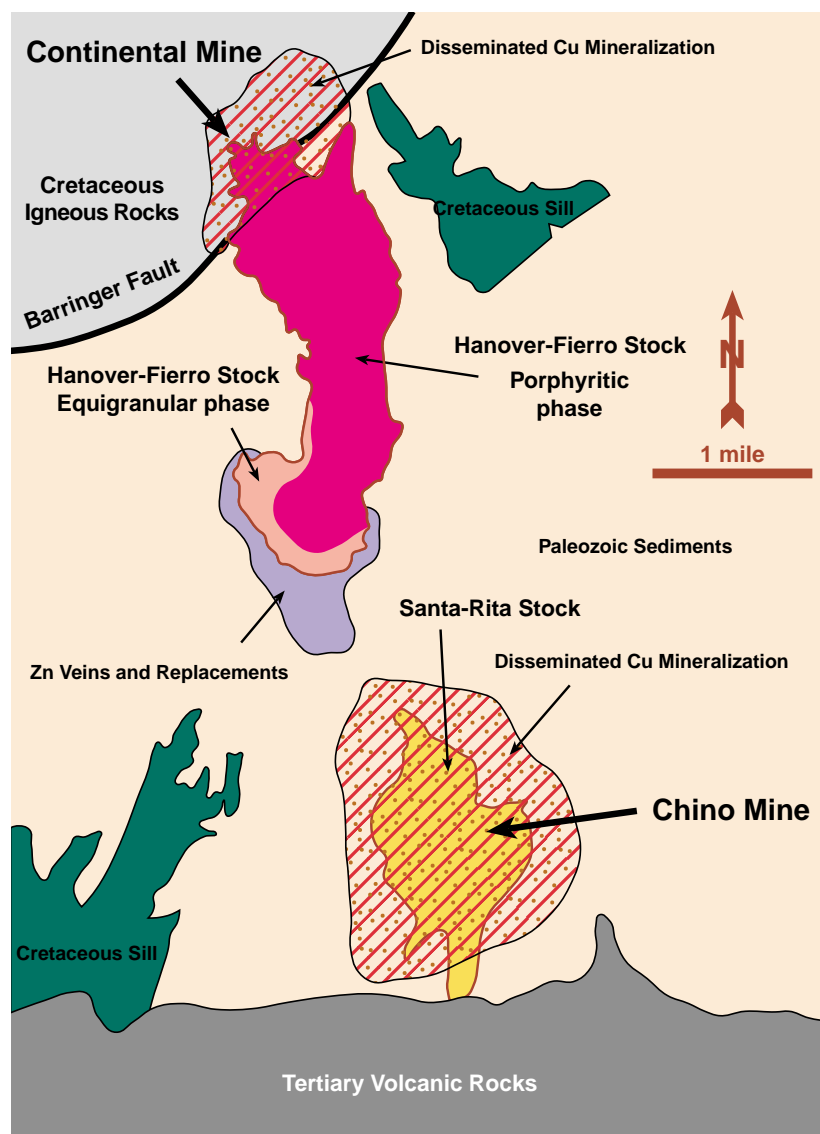


Figure A3.2. Geologic map of the Hanover-Fierro and Santa Rita districts showing intrusions and locations of deposits.

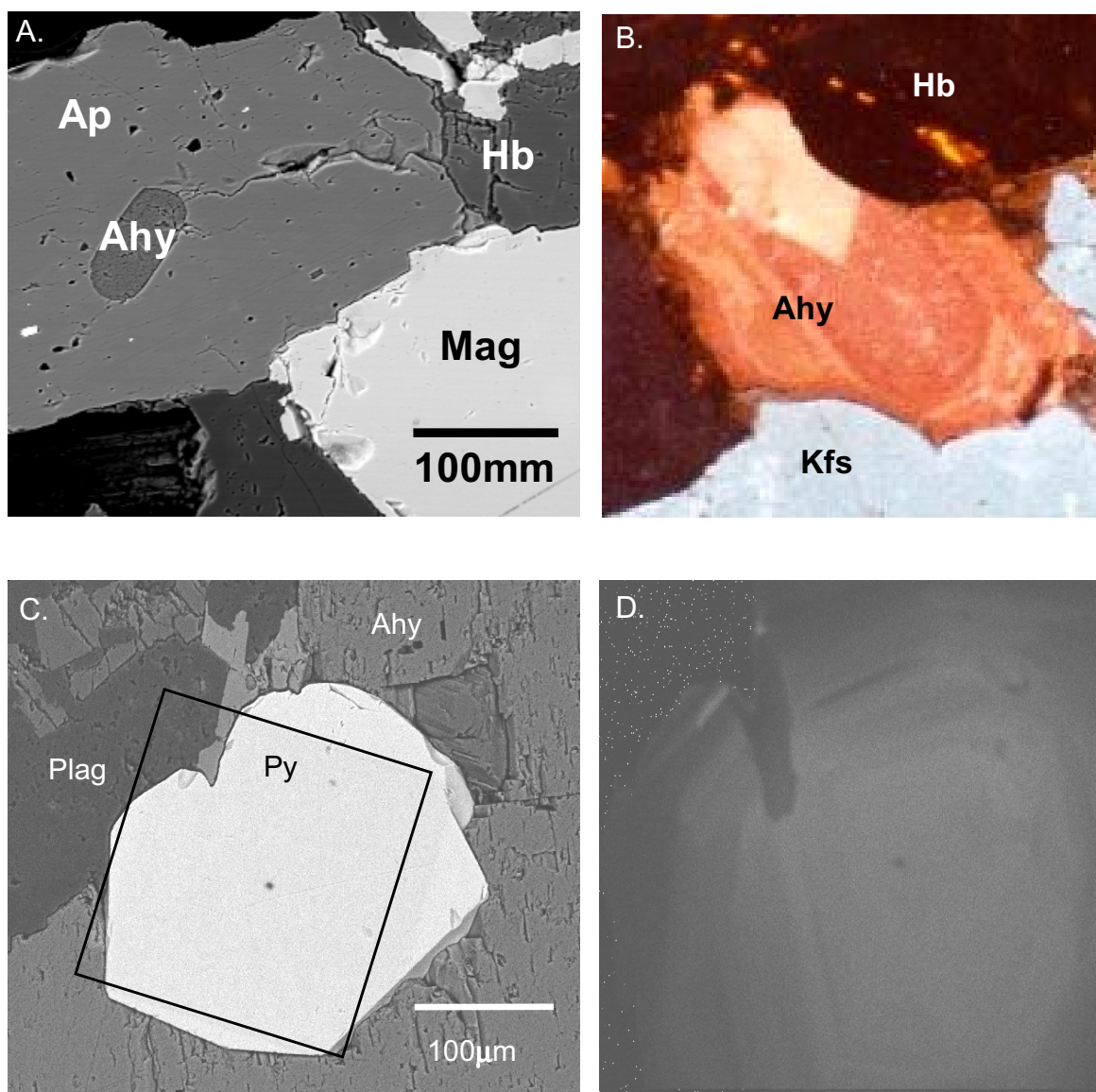


Figure A3.3. Textural relationships of anhydrite and pyrite in the Hanover-Fierro stock. A. BSE image showing an anhydrite inclusion inside of a magmatic apatite grain. B. Cathodoluminescence image of anhydrite showing magmatic zoning. C. BSE image of magmatic pyrite and anhydrite. Box shows area of map in part D. D. Co-K α X-ray map of pyrite from part C. Zoning appears to be magmatic.

Two samples of the porphyritic phase of the stock were found to contain abundant anhydrite and pyrite from depths of 300 and 320 meters. Most of the sulfur is hosted in anhydrite and pyrite with minor sulfate in apatite that contains up to 1.1 wt% SO₃.

The anhydrite and pyrite present in these samples appears to be largely magmatic in origin (Fig. A3.3). Both anhydrite and pyrite show sharp grain boundaries with magmatic phases and zoning of both minerals suggests crystallization from a magma. Irregular zoning in some anhydrites suggests that part of the anhydrite is hydrothermal, which is consistent with observations of anhydrite in the Pinatubo dacite and El Chichon trachyandesite where two populations of anhydrite are present (McKibben et al., 1996; Luhr and Logan, 2002).

Bingham-Park City belt, Utah

The Bingham-Park City belt (BPCB) consists of 15 granitoid intrusions and coeval volcanic rocks that crop out in an E-W trending belt. The BPCB magmas probably formed by partial melting of lower crustal equivalents of the amphibolites in the Little Willow Formation and were emplaced in an extensional tectonic regime (Vogel et al., 2001). The intrusions have varying depth of exposure and are associated with a range of alteration types (John, 1989).

The samples included in this study are from the Clayton Peak, Pine Creek, Alta, and Little Cottonwood stocks and the Keetely volcanic rocks in the central Wasatch Mountains (Fig. A3.4). All of the samples in the region contain minor amounts of magmatic sulfides as inclusions inside magmatic phases (Borrok et al., 1999). Secondary pyrite and chalcopyrite are present in the groundmass of a few samples. Microprobe analyses of apatites show that the apatite in these stocks contains up to 1 wt% SO₃. No samples from the Bingham district were included because the only unaltered samples available are too small to extract significant amounts of sulfur.

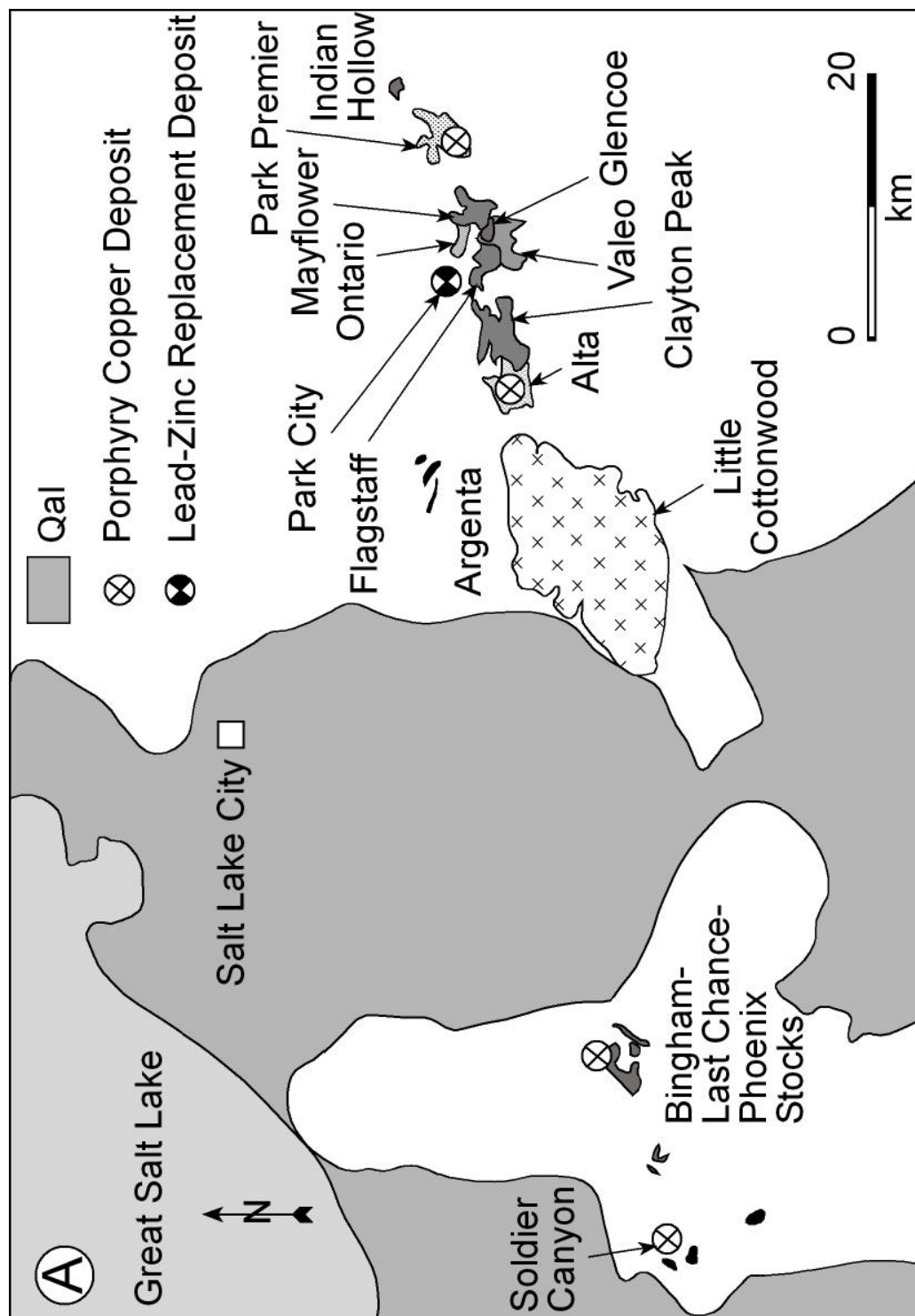


Figure A3.4. Geologic map of the Bingham-Park City belt showing location of intrusive rocks and ore bodies

Results

Standard Extractions

Results for two mixtures of standards show that the total sulfide yield was low due to small amounts of oxidation (Table A3.1). We have obtained similar results for the AVS and CRS steps as Rice et al. (1994). If SnCl_2 is not added to the extraction between 10-20% of the AVS was oxidized and was not recovered during the AVS step. The yield for the sulfate step was high in both extractions due to recovery of the sulfide oxidized during the first two steps. Less than 5% of the sulfate yield is due to oxidized sulfide from the previous steps. Total sulfur recovery was within 3% of the expected value given the weights of the standards used, well within expected weighing errors.

Extraction of Sulfur from Granitoids

Sulfur was extracted from 15 granitoids samples to test the BaSO_4 and HI sulfate recovery methods (Table A3.2). Sulfide in granitoids was found to range from 0-266 ppm with most samples containing less than 10 ppm. Sulfide levels were slightly higher than those predicted by Borrok et al. (1999), which may be due to sulfide substituting in biotite. In many cases the sulfide samples were too small to get meaningful isotopic measurements. When enough sulfur was recovered the $\delta^{34}\text{S}$ values range from -4.2 to 6.9 ‰.

As discussed above there are problems associated with sulfate extraction from granitoids. Due to the low levels of sulfate, very little BaSO_4 is formed and instead a large amount of amorphous Ba phosphate precipitated. This makes it impossible to quantify the amount of sulfate recovered and also causes problems in analyzing the sulfur isotopes since it is difficult to determine how much sulfur is in the precipitate. Only three samples using this method produced meaningful results using the BaSO_4 method, and two of those were anhydrite-bearing samples with >1000 ppm sulfate. Using the HI method for sulfate reduction, sulfate was recovered from all samples tested, and all but one was large enough to obtain an isotopic composition. These samples have sulfate contents from 7-

Table A3.1. Results of standard extractions.

	Mix 1	Mix 2
Starting mixture (mg)		
ZnS (AVS)	8.86	6.51
FeS ₂ (CRS)	3.13	7.13
BaSO ₄	11.46	11.31
S AVS	2.92	2.14
S CRS	1.67	3.81
S SO ₄	1.57	1.55
Total S	6.16	7.51
Recovered sulfur (mg)		
Ag ₂ S AVS	21.80	16.28
Ag ₂ S CRS	12.20	28.95
Ag ₂ S SO ₄	12.35	12.61
S AVS	2.82	2.11
S CRS	1.58	3.75
S SO ₄	1.60	1.63
Total S	6.00	7.48
% AVS recovered	96.76	98.34
% CRS recovered	94.36	98.29
% SO ₄ recovered	101.50	105.01
% Total S recovered	97.32	99.70

Table A3.2A. Sulfur content of granitoid sample in ppm for various forms of sulfur.

Sample	Location	Region	AVS	CRS	AVS+CRS	SO ₄	SO ₄ method
HF-11	Hanover-Fierro	New Mexico	0.0	266	266	3460	BaSO ₄
HF-10	Hanover-Fierro	New Mexico	0.0	28	28	1080	BaSO ₄
HF-4	Hanover-Fierro	New Mexico	0.0	13	13	<35	BaSO ₄
LC-2	Little Cottonwood	Utah	0.0	10.4	10.4	41	BaSO ₄
LC-6	Little Cottonwood	Utah	0.0	90	90	59	BaSO ₄
LC-1	Little Cottonwood	Utah	0.0	11.0	11.0	<42	BaSO ₄
TC93713-12	Clayton Peak	Utah	nd	nd	4.3	<35	BaSO ₄
TC93713-9	Clayton Peak	Utah	4.4	2.8	7.2	7.1	HI
TC93713-14	Clayton Peak	Utah	nd	nd	10.5	<28	BaSO ₄
93720-9	Alta	Utah	nd	nd	8.7	<32	BaSO ₄
93720-12	Alta	Utah	3.3	2.5	5.9	12.6	HI
93719-18	Alta	Utah	3.3	0.0	3.3	10.3	HI
930718-12	Alta	Utah	3.3	1.6	4.9	37.1	HI
TPC93905-10	Pine Creek	Utah	6.3	3.7	10.0	124.1	HI
TPC939706-9	Pine Creek	Utah	5.8	2.2	8.0	22.2	HI
KV950718-8	Keetely	Utah	0.0	4.9	4.9	27.6	HI
950718-9a	Keetely	Utah	5.3	3.1	8.4	22.1	HI

Table A3.2B. Sulfur isotopic composition of granitoid samples in per mil relative to Canyon Diablo Troilite for various forms of sulfur.

Sample	Location	Region	$\delta^{34}\text{S}$ AVS	$\delta^{34}\text{S}$ CRS	$\delta^{34}\text{S}$ S ²⁻	$\delta^{34}\text{S}$ SO ₄	Bulk $\delta^{34}\text{S}$
HF-11	Hanover-Fierro	New Mexico	na	-2.3	-2.3	6.7	6.1
HF-10	Hanover-Fierro	New Mexico	na	-2.8	-2.8	7.4	7.1
HF-4	Hanover-Fierro	New Mexico	na	-0.8	-0.8	cont	na
LC-2	Little Cottonwood	Utah	na	ts	ts	cont	na
LC-6	Little Cottonwood	Utah	na	-1.0	-1.0	6.5	2.0
LC-1	Little Cottonwood	Utah	na	ts	ts	cont	na
TC93713-12	Clayton Peak	Utah	nd	nd	5.9	cont	na
TC93713-9	Clayton Peak	Utah	4.8	ts	4.8	ts	na
TC93713-14	Clayton Peak	Utah	nd	nd	6.9	cont	na
93720-9	Alta	Utah	nd	nd	1.3	cont	na
93720-12	Alta	Utah	ts	ts	ts	4.3	na
93719-18	Alta	Utah	ts	ts	ts	1.8	na
930718-12	Alta	Utah	ts	ts	ts	5.9	na
TPC93905-10	Pine Creek	Utah	ts	ts	ts	8.9	na
TPC939706-9	Pine Creek	Utah	nd	nd	1.2	4.3	3.5
KV950718-8	Keetely	Utah	na	3	3	5.7	5.3
950718-9a	Keetely	Utah	5.4	ts	5.4	4.2	4.5

na = not analyzed because none was recovered; nd = not determined separately because AVS and CRS were combined; ts = sample too small; cont = sulfate precipitates contaminated with barium phosphate.

124 ppm and sulfate S isotopic values between 1.8 and 9 ‰. The bulk $\delta^{34}\text{S}$ of the granitoids ranges from 2.0 to 7.5 ‰ with an average of 4.5 ‰.

Discussion

Sulfur extraction methods

The method presented above provides several advantages over previous extraction methods. The major advantage over the techniques of Rice et al. (1993) and Hall et al. (1988) is that the extraction is done continuously in a single reaction vessel, eliminating the need for transferring the sample and filtering the rock powder. This reduces loss of sample through transferring and saves time expended during filtration. The method presented in this study sacrifices the ability to separate acid soluble sulfate, native sulfur and organically bound sulfur, but these are not significant components in most igneous and metamorphic rocks.

The method of Ueda and Sakai (1983) requires the use of a vacuum line and heating up to 280°C whereas the above method can be done at 100°C under a N_2 atmosphere. Their method also requires the Kiba reagent, which attacks glassware and will reduce sulfate to H_2S in the presence of water making it difficult to separate sulfide and sulfate. Ueda and Sakai (1983) also had a lower yield for pyrite sulfur of 90% compared to 96% for the above method indicating that CrCl_2 reduction is a more effective means of recovering disulfide.

Sulfur isotopic composition of granitoids

Typical arc volcanic rocks have bulk $\delta^{34}\text{S}$ from 0 to 10‰ (Alt et al., 1993; McKibben et al., 1996; Luhr and Logan, 2002). Enrichment of ^{34}S in arc volcanic rocks has been explained by contributions of sulfur from the subducting slab, contamination with hydrothermal sulfate, and open system degassing. The bulk $\delta^{34}\text{S}$ of the Hanover-Fierro stock is 6.5‰, suggesting that some or all of these processes occurred during the formation and crystallization of the Hanover-Fierro stock. Since the Hanover-Fierro stock formed during subduction, contribution of sulfur from the subducting slab is likely. There

is also evidence of both primary magmatic anhydrite and later hydrothermal anhydrite. Any later anhydrite would likely be isotopically heavier than magmatic anhydrite because it would form at a lower temperature. If there is not corresponding sulfide, the bulk $\delta^{34}\text{S}$ of the stock would be overestimated. Ion microprobe analysis of sulfur isotopes in anhydrite from the Pinatubo dacite and El Chichon trachyandesite show two populations of anhydrite suggesting that one is primary magmatic anhydrite and the other is hydrothermal (McKibben et al., 1996; Luhr and Logan, 2002). Degassing probably did not have a large affect on the isotopic composition of the Hanover-Fierro stock because the stock crystallized at extremely high $f\text{O}_2$. This would indicate most of the sulfur present in the magma would be sulfate and the vapor phase would be SO_2 -rich. Degassing under these conditions has little effect on bulk $\delta^{34}\text{S}$ (Alt et al., 1993).

The formation of the BPCB magmas is more complex because they formed after the cessation of subduction in the western US (Vogel et al., 2001). The magmas are thought to have formed through partial melting of a mafic lower crust that may have been ponded mafic magmas emplaced during earlier subduction. If this is the case, the bulk $\delta^{34}\text{S}$ would be expected to be enriched in ^{34}S similar to typical arc rocks. BPCB rocks have bulk $\delta^{34}\text{S}$ from 2.0 to 5.3 ‰ consistent with origin from ponded mafic magmas. The BPCB magmas crystallized at lower oxygen fugacity than the Hanover-Fierro stock suggesting that degassing could have an important affect on the sulfur isotopic composition of the magmas. However, the narrow range of compositions observed suggests a similar source for the sulfur in the different intrusions and that degassing had very little effect.

Sulfide-sulfate fractionation

The expected fractionation between sulfide and sulfate is 7 to 8 ‰ at 800°C and increases to 9 to 9.5 ‰ at 700°C (Ohmoto and Lasaga, 1982). The observed fractionation between sulfide and sulfate in the granitoids in this study is between -1.2 to 10 ‰, indicating that processes other than simple fractionation at magmatic temperature are

necessary to explain the sulfur isotopic compositions. The isotopic fractionation observed between pyrite and anhydrite for the anhydrite-bearing samples of the Hanover-Fierro stock indicates equilibrium temperatures of 650-700°C. Consistent with near-solidus equilibration of the sulfur isotopic composition. The fractionation is larger than the 7.5‰ observed between magmatic chalcopyrite and anhydrite in the Pinatubo dacite (McKibben et al., 1996). Hydrothermal anhydrite in the Pinatubo dacite is isotopically heavier than the magmatic anhydrite, indicating that larger fractionation observed in the Hanover-Fierro stock may be the result of hydrothermal anhydrite in addition to the magmatic anhydrite.

The Little Cottonwood stock has sulfide $\delta^{34}\text{S}$ of -1.0‰ and sulfate $\delta^{34}\text{S}$ of 6.5‰ indicating temperatures of approximately 800°C, assuming isotopic equilibrium. This temperature is high for the felsic and hydrous Little Cottonwood stock suggesting that the isotopic values are not magmatic. The only sample that produced enough sulfide for recovery contained abundant secondary pyrite so the sulfide is largely hydrothermal. The sulfate, however, is likely magmatic sulfur recovered from apatite.

In the Alta and Pine Creek stocks and Keetely volcanic units the $\delta^{34}\text{S}$ of sulfide and sulfate are similar and would indicate temperature of equilibration of over 1000°C. In these cases it is likely that the sulfide and sulfate are not in equilibrium. This could result from weathering of sulfide minerals to produce sulfate. That process would lead to sulfate with the same isotopic composition as the sulfide (Taylor et al., 1984).

The sulfides present in most samples in this study are small inclusions of magmatic sulfides in mafic minerals. For all samples except LC-6 there is a general trend between the percentage of sulfide sulfur and the $\delta^{34}\text{S}$ of the sulfide (Fig. A3.5). This correlation is likely due to fractionation between sulfide and sulfate during crystallization. The magmatic sulfide/sulfate ratio is dependent on the oxygen fugacity of the magma so the $\delta^{34}\text{S}$ of magmatic sulfide should relate to the magmatic oxygen fugacity. The correlation can be predicted using the equation of Wallace and Carmichael (1994) to

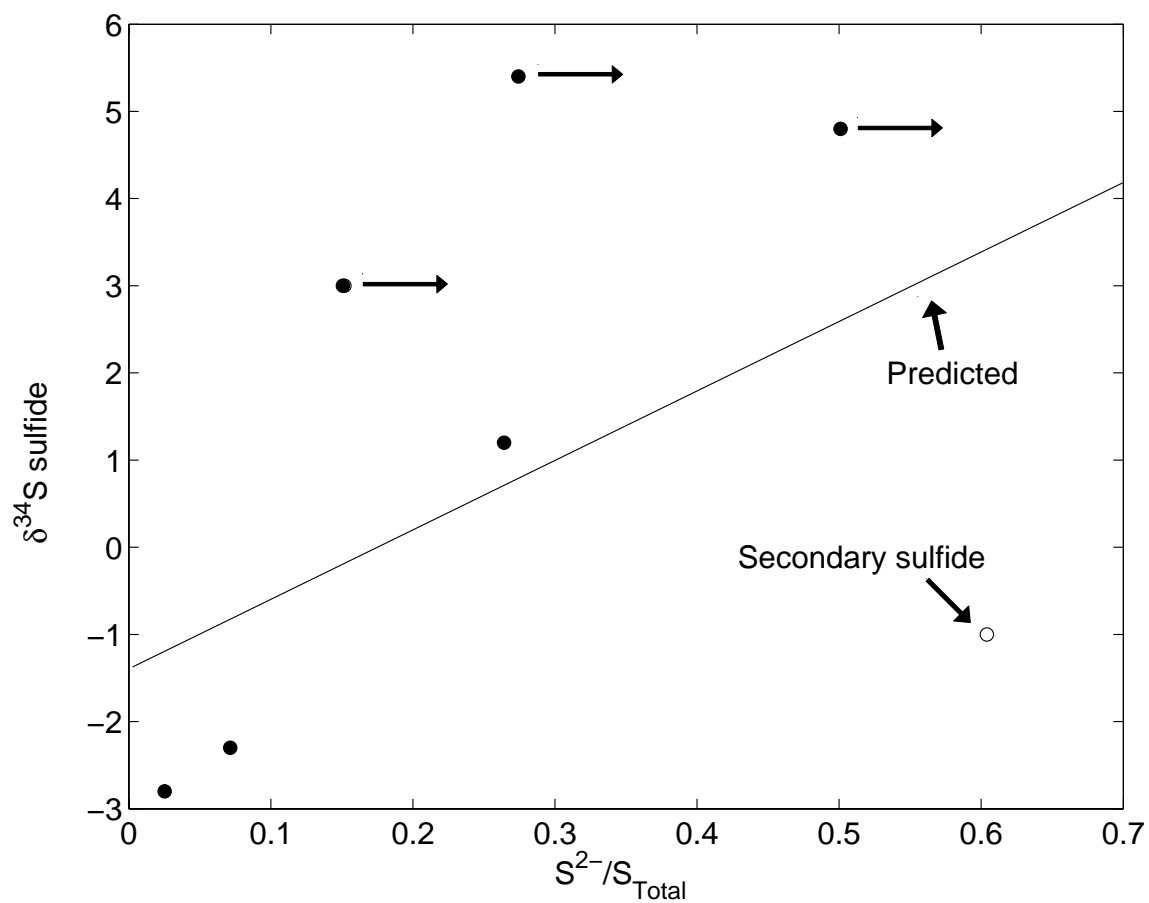


Figure A3.5. Fraction of sulfide sulfur plotted against the $\delta^{34}S$ of the sulfide sulfur. Line is the trend predicted for a typical granitoid at 800°C with fractionation of 7.5 ‰ and bulk $\delta^{34}S$ of 6 ‰. Samples with highest sulfide $\delta^{34}S$ show oxidation of sulfide, indicating that the original S^{2-}/S_{Total} was higher as indicated by the arrows.

determine sulfide/sulfate and an estimated fractionation of 7.5 ‰ at 800°C. Deviation of the data from the predicted line is likely due to oxidation of sulfides leading to changes in the S^{2-}/S_{Total} ratio and variations in bulk composition.

Conclusions

These data show that isotope composition of sulfide and sulfate in granitoids can provide valuable information about the behavior of sulfur during the crystallization and subsolidus alteration of granitoids. Bulk analysis of sulfur isotopes may be misinterpreted due to the presence of secondary sulfide and sulfate minerals. Such problems are more evident when looking at the $\delta^{34}\text{S}$ of sulfide and sulfate independently.

References

- Alt, J. C., Shanks, W. C., III, and Jackson, M. C., 1993, Cycling of sulfur in subduction zones; the geochemistry of sulfur in the Mariana island arc and back-arc trough: *Earth and Planetary Science Letters*, v. 119, p. 477-494.
- Borrok, D., Kesler, S. E., and Vogel, T. A., 1999, Sulfide mineral in intrusive and volcanic rocks of the Bingham-Park City Belt, Utah: *Economic Geology*, v. 94, p. 1213-1230.
- Canfield, D. E., Raiswell, R., Westrich, J. T., Reaves, C. M., and Berner, R. A., 1986, The use of chromium reduction in the analysis of reduced inorganic sulfur in sediments and shales: *Chemical Geology*, v. 54, p. 149-155.
- Hall, G. E. M., Pelchat, J.-C., and Loop, J., 1988, Separation and recovery of various sulphur species in sedimentary rocks for stable sulphur isotopic determination: *Chemical Geology*, v. 67, p. 35-45.
- Ishihara, S., and Sasaki, A., 1989, Sulfur isotopic ratios of the magnetite-series and ilmenite-series granitoids of the Sierra Nevada Batholith: a reconnaissance study: *Geology*, v. 17, p. 788-791.
- John, D. A., 1989, Geologic setting, depths of emplacement, and regional distribution of fluid inclusions in intrusions of the central Wasatch Mountains, Utah: *Economic Geology*, v. 84, p. 386-409.
- Luhr, J. F., and Logan, M. A. V., 2002, Sulfur isotope systematics of the 1982 El Chichon trachyandesite: an ion microprobe study: *Geochimica et Cosmochimica Acta*, v. 66, p. 3303-3316.
- McKibben, M. A., Eldridge, C. S., and Reyes, A. G., 1996, Sulfur isotopic systematics of the June 1991 Mount Pinatubo eruptions; a SHRIMP ion microprobe study, *in* Newhall, C. G., and Punongbayan, R. S., eds., *Fire and Mud: Eruptions and Lahars of Mount Pinatubo, Philippines*, p. 825-843.
- Ohmoto, H., and Lasaga, A. C., 1982, Kinetics of reactions between aqueous sulfates and

- sulfides in hydrothermal systems: *Geochimica et Cosmochimica Acta*, v. 46, p. 1727-1745.
- Rice, C. A., Tuttle, M. L., and Reynolds, R. L., 1993, The analysis of forms of sulfur in ancient sediments and sedimentary rocks: comments and cautions: *Chemical Geology*, v. 107, p. 83-95.
- Rose, A. W., and Baltosser, W. W., 1966, The porphyry copper deposit at Santa Rita, New Mexico, *in* Titley, S. R., and Hicks, C. L., eds., *Geology of the Porphyry Copper Deposits, Southwestern North America*.
- Sasaki, A., Arikawa, Y., and Folinsbee, R. E., 1979, Kiba reagent method of sulfur extraction applied to isotopic work: *Japan Geological Survey Bulletin*, v. 30, p. 241-245.
- Sasaki, A., and Ishihara, S., 1979, Sulfur isotopic composition of the magnetite-series and ilmenite-series granitoids in Japan: *Contributions to Mineralogy and Petrology*, v. 68, p. 107-115.
- Taylor, B. E., Wheeler, M. C., and Nordstrom, D. K., 1984, Isotope composition of sulfate in acid mine drainage as a measure of bacterial oxidation: *Nature*, v. 308, p. 538-541.
- Thode, H. G., Monster, J., and Dunford, H. B., 1961, Sulphur isotope geochemistry: *Geochimica et Cosmochimica Acta*, v. 25, p. 159-174.
- Titley, S. R., 1993, Characteristics of porphyry copper occurrence in the American Southwest: *Geological Association of Canada Special Paper*, v. 40, p. 433-464.
- Tuttle, M. L., Goldhaber, M. B., and Williamson, D. L., 1986, An analytical scheme for determining forms of sulphur in oil shales and associated rocks: *Talanta*, v. 33, p. 953-961.
- Ueda, A., and Sakai, H., 1983, Simultaneous determinations of the concentration and isotope ratio of sulfate- and sulfide-sulfur and carbonate-carbon in geological samples: *Geochemical Journal*, v. 17, p. 185-196.
- Vogel, T. A., Cambray, F. W., and Constenius, K. N., 2001, Origin and emplacement of

igneous rocks in the central Wasatch Mountains, Utah: Rocky Mountain Geology,
v. 36, p. 119-162.

Appendix IV

Copper and Zinc Content of Magmatic Silicate and Oxide Minerals

Introduction

Granitoid magmas are associated with a wide range of magmatic-hydrothermal ore deposits containing Cu and Zn, and are thought to be the main source of these metals. Many chemical and physical factors affect whether an intrusion can form an ore deposit. One of these is the availability of metals when a magmatic vapor phase separates from the magma. If metals have partitioned into phases crystallizing from the melt, they will not enter a magmatic vapor phase. Information on metal content and zoning in magmatic silicate and oxide minerals in granitoids is needed to determine conditions under which this could be an important constraint on formation of metal-rich magmatic hydrothermal solutions. Surprisingly little information of this type is available because metal concentrations are below detection limit of most analytical methods. In this study, Zn and Cu were measured in silicates and oxides using synchrotron X-ray fluorescence (SXRF) and zoning of these metals was examined with traverses across grains. Preliminary results suggest that copper and zinc behave very differently during magmatic crystallization and that both metals are redistributed in otherwise fresh igneous rocks by late hydrothermal fluids.

Geologic Setting of Samples Used in the Study

The Bingham-Park City belt (BPCB) consists of 15 granitoid intrusions and coeval dike and volcanic rocks that crop out in an E-W trending belt. The BPCB magmas probably formed by partial melting of lower crustal equivalents of the amphibolites in the Little Willow Formation and were emplaced in an extensional tectonic regime (Vogel et

al., 2001). The intrusions have varying depths of exposure and are associated with a range of alteration types (John, 1989).

The intrusive system at Bingham is associated with the largest porphyry copper deposit (PCD) in North America. The Bingham PCD formed between 37.5 to 37.0 Ma and is associated with a composite intrusion (Chesley et al., 1997; Deino and Keith, 1997; Parry et al., 2001). The first intrusive phases at Bingham are the equigranular Last Chance and Bingham stocks and the Phoenix dike, which are 38.6 ± 0.2 m.y. old and are not associated with significant mineralization (Parry et al., 2001). They were followed by the quartz monzonite porphyry (QMP) that is associated with the majority of mineralization and the later quartz latite porphyry (QLP) and latite porphyry (LP) that are associated with small amounts of mineralization (Redmond, 2002). All phases are cut by the Ohio Copper post-mineral dike.

Analytical Methods

Samples were obtained from seven intrusions in the Bingham-Park City belt and the Keetely volcanic units. Thin sections of each sample were examined to determine the degree of alteration and least altered samples were selected for further analysis.

Synchrotron X-ray fluorescence

Minerals were analyzed by synchrotron X-ray fluorescence (SXRF) using the sector seven beamline (MHATT-CAT) at the Advanced Photon Source at Argonne National Labs. Analyses were made on grains in thin sections mounted on Suprasil pure silica glass to avoid high background concentrations in normal glass. In order to minimize the volume sampled during the analysis, thin sections were ground to a thickness of 10 μm . The samples were examined optically and unaltered grains with clear paragenesis were selected for analysis.

SXRF analyses were made using an X-ray beam with incident energy of 14 keV. The beam was focused to a spot size of approximately 4 μm using Pd coated mirrors in a Kirkpatrick-Baez (KB) orientation (Kirkpatrick and Baez, 1948). The beam was focused

on a Nd-YAG crystal and the light from the fluorescence of the YAG was reflected to a camera. The size of the beam was minimized by adjusting the KB mirrors. The size of the beam was checked by moving a tungsten wire into the path of the beam and monitoring the flux with an ion chamber located behind the wire.

The samples were viewed through a microscope objective with a long working distance, which was attached to a closed circuit video system. The beam caused visible fluorescence allowing determination of its approximate location on the sample. In a few samples a map of the Fe content in the area of interest was used to provide additional information about the location of spot analyses. This map permitted location of the beam within 5 microns.

Data were collected using a single element Ge detector placed 8 cm from the sample. A 100 μ m high-purity aluminum filter was placed in front of the detector to prevent the detector from being flooded by the high X-ray flux. Peak intensities were corrected for absorption by the Al filter. Spectra were collected for 120s and background subtraction was done using MCApro (Smith and Rivers, 1995). Concentrations of Cu and Zn were determined using Fe as an internal standard. Ratios of Cu to Fe were calculated using the method of Criss (1977). Detection limits for Cu were between 0.1-0.5 ppm for silicates and 5-10 ppm for oxides depending on the Fe content of the mineral. Precision of these analyses is generally less than 2% 2-sigma. Accuracy is not this high due to errors introduced from using an internal standard, but should be less than 10% 2-sigma. In addition to point analyses, traverses and maps were made on some of the grains. Step sizes of 2 and 5 microns were used for traverses and maps, respectively. The K α peaks of the elements were monitored for 1-2 seconds on each step.

Electron Microprobe

The major element composition of all phases was determined by electron microprobe analysis (EMPA) using a Cameca SX100 electron microprobe at the University of Michigan. All minerals were analyzed for Fe, Ca, Na, Al, Si, Ti, Ba, Mg,

Mn, and K. The incident beam had energy of 15 kV and the sample current was 10 nA. A focused beam was rastered on a 5 μm spot to minimize beam damage and element migration. Natural and synthetic oxide and silicate minerals were used as standards. Counting times were 20 seconds for all elements except Fe, which was analyzed for 40 seconds.

Results

Cu and Zn content

The Cu content of unaltered silicate and oxide minerals was found to be low (Tables A4.1 – A4.12). Many grains had erratic zones with approximately an order of magnitude more Cu. Zinc contents of grains was found to be much higher and not as variable as the Cu content. Unaltered biotite was found to contain 0.6 to 74 ppm Cu with a median value of 8 ppm and high Cu zones that contain 20 to 1000 ppm Cu. The highest Cu content of biotite was found in the Soldier Canyon and Clayton Peak stocks. Zinc content was found to range from 468 to 958 ppm with a median value of 728.3 ppm. The Pine Creek stock had the highest concentration of Zn in biotite. Chlorite grains from the Alta stock were analyzed and found to contain 29 to 570 ppm Cu and 1150 to 1540 ppm Zn.

Clinopyroxene was analyzed in the Clayton Peak, Last Chance, and Soldier Canyon stocks. It contains 1.7 to 19.4 ppm Cu with a median value of 5.5 ppm and enriched zones with 26 to 120 ppm Cu. The Last Chance stock contains clinopyroxene with the lowest Cu content. Concentration of Zn are higher than Cu at 200 to 611 ppm with a median value of 345 ppm.

Hornblende was found to contain 2.0 to 59.2 ppm Cu with a median value of 5.1 ppm. The hornblende with highest Cu are from the Ontario stock and the Keetely volcanic units. All other hornblende has very low Cu content. Enriched zones in the hornblende contain 38 to 200 ppm Cu. The range of Zn concentration for hornblende was

Table A4.1. SXRF analyses of unaltered biotite.

Sample	Unit	Type	SXRF Zn (ppm)	SXRF Cu (ppm)	EMPA Fe (ppm)
A19-18	Alta	core	738	3.8	128870
A20-12	Alta	rim	632	5.8	128610
A20-12	Alta	core	638	7.0	129560
A20-12	Alta	core	631	3.7	129680
A20-12	Alta	rim	695	9.9	135640
CP13-14	Clayton Peak	core	838	13.7	127800
CP13-14	Clayton Peak	core	757	22.4	112370
CP13-18	Clayton Peak	core	728	26.6	106910
KV18-12	Keetely	core	699	15.5	113260
KV18-12	Keetely	core	740	9.2	114420
KV18-12	Keetely	core	549	8.5	84380
KV18-12	Keetely	core	468	16.9	85530
LC10	Last Chance	core	557	6.3	89940
LC5	Last Chance	core	652	3.3	109950
LC5	Last Chance	core	670	6.7	110250
LC5	Last Chance	rim	707	8.9	106160
LC7	Last Chance	core	846	6.6	102430
LC7	Last Chance	rim	836	3.3	97470
LC7	Last Chance	core	941	8.1	107290
LC7	Last Chance	rim	800	0.6	93520
LC7	Last Chance	core	838	6.0	101910
LC7	Last Chance	rim	880	7.1	103440
LC7	Last Chance	core	828	14.7	100430
O11-4	Ontario	core	522	5.3	85800
O11-4	Ontario	rim	500	6.0	82980
O11-4	Ontario	core	531	9.9	86380
PC5-10	Pine Creek	core	958	7.3	113040
PC6-9	Pine Creek	rim	683	5.5	92140
PC6-9	Pine Creek	core	949	9.8	120490
PC6-9	Pine Creek	core	915	17.0	118640
SC5	Soldier Canyon	core	835	57.7	109550
SC5	Soldier Canyon	rim	832	56.0	104880
SC5	Soldier Canyon	core	761	20.9	115730
SC5	Soldier Canyon	rim	720	74.3	98000
SC5	Soldier Canyon	core	700	55.0	111770

Table A4.2. SXRF analyses of high-Cu biotite.

Sample	Unit	Type	SXRF	SXRF	EMPA
			Zn (ppm)	Cu (ppm)	Fe (ppm)
A19-18	Alta	rim	803	20	131610
A20-12	Alta	core	787	98	130370
A20-12	Alta	core	588	22	128280
A20-12	Alta	core	723	94	127020
A20-12	Alta	rim	790	48	125260
A20-12	Alta	rim	1655	741	166740
A20-12	Alta	rim	786	132	125040
A20-12	Alta	core	904	36	133490
A20-12	Alta	core	644	20	130370
CP13-14	Clayton Peak	rim	1150	2706	128250
CP13-14	Clayton Peak	core	796	65	123390
CP13-14	Clayton Peak	core	834	202	129540
CP13-14	Clayton Peak	core	846	163	126460
CP13-14	Clayton Peak	core	972	122	137790
CP13-14	Clayton Peak	rim	843	90	122890
CP13-18	Clayton Peak	rim	682	62	107250
CP13-18	Clayton Peak	core	659	107	111230
CP13-18	Clayton Peak	rim	658	97	107530
KV18-12	Keetely	rim	694	176	116470
KV18-12	Keetely	rim	762	228	117690
KV18-12	Keetely	core	699	118	113180
LC10	Last Chance	core	805	47	103840
LC10	Last Chance	rim	751	40	100490
LC10	Last Chance	rim	743	135	86340
LC10	Last Chance	core	1988	959	90190
LC10	Last Chance	core	927	131	109680
LC10	Last Chance	rim	643	75	89710
LC5	Last Chance	rim	725	56	105150
LC5	Last Chance	core	746	39	110530
LC7	Last Chance	rim	777	207	96460
O11-4	Ontario	rim	539	35	89330
OC1	Ohio Copper	core	841	53	101060
OC1	Ohio Copper	rim	718	32	92410
OC1	Ohio Copper	core	780	51	106670
OC1	Ohio Copper	rim	662	10	94070
PC5-10	Pine Creek	core	817	104	104940
PC5-10	Pine Creek	rim	746	33	95570
PC5-10	Pine Creek	rim	859	52	100030
PC6-9	Pine Creek	rim	721	107	90370
PC6-9	Pine Creek	core	937	35	119940
SC5	Soldie Canyon	rim	1389	683	104860
SC5	Soldie Canyon	core	877	159	110060

Table A4.3. SXRF analyses of chlorite.

Sample	Unit	Type	SXRF	SXRF	EMPA
			Zn (ppm)	Cu (ppm)	Fe (ppm)
A19-18	Alta	core	1197	29	153330
A19-18	Alta	core	1191	27	150290
A20-12	Alta	rim	1147	574	129560
A20-12	Alta	rim	1221	367	166830
A20-12	Alta	core	1544	269	162440

Table A4.4. SXRF analyses unaltered clinopyroxene.

Sample	Unit	Type	SXRF	SXRF	EMPA
			Zn (ppm)	Cu (ppm)	Fe (ppm)
CP13-14	Clayton Peak	core	447	13.1	75480
CP13-14	Clayton Peak	core	241	9.8	78770
CP13-18	Clayton Peak	core	330	19.4	72470
CP13-18	Clayton Peak	rim	345	4.2	72150
LC10	Last Chance	core	290	1.7	63830
LC10	Last Chance	rim	309	14.9	61700
LC5	Last Chance	core	318	4.2	66790
LC5	Last Chance	core	412	4.0	71950
LC5	Last Chance	rim	611	5.0	80000
LC7	Last Chance	rim	361	3.7	59300
LC7	Last Chance	core	414	1.8	69200
LC7	Last Chance	rim	398	5.5	58490
SC5	Soldier Canyon	core	200	10.6	40980
SC5	Soldier Canyon	rim	248	6.8	58060
SC5	Soldier Canyon	rim	402	18.1	56210

Table A4.5. SXRF analyses of high-Cu clinopyroxene.

Sample	Unit	Type	SXRF	SXRF	EMPA
			Zn (ppm)	Cu (ppm)	Fe (ppm)
CP13-14	Clayton Peak	rim	562	120	75870
CP13-18	Clayton Peak	rim	391	46	82440
CP13-18	Clayton Peak	core	329	69	70010
LC10	Last Chance	rim	370	70	60590
LC7	Last Chance	core	357	42	58680
LC7	Last Chance	core	426	73	65510
SC5	Soldier Canyon	rim	359	87	57100
SC5	Soldier Canyon	core	315	26	52880

Table A4.6. SXRF analyses of unaltered hornblende.

Sample	Region	Type	SXRF	SXRF	EMPA
			Zn (ppm)	Cu (ppm)	Fe (ppm)
A19-18	Alta	core	655	3.8	94090
A19-18	Alta	rim	517	3.1	89090
A19-18	Alta	core	609	4.2	96110
A19-18	Alta	rim	545	3.6	91220
A19-18	Alta	core	556	9.1	89680
A19-18	Alta	rim	519	4.0	88780
A20-12	Alta	core	483	9.1	92850
A20-12	Alta	rim	493	7.0	85970
CP13-14	Clayton Peak	core	220	5.3	40880
KV18-12	Keetely	core	251	19.5	86000
KV18-12	Keetely	rim	394	21.1	94330
KV18-8	Keetely	core	347	10.1	103290
KV18-8	Keetely	rim	337	4.1	91860
KV18-9	Keetely	core	418	4.8	98060
KV18-9	Keetely	rim	409	4.3	95840
LC5	Last Chance	rim	397	9.1	80000
LC5	Last Chance	rim	520	2.0	95800
O11-4	Ontario	core	411	59.2	69090
PC5-10	Pine Creek	core	684	5.2	125880
PC5-10	Pine Creek	rim	701	4.7	128940
PC5-10	Pine Creek	core	684	4.9	132070
PC5-10	Pine Creek	rim	669	5.9	125890

Table A4.7. SXRF analyses of high-Cu hornblende.

Sample	Region	Type	SXRF	SXRF	EMPA
			Zn (ppm)	Cu (ppm)	Fe (ppm)
CP13-14	ayton Pe	core	586	103	103680
KV18-12	Keetely	rim	749	92	111980
KV18-12	Keetely	rim	468	132	88640
KV18-12	Keetely	core	359	199	86890
KV18-12	Keetely	core	308	106	86000
KV18-8	Keetely	core	448	38	97650
KV18-8	Keetely	rim	486	101	93160
KV18-8	Keetely	core	394	60	96410
KV18-8	Keetely	rim	457	90	99460
KV18-9	Keetely	core	332	91	94870
O11-4	Ontario	rim	403	113	62190

Table A4.8. SXRF analyses of unaltered magnetite.

Sample	Region	Type	SXRF	SXRF	EMPA
			Zn (ppm)	Cu (ppm)	Fe (ppm)
A19-18	Alta	core	109	10.1	694960
A19-18	Alta	rim	88	20.6	694650
A19-18	Alta	core	104	16.0	697260
A20-12	Alta	core	168	10.5	712940
CP13-14	Clayton Peak	core	7831	16.6	691020
CP13-14	Clayton Peak	core	1336	26.5	606470
CP13-18	Clayton Peak	core	1841	29.8	672210
KV18-12	Keetely	core	2121	72.7	584350
KV18-12	Keetely	core	3086	95.8	581020
KV18-8	Keetely	core	1881	21.9	568470
KV18-8	Keetely	rim	1721	30.4	572870
KV18-8	Keetely	core	1890	37.9	581260
KV18-8	Keetely	rim	2040	24.7	586580
KV18-9	Keetely	core	1735	39.7	593520
KV18-9	Keetely	core	1422	22.3	611690
KV18-9	Keetely	rim	1524	14.9	616960
LC10	Last Chance	core	624	40.9	689440
LC10	Last Chance	rim	1074	21.8	691540
O11-4	Ontario	core	7411	42.9	668150
O11-4	Ontario	rim	5421	30.7	642550
O11-4	Ontario	core	4475	48.4	654330
O11-4	Ontario	rim	5919	31.7	664450
OC1	Ohio Copper	rim	604	77.9	689840
OC1	Ohio Copper	core	1545	18.8	689670
OC1	Ohio Copper	rim	1084	15.2	690500
PC5-10	Pine Creek	core	347	11.6	640110
PC5-10	Pine Creek	rim	325	9.6	684740
PC5-10	Pine Creek	core	1692	20.5	658250
PC5-10	Pine Creek	rim	1662	5.9	677820
SC5	Soldier Canyon	rim	372	17.5	695240

Table A4.9. SXRF analyses of high-Cu magnetite.

Sample	Region	Type	SXRF	SXRF	EMPA
			Zn (ppm)	Cu (ppm)	Fe (ppm)
CP13-18	Clayton Peak	core	523	110	671650
KV18-12	Keetely	core	5942	1844	584350
KV18-12	Keetely	core	3586	825	584350
KV18-12	Keetely	core	5820	1930	584350
KV18-12	Keetely	core	3486	620	584350
KV18-12	Keetely	rim	4600	1261	546380
KV18-12	Keetely	rim	5919	358	584350
KV18-9	Keetely	rim	1746	217	592100
SC5	Soldier Canyon	core	380	51	694110

Table A4.10. SXRF analyses of unaltered ilmenite.

Sample	Region	Type	SXRF	SXRF	EMPA
			Zn	Cu	Fe
LC5	Last Chance	rim	1101	53.4	383460
LC10	Last Chance	core	308	24.2	383630
LC10	Last Chance	rim	479	24.1	369890
LC5	Last Chance	core	427	5.2	377920
LC7	Last Chance	core	599	15.6	507530
LC7	Last Chance	rim	454	14.1	308900
LC7	Last Chance	core	468	20.7	563500

Table A4.11. SXRF analyses of unaltered feldspars.

Sample	Region	Type	SXRF	SXRF	EMPA
			Zn (ppm)	Cu (ppm)	Fe (ppm)
K-feldspary					
A19-18	Alta	core	3.5	1.0	550
CP13-14	Clayton Peak	rim	20.6	8.3	1580
CP13-14	Clayton Peak	rim	19.2	9.4	1360
LC10	Last Chance	rim	14.4	3.4	2540
O11-4	Ontario	core	16.3	6.8	1010
OC1	Ohio Copper	core	6.6	1.3	100
Plagioclase					
A20-12	Utah	rim	8.9	1.8	1170
A20-12	Utah	core	6.1	3.8	620
KV18-12	Utah	core	19.5	4.2	2440
KV18-12	Utah	core	21.2	3.8	2500
KV18-12	Utah	rim	20.3	7.2	2650
KV18-12	Utah	rim	23.5	10.8	2510
KV18-8	Utah	core	21.5	3.4	2810
KV18-8	Utah	core	28.0	5.8	3150
KV18-9	Utah	core	24.1	10.6	2510
OC1	Utah	core	17.0	6.8	1970
PC5-10	Utah	core	2.5	2.0	200
PC6-9	Utah	core	22.3	6.5	1140
PC6-9	Utah	rim	16.4	4.3	1100
PC6-9	Utah	rim	15.2	6.0	1720
PC6-9	Utah	core	6.0	1.1	1620
PC6-9	Utah	rim	7.0	1.3	2300
PC6-9	Utah	rim	4.6	0.7	1430
SC5	Utah	rim	17.6	6.5	3490
SC5	Utah	core	5.1	7.1	1450

Table A4.12. SXRF analyses of unaltered feldspars.

Sample	Region	Type	SXRF	SXRF	EMPA
			Zn (ppm)	Cu (ppm)	Fe (ppm)
K-feldspar					
O11-4	Ontario	core	14.0	52.0	750
O11-4	Ontario	rim	6.3	461.0	810
Plagioclase					
KV18-12	Utah	rim	32.7	19.9	3080
KV18-12	Utah	core	36.4	17.6	3350
KV18-8	Utah	rim	37.3	27.7	3090
KV18-8	Utah	rim	43.1	25.7	3790
O11-4	Utah	core	33.9	20.4	2780
PC5-10	Utah	core	14.9	14.8	1740

determined to be 220 to 701 ppm with median value of 505 ppm. The highest Zn values were observed in the Pine Creek stock.

Magnetite was found to contain the highest Cu concentration ranging from 5.9 to 95.8 ppm with a median of 22.1 ppm. High Cu zones within magnetite grains contain between 51 to 1930 ppm Cu. Concentration of Zn in magnetite were also found to be the highest of any mineral with a range of 88 to 7830 ppm and median of 1604 ppm. Magnetite from the Alta stock was found to contain much less Zn than from other stocks. Ilmenite was analyzed from the Last Chance stock and was found to contain 5.2 to 53 ppm Cu with a median value of 20.7 ppm. Zinc in ilmenite ranged from 310 to 1100 ppm with median of 470 ppm.

Metal content of feldspars was found to be less than mafic silicates and oxides. The Cu content of feldspars ranged from 0.7 to 10.8 ppm with a median of 4.3 ppm. There were a few high Cu zones in feldspars with 17.6 to 461 ppm. Concentration of Zn was found to range from 2.5 to 28 ppm with a median value of 16.4 ppm.

Zoning of Cu and Zn

Examination of Cu and Zn zoning in silicate minerals focused on metal enrichment on rims of biotite grains (Fig. A4.1). The enriched rims are often a complex mixture of chlorite, magnetite, sphene, and K-feldspar. Enrichment was observed in samples of intrusive rocks regardless of degree of weathering. One biotite analyzed from the Keetely volcanic units shows gradual enrichment of Cu toward the rim rather than enrichment at the grain boundary.

Discussion

Behavior of base metals during crystallization

Our results indicate that the Cu content of unaltered silicates has a median value below 10 ppm Cu. Oxide minerals are slightly more enriched in Cu with around 20 ppm as a median value. This confirms that Cu is not concentrated in these phases during crystallization, in agreement with earlier studies (Banks, 1974, 1982; Hendry et al., 1982;

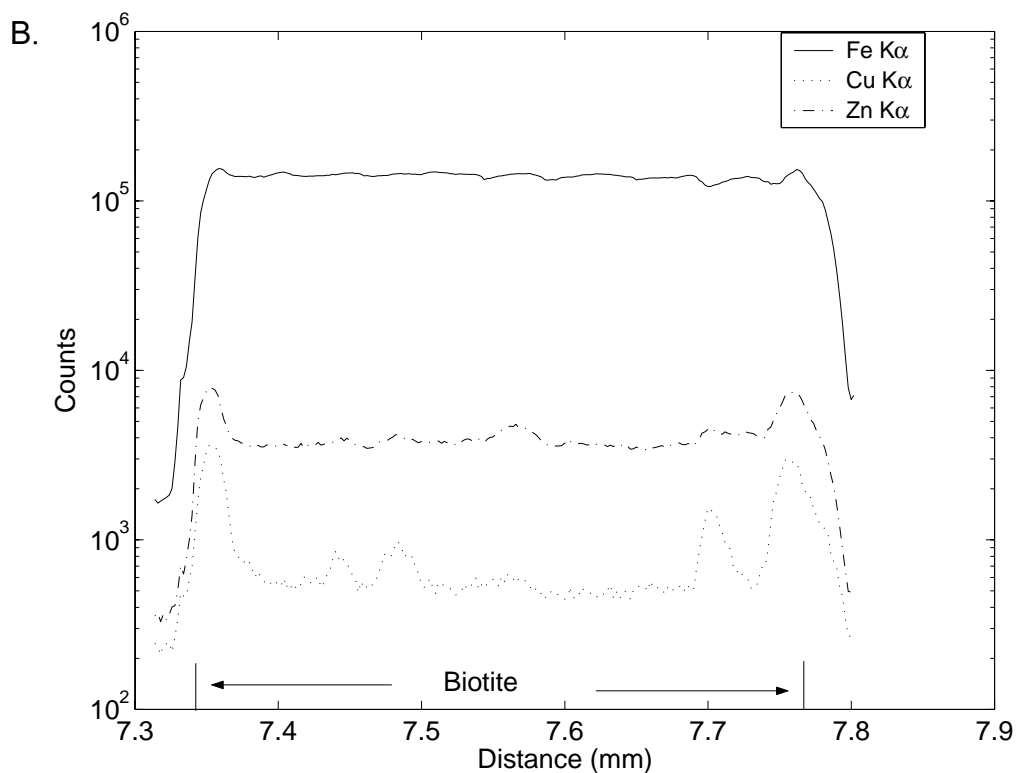
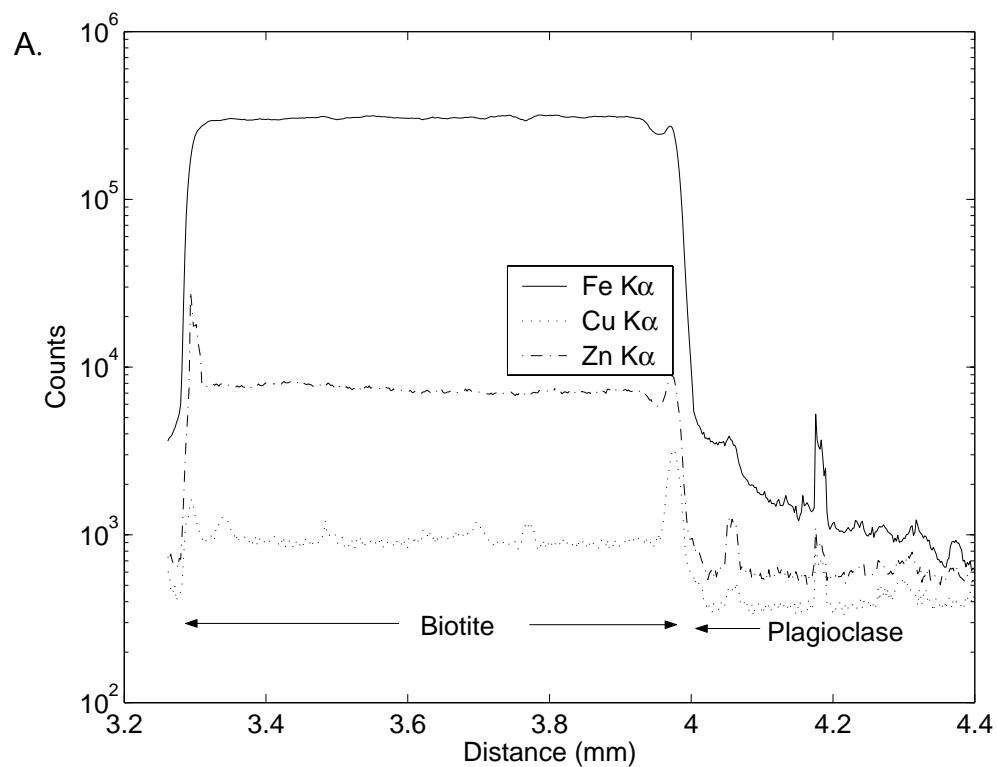


Figure A4.1. Traverses across biotite grains showing counts vs. distance. A. From Alta stock (A20-12) showing enrichment of both Cu and Zn at the grain boundary between biotite and plagioclase and irregular zoning inside the grain. B. From Alta stock (A20-12) showing enrichment of both Cu and Zn at grain boundary and irregular zoning inside the grain.

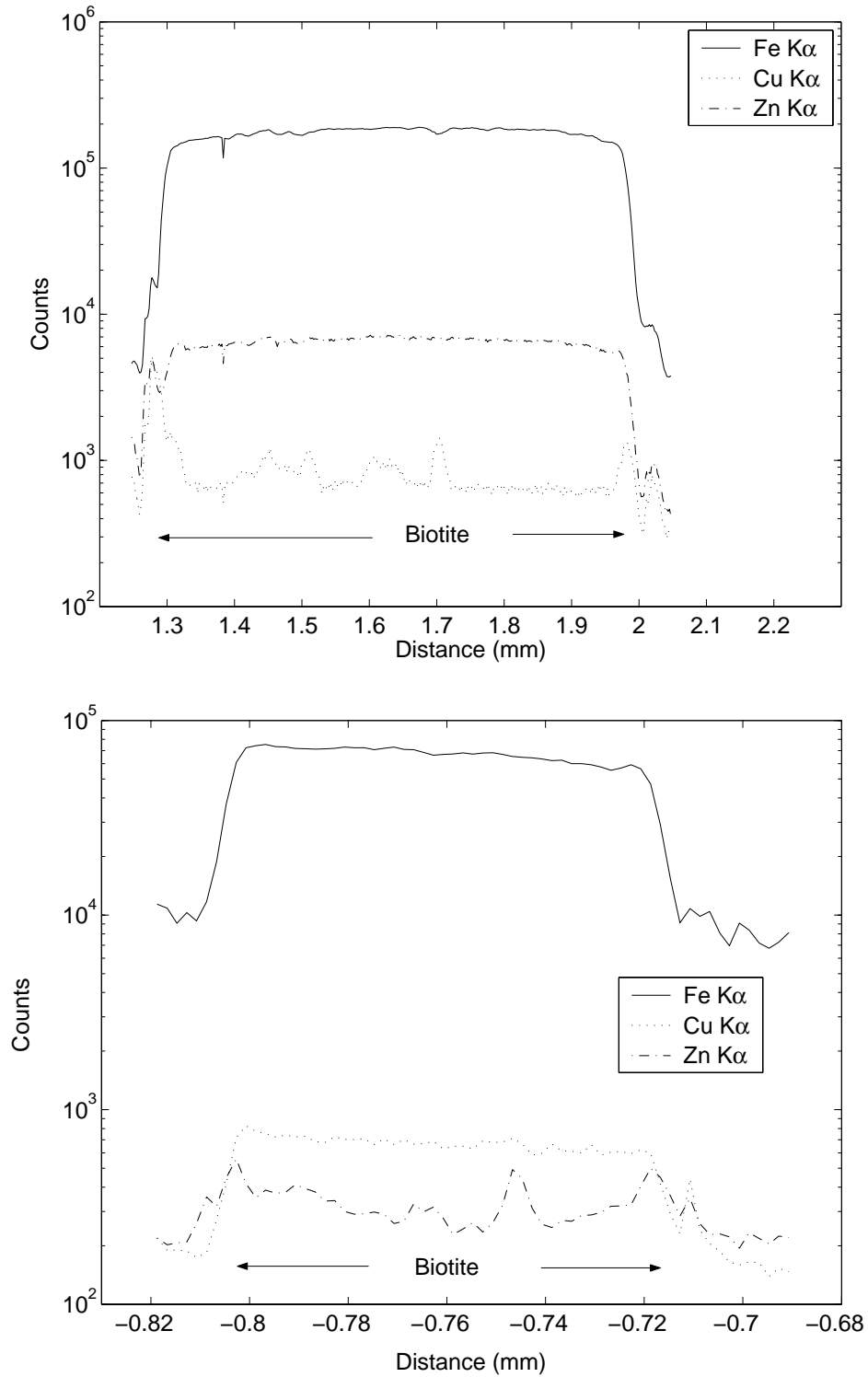


Figure A4.1 (cont'd). C. From Pine Creek (PC6-9) showing enrichment of Cu without Zn at the grain boundary and irregular zoning inside the grain. D. From Keetely volcanic units (KV18-12) showing gradual increase in Cu towards rim, suggesting magmatic zoning.

Hendry et al., 1985). Cu in magnetite was found to be erratic as shown in previous studies (Hendry et al., 1982; Hendry et al., 1985). Therefore, Cu should behave incompatibly during crystallization of a magma until as sulfide phase crystallizes or a magmatic vapor phase exsolves. A biotite scanned from the Keetely volcanic units appears to record magmatic zoning of Cu, showing slight enrichment towards the rim of the grain.

Zinc readily substitutes into Fe-bearing silicate minerals. Examples of this are petedunnite ($\text{CaZnSi}_2\text{O}_6$) solid solution in clinopyroxene and franklinite (ZnFe_2O_4) solid solution in magnetite. Zinc can also be found at varying levels in magmatic sulfides. Rarely magmatic sphalerite is reported as inclusions in igneous phases (Borrok et al., 1999). Zinc also substitutes at low levels into ISS and pyrrhotite during crystallization. Ewart and Griffin (1994) showed that Zn has a partition coefficient higher than one for most silicate and oxide phases. It most strongly partitions into magnetite with a coefficient as high as 70.

Our results indicate that Zn contents of typical mafic silicate and oxide minerals (500 to 1000 ppm) are considerably higher than Cu contents. Zinc content of magnetite can in this study has values up to 7000 ppm. Felsic minerals contain low levels of Zn (2.5 to 28 ppm). This suggests, in turn, that crystallization of most mafic minerals will deplete a melt in Zn. Because the Zn substitutes for Fe, magmas with high Zn/Fe ratios are most likely to form a Zn-rich MVP. These are likely to be highly felsic magmas such as granites and aplites. Zinc partitions strongly into magnetite suggesting that under high $f\text{O}_2$ conditions, when magnetite saturation would occur early, Zn could be stripped from the magma. Therefore, $f\text{O}_2$ may play an important role in Pb-Zn CRD generation, with low $f\text{O}_2$ intrusions being more likely to cause mineralization.

High Cu rims on biotite

Previous studies have shown that Cu is commonly enriched in biotite (Banks, 1974, 1982; Ilton and Veblen, 1988, 1993). In this study, SXRF analyses of biotites showed strong enrichment of Cu along rims in biotites from many of the intrusive rocks

used in this study (Fig. A4.1). Smaller amounts of Zn enrichment are typically present along with the high Cu values. The host for metals in the rims is thought to be chlorite on the edges of biotite produced during minor propylitic alteration. There is no visible sulfide in the rims, but sulfides could not be ruled out as a host of Cu since S could not be analyzed at the same time as Cu, Zn, and Fe.

Samples in this study did not undergo extensive weathering but the biotites showed minor propylitic alteration. This distinction is important because previous studies have shown that Cu is enriched in biotite that has been weathered or altered. In weathered biotite, expanded layers contain native copper that is thought to have formed during oxidation of nearby sulfides (Ilton and Veblen, 1988, 1993). In chlorite that forms by alteration of biotite, copper is also enriched, usually in areas containing copper minerals (Banks, 1974, 1982). Petrographic and SEM examination of the Cu-rich biotite rims that were observed here show minor propylitic alteration with thin rims of chlorite, sphene, magnetite, and K-feldspar that are typically less than 10 μ m wide.

Enrichment of Cu in biotite during alteration suggests that the biotites have been exposed to a hydrothermal fluid with a high Cu content. These rims are present in both barren and fertile intrusions in this study. However, not enough samples were examined to determine if this method holds potential for locating mineralization. Mapping of Cu enrichment in biotite needs to be done to determine distribution within an intrusive body. This may provide a means of vectoring towards mineralization using samples that do not show significant alteration.

References

- Banks, N. G., 1974, Distribution of copper in biotite and biotite alteration products in intrusive rocks near two Arizona porphyry copper deposits: *Journal of Research of the United States Geological Survey*, v. 2, p. 195-211.
- Banks, N. G., 1982, Sulfur and copper in magma and rocks: Ray porphyry copper deposit, Pinal County, Arizona, *in* Titley, S. R., ed., *Advances in Geology of Porphyry Copper Deposits, Southwestern North America*: Tucson, AZ, University of Arizona Press, p. 227-257.
- Borrok, D., Kesler, S. E., and Vogel, T. A., 1999, Sulfide mineral in intrusive and volcanic rocks of the Bingham-Park City Belt, Utah: *Economic Geology*, v. 94, p. 1213-1230.
- Chesley, J. T., and Ruiz, J., 1997, Preliminary geochronology on molybdenite mineralization from the Bingham Canyon ore deposit, Utah: *Geological Society of America Abstracts with Programs*, v. 29, p. 282.
- Criss, J. W., 1977, NRLXRF, A Fortran Program for X-Ray Fluorescence Analysis: Users' Reference Manual and General Documentation, COSMIC DOD-00065.
- Deino, A., and Keith, J. D., 1997, Ages of volcanic and intrusive rocks in the Bingham mining district, Utah: *Society of Economic Geologists Guidebook Series*, v. 29, p. 91-100.
- Ewart, A., and Griffin, W. L., 1994, Application of proton-microprobe data to trace-element partitioning in volcanic rocks: *Chemical Geology*, v. 117, p. 251-284.
- Hendry, D. A., Chivas, A. R., Long, J. V., and Reed, S. J., 1985, Chemical differences between minerals from mineralizing and barren intrusions from some North American porphyry copper deposits: *Contributions to Mineralogy and Petrology*, v. 89, p. 319-329.
- Hendry, D. A. F., Chivas, A. R., Reed, S. J. B., and Long, J. V. P., 1982, Geochemical evidence for magmatic fluids in porphyry copper mineralization. Part II. Ion-probe

- analysis of Cu contents of mafic minerals, Koloula igneous complex:
Contributions to Mineralogy and Petrology, v. 78, p. 404-412.
- Ilton, E. S., and Veblen, D. R., 1988, Copper inclusions in sheet silicates from porphyry
Cu deposits: Nature, v. 334, p. 516-518.
- Ilton, E. S., and Veblen, D. R., 1993, Origin and mode of copper enrichment in biotite
from rocks associated with porphyry copper deposits: a transmission electron
microscopy investigation: Economic Geology, v. 88, p. 885-900.
- John, D. A., 1989, Geologic setting, depths of emplacement, and regional distribution of
fluid inclusions in intrusions of the central Wasatch Mountains, Utah: Economic
Geology, v. 84, p. 386-409.
- Kirkpatrick, P., and Baez, V., 1948, Formation of optical images by X-rays: Journal of the
Optical Society of America, v. 38, p. 766-774.
- Parry, W. T., Wilson, P. N., Moser, D., and Heizler, M. T., 2001, U-Pb dating of zircon
and $^{40}\text{Ar}/^{39}\text{Ar}$ dating of biotite at Bingham, Utah: Economic Geology, v. 96, p.
1671-1683.
- Redmond, P. B., 2002, Magmatic-hydrothermal fluids and copper-gold ore formation at
Bingham Canyon, Utah [Ph.D. thesis]: Stanford, University, 228 p.
- Smith, J. V., and Rivers, M. L., 1995, Synchrotron X-ray microanalysis, *in* Potts, P. J.,
Bowles, J. F. W., Reed, S. J. B., and Cave, M. R., eds., Microprobe Techniques in
the Earth Sciences: London, Chapman and Hall, p. 163-233.
- Vogel, T. A., Cambray, F. W., and Constenius, K. N., 2001, Origin and emplacement of
igneous rocks in the central Wasatch Mountains, Utah: Rocky Mountain Geology,
v. 36, p. 119-162.

Appendix V

Additional Field Locations

Samples were collected from field areas that were not included in *Chapter III* (Table A5.1). Most of these areas were excluded because they did not contain the appropriate assemblage (two oxide or clinopyroxene-oxide) for fO_2 estimation. Many of these samples would be suitable for application of biotite-K-feldspar-magnetite equilibria to determine fO_2 . Samples from the remaining areas require additional study to determine if they are suitable for fO_2 calculation.

Table A5.1. Additional field areas not included in *Chapter III*.

District - intrusions sampled	Two oxides	Cpx-oxide	Biotite-oxide	Alteration
Ajo				
Cornelia (CO)	1 sample	n	y	strong
Growler Pass (GP)	n	n	y	strong
Cardigan Peak (CP)	n	n	y	strong
Ray				
Tortilla diorite				
Tortilla diorite (TO)	n	y	y	weak
Granite Mountain porphyry (GM)	n	n	y	weak
Ruby Star				
Ruby Star granodiorite (RS)	n	n	y	mod-strong
Hanover-Fierro				
Hanover-Fierro stock (HF)	n	n	y	weak
Cameron Creek stock (CC)	n	n	y	strong
Dikes and sill (NLS, ELS, FB, CQS)	n	n	y	strong
Tyrone				
Tyrone laccolith (TY)	n	n	y	weak
San Martin-Sabinas				
La Gloria granodiorite (SM or SA)	n	n	y	weak
Porphyry dikes (SM or SA)	n	n	y	strong
Zimapan				
Las Animas (LA)	n	n	y	strong
La Milpas (LM)	n	n	y	strong
Villa Juarez (VJ)	-	-	-	-
Taxhay (TA)	-	-	-	-
Charcas				
Unaltered rhyolite dike (SR5)	n	n	y	weak
Altered porphyry dikes (SR)	n	n	y	strong
El Sabino (ESAB)				
Bismark				
Bismark (BI, drill core with LC prefix)	n	n	y	strong
Microondas (MI)	n	n	n	strong
Concepcion del Oro				
Canada Grande (CG)	-	-	-	-
Tanque Nueve (TN)	-	-	-	-
Matuhuapil (MA)	n	n	y	strong
Nochebuena (NB)	n	y	n	moderate
Kamloops				
Iron Mask Batholith (SLH)	n	y	y	moderate
Tulamene (TU)	-	-	-	-
Mount Lolo (ML)	-	-	-	-
Vinsulla (VI)	-	-	-	-

Abbreviations in parentheses are prefixes for sample numbers. - indicates that no thin sections of samples were cut.